



**Calhoun: The NPS Institutional Archive**  
**DSpace Repository**

---

Theses and Dissertations

1. Thesis and Dissertation Collection, all items

---

1994-09

# A numerical study of wind forcing effects on the California Current System

Vann, James R.

Monterey, California. Naval Postgraduate School

---

<http://hdl.handle.net/10945/43035>

---

This publication is a work of the U.S. Government as defined in Title 17, United States Code, Section 101. Copyright protection is not available for this work in the United States.

*Downloaded from NPS Archive: Calhoun*



Calhoun is the Naval Postgraduate School's public access digital repository for research materials and institutional publications created by the NPS community. Calhoun is named for Professor of Mathematics Guy K. Calhoun, NPS's first appointed -- and published -- scholarly author.

**Dudley Knox Library / Naval Postgraduate School**  
**411 Dyer Road / 1 University Circle**  
**Monterey, California USA 93943**

<http://www.nps.edu/library>

①

NPS-OC-94-006

# NAVAL POSTGRADUATE SCHOOL

## Monterey, California

AD-A286 205



DTIC  
ELECTE  
NOV 15 1994  
S B D

### THESIS

A NUMERICAL STUDY OF  
WIND FORCING EFFECTS ON THE  
CALIFORNIA CURRENT SYSTEM

by

James R. Vann

September, 1994

Thesis Advisor:

Mary L. Batteen

Approved for public release; distribution is unlimited.

Prepared for:  
Office of Naval Research  
800 N. Quincy Street  
Arlington, VA 22217-5000

DTIC... 8

94-35200



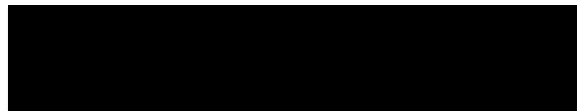
**NAVAL POSTGRADUATE SCHOOL**  
**Monterey, CA 93943**

**Rear Admiral Thomas A. Mercer**  
**Superintendent**

**This thesis was prepared in conjunction with research sponsored in part by the Office of Naval Research, 800 N. Quincy Street, Arlington, VA 22217-5000.**

**Reproduction of all or part of this report is authorized.**

**Released by:**

A solid black rectangular box used to redact the signature of the Dean of Research.

**P.J. MARTO, Dean of Research**

REPORT DOCUMENTATION PAGE			Form Approved OMB No. 0704	
Public reporting burden for this collection of information is estimated to average 1 hour per response, including the time for reviewing instruction, searching existing data sources, gathering and maintaining the data needed, and completing and reviewing the collection of information. Send comments regarding this burden estimate or any other aspect of this collection of information, including suggestions for reducing this burden, to Washington Headquarters Services, Directorate for Information Operations and Reports, 1215 Jefferson Davis Highway, Suite 1204, Arlington, VA 22202-4302, and to the Office of Management and Budget, Paperwork Reduction Project (0704-0188) Washington DC 20503.				
1. AGENCY USE ONLY (Leave blank)	2. REPORT DATE September 1994	3. REPORT TYPE AND DATES COVERED Master's Thesis		
4. TITLE AND SUBTITLE A NUMERICAL STUDY OF WIND FORCING EFFECTS ON THE CALIFORNIA CURRENT SYSTEM (U)		5. FUNDING NUMBERS		
6. AUTHOR(S) Vann, James R. in conjunction with Mary Batteen				
7. PERFORMING ORGANIZATION NAME(S) AND ADDRESS(ES) Naval Postgraduate School Monterey CA 93943-5000		8. PERFORMING ORGANIZATION REPORT NUMBER NPS-OC-94-006		
9. SPONSORING/MONITORING AGENCY NAME(S) AND ADDRESS(ES) Office of Naval Research 800 N. Quincy St. Arlington, VA 22217-5000		10. SPONSORING/MONITORING AGENCY REPORT NUMBER		
11. SUPPLEMENTARY NOTES The views expressed in this thesis are those of the author and do not reflect the official policy or position of the Department of Defense or the U.S. Government.				
12a. DISTRIBUTION/AVAILABILITY STATEMENT Approved for public release; distribution is unlimited.		12b. DISTRIBUTION CODE A		
13. ABSTRACT (maximum 200 words)  A high-resolution, multi-level, primitive equation ocean model is used to examine the response of an idealized, flat-bottom, eastern boundary oceanic regime on a beta-plane to climatological average (1980-1989), individual year, and multiple year wind forcing. The focus of this study is the California Current System along the coastal region, from 35° N to 47.5° N, off the West Coast of North America.  Two types of experiments are conducted. The first type forces the model from rest with climatological, 1981, and 1983 monthly winds to examine the generation phase of features such as currents, upwelling, meanders, eddies, and filaments. The second type continues the forcing from the previous years to examine the maintenance of these features.  In the first type of experiments, the following features are observed: a poleward coastal surface current near the start and end of each year, an equatorward surface current, a poleward undercurrent, upwelling, meanders, and eddies. In the second type of experiments, meanders and eddies were already present at the start of the experiment. In addition to the features observed during the first type of experiment, filaments are generated. The results support the hypothesis that wind forcing is an important mechanism for the generation of many of the observed features in the California Current System.				
14. SUBJECT TERMS Primitive equation model, California Current System, eddies, filaments, jets, undercurrent, wind forcing, currents.			15. NUMBER OF PAGES 235	
			16. PRICE CODE	
17. SECURITY CLASSIFICATION OF REPORT Unclassified	18. SECURITY CLASSIFICATION OF THIS PAGE Unclassified	19. SECURITY CLASSIFICATION OF ABSTRACT Unclassified	20. LIMITATION OF ABSTRACT UL	

NSN 7540-01-280-5500

Standard Form 298 (Rev. 2-89)

Prescribed by ANSI Std. Z39-18



Approved for public release; distribution is unlimited.

**A NUMERICAL STUDY OF  
WIND FORCING EFFECTS ON THE  
CALIFORNIA CURRENT SYSTEM**

by

**James R. Vann  
Lieutenant, United States Navy  
B.S., United States Naval Academy, 1984**

**Submitted in partial fulfillment  
of the requirements for the degree of**

**MASTER OF SCIENCE IN  
METEOROLOGY AND PHYSICAL OCEANOGRAPHY**

from the

**NAVAL POSTGRADUATE SCHOOL  
September 1994**

**Author:**

  
**James R. Vann**

**Approved by:**

  
**Mary L. Batteen, Thesis Advisor**

  
**Curtis A. Collins, Second Reader**

  
**Robert H. Bourke, Chairman,  
Department of Oceanography**



## ABSTRACT

A high-resolution, multi-level, primitive equation ocean model is used to examine the response of an idealized, flat-bottom, eastern boundary oceanic regime on a beta-plane to climatological average (1980-1989), individual year, and multiple year wind forcing. The focus of this study is the California Current System along the coastal region, from  $35^{\circ}$  N to  $47.5^{\circ}$  N, off the West Coast of North America.

Two types of experiments are conducted. The first type forces the model from rest with climatological, 1981, and 1983 monthly winds to examine the generation phase of features such as currents, upwelling, meanders, eddies, and filaments. The second type continues the forcing from the previous years to examine the maintenance of these features.

In the first type of experiments, the following features are observed: a poleward coastal surface current near the start and end of each year, an equatorward surface current, a poleward undercurrent, upwelling, meanders, and eddies. In the second type of experiments, meanders and eddies were already present at the start of the experiment. In addition to the features observed during the first type of experiment, filaments are generated. The results support the hypothesis that wind forcing is an important mechanism for the generation of many of the observed features in the California Current System.

Availability Codes	
Dist	Avail and/or Special
A-1	





## TABLE OF CONTENTS

I.	INTRODUCTION . . . . .	1
II.	BACKGROUND . . . . .	3
	A. BRIEF DESCRIPTION OF REGION . . . . .	3
	B. CLIMATOLOGICAL WINDS . . . . .	5
	C. EL NIÑO-SOUTHERN OSCILLATION . . . . .	7
	D. NUMERICAL MODEL STUDIES . . . . .	8
III.	MODEL DESCRIPTION AND EXPERIMENTAL DESIGN . . . . .	19
	A. MODEL DESCRIPTION . . . . .	19
	1. Basic Model . . . . .	19
	2. Friction . . . . .	19
	3. Boundary Conditions . . . . .	20
	4. Domain and Resolution . . . . .	20
	5. Finite Difference Scheme . . . . .	21
	6. Method of Solution . . . . .	22
	7. Initial Conditions . . . . .	22
	B. WIND AND ATMOSPHERIC FORCING . . . . .	22
	C. SPECIFIC EXPERIMENTAL DESIGN . . . . .	23
	D. ENERGY ANALYSIS TECHNIQUES . . . . .	24
IV.	RESULTS OF EXPERIMENTS . . . . .	25
	A. EXPERIMENTS STARTED FROM REST . . . . .	25
	1. Experiment 1 - Climatological Winds . . . . .	25
	2. Experiment 2 - 1981 Winds . . . . .	29
	3. Experiment 3 - 1983 Winds . . . . .	31
	4. Summary of First Year Run Results . . . . .	33
	B. EXPERIMENTS SPUN UP FROM THE PREVIOUS YEAR . . . . .	34
	1. Experiment 4 - Climatological Winds . . . . .	34
	2. Experiment 5 - 1982 Winds . . . . .	36
	3. Experiment 6 - 1984 Winds . . . . .	38
	4. Summary of Second Year Run Results . . . . .	40
	5. Experiment 7 - Multiple Climatological Runs . . . . .	41
	6. Experiment 8 - Multiple Years (1981 - 1984) . . . . .	42
	7. Summary of Multiple Year Run Results . . . . .	44
V.	SUMMARY AND RECOMMENDATIONS . . . . .	133
	A. SUMMARY . . . . .	133
	B. COMPARISON WITH OBSERVATIONS DURING AN EL NIÑO YEAR . . . . .	136
	C. NAVAL RELEVANCE . . . . .	137
	D. RECOMMENDATIONS . . . . .	138

APPENDIX A.	INSTABILITIES FOR EXPERIMENT 1 (CLIMO)	. .	149
APPENDIX B.	INSTABILITIES FOR EXPERIMENT 2 (1981)	. .	157
APPENDIX C.	INSTABILITIES FOR EXPERIMENT 3 (1983)	. .	167
APPENDIX D.	INSTABILITIES FOR EXPERIMENT 4 (CLIMO II)		183
APPENDIX E.	INSTABILITIES FOR EXPERIMENT 5 (1982)	. .	193
APPENDIX F.	INSTABILITIES FOR EXPERIMENT 6 (1984)	. .	199
LIST OF REFERENCES	. . . . .		207
INITIAL DISTRIBUTION LIST	. . . . .		211

## LIST OF TABLES

4.1	SUMMARY OF INSTABILITIES FOR CLIMATOLOGICAL YEAR (TOP), 1981 (CENTER), AND 1983 (BOTTOM). .	46
4.2	SUMMARY OF EXPERIMENTS - FIRST YEAR. . . . .	47
4.3	SUMMARY OF INSTABILITIES FOR CLIMATOLOGICAL II YEAR (TOP), 1982 (CENTER), AND 1984 (BOTTOM). .	48
4.4	SUMMARY OF EXPERIMENTS - SECOND YEAR. . . . .	49
4.5	SUMMARY OF EXPERIMENTS - MULTIPLE YEARS. . . . .	50
5.1	COMPARISON OF OBSERVED AND MODEL RESULTS DURING AN EL NIÑO YEAR (1983). . . . .	140



## LIST OF FIGURES

2.1	Generalized circulation schematic of the California Current System (CCS) . . . . .	11
2.2	Section of California Current System with schematized positions of jets and synoptic-scale eddies . . . . .	12
2.3	Domain of model off the western coast of the United States of America. . . . .	13
2.4	Map of a portion of the west coast of North America, showing the location of some of the past studies in the CCS . . . . .	14
2.5	Long-term mean atmospheric pressure at sea level for (a) January and (b) July . . . . .	15
2.6	Long-term (1854-1972) mean wind stress ( $\text{dynes cm}^{-2}$ ) by one-degree squares, from ship reports . . . . .	16
2.7	An illustration of the distributions of key properties involved in the teleconnection process during a typical El Niño-Southern Oscillation event. . . . .	17
4.1	Mid-monthly averaged climatological (1980 - 1989) ECMWF winds in $\text{m s}^{-1}$ : (a) January, (b) February, (c) March, (d) April, (e) May, (f) June, (g) July, (h) August, (i) September, (j) October, (k) November, and (l) December. . . . .	51
4.1	(continued). . . . .	52
4.1	(continued). . . . .	53
4.2	Experiment 1: Surface meridional component of velocity at day 30. . . . .	54
4.3	Experiment 1: Surface velocity vectors at day 90. . . . .	55
4.4	Experiment 1: Cross-section at $y \sim 704$ km ( $41.25^\circ$ N) of the meridional component of velocity at day 60. . . . .	56
4.5	Experiment 1: Cross-section at $y \sim 704$ km ( $41.25^\circ$ N) of the meridional component of velocity at day 90. . . . .	57
4.6	Experiment 1: Surface temperature at day 120. . . . .	58
4.7	Experiment 1: Surface velocity vectors at day 210. . . . .	59
4.8	Experiment 1: Surface temperature at day 210. . . . .	60
4.9	Experiment 1: Surface temperature at day 240. . . . .	61

4.10	Experiment 1: Surface velocity vectors at day 240 . . . . .	62
4.11	Experiment 1: Surface temperature at day 360 . . . . .	63
4.12	Experiment 1: Surface velocity vectors at day 360 . . . . .	64
4.13	Experiment 1: Cross-section of the meridional component of velocity at day 360. . . . .	65
4.14	Experiment 1: Total kinetic energy per unit mass time series for climatological (1980-1989) year over the entire domain . . . . .	66
4.15	Mid-monthly ECMWF winds for 1981 in $\text{m s}^{-1}$ : (a) January, (b) February, (c) March, (d) April, (e) May, (f) June, (g) July, (h) August, (i) September, (j) October, (k) November, and (l) December. . . . .	67
4.15	(continued). . . . .	68
4.15	(continued). . . . .	69
4.16	Experiment 2: Surface meridional component of velocity at day 45. . . . .	70
4.17	Experiment 2: Surface velocity vectors at day 90. . . . .	71
4.18	Experiment 2: Cross-section at $y \sim 704$ km ( $41.25^\circ$ N) of the meridional component of velocity at day 90. . . . .	72
4.19	Experiment 2: Layer 5 (316 m) velocity vectors at day 210. . . . .	73
4.20	Experiment 2: Surface temperature at day 120. . . . .	74
4.21	Experiment 2: Surface velocity vectors at day 210. . . . .	75
4.22	Experiment 2: Surface temperature at day 210. . . . .	76
4.23	Experiment 2: Surface velocity vectors at day 270. . . . .	77
4.24	Experiment 2: Surface temperature at day 270. . . . .	78
4.25	Experiment 2: Surface temperature at day 360. . . . .	79
4.26	Experiment 2: Cross-section at $y \sim 704$ km ( $41.25^\circ$ N) of the meridional component of velocity at day 360. . . . .	80
4.27	Experiment 2: Total kinetic energy per unit mass time series for 1981 over the entire domain . . . . .	81
4.28	Mid-monthly ECMWF winds for 1983 in $\text{m s}^{-1}$ : (a) January, (b) February, (c) March, (d) April, (e) May, (f) June, (g) July, (h) August, (i) September, (j) October, (k) November, and (l) December. . . . .	82

4.28	(continued) . . . . .	83
4.28	(continued) . . . . .	84
4.29	Experiment 3: Surface velocity vectors at day 30. . . . .	85
4.30	Experiment 3: Surface velocity vectors at day 120. . . . .	86
4.31	Experiment 3: Cross-section at y~704 km (41.25° N) of the meridional component of velocity at day 90. . . . .	87
4.32	Experiment 3: Surface temperature at day 150. . . . .	88
4.33	Experiment 3: Surface velocity vectors at day 150. . . . .	89
4.34	Experiment 3: Surface velocity vectors at day 240. . . . .	90
4.35	Experiment 3: Surface temperature at day 240. . . . .	91
4.36	Experiment 3: Surface temperature at day 360. . . . .	92
4.37	Experiment 3: Cross-section at y~704 km (41.25° N) of the meridional component of velocity at day 360. . . . .	93
4.38a	Experiment 3: Total kinetic energy per unit mass time series for 1983 (days 1-306) over the entire domain . . . . .	94
4.38b	Experiment 3: Total kinetic energy per unit mass time series for 1983 (days 309-363) over the entire domain . . . . .	95
4.39	Experiment 4: Surface velocity vectors at day 396 (yd 30). . . . .	96
4.40	Experiment 4: Surface temperature at day 396 (yd 30). . . . .	97
4.41	Experiment 4: Cross-section at y~704 km (41.25° N) of the meridional component of velocity at day 426 (yd 60). . . . .	98
4.42	Experiment 4: Surface temperature at day 546 (yd 180). . . . .	99
4.43	Experiment 4: Surface temperature at day 606 (yd 240). . . . .	100
4.44	Experiment 4: Surface velocity vectors at day 456 (yd 90). . . . .	101
4.45	Experiment 4: Cross-section at y~704 km (41.25° N) of the meridional component of velocity at day 666 (yd 300). . . . .	102
4.46	Experiment 4: Surface temperature at day 696 (yd 330). . . . .	103
4.47	Experiment 4: Surface temperature at day 726 (yd 360). . . . .	104
4.48	Experiment 4: Total kinetic energy per unit mass time series for Climo II over the entire domain . . . . .	105



4.49	Mid-monthly ECMWF winds for 1982 in $\text{m s}^{-1}$ : (a) January, (b) February, (c) March, (d) April, (e) May, (f) June, (g) July, (h) August, (i) September, (j) October, (k) November, and (l) December. . . . .	106
4.49	(continued). . . . .	107
4.49	(continued). . . . .	108
4.50	Experiment 5: Surface velocity vectors at day 396 (yd 30). . . . .	109
4.51	Experiment 5: Surface meridional component of velocity at day 426 (yd 60). . . . .	110
4.52	Experiment 5: Cross-section at $y \sim 704$ km ( $41.25^\circ$ N) of the meridional component of velocity at day 426 (yd 60). . . . .	111
4.53	Experiment 5: Surface velocity vectors at day 426 (yd 60). . . . .	112
4.54	Experiment 5: Surface temperature at day 516 (yd 150). . . . .	113
4.55	Experiment 5: Surface temperature at day 606 (yd 240). . . . .	114
4.56	Experiment 5: Surface temperature at day 696 (yd 330). . . . .	115
4.57	Experiment 5: Total kinetic energy per unit mass time series for 1982 over the entire domain . . . . .	116
4.58	Mid-monthly ECMWF winds for 1984 in $\text{m s}^{-1}$ : (a) January, (b) February, (c) March, (d) April, (e) May, (f) June, (g) July, (h) August, (i) September, (j) October, (k) November, and (l) December. . . . .	117
4.58	(continued). . . . .	118
4.58	(continued). . . . .	119
4.59	Experiment 6: Surface velocity vectors at day 396 (yd 30). . . . .	120
4.60	Experiment 6: Surface meridional component of velocity at day 426 (yd 60). . . . .	121
4.61	Experiment 6: Cross-section at $y \sim 704$ km ( $41.25^\circ$ N) of the meridional component of velocity at day 546 (yd 180). . . . .	122
4.62	Experiment 6: Surface temperature at day 456 (yd 90). . . . .	123
4.63	Experiment 6: Surface temperature at day 576 (yd 210). . . . .	124
4.64	Experiment 6: Surface temperature at day 666 (yd 300). . . . .	125
4.65	Experiment 6: Total kinetic energy per unit mass time series for 1984 over the entire domain . . . . .	126
4.66	Experiment 7: Total kinetic energy per unit mass time series for Climo III over the entire domain . . . . .	127

4.67	Experiment 7: Total kinetic energy per unit mass time series for Climo IV over the entire domain . . . . .	128
4.68	Experiment 7: Total kinetic energy per unit mass time series for Climo, Climo II, Climo III, and Climo IV over the entire domain . . . . .	129
4.69	Experiment 8: Total kinetic energy per unit mass time series for 1983 over the entire domain . . . . .	130
4.70	Experiment 8: Total kinetic energy per unit mass time series for 1984 over the entire domain . . . . .	131
4.71	Experiment 8: Total kinetic energy per unit mass time series for 1981, 1982, 1983, and 1984 over the entire domain . . . . .	132
5.1a	Experiments 1-3: Total kinetic energy per unit mass time series for climatology (1980-1989), 1981, and 1983 over the entire domain . . . . .	141
5.1b	Experiments 1-3: Mean kinetic energy per unit mass time series for climatology (1980-1989), 1981, and 1983 over the entire domain . . . . .	142
5.1c	Experiments 1-3: Eddy kinetic energy per unit mass time series for climatology (1980-1989), 1981, and 1983 over the entire domain . . . . .	143
5.2a	Experiments 4-6: Total kinetic energy per unit mass time series for Climo II, 1981, and 1983 over the entire domain . . . . .	144
5.2b	Experiments 4-6: Mean kinetic energy per unit mass time series for Climo II, 1981, and 1983 over the entire domain . . . . .	145
5.2c	Experiments 4-6: Eddy kinetic energy per unit mass time series for Climo II, 1981, and 1983 over the entire domain . . . . .	146
5.3	Experiment 3: Surface meridional component of velocity at day 45. . . . .	147
A.1	Experiment 1: Energy transfers of mean to eddy kinetic energy (i.e., barotropic energy transfer) for climatological (1980-1989) year, for model days 207 to 216. . . . .	150
A.2	Experiment 1: Energy transfers of eddy potential to eddy kinetic energy (i.e., baroclinic energy transfer) for climatological (1980-1989) year, for model days 207 to 216. . . . .	151
A.3	Experiment 1: Energy transfers of mean to eddy kinetic energy (i.e., barotropic energy transfer) for climatological (1980-1989) year, for model days 228 to 231. . . . .	152

A.4	Experiment 1: Energy transfers of eddy potential to eddy kinetic energy (i.e., baroclinic energy transfer) for climatological (1980-1989) year, for model days 228 to 231. . . . .	153
A.5	Experiment 1: Energy transfers of mean to eddy kinetic energy (i.e., barotropic energy transfer) for climatological (1980-1989) year, for model days 297 to 303. . . . .	154
A.6	Experiment 1: Energy transfers of eddy potential to eddy kinetic energy (i.e., baroclinic energy transfer) for climatological (1980-1989) year, for model days 297 to 303. . . . .	155
B.1	Experiment 2: Energy transfers of mean to eddy kinetic energy (i.e., barotropic energy transfer) for 1981, for model days 210 to 222. . . . .	158
B.2	Experiment 2: Energy transfers of eddy potential to eddy kinetic energy (i.e., baroclinic energy transfer) for 1981, for model days 210 to 222. . . . .	159
B.3	Experiment 2: Energy transfers of mean to eddy kinetic energy (i.e., barotropic energy transfer) for 1981, for model days 240 to 252. . . . .	160
B.4	Experiment 2: Energy transfers of eddy potential to eddy kinetic energy (i.e., baroclinic energy transfer) for 1981, for model days 240 to 252. . . . .	161
B.5	Experiment 2: Energy transfers of mean to eddy kinetic energy (i.e., barotropic energy transfer) for 1981, for model days 297 to 303. . . . .	162
B.6	Experiment 2: Energy transfers of eddy potential to eddy kinetic energy (i.e., baroclinic energy transfer) for 1981, for model days 297 to 303. . . . .	163
B.7	Experiment 2: Energy transfers of mean to eddy kinetic energy (i.e., barotropic energy transfer) for 1981, for model days 309 to 333. . . . .	164
B.8	Experiment 2: Energy transfers of eddy potential to eddy kinetic energy (i.e., baroclinic energy transfer) for 1981, for model days 309 to 333. . . . .	165
C.1	Experiment 3: Energy transfers of mean to eddy kinetic energy (i.e., barotropic energy transfer) for 1983, for model days 186 to 192. . . . .	168

C.2	Experiment 3: Energy transfers of eddy potential to eddy kinetic energy (i.e., baroclinic energy transfer) for 1983, for model days 186 to 192. . . . .	169
C.3	Experiment 3: Energy transfers of mean to eddy kinetic energy (i.e., barotropic energy transfer) for 1983, for model days 222 to 234. . . . .	170
C.4	Experiment 3: Energy transfers of eddy potential to eddy kinetic energy (i.e., baroclinic energy transfer) for 1983, for model days 222 to 234. . . . .	171
C.5	Experiment 3: Energy transfers of mean to eddy kinetic energy (i.e., barotropic energy transfer) for 1983, for model days 249 to 258. . . . .	172
C.6	Experiment 3: Energy transfers of eddy potential to eddy kinetic energy (i.e., baroclinic energy transfer) for 1983, for model days 249 to 258. . . . .	173
C.7	Experiment 3: Energy transfers of mean to eddy kinetic energy (i.e., barotropic energy transfer) for 1983, for model days 279 to 288. . . . .	174
C.8	Experiment 3: Energy transfers of eddy potential to eddy kinetic energy (i.e., baroclinic energy transfer) for 1983, for model days 279 to 288. . . . .	175
C.9	Experiment 3: Energy transfers of mean to eddy kinetic energy (i.e., barotropic energy transfer) for 1983, for model days 312 to 315. . . . .	176
C.10	Experiment 3: Energy transfers of eddy potential to eddy kinetic energy (i.e., baroclinic energy transfer) for 1983, for model days 312 to 315. . . . .	177
C.11	Experiment 3: Energy transfers of mean to eddy kinetic energy (i.e., barotropic energy transfer) for 1983, for model days 324 to 327. . . . .	178
C.12	Experiment 3: Energy transfers of eddy potential to eddy kinetic energy (i.e., baroclinic energy transfer) for 1983, for model days 324 to 327. . . . .	179
C.13	Experiment 3: Energy transfers of mean to eddy kinetic energy (i.e., barotropic energy transfer) for 1983, for model days 342 to 348. . . . .	180

C.14	Experiment 3: Energy transfers of eddy potential to eddy kinetic energy (i.e., baroclinic energy transfer) for 1983, for model days 342 to 348. . . . .	181
D.1	Experiment 4: Energy transfers of mean to eddy kinetic energy (i.e., barotropic energy transfer) for Climo II, for model days 378 to 408 (yd 12 - 42). . . . .	184
D.2	Experiment 4: Energy transfers of eddy potential to eddy kinetic energy (i.e., baroclinic energy transfer) for Climo II, for model days 378 to 408 (yd 12 - 42). . . . .	185
D.3	Experiment 4: Energy transfers of mean to eddy kinetic energy (i.e., barotropic energy transfer) for Climo II, for model days 453 to 465 (yd 87 - 99). . . . .	186
D.4	Experiment 4: Energy transfers of eddy potential to eddy kinetic energy (i.e., baroclinic energy transfer) for Climo II, for model days 453 to 465 (yd 87 - 99). . . . .	187
D.5	Experiment 4: Energy transfers of mean to eddy kinetic energy (i.e., barotropic energy transfer) for Climo II, for model days 504 to 516 (yd 138 - 150). . . . .	188
D.6	Experiment 4: Energy transfers of eddy potential to eddy kinetic energy (i.e., baroclinic energy transfer) for Climo II, for model days 504 to 516 (yd 138 - 150). . . . .	189
D.7	Experiment 4: Energy transfers of mean to eddy kinetic energy (i.e., barotropic energy transfer) for Climo II, for model days 624 to 636 (yd 258 - 270). . . . .	190
D.8	Experiment 4: Energy transfers of eddy potential to eddy kinetic energy (i.e., baroclinic energy transfer) for Climo II, for model days 624 to 636 (yd 258 - 270). . . . .	191
E.1	Experiment 5: Energy transfers of mean to eddy kinetic energy (i.e., barotropic energy transfer) for 1982, for model days 507 to 516 (yd 141 - 150). . . . .	194
E.2	Experiment 5: Energy transfers of eddy potential to eddy kinetic energy (i.e., baroclinic energy transfer) for 1982, for model days 507 to 516 (yd 141 - 150). . . . .	195
E.3	Experiment 5: Energy transfers of mean to eddy kinetic energy (i.e., barotropic energy transfer) for 1982, for model days 525 to 528 (yd 159 - 162). . . . .	196

E.4	Experiment 5: Energy transfers of eddy potential to eddy kinetic energy (i.e., baroclinic energy transfer) for 1982, for model days 525 to 528 (yd 159 - 162). . . . .	197
F.1	Experiment 6: Energy transfers of mean to eddy kinetic energy (i.e., barotropic energy transfer) for 1984, for model days 576 to 591 (yd 210 - 225). . . . .	200
F.2	Experiment 6: Energy transfers of eddy potential to eddy kinetic energy (i.e., baroclinic energy transfer) for 1984, for model days 576 to 591 (yd 210 - 225). . . . .	201
F.3	Experiment 6: Energy transfers of mean to eddy kinetic energy (i.e., barotropic energy transfer) for 1984, for model days 606 to 624 (yd 240 - 258). . . . .	202
F.4	Experiment 6: Energy transfers of eddy potential to eddy kinetic energy (i.e., baroclinic energy transfer) for 1984, for model days 606 to 624 (yd 240 - 258). . . . .	203
F.5	Experiment 6: Energy transfers of mean to eddy kinetic energy (i.e., barotropic energy transfer) for 1984, for model days 645 to 657 (yd 279 - 291). . . . .	204
F.6	Experiment 6: Energy transfers of eddy potential to eddy kinetic energy (i.e., baroclinic energy transfer) for 1984, for model days 645 to 657 (yd 279 - 291). . . . .	205

.

### **ACKNOWLEDGEMENT**

The author wants to thank Dr. Mary Batteen for her guidance and patience during the work in performing this investigation. Additional thanks to Mike Cook for his endless assistance with UNIX, FORTRAN, and MATLAB programming, and to Pete Braccio for his invaluable assistance with numerous model runs and visualization of the results.



## I. INTRODUCTION

The California Current System (CCS) is an eastern boundary current (EBC) off the west coast of the United States of America. A primitive equation numerical model developed by Batteen et al. (1989) is used to simulate the currents, eddies and filaments in the CCS. In this study monthly winds from the European Centre for Medium-Range Weather Forecasts (ECMWF) global data set from 1980 to 1989 (which include El Niño events) are used to force the model.

The thesis is organized as follows: Chapter II describes the region modeled, the El Niño-Southern Oscillation (ENSO), and some previous modeling work in this region. The numerical model which was used here along with the experimental setup are presented in Chapter III. The results of the various model simulations are presented in Chapter IV. Chapter V summarizes the work, discusses naval relevance, and presents recommendations for future research. Comparisons of model simulations with available observations are shown in both Chapters IV and V. Six appendices follow which contain the detailed results of the barotropic and baroclinic instability analyses for the main experiments.



## II. BACKGROUND

### A. BRIEF DESCRIPTION OF REGION

The west coast of North America serves as an eastern boundary for the circulation of water in the North Pacific Ocean. The entire flow along the coast is referred to as the CCS, which is a classical subtropical EBC system.

The CCS consists of three separate component flows, each of which varies both spatially and seasonally (see Figure 2.1): an equatorward surface current, a poleward undercurrent and a poleward surface current adjacent to the coast (Tisch et al., 1992). This latter current can be a surface manifestation of the undercurrent or a separate current.

The predominant flow is an equatorward surface flow called the California Current (CC). The second basic flow is the poleward undercurrent which has been called both the California Undercurrent (CUC) (e.g., by Batteen et al., 1989) and the California Counter Current (CCC) (e.g., by Hickey, 1979). This is a relatively weak subsurface flow (around  $5 \text{ cm s}^{-1}$ ).

The third basic flow is the Inshore Current (IC), which is known as the Davidson Current (DC) north of Pt. Conception. This is also a relatively weak poleward flow

found at the surface and near the coast. There are other ICs known as the Southern California Countercurrent (SCC) to the south, and the Southern California Eddy (SCE) inshore of the Channel Islands within the California Bight (Hickey, 1979), which are both equatorward of the model region (see below) to be studied.

The CC is a broad, slow ( $\sim 10 \text{ cm s}^{-1}$ ) flow which can extend offshore around 1000 km (Hickey, 1979). Superimposed on this mean flow are highly energetic mesoscale eddies and meandering jets which can have peak velocities near  $80 \text{ cm s}^{-1}$  (Mooers and Robinson, 1984). Figure 2.2 depicts these features.

A section of the CCS from  $35^\circ$  to  $47.5^\circ \text{ N}$  and extending 12.5 degrees offshore from the coast will be the model study area and is depicted in Figure 2.3. Major observational programs which have sampled this region are quite numerous and include: California Cooperative Oceanic Fisheries Investigation (CalCOFI), Coastal Ocean Dynamics Experiment (CODE) I and II, Large-Scale West Coast Shelf Experiment (nicknamed SuperCODE), Coastal Upwelling Experiment (CUE) I and II, Ocean Prediction Through Observation, Modeling and Analysis program (OPTOMA), and Central California Coastal Circulation Study (CCCS). Figure 2.4 depicts some of the areas of observations.

## B. CLIMATOLOGICAL WINDS

The North Pacific Subtropical High dominates the atmospheric circulation off the west coast of the United States of America, and varies in position and strength by season (Huyer, 1983). In the winter (January) the high is about 1020 mb and centered near 30° N, 135° W (Figure 2.5a). In the summer (July) the pressure increases to 1025 mb and the center moves northward to 38° N, 150° W (Figure 2.5b). Over the continental west coast the typical pressure is 1020 mb in the winter, and 1015 mb during the summer, the latter in response to a thermal low (of 1005 mb) in the central valley of California (Huyer, 1983). This results in a tighter pressure gradient against the west coast during the summer. As this gradient tightens, stronger winds can result.

Propagating atmospheric disturbances (Halliwell and Allen, 1987), along with other atmospheric mesoscale phenomena (Huyer, 1983), further complicate the wind pattern on a daily, as well as on a seasonal basis along the coast. The winds are also affected by coastal atmospheric boundary layer processes within 100 to 200 km of the coast (Halliwell and Allen, 1987).

The oceanic response to summer and winter wind patterns are most notable near the coast. The equatorward winds of summer can produce nearshore upwelling, while the divergent

wind flow of winter can force downwelling in some areas (Rienecker and Mooers, 1986).

The shifting of the Pacific High, along with the Aleutian Low moving to the southeast, can cause the winds to diverge near Cape Mendocino (located at about  $40^{\circ}$  N) during the winter. North of the Cape, northerly winds are encountered as the wind blows around the eastern side of the Aleutian Low, while south of the Cape, southerly winds result as wind flows around the North Pacific High.

The summer wind pattern is established by the interaction between the North Pacific High and the thermal low in the southwest United States (Nelson, 1977; Halliwell and Allen, 1987). Winds are predominately equatorward on both sides of Cape Mendocino during the summer (Nelson, 1977).

Climatological wind stress fields, shown in Figure 2.6 for the months of January, April, July, and October, depict regions of maximum wind stress in the CCS as shaded areas. The strongest wind stress is located off Point Conception in April and migrates northward until it is at a maximum in July off Cape Mendocino. The average summer wind stress close to the shore is equatorward and is thus favorable for upwelling at the coast (Halliwell and Allen, 1987; Nelson, 1977; Wickham et al., 1987).

### C. EL NIÑO-SOUTHERN OSCILLATION

One large-scale two way coupling of the atmosphere and ocean has been studied for many years and is referred to as the El Niño-Southern Oscillation (ENSO). El Niño refers to the warming of Eastern Pacific ocean waters, while the Southern Oscillation is an atmospheric pressure fluctuation between the Indian Ocean and the Eastern Tropical Pacific Ocean (Philander, 1990). Figure 2.7 illustrates key properties of the teleconnection including upper troposphere and surface pressure anomalies. Note the shift in the Eastern Pacific Subtropical High during an ENSO event.

Explanations for this phenomena involve both an oceanic and atmospheric teleconnection. Rienecker and Mooers (1986) explain that the oceanic connection occurs when eastward propagating equatorial Kelvin waves turn poleward upon impacting the west coast of the Americas. In contrast, the atmospheric teleconnection links the tropical sea surface temperature (SST) anomalies to the Aleutian Low by momentum transfer through an intensified Hadley Cell circulation (Bjerknes, 1966; Philander, 1990). A stronger poleward wind stress subsequently develops at the coast near 36° N when the Aleutian Low deepens and moves to the southwest. Simultaneously the North Pacific High weakens and moves offshore.

The El Niño of 1982 - 1983 was one of the strongest on record. The Aleutian Low was much deeper than normal during

the winter and wind stress anomalies were at a maximum in the region between 35° N and 45° N (Trenberth et al., 1990). Anomalous conditions were observed from San Diego to Vancouver Island (Rienecker and Mooers, 1986). There were two anomalous peaks in the SST, the first occurring in February to March of 1983 off northern California, while the second one was evident in September to October of 1983 near Point Conception (Rienecker and Mooers, 1986), the latter equatorward of our model domain.

#### D. NUMERICAL MODEL STUDIES

There have been numerous models used over the past few decades to model EBCs, particularly the CCS. Extensive reviews can be found in Allen (1980), Chelton (1984), and O'Brien et al. (1977). No attempt is made to provide a comprehensive review of the models here; instead, a summary of modeling work that has led directly to this study is presented.

Early work included that of Pedlosky (1974) and Philander and Yoon (1982) who used steady wind stress and transient wind forcing, respectively. Carton (1984) and Carton and Philander (1984) investigated the response of reduced gravity models to realistic coastal winds. At periods exceeding 100 days the alongshore currents began to weaken and disperse as a series of alternating jets.



Another series of experiments were done by McCreary et al. (1987) utilizing a linear model with both transient and steady wind forcing with Laplacian diffusion in which no eddies or filaments developed. This work was extended using a full primitive equation model by Tielking (1988) who obtained similar results.

Batteen et al. (1989) used a primitive equation, multi-level model with biharmonic heat and momentum diffusion which had both steady forcing constant throughout the domain and meridionally varying forcing. In both cases, when the baroclinic shear between the surface current and undercurrent became strong enough, eddies and filaments developed. This was the first EBC model to simulate currents, eddies and jets in the CCS.

The work of Batteen et al. (1989) was extended by Mitchell (1993) and Haines (1994). Mitchell (1993) forced the model with different sets of averaged winds and obtained reasonable results utilizing a set of seasonally varying full climatological wind fields. Haines (1994) enlarged the model domain, improved resolution to 8 x 13 km and used interannual vice steady or seasonal winds.

This effort builds on the model used by Batteen et al. (1989) and the work of Mitchell (1993) and Haines (1994). The computer code for the model has been modified to include a barotropic component, while the model resolution has been refined to 8 x 11 km grid spacing. Seasonal and interannual

wind forcing was used to force the model. Model simulation times have been expanded from one year, as in Mitchell (1993) and Haines (1994), to two to four years for each model run. The enhanced simulation times should allow analysis of the maintenance of currents and eddies as well as the generation of these features.

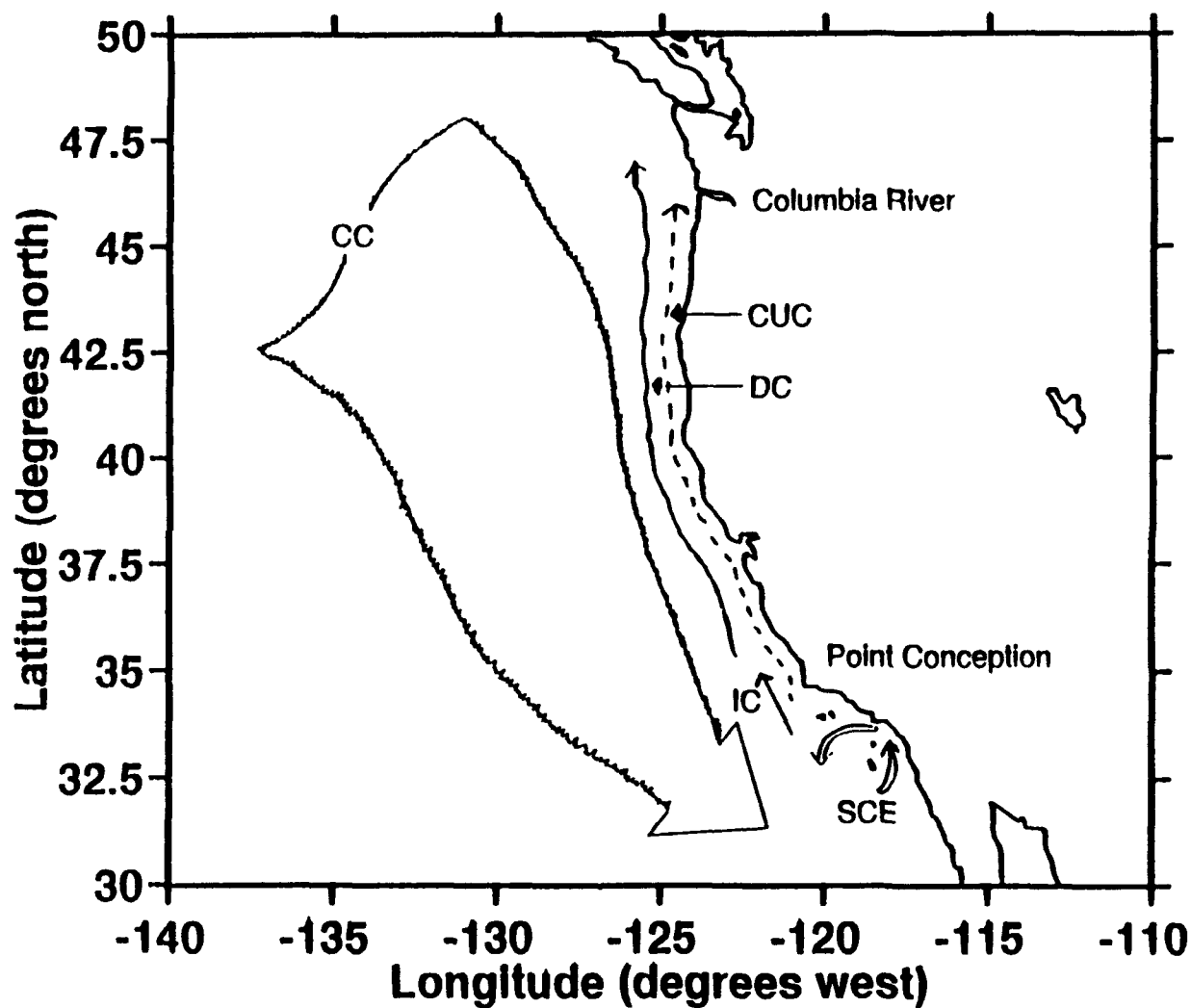


**Figure 2.1** Generalized circulation schematic of the California Current System (CCS). The broad, slow surface equatorward California Current (CC) overlies the poleward California Undercurrent (CUC) along with the Inshore Current (IC), also known as the Davidson Current (DC), Southern California Countercurrent (SCC), and Southern California Eddy (SCE).

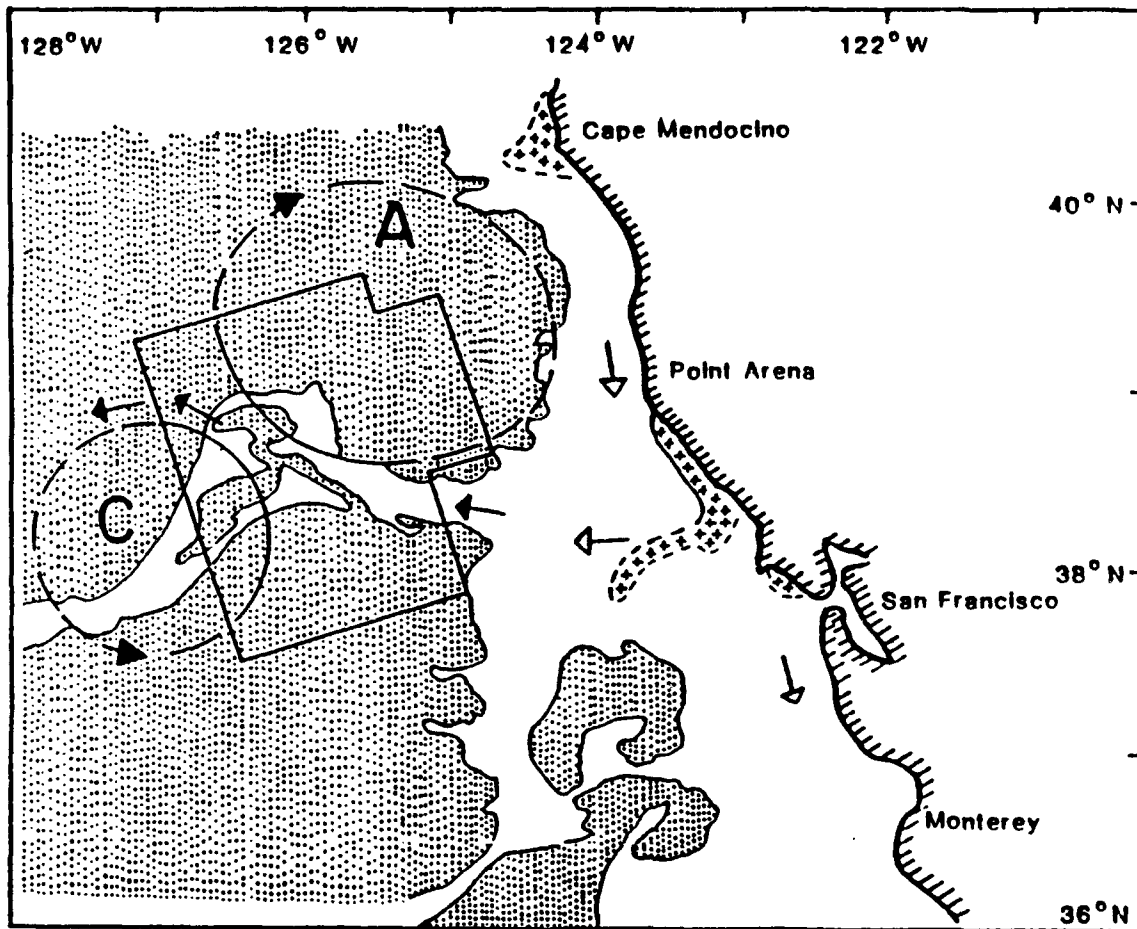


**Figure 2.2** Section of California Current System with schematized positions of jets and synoptic-scale eddies; C, cyclonic eddy; A, anticyclonic eddy. Arrows indicate principal surface flows; solid arrows are definite and open arrows are inferential. Also shown is a qualitative analysis of satellite infrared image gray shades for sea-surface temperature (SST) predominant patterns on 1 August 1982: coolest SST, crosses; warmest SST, dots (from Mooers and Robinson, 1984).

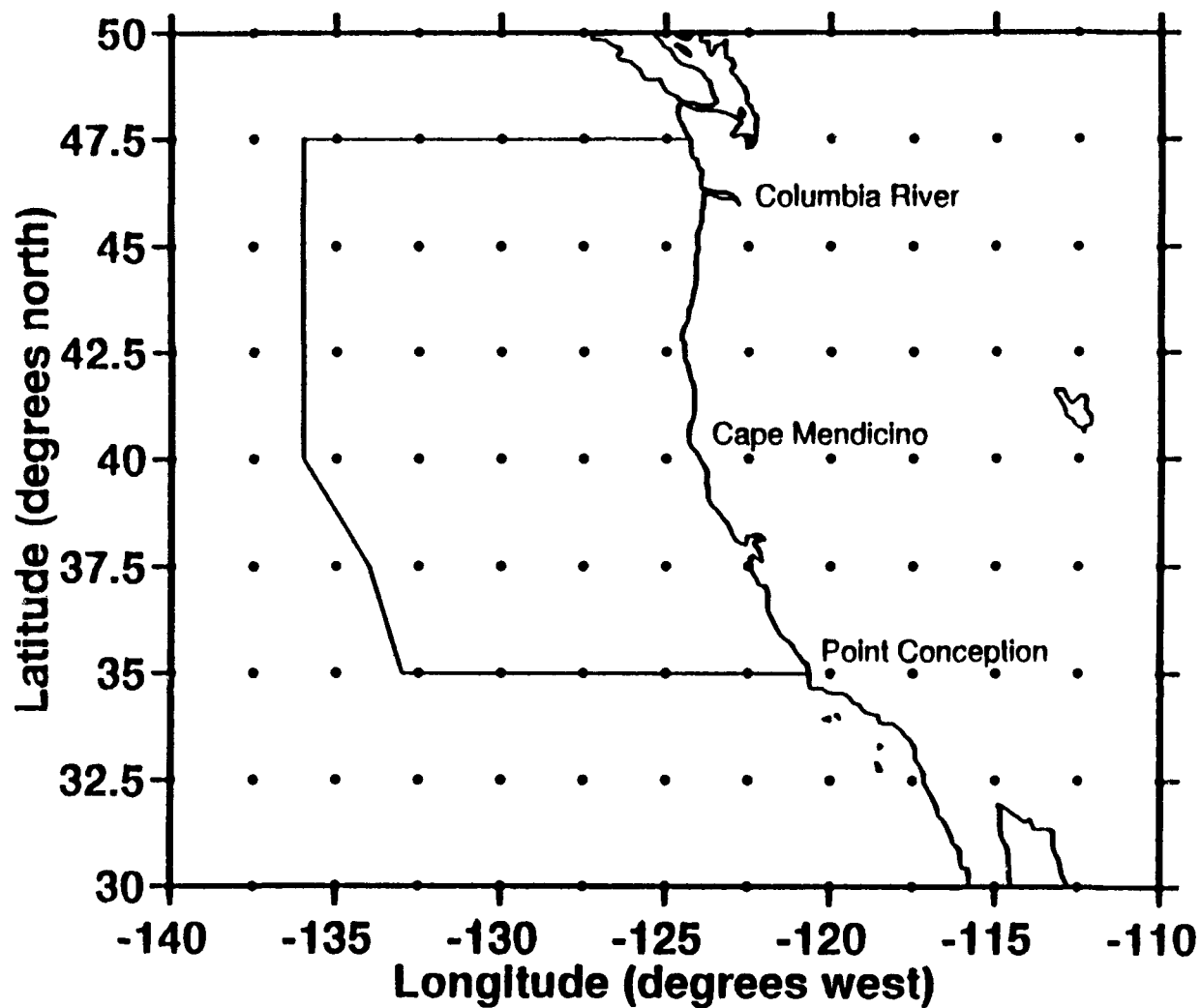


**Figure 2.3** Domain of model off the western coast of the United States of America. Domain bounded by 35° to 47.5° N and from the coast to 12.5 degrees offshore. Model covers an area 1024 km (1408 km) in the cross-shore (alongshore) direction and the cross-shore (alongshore) horizontal resolution is 8 km (11 km).

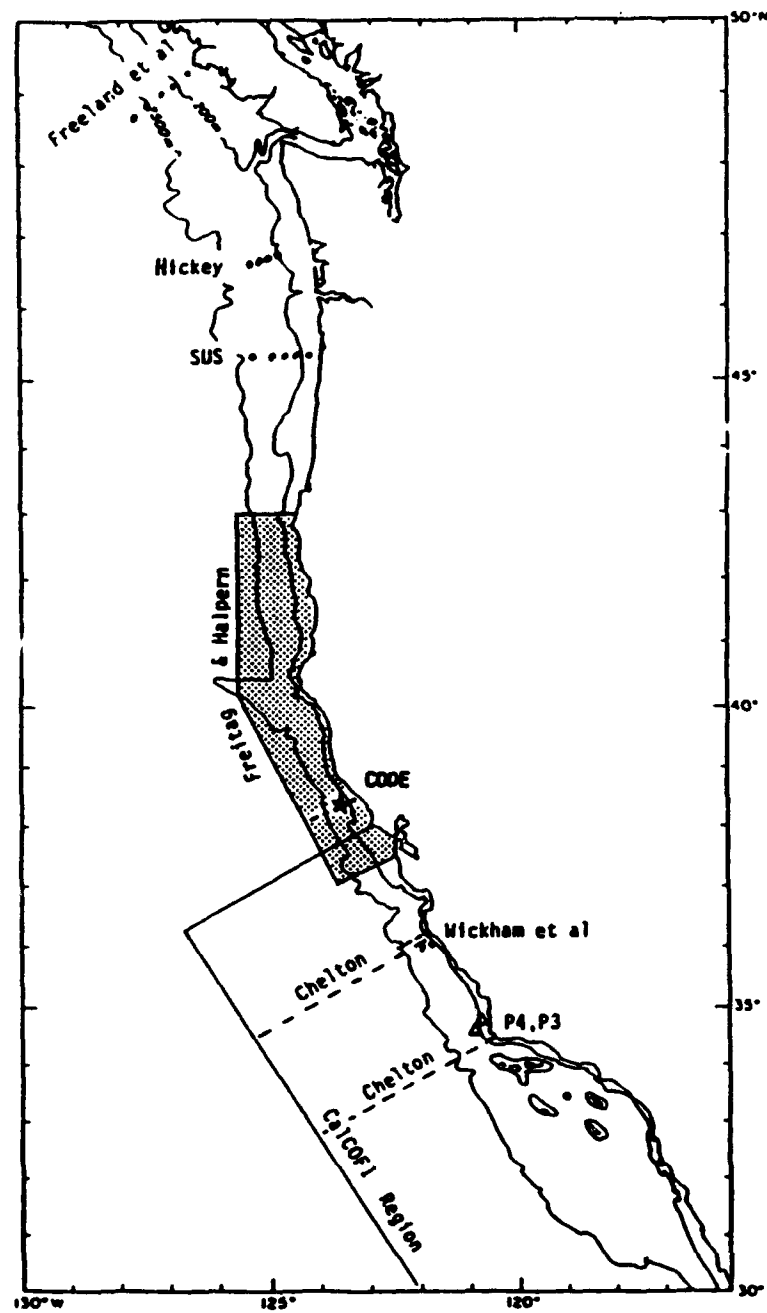


**Figure 2.4** Map of a portion of the west coast of North America, showing the location of some of the past studies in the CCS (from Huyer *et al.*, 1989).

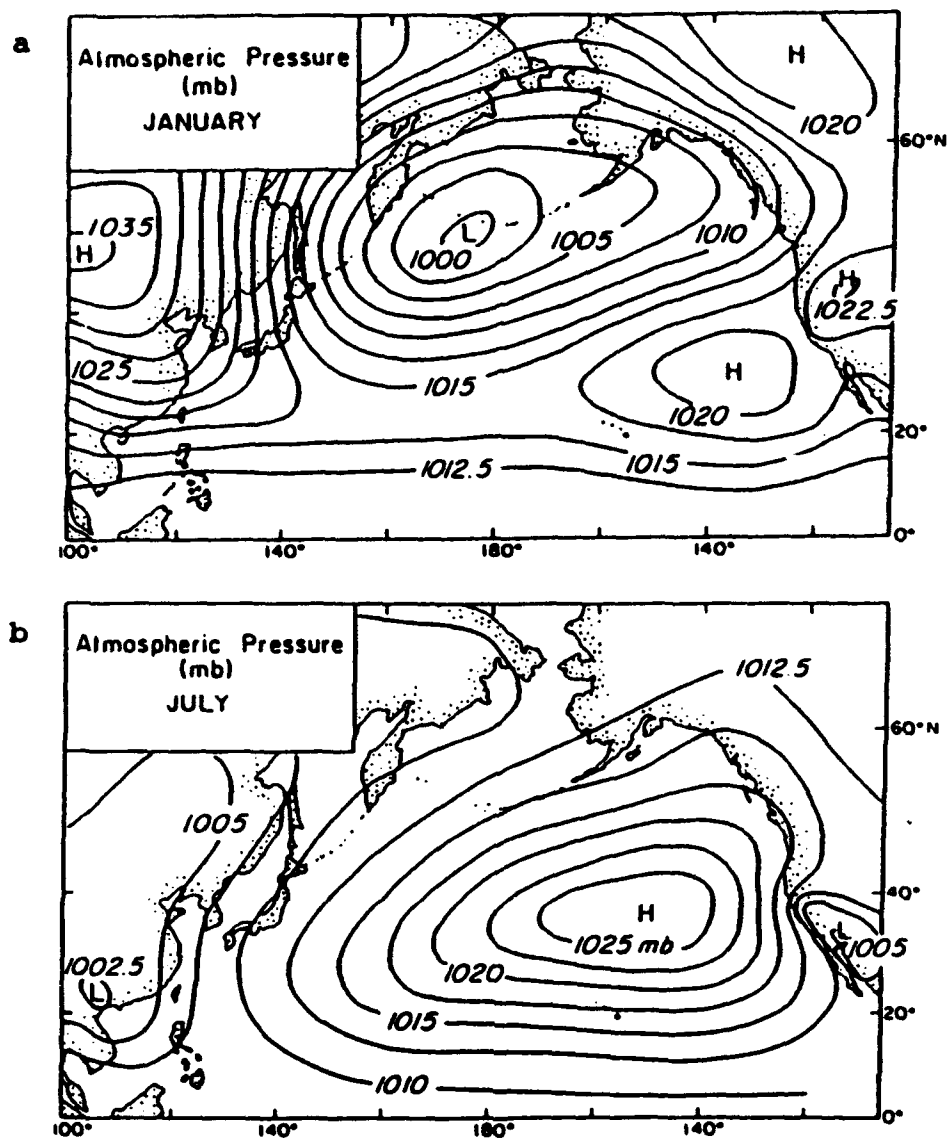


**Figure 2.5** Long-term mean atmospheric pressure at sea level for (a) January and (b) July (from Huyer, 1983).

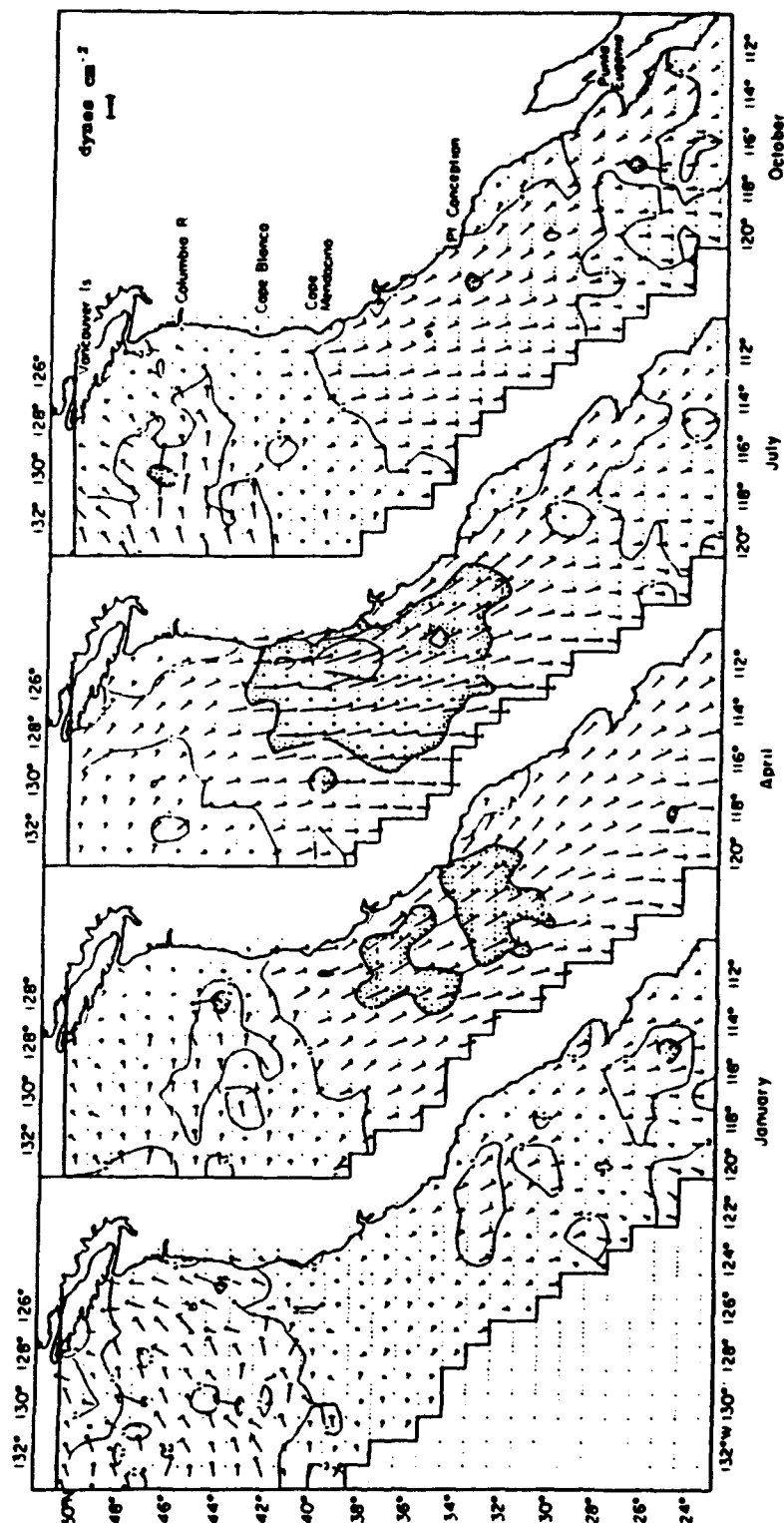


**Figure 2.6** Long-term (1854-1972) mean wind stress (dynes cm<sup>-2</sup>) by one-degree squares, from ship reports (Nelson, 1977). Contours correspond to constant magnitudes of 0.5, 1.0, and 1.5 dynes cm<sup>-2</sup>; areas where the wind stress exceeds 1.0 dynes cm<sup>-2</sup> are shaded (from Huyer, 1983).



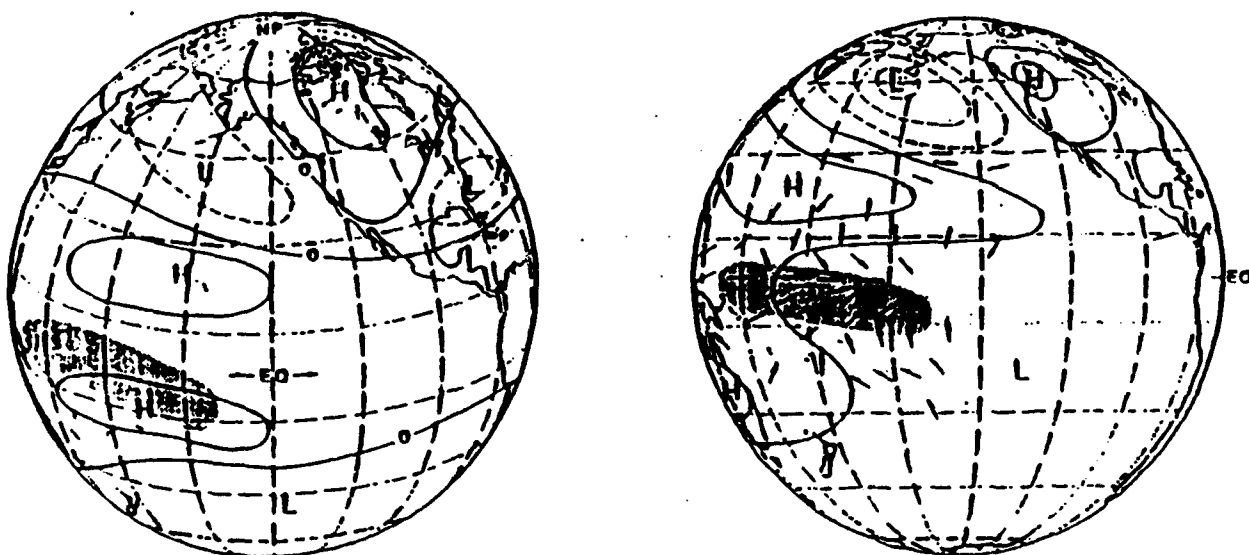


**Figure 2.7** An illustration of the distributions of key properties involved in the teleconnection process during a typical El Niño-Southern Oscillation event. (Left) Upper troposphere anomalies of geopotential height for the Northern Hemisphere winter. (Right) Contours of surface barometric pressure, with surface wind anomalies (arrows) in the tropics (from Enfield, 1989).



### III. MODEL DESCRIPTION AND EXPERIMENTAL DESIGN

#### A. MODEL DESCRIPTION

##### 1. Basic Model

The model used in this research is a slightly modified version of that used by Batteen *et al.* (1989, 1992) which was adapted from Haney's (1974, 1985) closed basin model. This limited area EBC model is multi-level, uses non-adiabatic primitive equations on a  $\beta$  plane, and has both barotropic and baroclinic components. The following approximations are made: hydrostatic, Boussinesq, and rigid lid. (For a more detailed summary of the model and the governing equations, refer to Batteen *et al.* (1989)).

##### 2. Friction

The type of diffusion used can be important for the generation of mesoscale eddies. Biharmonic rather than Laplacian lateral heat and momentum diffusion is used in this study. The use of biharmonic lateral diffusion allows mesoscale eddy generation via barotropic (horizontal-shear) or baroclinic (vertical-shear) instability mechanisms, or both, as Holland (1978) and Holland and Batteen (1986) have shown. The biharmonic coefficients are the same (i.e.,  $2.0 \times 10^{17} \text{ cm}^4 \text{ s}^{-1}$ ) as used in Batteen *et al.* (1989). Weak ( $0.5 \text{ cm}^2 \text{ s}^{-1}$ ) vertical eddy viscosities and conductivity are used.

A simplified quadratic drag law is used to parameterize bottom stress (Weatherly, 1972).

### **3. Boundary Conditions**

The domain of the model on the eastern boundary is closed and is modeled as a straight, vertical wall. A no-slip condition on the alongshore velocity is used. The kinematic boundary condition of no flow through the eastern boundary is imposed on the cross-shore velocity component. A modified version of the radiation boundary conditions of Camerlengo and O'Brien (1980) is used for the open boundaries to the south, west, and north.

At the surface, the rigid lid approximation filters out external gravity waves and allows a longer time step. On the ocean bottom, no vertical heat flux or vertical velocity is allowed.

### **4. Domain and Resolution**

The domain of the model is an elbow shaped region off California's coast from  $35^{\circ}$  N to  $42.5^{\circ}$  N as shown in Figure 2.3. This covers an area 1408 km alongshore and 1024 km in the cross-shore direction. The horizontal resolution is 8 km in the cross-shore direction and 11 km in the alongshore direction. Mesoscale features within the CCS should be resolvable with this resolution because typical eddy wavelengths are around 100 km (Breaker and Mooers, 1986). Bottom topography and variations in the coastline

have been omitted to focus on the role played by wind forcing in the CCS.

#### 5. Finite Difference Scheme

A staggered grid model, using the Arakawa and Lamb (1977) B-scheme is used in the horizontal. Variables are defined as follows:  $u$ ,  $v$ , and  $w$  are velocity components eastward, northward and vertical, respectively,  $t$  denotes time,  $T$  is temperature,  $\rho$  is density,  $p$  is pressure, and  $\psi$  is the streamfunction. The center of each grid point defines  $u$  and  $v$  while  $T$ ,  $\rho$ ,  $\psi$ ,  $w$ , and  $p$  are defined at the corners. The B-scheme is used because it gives a superior representation of the geostrophic adjustment process (Batteen and Han, 1981).

The model uses ten layers in the vertical, with constant  $z$ -levels at depths of: 13, 46, 98, 182, 316, 529, 870, 1416, 2283, and 3656 m. This spacing scheme concentrates more layers above the thermocline in the dynamically active portion of the ocean, consistent with Haney (1974). Variables are staggered in the vertical with  $u$ ,  $v$ ,  $\rho$ , and  $T$  defined at each level, while  $w$  and  $p$  are defined between the levels which lie between the ocean surface ( $w=0$ ) and at the bottom ( $z=-H$ , where  $H$  is the depth). A Matsuno time step followed by ten leapfrog time steps is used and continuously repeated during the model run.

## 6. Method of Solution

The method of solution is straightforward with the rigid lid and flat bottom assumption because the vertically integrated horizontal velocity is subsequently non-divergent. The vertical mean flow can be described by a streamfunction  $\psi$  which can be predicted from the vorticity equation, while the vertical shear currents can be predicted after the vertical mean flow is subtracted from the original equations. The other variables  $T$ ,  $\rho$ ,  $w$ , and  $p$  can be explicitly obtained from the thermodynamic energy equation, equation of state, continuity equation, and hydrostatic relation, respectively.

## 7. Initial Conditions

An exponential temperature profile with a vertical length scale of  $h=450$  m is used as the initial mean stratification. The bottom temperature is assumed to be  $2^\circ$  C and the change in temperature between the bottom and surface is  $13^\circ$  C. This profile was derived by Blumberg and Mellor (1987) and has been used by Batteen (1989) and Batteen *et al.* (1989).

## B. WIND AND ATMOSPHERIC FORCING

The winds used to force the model are from the European Centre for Medium-Range Weather Forecasts (ECMWF) (Trenberth *et al.*, 1990) and have been provided by the National Center for Atmospheric Research (NCAR). Winds were extracted from

world wide mean monthly wind velocities that were provided at 2.5 degree spacing for the years 1980 to 1989 along with 120 month climatology for the area of study. This data was linearly interpolated in space and then in time to provide daily forcing at the desired grid points.

The total heat flux across the surface is initially set to zero by choosing an initial air temperature that forces the net flux of longwave radiation, sensible heat, and latent heat to zero, as in Batteen et al. (1989). The air temperature is then used in the model. Any subsequent surface heat flux forcing is thus a secondary effect of the changes to SST due to the wind and/or thermal structure of the ocean.

### **C. SPECIFIC EXPERIMENTAL DESIGN**

Climatological winds were used for 365 days (Experiment 1) and then used to restart the model to run climatological winds for another 365 days (Experiment 4). Next, 1981 winds were run for 365 days (Experiment 2) and used to initialize the run of 365 days with 1982 winds (Experiment 5). Then 1983 winds from a cold restart were run for 365 days (Experiment 3) and then used to initialize the run of 366 days (leap year) with 1984 winds (Experiment 6). Two additional extended runs were conducted in which the model ran for four years. Experiment 7 used the climatological

winds four times, while Experiment 8 used the monthly winds of 1981 through 1984.

#### **D. ENERGY ANALYSIS TECHNIQUES**

The energy technique used is the same as that used and described in Batteen et al. (1992), and is based on that of Han (1975) and Semtner and Mintz (1977). This is done to gain a better understanding of the flow within the CCS and of the types of energy transfer during unstable flow. A brief summary of the method follows.

Kinetic energy (K) is calculated for the horizontal components. After quasi-steady state is reached where the total kinetic energy is nearly constant, mean and eddy kinetic energies are calculated using the averaged sum of squared mean and eddy horizontal fields, respectively. Next, the available potential energy is calculated and used to determine when a quasi-steady state is reached and when statistics should be collected. Then, both mean and eddy available potential energy are computed.

The energy transfers follow that of Semtner and Mintz (1977), and are used to argue for the type of instability mechanism (e.g., barotropic, baroclinic, or mixed) which leads to the initial eddy generation in each experiment.



#### **IV. RESULTS OF EXPERIMENTS**

Experiments 1 through 3 study the effects of forcing a model ocean domain that is initially at rest. Experiment 1 uses monthly climatological average (1980 - 1989) wind fields, while Experiments 2 and 3 use monthly average wind fields for 1981 and 1983, respectively. Experiments 4 through 6 study the effects of forcing a model domain that has been spun up by the wind field from the previous year. Experiment 4 uses the results of Experiment 1 as the start for a second year of climatological average wind fields, while Experiment 5 and 6 use the results of Experiment 2 and 3 as the start for 1982 and 1984, respectively. Experiments 7 and 8 use the results of longer (4-year) time runs from climatological and 1981 - 1984 wind fields, respectively, to examine the maintenance of features after initial spin up.

##### **A. EXPERIMENTS STARTED FROM REST**

###### **1. Experiment 1 - Climatological Winds**

Experiment 1 was forced with monthly averaged climatological (1980 - 1989) winds. Figure 4.1 depicts the monthly wind patterns over the model domain starting with January 15 (day 15) and ending on December 15 (day 345). The atmospheric pressure pattern for January has a low to the north and a high to the south which results in a wind

divergence near  $40^{\circ}$  N (Figure 4.1a). This pattern of poleward winds north of  $40^{\circ}$  N and equatorward winds to the south, continues through February and March (Figures 4.1b and c). During April and May (Figures 4.1d and e), the divergence in the wind flow is observed to migrate poleward. By June (Figure 4.1f), an equatorward component in the wind field is observed along the entire model domain. July, August, and September (Figures 4.1g through i) depict the strongest and most equatorward winds. By October (Figure 4.1j), the winds start to weaken throughout the domain and a divergence in the wind flow is observed in the north. This divergent wind flow pattern continues through November (Figure 4.1k). By December (Figure 4.1l) the wind divergence has returned to around  $40^{\circ}$  N.

In response to the prevailing poleward winds in the north, a relatively weak poleward coastal surface current of  $\sim 3 \text{ cm s}^{-1}$  was observed by model day 30 (Figure 4.2). It retreated further northward until by day 60 (not shown) it was not discernible. An equatorward surface current was observed along most of the coast by model day 90 (Figure 4.3) due to the prevailing equatorward winds over most of the model domain. A poleward undercurrent, caused by the meridional variation of the wind field (Batteen *et al.*, 1989), first became evident at model day 60 (Figure 4.4), and was fully established by model day 90 (Figure 4.5).

Along with the equatorward surface current, upwelling also occurred and was discernible by day 120 (Figure 4.6). Meanders in the equatorward surface current formed by model day 210 and are evident in both the velocity and temperature contour plots (Figures 4.7 and 4.8, respectively). By model day 240, meanders began to form cold core, cyclonic eddies as seen in the temperature contour and velocity plots (Figures 4.9 and 4.10, respectively) due to vertical and/or horizontal shear instabilities between the equatorward jet and the poleward undercurrent. The eddies initially appear to be about 30 km (Rossby radius of deformation) in diameter and extend about 100 km off the coast, and appear during the period of maximum wind stress (July - September).

The coldest temperatures due to upwelling were reached by model day 240. After model day 270 no upwelling was discernible (not shown). At the end of the year, meanders and eddies in a weak equatorward surface current were still present (Figures 4.11 and 4.12). A very weak poleward coastal surface current (not shown), and a poleward undercurrent were also present at the end of the year (Figure 4.13). Note that no filaments developed during this first climatological year.

Except for the lack of development of filaments, these model results are consistent with available observations cited in the literature. For example, the

eddies have rotational velocities of around  $50\text{-}80\text{ cm s}^{-1}$  which is in agreement with observations of Mooers and Robinson (1984). The poleward undercurrent is relatively weak ( $\sim 5\text{ cm s}^{-1}$  or less) and is in agreement with available observations by Huyer et al. (1989).

A time series of total kinetic energy per unit mass over the entire domain is shown in Figure 4.14. In this figure there are around three periods when the kinetic energy becomes quasi-steady. These time frames correspond to model days: 207 - 216, 228 - 231, and 297 - 303. Since meanders and/or eddies appeared during these time periods, more detailed analysis was performed on these intervals to determine the type of instability mechanism that could generate these features. Barotropic instability can result from horizontal shear while baroclinic instability can result from vertical shear in the current. As Figure 4.12 shows, there is considerable horizontal and vertical shear between the equatorward surface current and the poleward undercurrent. As a result, both types of instabilities (mixed), can be present simultaneously. Energy transfer calculations which consist of barotropic (mean kinetic energy to eddy kinetic energy) and baroclinic (eddy potential energy to eddy kinetic energy) components were performed on the three time frames above.

The results for the instability analyses for these periods are summarized in Table 4.1 (see Appendix A for the

energy transfer plots for this experiment), and show the following: For model days 207 to 216, 228 to 231, and 297 to 303 both barotropic and baroclinic (i.e., mixed) instabilities were present in the coastal, equatorward region of the domain. Additional analysis of model days 297 to 303 shows barotropic instabilities to be weak (Figure A.5) and baroclinic instabilities to be dominant (Figure A.6) during this period.

## **2. Experiment 2 - 1981 Winds**

Experiment 2 was forced with the monthly ECMWF winds from 1981. Figure 4.15 depicts the monthly wind patterns within the model domain starting with January and running through December. Unlike the climatological winds, January starts off with poleward flow throughout the model domain (Figure 4.15a). February (Figure 4.15b) shows the typical wind divergence at  $40^{\circ}$  N, consistent with the climatological data. March through June (Figures 4.15c through f) depict the wind divergence moving poleward and also shows the wind speed increasing to a maximum in June, especially in the southern half of the region. Figures 4.15g and h (July and August) depict strong winds and equatorward flow throughout the model domain. By September (Figure 4.15i), the wind divergence reappears in the north and migrates equatorward over the remaining three months of the year (Figures 4.15j to l). By December the wind divergence is at  $37.5^{\circ}$  N

(Figure 4.151), which is around  $2.5^\circ$  farther equatorward than the climatological wind divergence.

As in Experiment 1, a relatively weak poleward coastal surface flow  $\sim 2 \text{ cm s}^{-1}$  was observed in the poleward region of the model domain (Figure 4.16). In response to the wind pattern, an equatorward surface current was observed along most of the coast by model day 90 (Figure 4.17). A weak poleward undercurrent became evident by model day 90 (Figure 4.18), and became as large as  $5 \text{ cm s}^{-1}$  in layer 5 (316 m) by day 210 (Figure 4.19).

Upwelling of temperatures cooler than  $15^\circ \text{ C}$  was observed by model day 120 (as observed in the climatological run), as seen in Figure 4.20. Meanders in the surface current also formed by the same model day as in the climatological run (day 210) as depicted in the velocity and temperature contour plots (Figures 4.21 and 4.22, respectively). By model day 270, the first sign of eddies appear (see the velocity and temperature contour plots of Figures 4.23 and 4.24), which is  $\sim 30$  days later than in the climatological run. The amplitude of the meander of the coastal current increases to the south as a result of the stronger equatorward winds in this region. Again, these eddies are cold core, cyclonic, and about 30 km in diameter.

Upwelling of the coldest surface water occurred by model day 240 (not shown), corresponding to the period of strongest equatorward winds. Upwelling did not disappear

until model day 330 (not shown), which is ~60 days later than the climatological results. At the end of the year, meanders in the equatorward surface current along with embedded eddies remain (Figure 4.25). A poleward undercurrent is also discernible at the end of the year (Figure 4.26). A very weak poleward coastal surface current (not shown) has reappeared in the poleward region of the model domain. As in Experiment 1, no filaments developed during this experiment.

Figure 4.27 shows the time series of total kinetic energy per unit mass over the entire domain for 1981 and shows four periods when the kinetic energy becomes quasi-steady, model days: 210 - 222, 240 - 252, 297 - 303, and 309 - 333. Energy transfer plots were obtained for these periods and yielded mixed (i.e., both barotropic and baroclinic) instabilities in all cases in the coastal, equatorward region of the model domain. These results are summarized in Table 4.1 (see Appendix B for the energy transfer plots for this experiment). During the time frame 297 to 303, barotropic instability (Figure B.5) was much greater than baroclinic (Figure B.6) instability.

### **3. Experiment 3 - 1983 Winds**

Experiment 3 represents the El Niño year of 1983 and was forced with the monthly winds depicted in Figure 4.28 representing January through December. The year starts off

with predominantly poleward winds for the first three months as seen in Figures 4.28a - c. April shows a change in the wind pattern as equatorward winds are present throughout (Figure 4.28d). These winds remain equatorward and strengthen from May through September (Figures 4.28e - i). The winds weaken in October (Figure 4.28j). A divergence in the wind field appears near  $38^{\circ}$  N during November (Figure 4.28k) and remains through December (Figure 4.28l).

In response to the three consistent months of strong poleward winds at the start of 1983, a poleward coastal surface current with velocities as high as  $5 \text{ cm s}^{-1}$  is established by model day 30 (Figure 4.29) and remains through model day 60 (not shown). By model day 120 an equatorward surface current develops along most of the coast (Figure 4.30). A weak poleward undercurrent is present at model day 90 as seen in Figure 4.31, and strengthens to around  $6 \text{ cm s}^{-1}$  by model day 195 (not shown).

Upwelling and meanders both appear by model day 150 (Figure 4.32). The meanders are also discernible in the velocity plot (Figure 4.33). Note that the meanders appear farther poleward than in the previous experiments. Eddies start to form by model day 240 as seen in the velocity (Figure 4.34) and temperature (Figure 4.35) fields. As in the previous experiments, these eddies are cold core and cyclonic.



The coldest upwelling temperatures were reached by model day 240 but were warmer (only  $14.0^{\circ}\text{C}$  as compared to  $13.5^{\circ}\text{C}$  and  $11.5^{\circ}\text{C}$  for climatology and 1981, respectively) than observed in previous runs. No upwelling was discernible after model day 270. By the end of the year, meanders in the equatorward surface current along with embedded eddies (Figure 4.36), a weak poleward coastal current (not shown), and a poleward undercurrent (Figure 4.37) were discernible. As in the previous experiments, no filaments developed during the experiment.

Figures 4.38a and b show the time series of total kinetic energy per unit mass for 1983. Quasi-steady periods that prompted additional evaluation were, model days: 186 - 192, 222 - 234, 249 - 258, 279 - 288, 312 - 315, 324 - 327, and 342 - 348. The results for the instability analysis for this year are summarized in Table 4.1 (see Appendix C for the energy transfer plots). Every period showed mixed (both barotropic and baroclinic) instabilities to be present. The instability analysis for model day 279 to 288 was the only case where one type of instability was noticeably greater than the other, and in this case barotropic (Figure C.7) was greater than baroclinic (Figure C.8).

#### **4. Summary of First Year Run Results**

Table 4.2 summarizes the climatological, 1981, and 1983 experiment runs for the first year. In all first year

runs, both a surface equatorward current and a poleward undercurrent developed. There was also a poleward coastal surface current present during the winter season. Upwelling was a seasonal feature which, as expected, had the coolest temperatures during a non-El Niño year (1981) and warmest temperatures during an El Niño year (1983). Both meanders and eddies were generated. The eddies were cold core, cyclonic, and had a size around the Rossby radius of deformation (30 km). Along with an equatorward surface current, both meanders and eddies remained at the end of each year. Instability analyses revealed that both barotropic and baroclinic processes were important eddy generation mechanisms. In all first year runs, no filaments were observed.

## **B. EXPERIMENTS SPUN UP FROM THE PREVIOUS YEAR**

### **1. Experiment 4 - Climatological Winds**

Experiment 4 was forced with the same monthly averaged climatological winds as in Experiment 1 (Figure 4.1). In this experiment, the model was continued with the spun-up output from Experiment 1, rather than starting from rest. For convenience this experiment is referred to as "Climo II" because climatological winds are used a second time.

In response to the wind forcing, an equatorward surface current was observed by model day 396 (year day (yd)

30) (Figure 4.39). Embedded in this current are meanders and cyclonic eddies (Figures 4.39 and 4.40). A weak poleward coastal surface current was also present initially (not shown). A poleward undercurrent was established by model day 426 (yd 60) (Figure 4.41).

Upwelling was observed by model day 546 (yd 180) (Figure 4.42), and peaked by model day 606 (yd 240) (Figure 4.43), with a minimum temperature near  $12^{\circ}$  C. Cessation of upwelling occurred by model day 726 (yd 360) (not shown).

In previous model runs anticyclonic meanders were observed, but they did not close off to form anticyclonic eddies. During this experiment, in addition to the predominantly cyclonic eddies, a warm core anticyclonic eddy (defined by closed contour in streamline plot - not shown) formed by model day 456 (yd 90) (Figure 4.44). This anticyclonic eddy persisted for the remainder of the year.

Figure 4.45 is a cross section in the middle of the domain and depicts the broad meanders in the CC along with a strong core of the CUC near 250 m in depth. Between model days 696 (yd 330) and 726 (yd 360), an eddy formed as the result of a pinched-off meander (Figures 4.46 and 4.47). A filament was observed during this experiment by day 606 (yd 240) and extended about 300 km offshore ( $15^{\circ}$  C isotherm) near  $40^{\circ}$  N (Figure 4.43).

A time series of total kinetic energy per unit mass over the entire domain is shown in Figure 4.48. Four

periods were investigated further because the kinetic energy became quasi-steady. These time frames correspond to model days: 378 - 408 (yd 12 - 42), 453 - 465 (yd 87 - 99), 504 - 516 (yd 138 - 150), and 624 - 636 (yd 258 - 270). All four of these periods consisted of both barotropic and baroclinic instabilities. These results are summarized in Table 4.3 (see Appendix D for the energy transfer plots for this experiment).

## **2. Experiment 5 - 1982 Winds**

Experiment 5 was forced with monthly winds from 1982. This experiment continues the spun up case using the output of Experiment 2 (1981) as a starting point, rather than starting from rest. Figure 4.49 shows the monthly wind patterns within the model domain starting with January and running through December. January starts with the typical divergent flow, this year slightly to the north at  $42^{\circ}$  N (Figure 4.49a). February moves the divergence equatorward to  $40^{\circ}$  N and has weaker winds to the south (Figure 4.49b). The flow in March is onshore throughout the model domain with a slight poleward component in the north (Figure 4.49c). April has the divergence at  $42.5^{\circ}$  N (Figure 4.49d). May starts the all equatorward flow and is the strongest (Figure 4.49e), this regime continues in June (Figure 4.49f) through October (Figure 4.49i). A divergent flow returns in October at  $42.5^{\circ}$  N (Figure 4.49j), and migrates equatorward

to 38.5° N in November (Figure 4.49k) and remains in December (Figure 4.49l).

As in the previous experiment, the year starts with a fully developed equatorward surface current which contains embedded meanders and eddies (Figure 4.50). Also present is an anticyclonic eddy, and a poleward surface coastal current in the northern part of the model domain (Figures 4.50 and 4.51). A relatively strong ( $\sim 9.5 \text{ cm s}^{-1}$ ) poleward undercurrent is present by model day 426 (yd 60). A cross section in the middle of the domain (Figure 4.52) shows this feature along with a strong subsurface flow associated with an eddy (Figure 4.53).

Upwelling began by model day 516 (yd 150) (Figure 4.54), and peaked by model day 606 (yd 240) (Figure 4.55). The coolest water observed was around 12.0° C. The upwelling ceased by model day 696 (yd 330) (Figure 4.56).

Four cyclonic eddies and one anticyclonic eddy were present (e.g., Figure 4.53) throughout most of this experiment. The size ranged between 30 and 150 km in diameter and the westward propagation of these larger features was around 500 km. As in Experiment 4, a filament was observed during this experiment. By day 600 (yd 234) (not shown) this filament extended about 350 km offshore near 38.5° N. A cold core eddy pinched off from this filament by day 606 (yd 240) (Figure 4.55).

A time series of total kinetic energy per unit mass over the entire domain was produced (Figure 4.57), and showed two quasi-steady periods for additional study. These were model days: 507 - 516 (yd 141 - 150), and 525 - 528 (yd 159 - 162). As in the previous experiments, the energy transfer plots indicate the presence of both barotropic and baroclinic instabilities. Table 4.3 summarizes these results (see Appendix E for the energy transfer plots for this experiment).

### **3. Experiment 6 - 1984 Winds**

Experiment 6 was forced with monthly winds from 1984. This experiment continues the spun-up case using the output of Experiment 3 (1983) as a starting point, rather than starting from rest. Figure 4.58 shows the monthly wind patterns within the model domain starting with January and running through December. January has a divergent flow at  $43^{\circ}$  N (Figure 4.58a), while February shows that the divergence has moved equatorward to  $39^{\circ}$  N (Figure 4.58b). From March through May (Figures 4.58c through e), the wind divergence moves from  $41^{\circ}$  N to  $43^{\circ}$  N and the winds become stronger. June is the start of equatorward wind flow (Figure 4.58f), which continues through July and August (Figures 4.58g and h). In September, the wind divergence reappears in the north at  $47^{\circ}$  N (Figure 4.58i). During October and November, the divergence migrates equatorward to

37° N (Figures 4.58i and k). The year ends in December with weak winds along the coast with a divergence at 40° N, and with predominantly equatorward winds further off the coast (Figure 4.58l).

At the start of the experiment, there is a well-developed equatorward surface flow with embedded meanders and eddies (Figure 4.59). There is also a weak poleward coastal surface current in the northern corner of the model domain which remains until model day 426 (yd 60) (Figure 4.60). A relatively strong ( $\sim 10 \text{ cm s}^{-1}$ ) poleward undercurrent is evident, as seen in a cross-section in the middle of the model domain, at model day 546 (yd 180) (Figure 4.61).

Upwelling begins by model day 456 (yd 90) (Figure 4.62). Corresponding to the period of maximum equatorward winds, the peak occurs at model day 576 (yd 210) (Figure 4.63) in which cooler temperatures of around 10° C are present along the entire coast. This year had upwelling of cooler water earlier than previous years and also had the coldest water which was a result of the strong equatorward winds. Cessation of the cooler water occurs by model day 726 (yd 360) (not shown).

The eddies are around 90 km in diameter and stay within 300 km of the coast. A filament occurs by model day 666 (yd 300) (Figure 4.64). This filament is observed near

38° N as a plume of 15° C water and extends about 200 km off the coast.

The time series plot of total kinetic energy per unit mass over the entire domain is shown in Figure 4.65. The kinetic energy is still fluctuating because the model is still spinning up during the first part of the year. Three periods were selected for additional study, model days: 576 - 591 (yd 210 - 225), 606 - 624 (yd 240 - 258), and 645 - 657 (yd 279 - 291). All of these included both barotropic and baroclinic instabilities, and are summarized in Table 4.3 (see Appendix F for the energy transfer plots for this experiment).

#### **4. Summary of Second Year Run Results**

Table 4.4 summarizes the follow-on (second year) model runs. In general, a weak coastal poleward surface current was evident during the winter season in the northern region of the domain for all years (Climo II, 1982 and 1984). A meandering equatorward surface current, already present, at the start of these experiments was maintained. A poleward undercurrent was generated in all experiments. The eddies, already present at the start of the experiments, were both cold core, cyclonic, and warm core, anticyclonic eddies in Climo II and 1982, while in 1984 there were only cold core, cyclonic eddies. The size and offshore extent of the eddies were consistent with the first experimental runs.



Seasonal upwelling occurred with minimum temperatures of  $\sim 12^{\circ}$  C for Climo II and 1982, and of  $\sim 10^{\circ}$  C for 1984. The year 1984 had the largest extent of cool upwelled water as expected for a year with the strongest equatorward winds. Filaments developed in all three experiments, but was most pronounced (as expected) in 1984. The filaments had an offshore extent between 200 and 350 km. Instability analyses revealed that both barotropic and baroclinic processes were involved in eddy generation.

#### **5. Experiment 7 - Multiple Climatological Runs**

Experiment 7 was an extended climatological run in which the climatological winds used in Experiment 1 (Figure 4.1) were used in repetition four times. The third and fourth years of the run follow Experiment 4 (Climo II) and are dubbed "Climo III" and "Climo IV", respectively. (The values in the model on the last day of a run were retained for use at the start of the next run, rather than starting from scratch or rest as is done in a cold restart.)

In response to the wind forcing, an equatorward surface current was observed by model day 760 and 1125 (yd 30) for Climo III and Climo IV, respectively (not shown). Embedded in this current were meanders and cyclonic eddies (not shown). A weak poleward coastal surface current was also present initially (not shown). A poleward undercurrent

was evident early on by model day 820 and 1185 (yd 60) for Climo III and Climo IV, respectively (not shown).

Upwelling was observed by model day 850 and 1215 (yd 120) for Climo III and Climo IV, respectively (not shown). The upwelling peaked by model day 970 (yd 240) for Climo III (not shown) and day 1305 (yd 210) for Climo IV (not shown), with a minimum temperature near  $11^{\circ}$  C. Cessation of upwelling occurred by model day 1060 (yd 330) for Climo III (not shown), and was still present in small patches by day 1455 (yd 360) for Climo IV (not shown).

Figure 4.66 and 4.67 show the total kinetic energy per unit mass time series over the entire domain for Climo III and Climo IV, respectively. Climo III has a peak kinetic energy of  $166 \text{ cm}^2\text{s}^{-2}$  around model day 915 (yd 185) while Climo IV has a peak of  $145 \text{ cm}^2\text{s}^{-2}$  at model day 1293 (yd 198). Figure 4.68 depicts the total kinetic energy per unit mass time series for all four climatological runs together. It clearly shows that the first and second runs were involved in the generation or spin-up of features in the model, while the third and fourth runs oscillated about  $125 \text{ cm}^2\text{s}^{-2}$  and indicate the maintenance of these features (i.e., a quasi-steady state).

#### **6. Experiment 8 - Multiple Years (1981 - 1984)**

Experiment 8 was a run of two additional years of the model using the monthly winds of 1983 (Figure 4.28) and

1984 (Figure 4.58). This experiment differs from Experiment 3 (1983) which was started from scratch (cold restart). The runs in this experiment followed in succession after Experiment 5 (1982), and used the values in the model on the last day of the year as input to the restart.

In response to the wind forcing, an equatorward surface current was observed by model day 760 and 1125 (yd 30) for 1983 and 1984, respectively (not shown). Embedded in this current were meanders and cyclonic eddies (not shown). A weak poleward coastal surface current was also present initially (not shown). A poleward undercurrent was evident by model day 820 and 1185 (yd 60) for 1983 and 1984, respectively (not shown).

Upwelling was observed by model day 880 (yd 150) for 1983 (not shown), and day 1155 (yd 60) for 1984 (not shown). The upwelling peaked by model day 940 and 1305 (yd 210) for 1983 and 1984, respectively (not shown). The minimum temperature was near  $11^{\circ}\text{C}$  for both 1983 and 1984, but 1983 had only patches of this water while 1984 had this cool water along the entire coast. Upwelling was still present in small patches by day 1090 and 1455 (yd 360) for 1983 and 1984, respectively (not shown).

Figure 4.69 and 4.70 are the total kinetic energy per unit mass time series over the entire domain for 1983 and 1984, respectively. The year 1983 has a peak kinetic energy of  $128\text{ cm}^2\text{s}^{-2}$  around model day 963 (yd 233) and 1984

has a peak of  $215 \text{ cm}^2\text{s}^{-2}$  at model day 1368 (yd 273). Figure 4.71 depicts the runs for all four years (1981 through 1984) together on one total kinetic energy per unit mass time series. It appears that the first year (1981) as seen in Experiment 2 and the second year (1982) as seen in Experiment 5, were involved in generation or spinning up of the model. The third year (1983), which was an El Niño year, had an energy level on par with 1982, so that no increase in kinetic energy occurred. In the fourth year (1984), the energy level increase significantly to the highest value ( $215 \text{ cm}^2\text{s}^{-2}$ ). Comparing this figure to the climatological time series (Figure 4.68) for the last two years shows that the maximum (1984) and minimum (1983) kinetic energies lie on either side (as expected) of the climatological year. During a non-El Niño year, as is 1984, features such as equatorward currents and upwelling would strengthen while during an El Niño year, as in 1983, these features would be weaker.

#### **7. Summary of Multiple Year Run Results**

Table 4.5 summarizes the last two years of the extended (four year) runs. Listed here are Climo IV, 1983, and 1984. Similar results are obtained: A poleward coastal surface current, a surface equatorward current, a poleward undercurrent, along with embedded meanders and eddies. Of interest, upwelling occurs later in 1983 (at yd 150) than

for the other years (yd 60 to yd 90). Although the minimum temperature is the same ( $11.0^{\circ}$  C) for all years, 1984 experienced a larger area of cooler water (all along the coast) than that of the El Niño (1983) year. In all experiments, there were both cold and warm core eddies. Finally, filaments were observed during Climo IV and 1984, but not during 1983.

**TABLE 4.1** SUMMARY OF INSTABILITIES FOR CLIMATOLOGICAL YEAR (TOP), 1981 (CENTER), AND 1983 (BOTTOM).

MODEL DAYS for Climatology	FEATURE TYPE (Meander, Eddy, Both)	INSTABILITY (Barotropic, Baroclinic, Mixed)	LOCATION (Coastal, Offshore, Both)
207-216	Meander	Mixed	Coastal
228-231	Meander	Mixed	Both
297-303	Both	Mixed	Both

MODEL DAYS for 1981	FEATURE TYPE (Meander, Eddy, Both)	INSTABILITY (Barotropic, Baroclinic, Mixed)	LOCATION (Coastal, Offshore, Both)
210-222	Meander	Mixed	Coastal
240-252	Meander	Mixed	Both
297-303	Both	Mixed	Both
309-333	Both	Mixed	Both

MODEL DAYS for 1983	FEATURE TYPE (Meander, Eddy, Both)	INSTABILITY (Barotropic, Baroclinic, Mixed)	LOCATION (Coastal, Offshore, Both)
186-192	Meander	Mixed	Coastal
222-234	Meander	Mixed	Both
249-258	Meander	Mixed	Coastal
279-288	Meander	Mixed	Coastal
312-315	Both	Mixed	Both
324-327	Both	Mixed	Both
342-348	Both	Mixed	Both

**TABLE 4.2 SUMMARY OF EXPERIMENTS - FIRST YEAR.**

FEATURE	CLIMO	1981	1983
<b>CURRENTS:</b>			
Sfc Poleward	~1-60, & 330-360 days	~1-60, & 330-360 days	~1-60, & 330-360 days
Sfc Equatorward	~90 days	~90 days	~120 days
Undercurrent (poleward only)	~60 days	~120 days	~60 days
<b>UPWELLING: (<math>&lt;15^{\circ}\text{C}</math>)</b>			
Start	~120 days	~120 days	~150 days
Maximum (min temp)	~240 days ( $13.0^{\circ}\text{C}$ )	~240 days ( $11.0^{\circ}\text{C}$ )	~240 days ( $14.0^{\circ}\text{C}$ )
Cessation	~270 days	~330 days	~270 days
<b>MEANDERS:</b>			
Start	~210 days	~210 days	~150 days
<b>EDDIES:</b>			
Start	~240 days	~270 days	~240 days
Core	cold	cold	cold
Rotation	cyclonic	cyclonic	cyclonic
Size (diameter)	~30-60 km	~30-60 km	~30-80 km
<b>FILAMENTS:</b>			
Start	none	none	none
Offshore extent	n/a	n/a	n/a

**TABLE 4.3 SUMMARY OF INSTABILITIES FOR CLIMATOLOGICAL II YEAR (TOP), 1982 (CENTER), AND 1984 (BOTTOM).**

MODEL DAYS for Climo II	FEATURE TYPE (Meander, Eddy, Both)	INSTABILITY (Barotropic, Baroclinic, Mixed)	LOCATION (Coastal, Offshore, Both)
378-408 (12-42)	Both	Mixed	Both
453-465 (87-99)	Meander	Mixed	Coastal
504-516 (138-150)	Both	Mixed	Both
624-636 (258-270)	Both	Mixed	Both

MODEL DAYS for 1982	FEATURE TYPE (Meander, Eddy, Both)	INSTABILITY (Barotropic, Baroclinic, Mixed)	LOCATION (Coastal, Offshore, Both)
507-516 (141-150)	Both	Mixed	Both
525-528 (159-162)	Both	Mixed	Both

MODEL DAYS for 1984	FEATURE TYPE (Meander, Eddy, Both)	INSTABILITY (Barotropic, Baroclinic, Mixed)	LOCATION (Coastal, Offshore, Both)
576-591 (210-225)	Meander	Mixed	Coastal
606-624 (240-258)	Meander	Mixed	Coastal
645-657 (279-291)	Meander	Mixed	Coastal



**TABLE 4.4 SUMMARY OF EXPERIMENTS - SECOND YEAR.**

FEATURE	CLIMO II	1982	1984
<b>CURRENTS:</b>			
Sfc Poleward	~366-426 (1-60), & 696-726 (330-360) days	~366-426 (1-60), & 696-726 (330-360) days	~366-426 (1-60), & 696-726 (330-360) days
Sfc Equatorward	~396 days (30)	~396 days (30)	~396 days (30)
Undercurrent (poleward only)	~426 days (60)	~426 days (60)	~546 days (180)
<b>UPWELLING: (<math>&lt;15^{\circ}\text{C}</math>)</b>			
Start	~546 days (180)	~516 days (150)	~456 days (90)
Maximum (min temp)	~606 days (240) ( $12.0^{\circ}\text{C}$ )	~606 days (240) ( $12.0^{\circ}\text{C}$ )	~576 days (210) ( $10.0^{\circ}\text{C}$ )
Cessation	~726 days (360)	~696 days (330)	~726 days (360)
<b>MEANDERS:</b>			
Start	~396 days (30)	~396 days (30)	~396 days (30)
<b>EDDIES:</b>			
Start	~396 days (30)	~396 days (30)	~396 days (30)
Core	cold & warm	cold & warm	cold
Rotation	cyclonic & anticyclonic	cyclonic & anticyclonic	cyclonic
Size (diameter)	~30-90 km	~30-150 km	~30-90 km
<b>FILAMENTS:</b>			
Start	~606 days (240)	~600 days (234)	~666 days (300)
Offshore extent	~300 km	~350 km	~200 km

**TABLE 4.5 SUMMARY OF EXPERIMENTS - MULTIPLE YEARS.**

FEATURE	CLIMO IV	1983	1984
<b>CURRENTS:</b>			
Sfc Poleward	~1096-1215 (1-120), & 1395-1455 (300-360) days	~731-850 (1-120), & 1060-1090 (330-360) days	~1096-1185 (1-90), & 1425-1455 (330-360) days
Sfc Equatorward	~1125 days (30)	~760 days (30)	~1125 days (30)
Undercurrent (poleward only)	~1155 days (60)	~790 days (60)	~1155 days (60)
<b>UPWELLING: (<math>&lt;15^{\circ}\text{C}</math>)</b>			
Start	~1185 days (90)	~880 days (150)	~1155 days (60)
Maximum (min temp)	~1305 days (210) ( $11.0^{\circ}\text{C}$ )	~940 days (210) ( $11.0^{\circ}\text{C}$ )	~1305 days (210) ( $11.0^{\circ}\text{C}$ )
Cessation	~1455 days (360)	~1090 days (360)	~1455 days (360)
<b>MEANDERS:</b>			
Start	~1125 days (30)	~760 days (30)	~1125 days (30)
<b>EDDIES:</b>			
Start	~1125 days (30)	~760 days (30)	~1125 days (30)
Core	cold & warm	cold & warm	cold & warm
Rotation	cyclonic & anticyclonic	cyclonic & anticyclonic	cyclonic & anticyclonic
Size (diameter)	~30-80 km	~30-80 km	~30-80 km
<b>FILAMENTS:</b>			
Start	~1305 days (210)	none	~1305 days (210)
Offshore extent	~350 km	n/a	~350 km

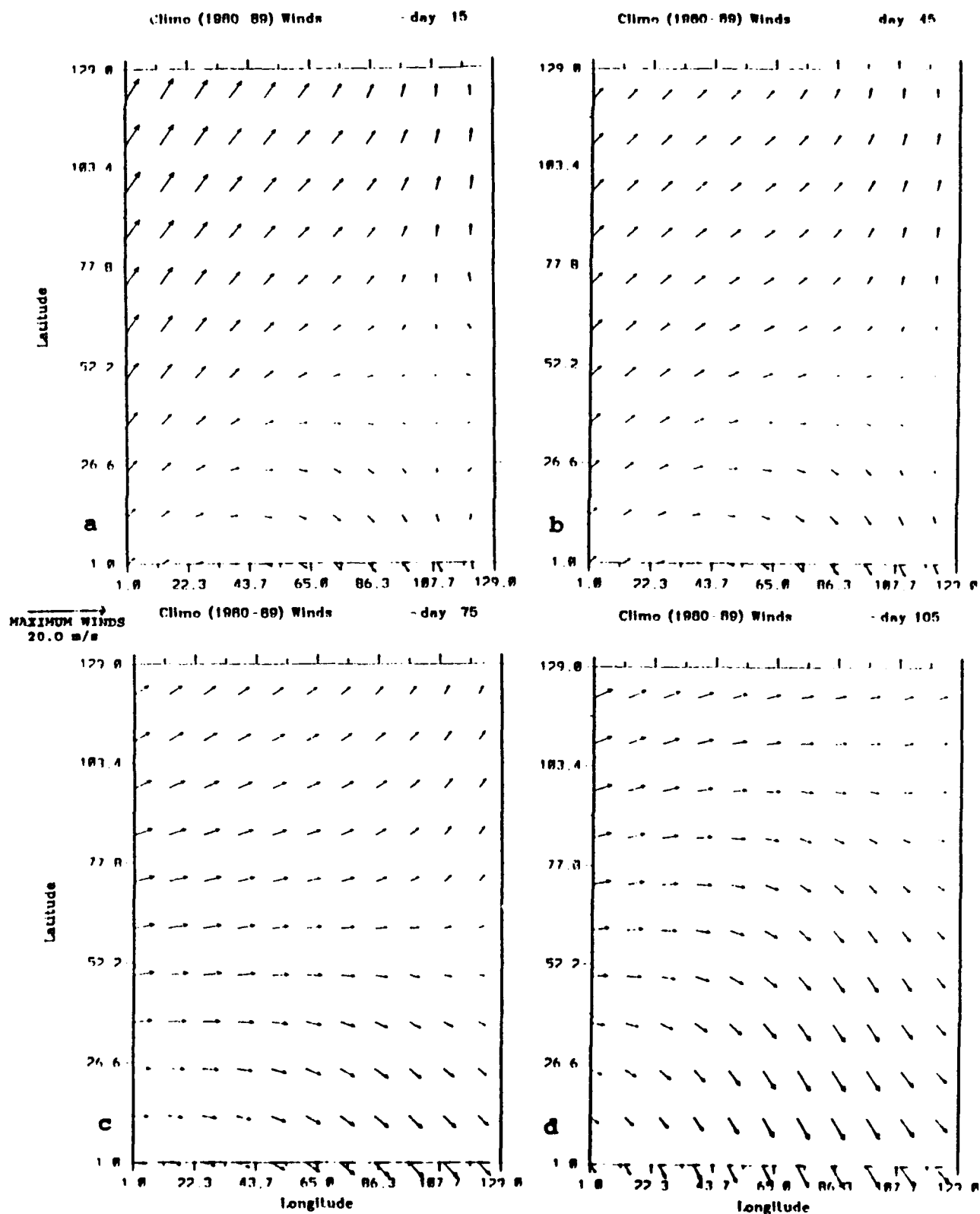


**Figure 4.1** Mid-monthly averaged climatological (1980 - 1989) ECMWF winds in  $\text{m s}^{-1}$ : (a) January, (b) February, (c) March, (d) April, (e) May, (f) June, (g) July, (h) August, (i) September, (j) October, (k) November, and (l) December. The latitudinal grid point 1 (129) corresponds to  $35^{\circ}$  N ( $47.5^{\circ}$  N); so that the latitudinal grid point of 52 corresponds to  $40^{\circ}$  N. Maximum wind vector is  $20 \text{ m s}^{-1}$ .

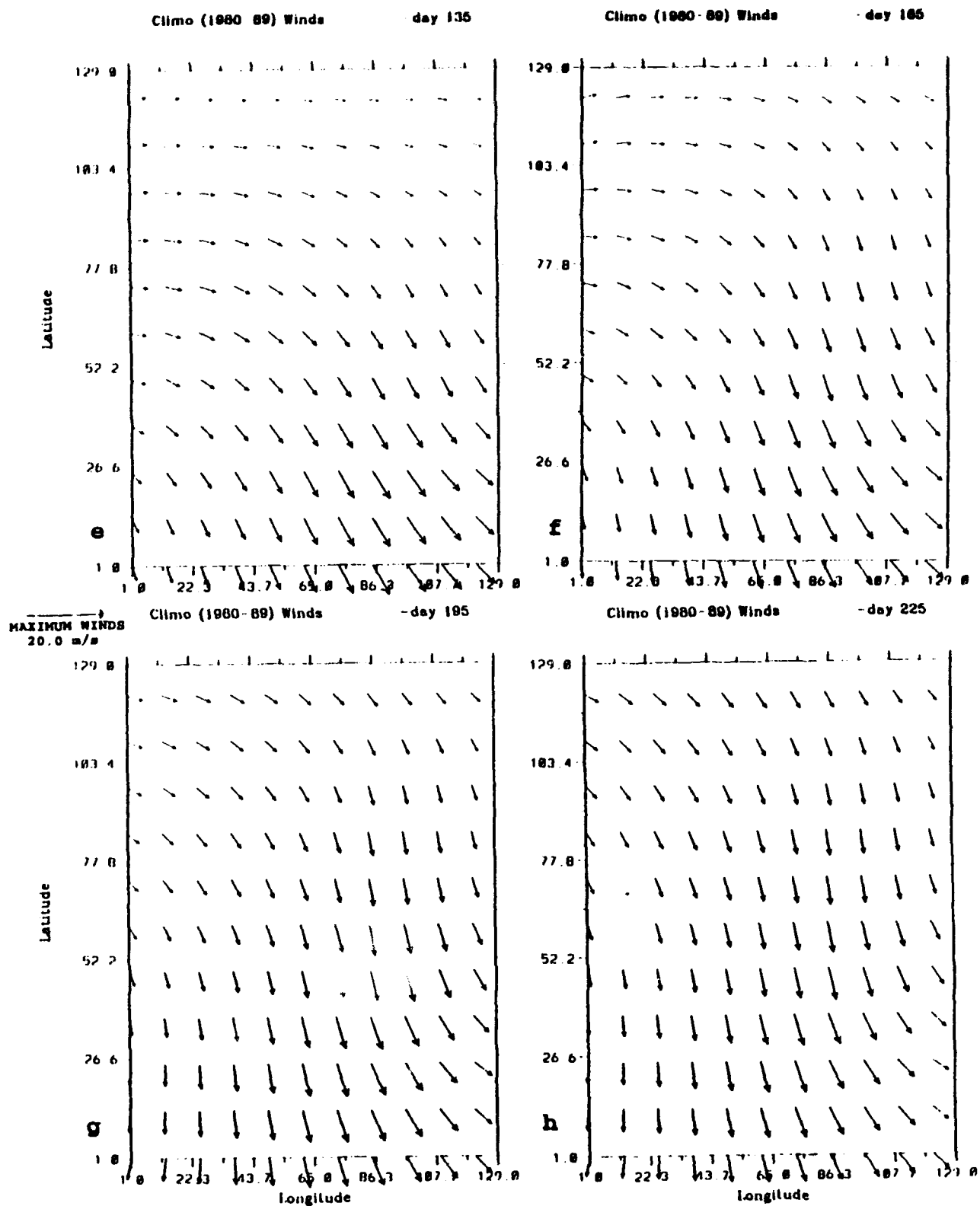


Figure 4.1 (continued).

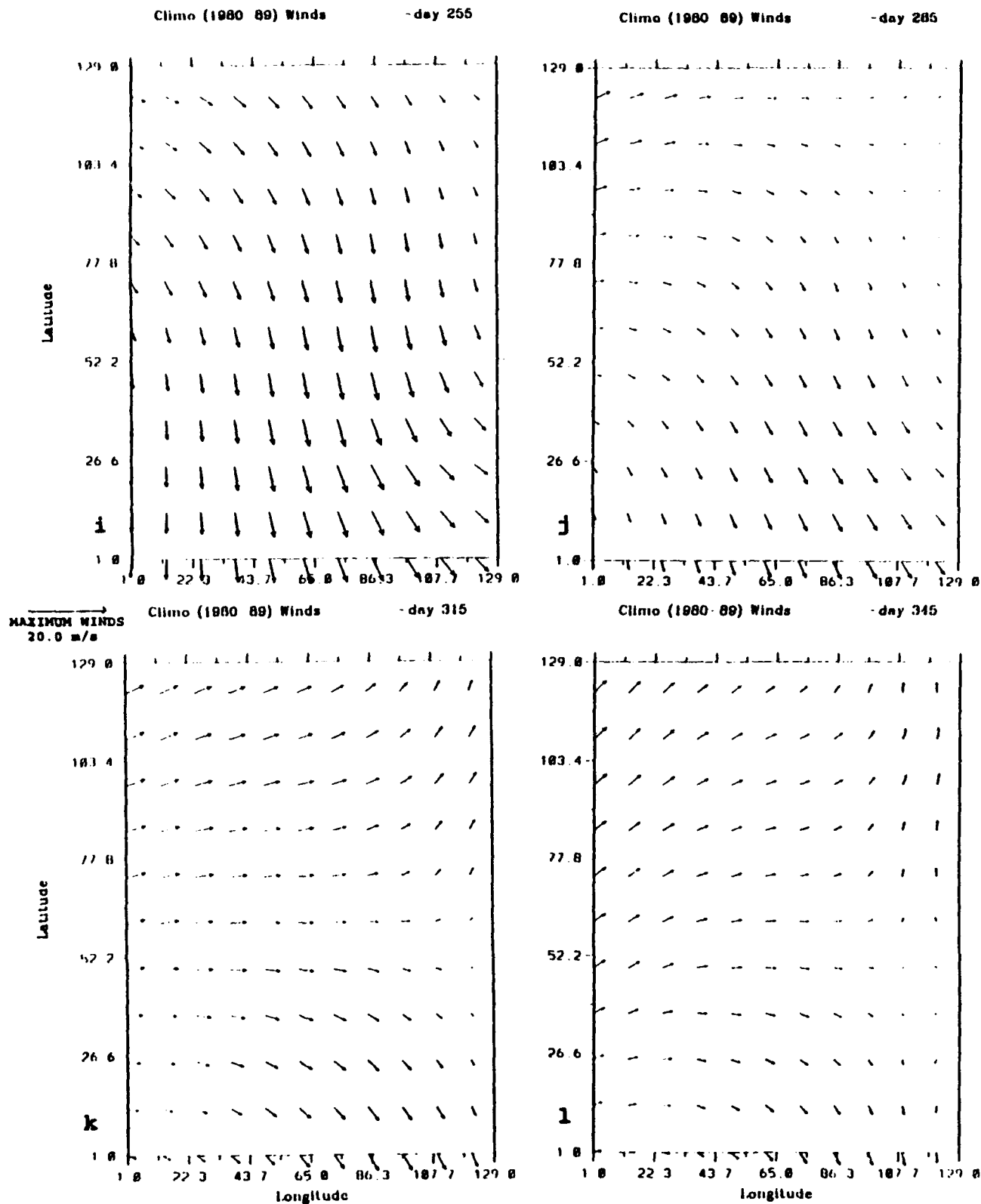
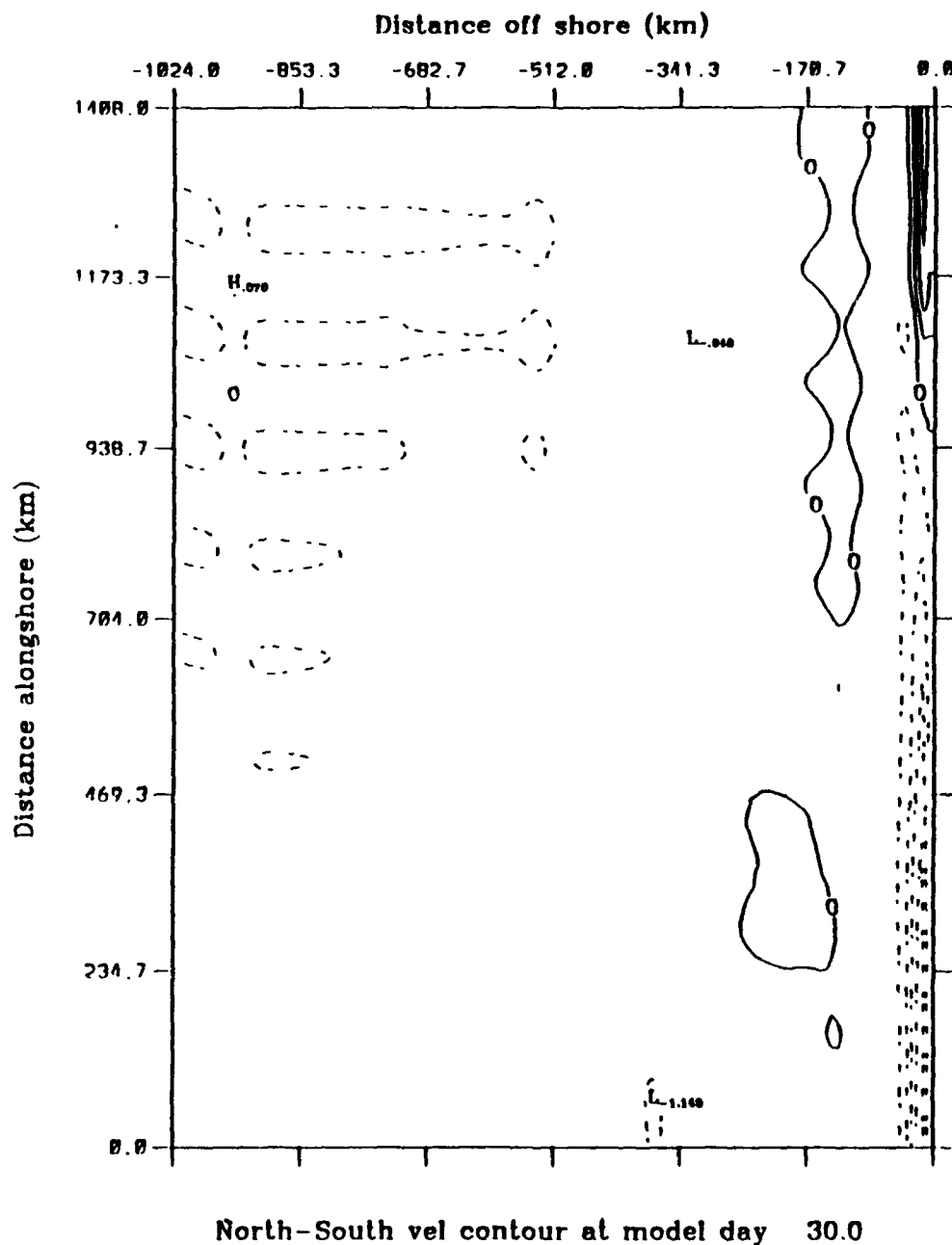
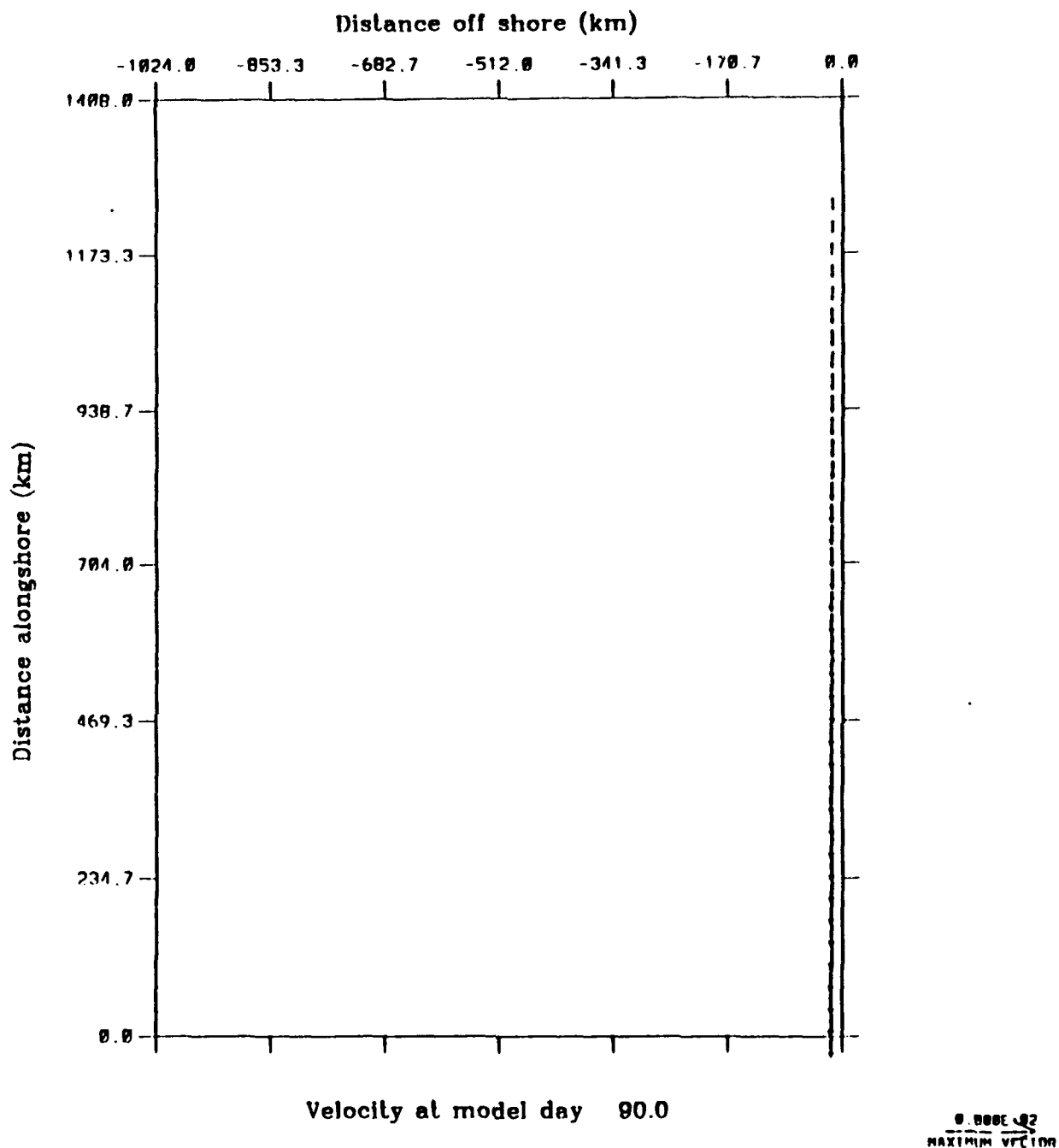


Figure 4.1 (continued).



**Figure 4.2** Experiment 1: Surface meridional component of velocity at day 30. The contour interval is  $1 \text{ cm s}^{-1}$ . The dashed lines indicate equatorward velocities. The maximum poleward velocity is  $\sim 3 \text{ cm s}^{-1}$ . Latitudinal alongshore distance 0 (1408) km corresponds to  $35^\circ \text{ N}$  ( $47.5^\circ \text{ N}$ ).



**Figure 4.3**    Experiment 1: Surface velocity vectors at day 90. To avoid clutter, velocity vectors are plotted at every third grid point in both the cross-shore and alongshore direction, and velocities less than  $5 \text{ cm s}^{-1}$  are not plotted.

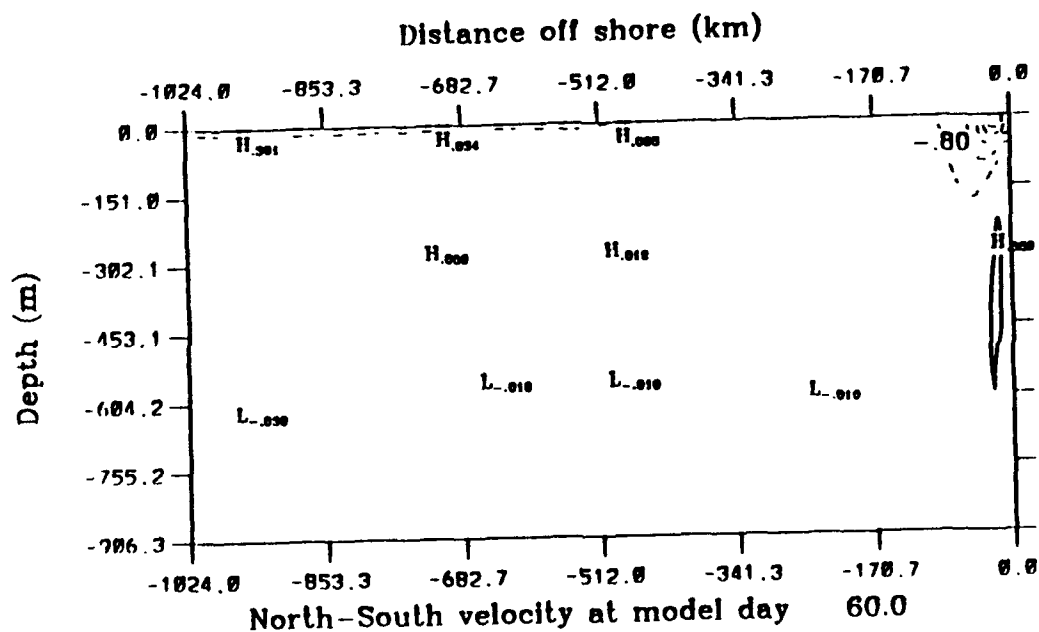


**Figure 4.4** Experiment 1: Cross-section at  $y \sim 704$  km ( $41.25^\circ$  N) of the meridional component of velocity at day 60. Dashed lines indicate equatorward flow, while solid lines indicate poleward flow.



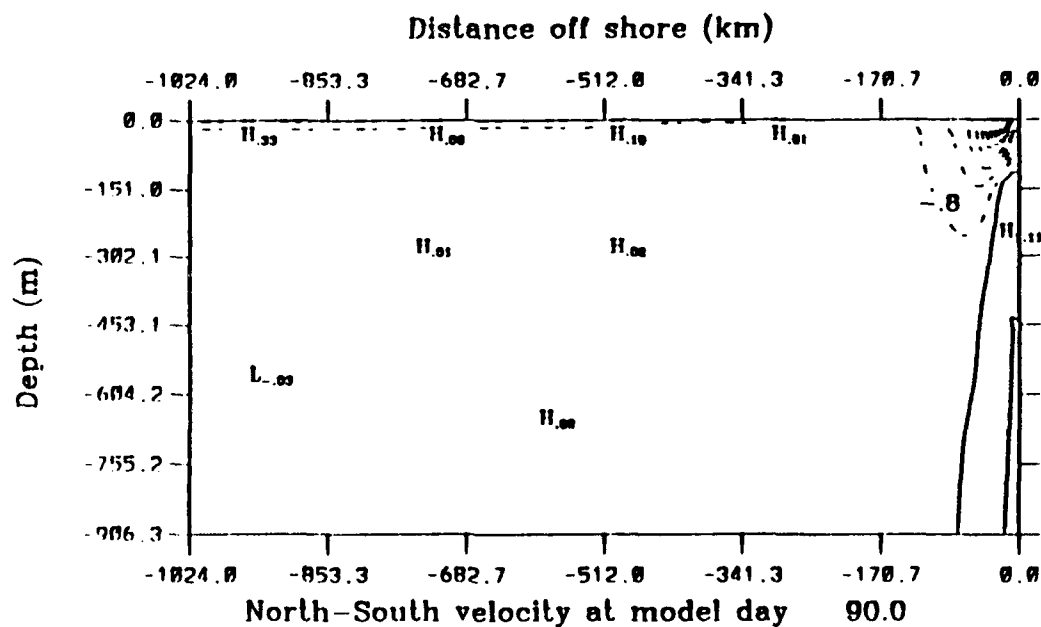


**Figure 4.5** Experiment 1: Cross-section at  $y \sim 704$  km ( $41.25^\circ$  N) of the meridional component of velocity at day 90. Dashed lines indicate equatorward flow, while solid lines indicate poleward flow.

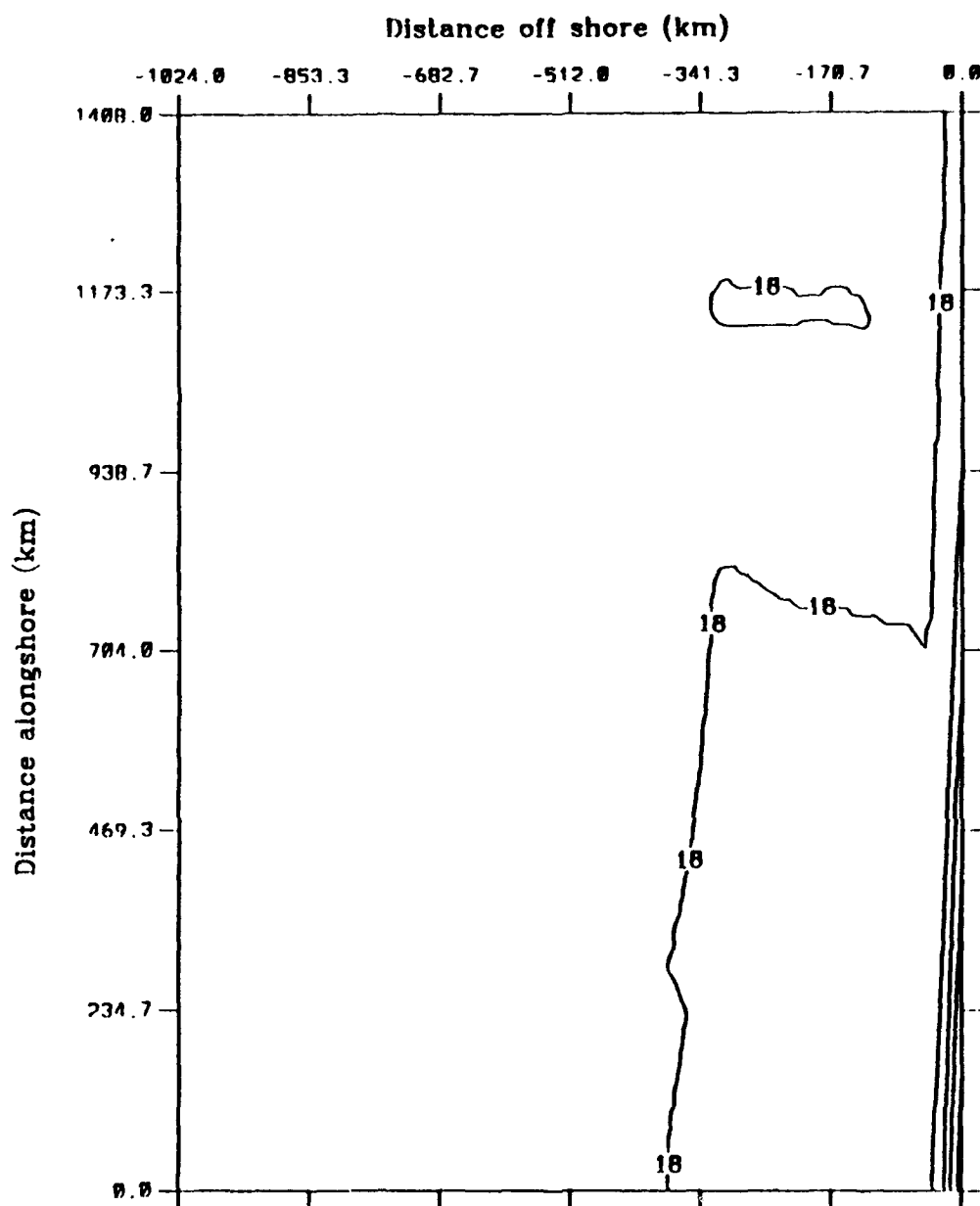


**Figure 4.6** Experiment 1: Surface temperature at day 120. The contour interval is 1° C. The temperature decreases towards the coast.

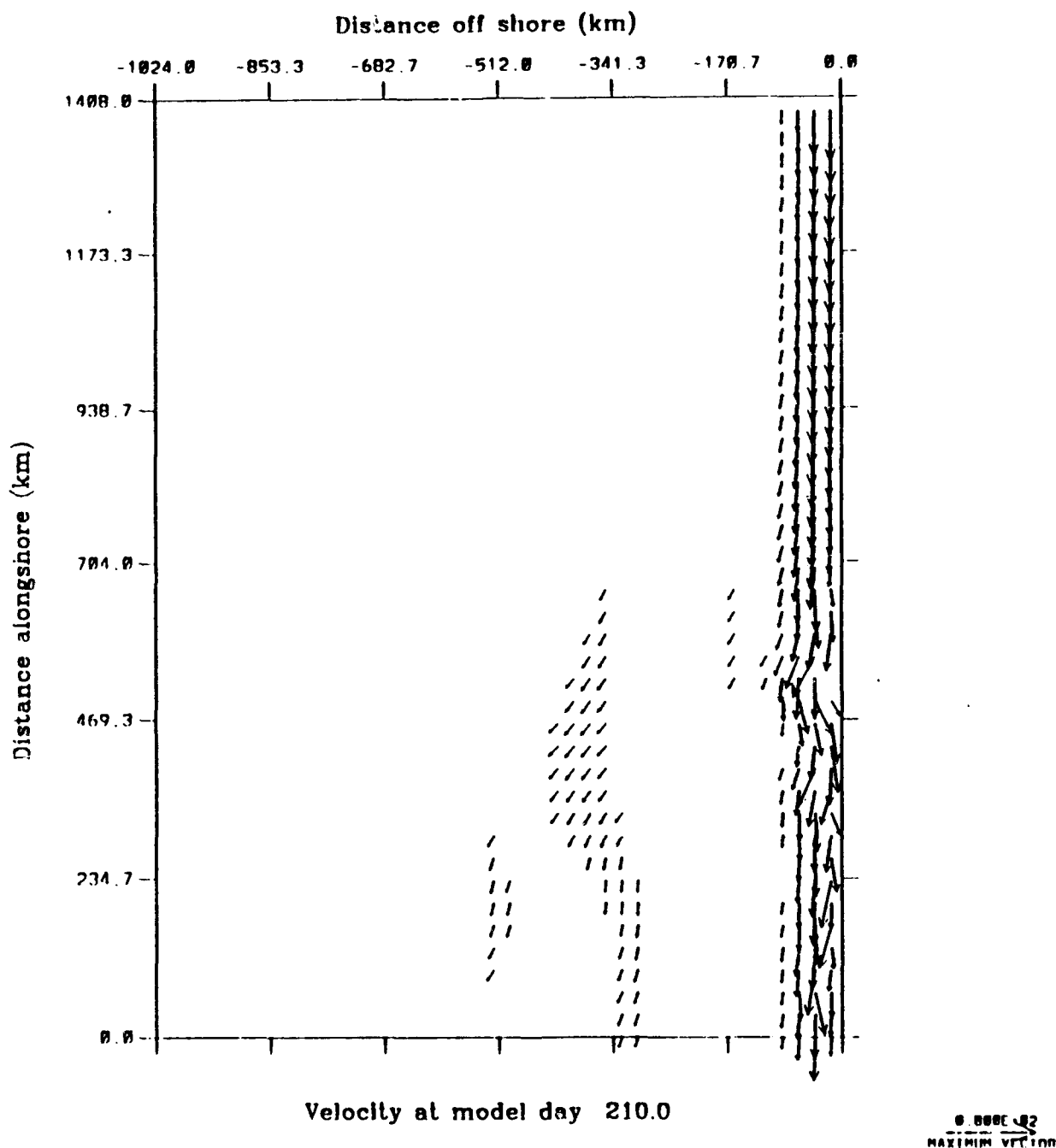


**Figure 4.7** Experiment 1: Surface velocity vectors at day 210. To avoid clutter, velocity vectors are plotted at every third grid point in both the cross-shore and alongshore direction, and velocities less than  $5 \text{ cm s}^{-1}$  are not plotted. Note start of meander at  $y \sim 500 \text{ km}$ .

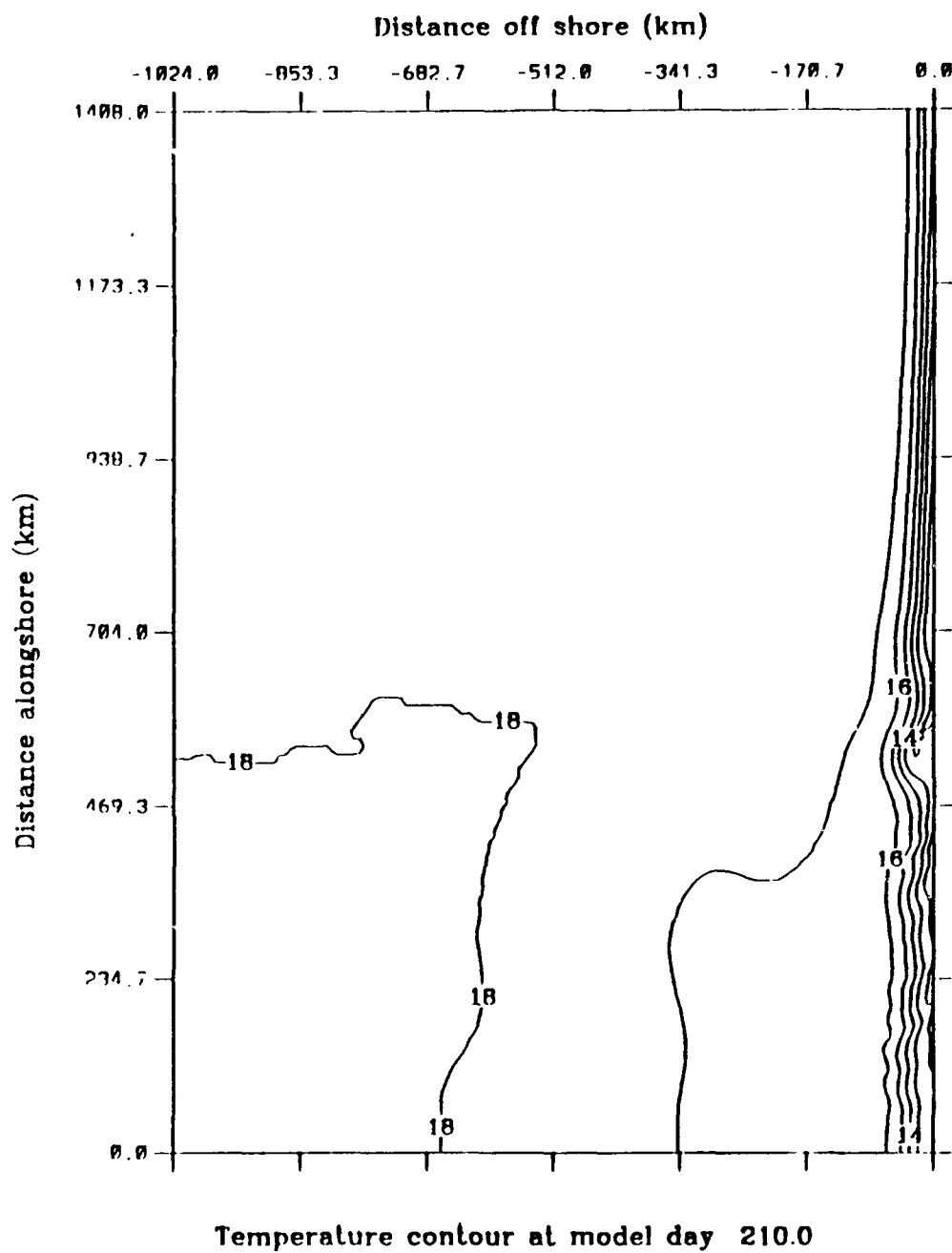


**Figure 4.8** Experiment 1: Surface temperature at day 210. The contour interval is  $1^{\circ}\text{C}$ . The temperature decreases towards the coast. Note start of meander at  $y \sim 500$  km.

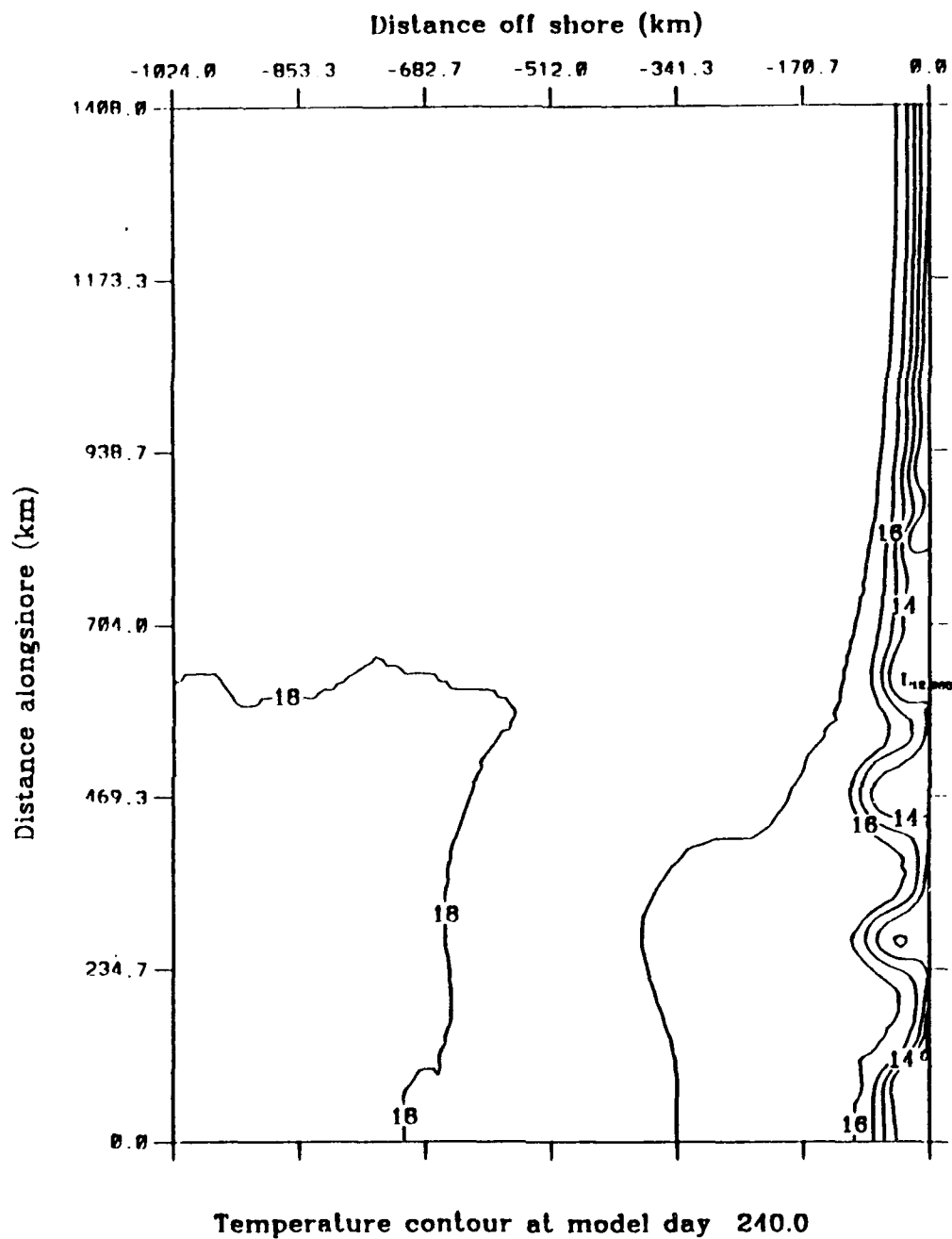


**Figure 4.9** Experiment 1: Surface temperature at day 240. The contour interval is  $1^{\circ}\text{C}$ . The temperature decreases towards the coast. Note the formation of cold core eddy at  $y \sim 230$  km.

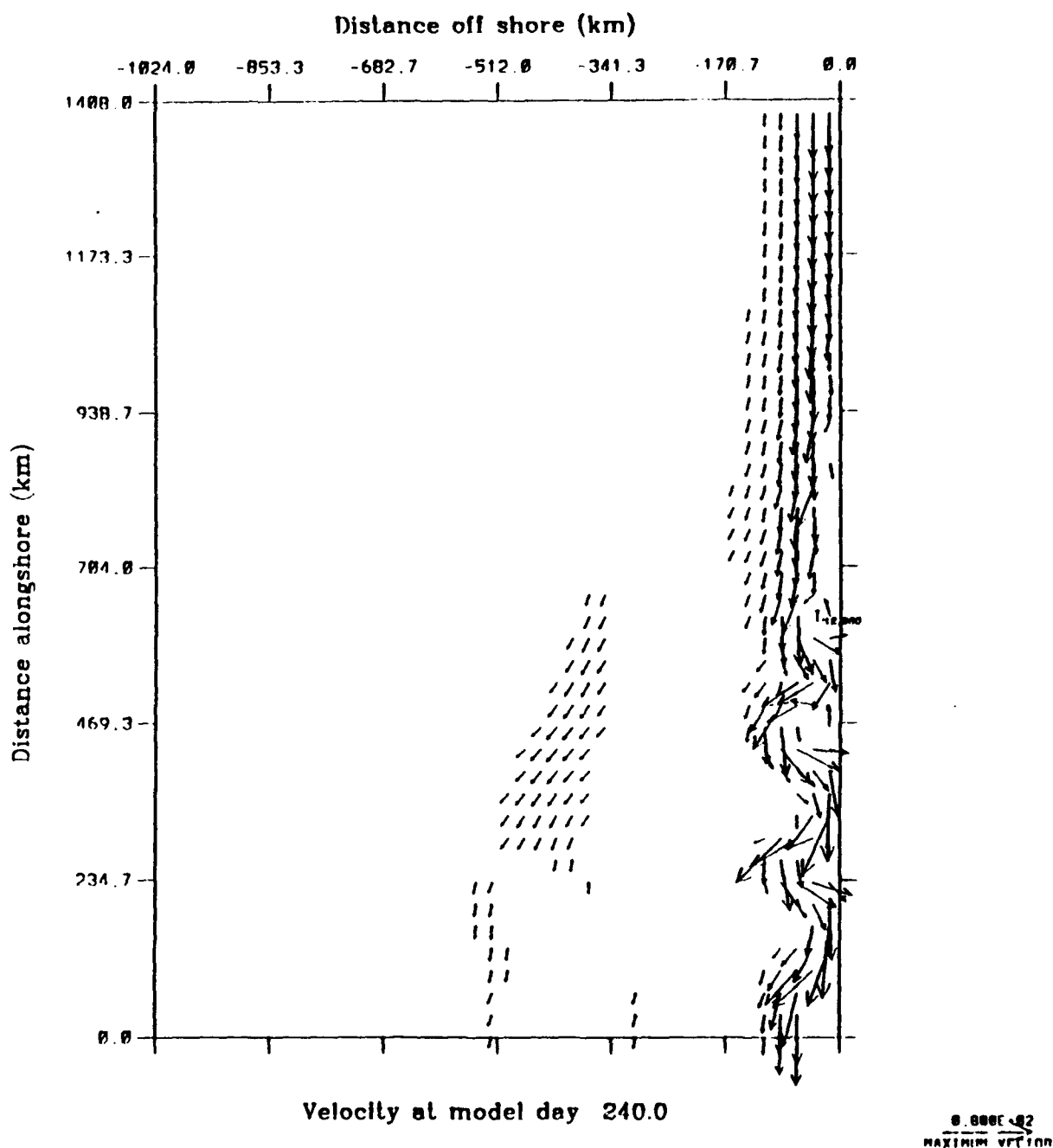


**Figure 4.10** Experiment 1: Surface velocity vectors at day 240 as in Figure 4.3. Note the formation of cold core eddy at  $y \sim 230$  km. The number associated with the low at  $y \sim 700$  km corresponds to temperature, not velocity.

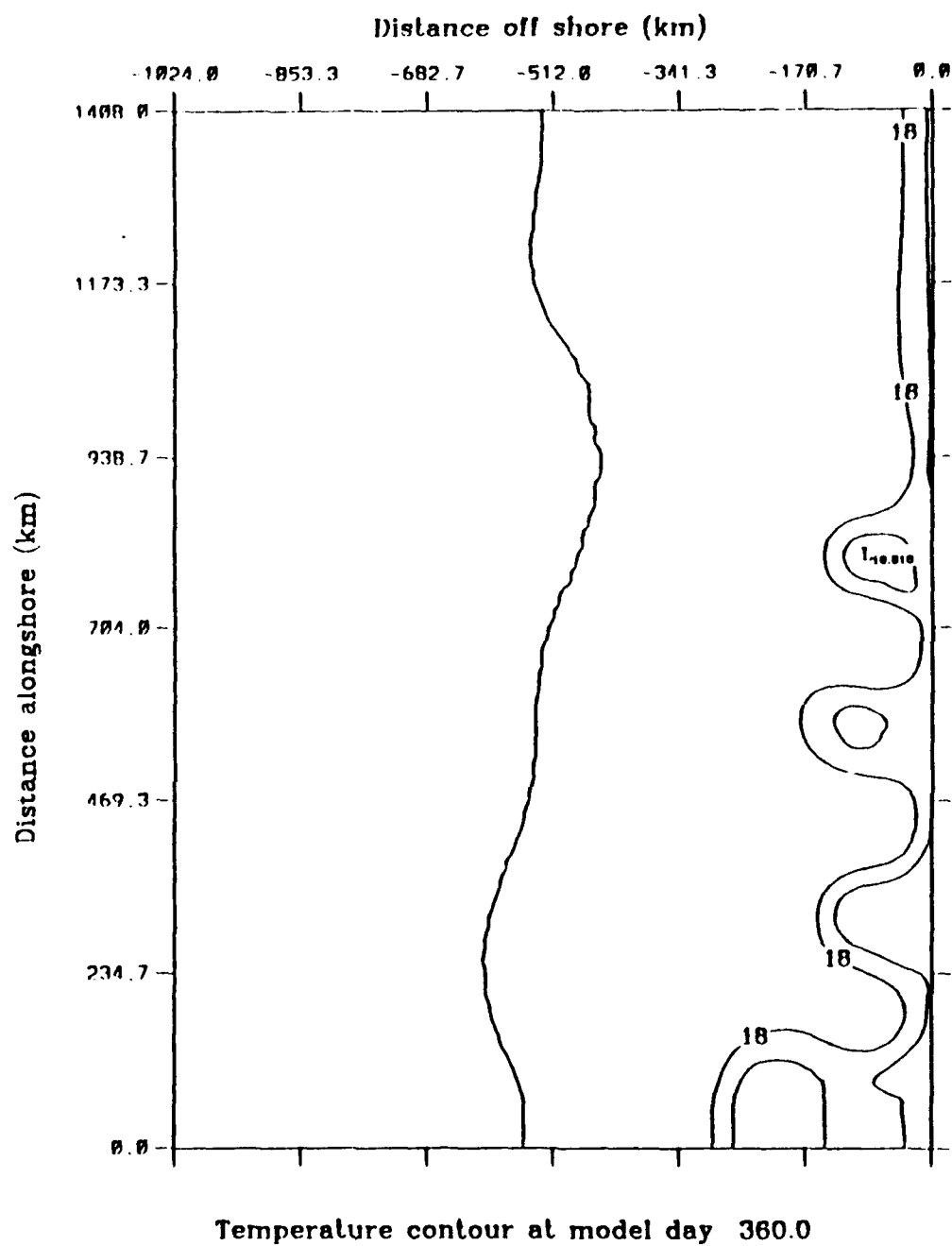


**Figure 4.11** Experiment 1: Surface temperature at day 360. The contour interval is  $1^{\circ}$  C. Note meanders and eddies are still discernible in temperature contours.

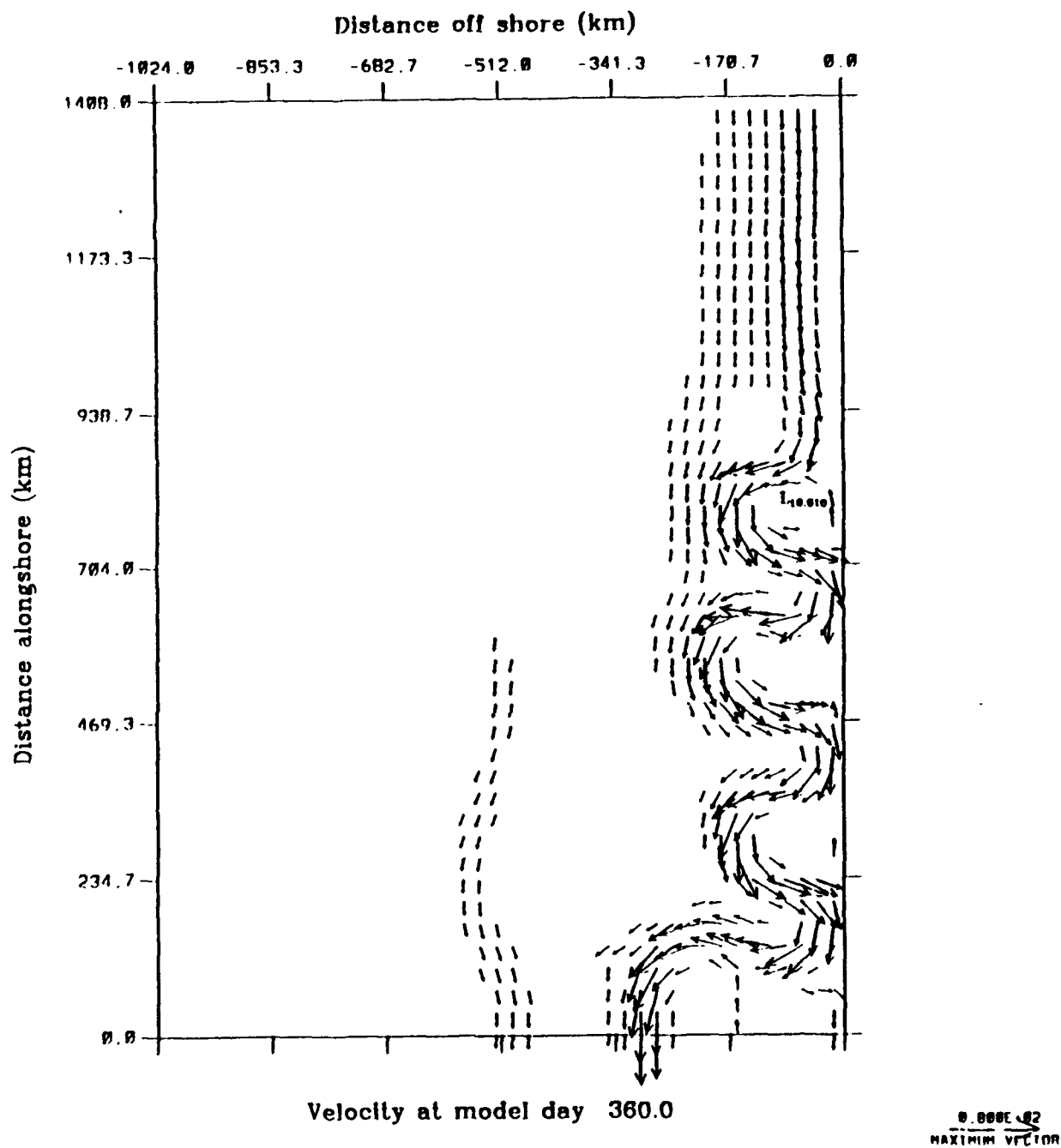
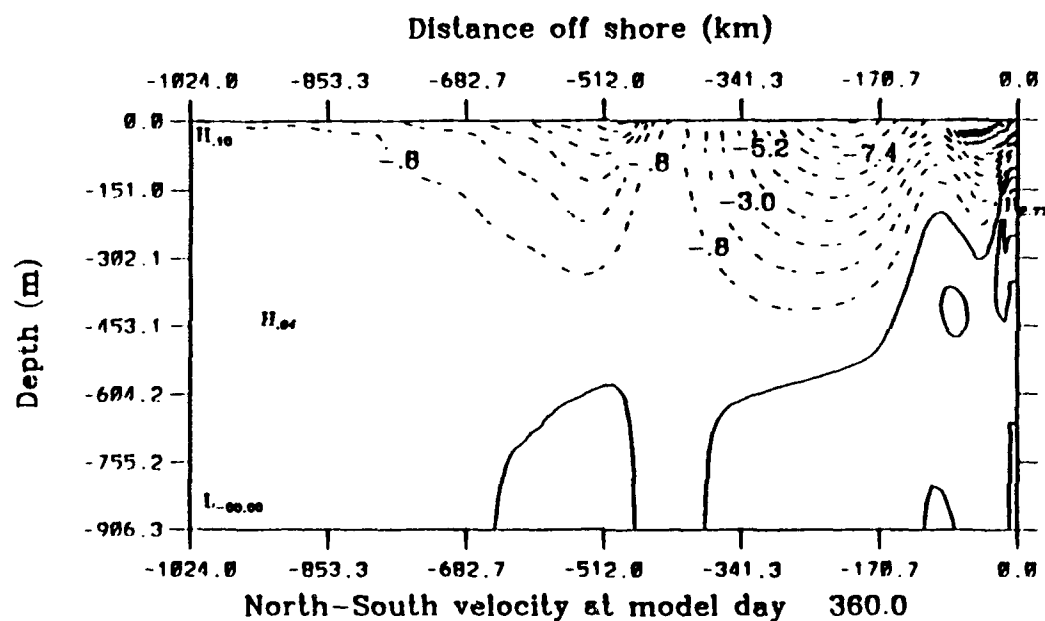
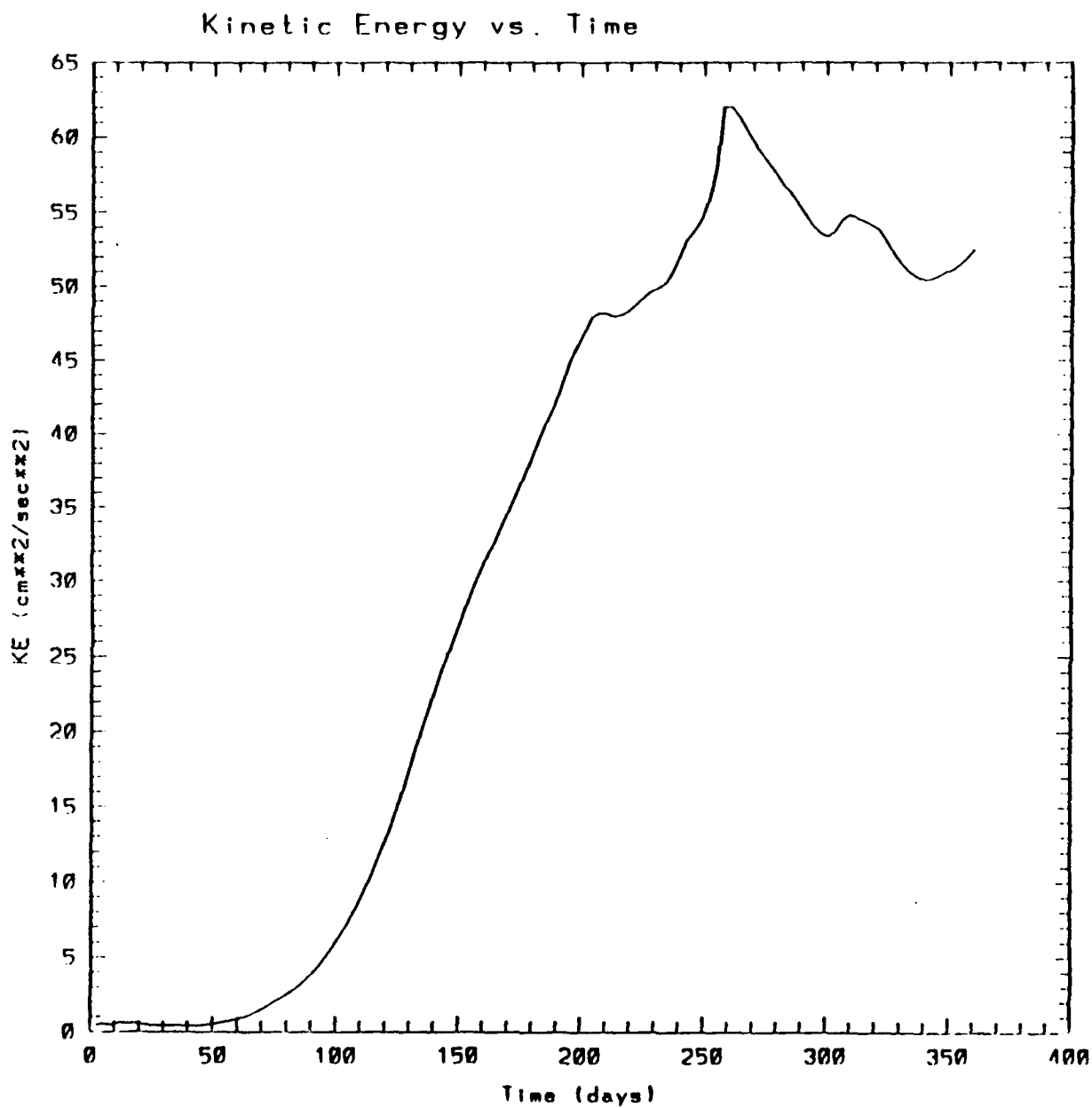


Figure 4.12 Experiment 1: Surface velocity vectors at day 360 as in Figure 4.3. Note equatorward surface current over a poleward undercurrent. The number associated with the low at y~800 km corresponds to temperature, not velocity.





**Figure 4.13** Experiment 1: Cross-section of the meridional component of velocity at day 360. Note meanders and eddies are still discernible in a weak equatorward surface current.



**Figure 4.14** Experiment 1: Total kinetic energy per unit mass time series for climatological (1980-1989) year over the entire domain (Units of the kinetic energy are  $\text{cm}^2\text{s}^{-2}$ ).

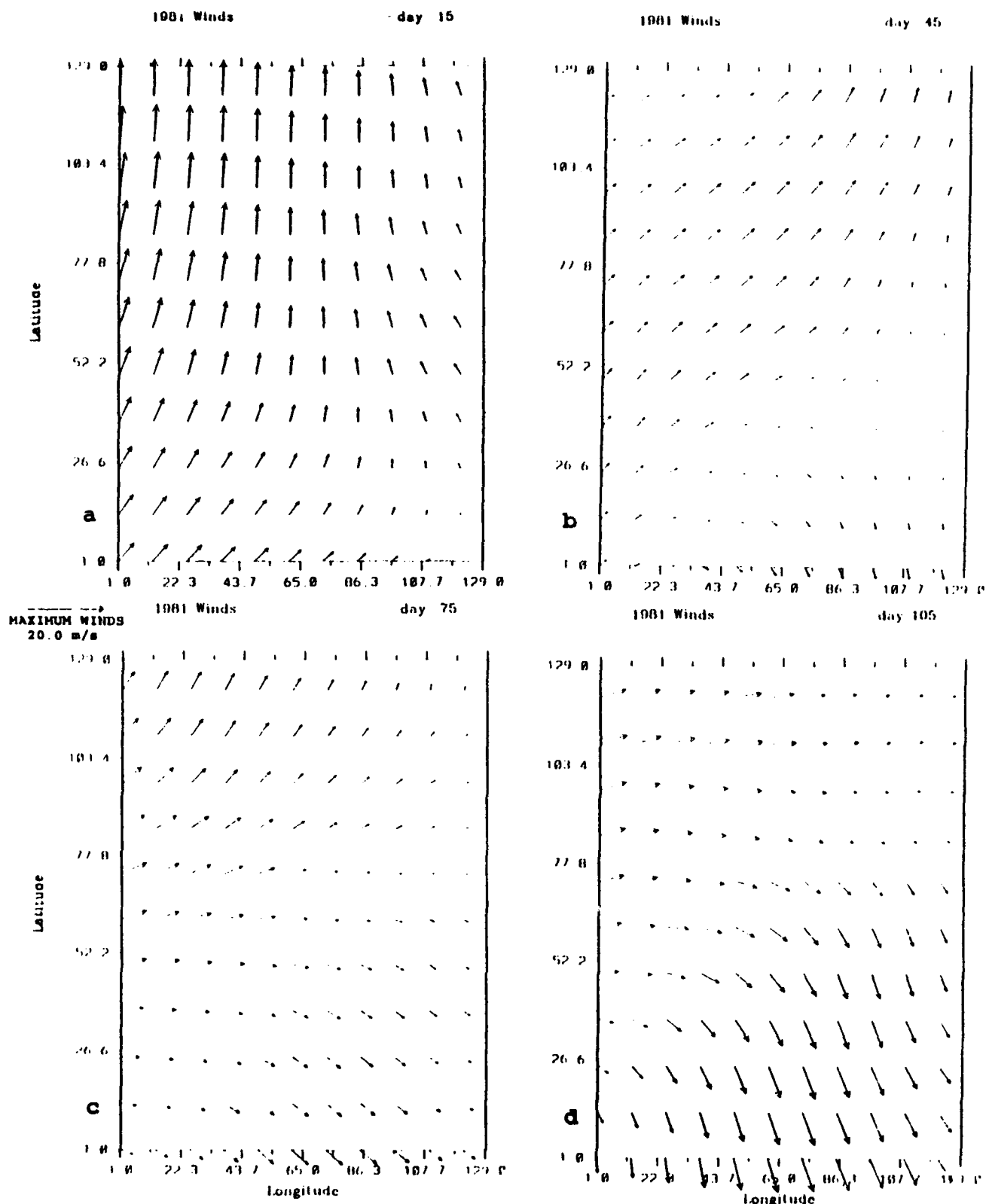


**Figure 4.15** Mid-monthly ECMWF winds for 1981 in  $\text{m s}^{-1}$ : (a) January, (b) February, (c) March, (d) April, (e) May, (f) June, (g) July, (h) August, (i) September, (j) October, (k) November, and (l) December. The latitudinal grid point 1 (129) corresponds to  $35^\circ \text{ N}$  ( $47.5^\circ \text{ N}$ ); so that the latitudinal grid point of 52 corresponds to  $40^\circ \text{ N}$ . Maximum wind vector is  $20 \text{ m s}^{-1}$ .

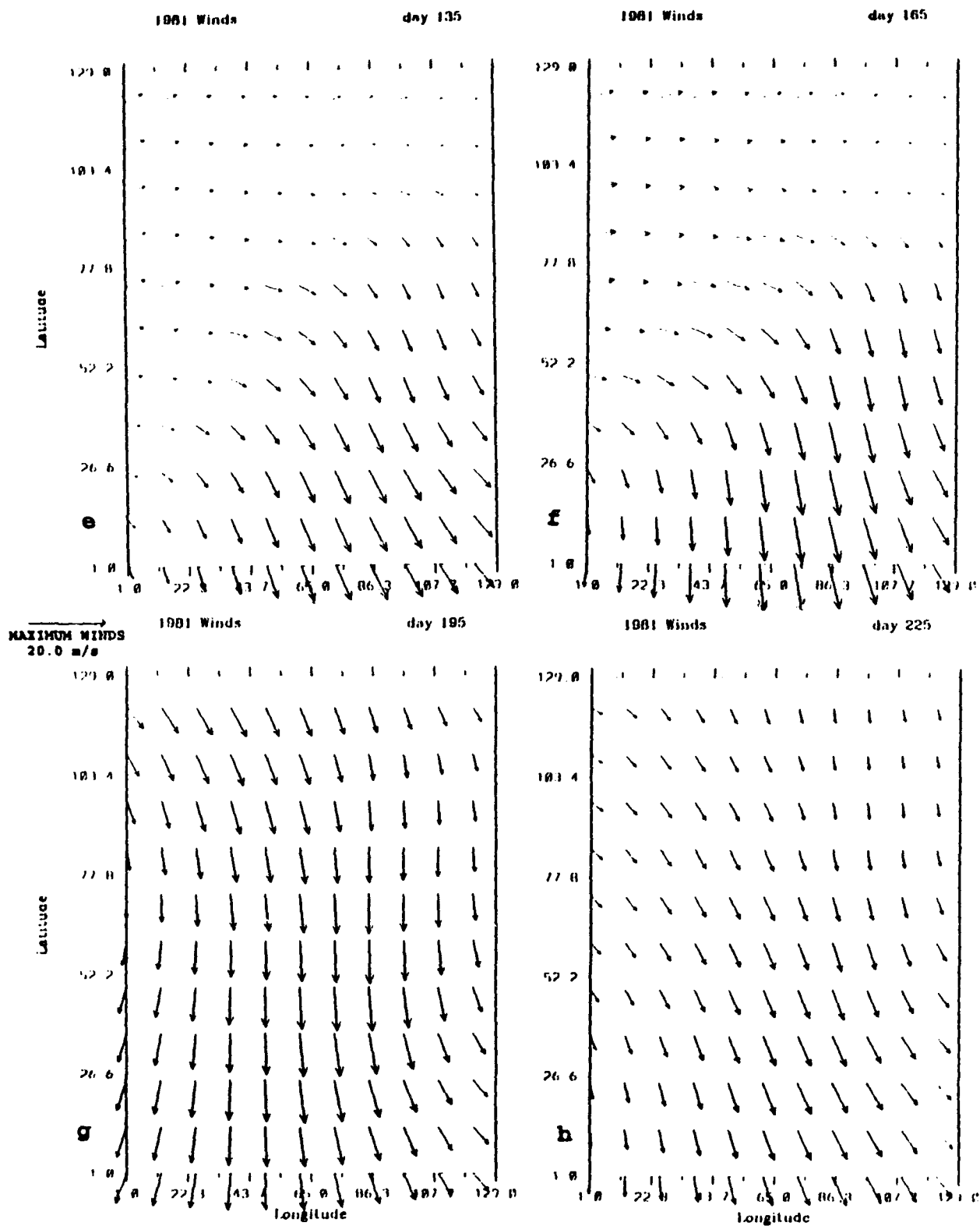


Figure 4.15 (continued).

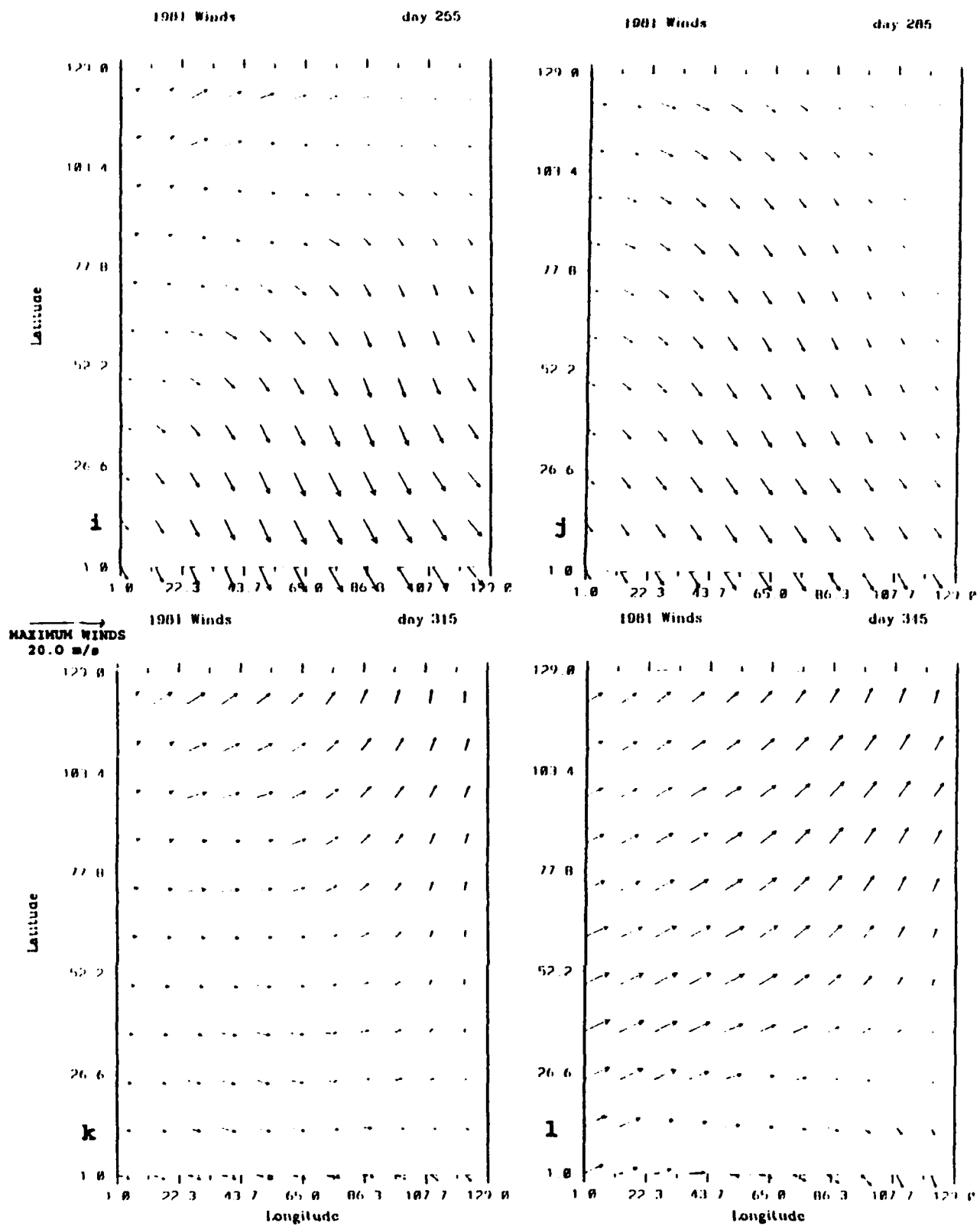
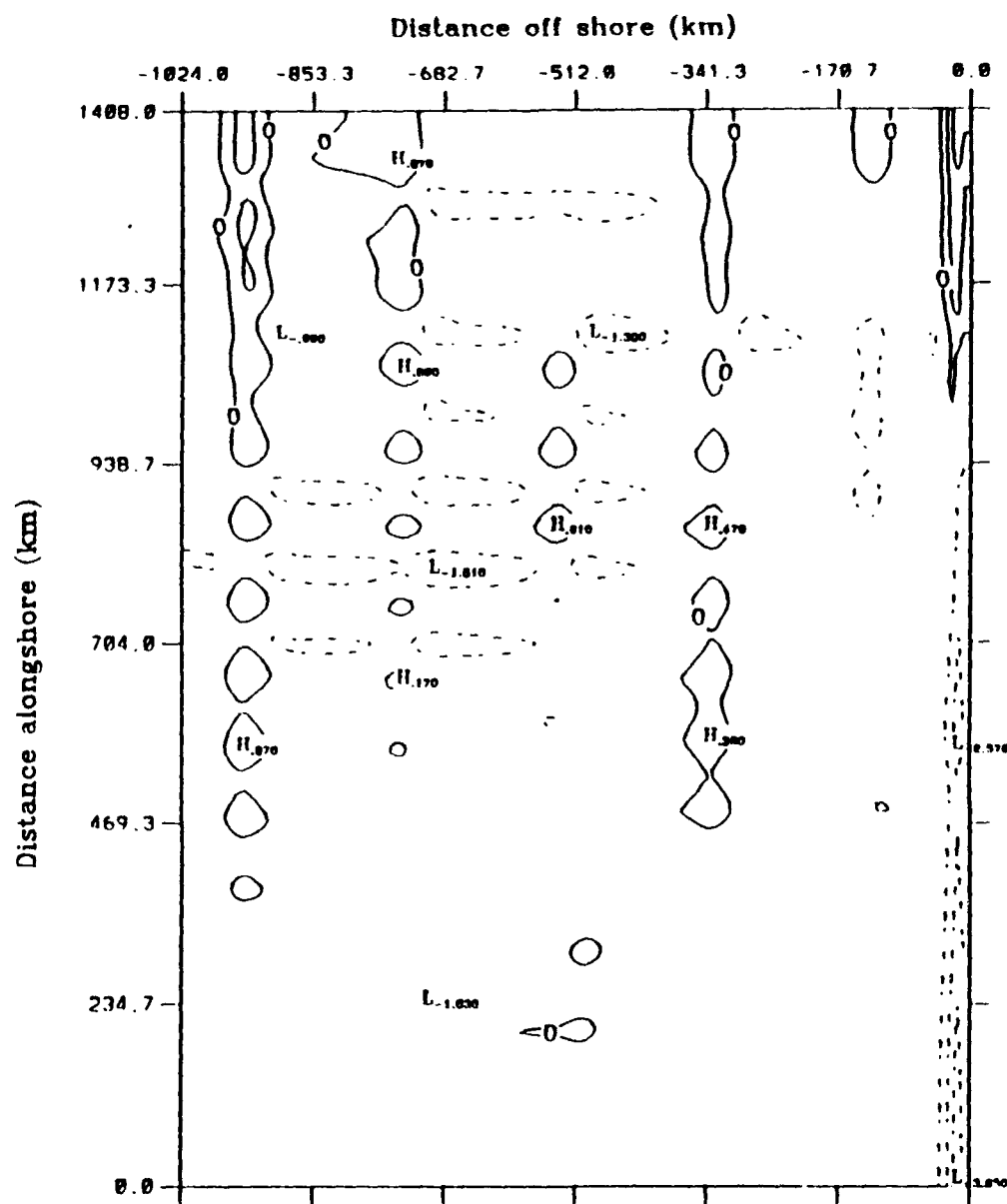
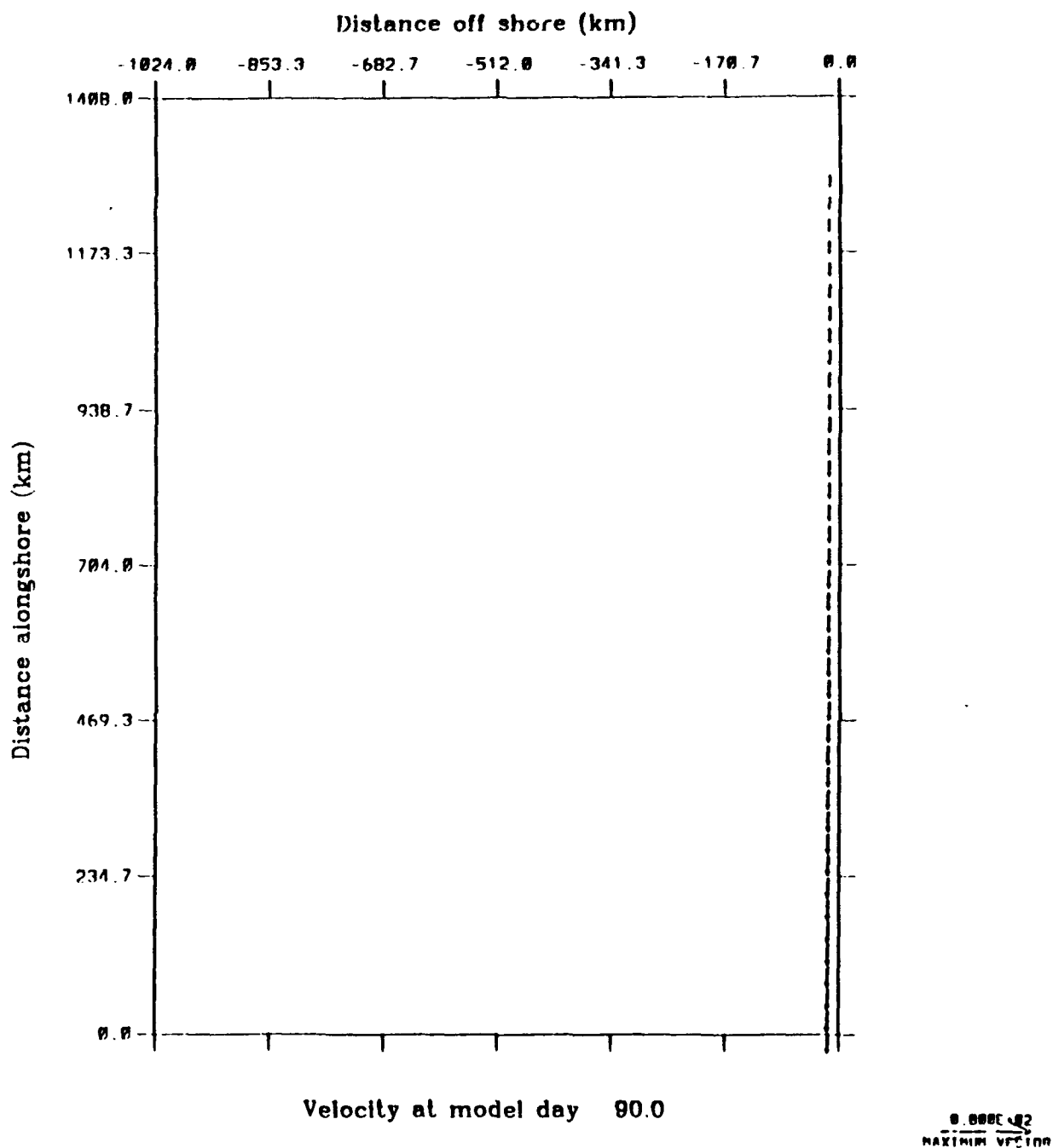


Figure 4.15 (continued).



**Figure 4.16** Experiment 2: Surface meridional component of velocity at day 45. The contour interval is  $1 \text{ cm s}^{-1}$ . The dashed lines indicate equatorward velocities. The maximum poleward velocity is  $\sim 2 \text{ cm s}^{-1}$ . Latitudinal alongshore distance 0 (1408) km corresponds to  $35^\circ \text{ N}$  ( $47.5^\circ \text{ N}$ ).



**Figure 4.17** Experiment 2: Surface velocity vectors at day 90. To avoid clutter, velocity vectors are plotted at every third grid point in both the cross-shore and alongshore direction, and velocities less than  $5 \text{ cm s}^{-1}$  are not plotted.

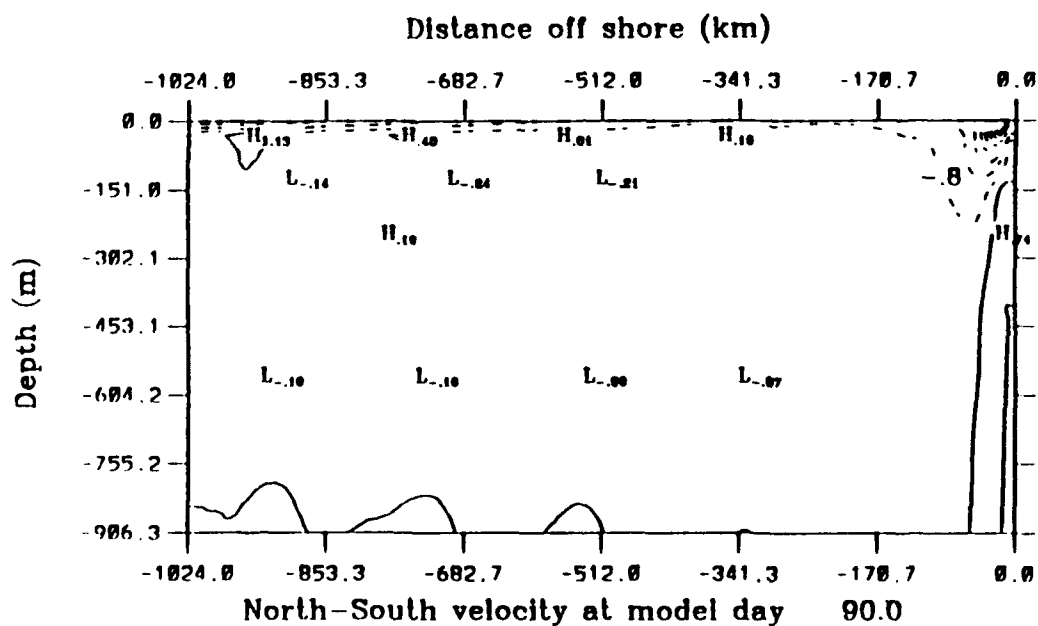


**Figure 4.18** Experiment 2: Cross-section at  $y \sim 704$  km ( $41.25^\circ$  N) of the meridional component of velocity at day 90. Dashed lines indicate equatorward flow, while solid lines indicate poleward flow. Note weak poleward undercurrent.



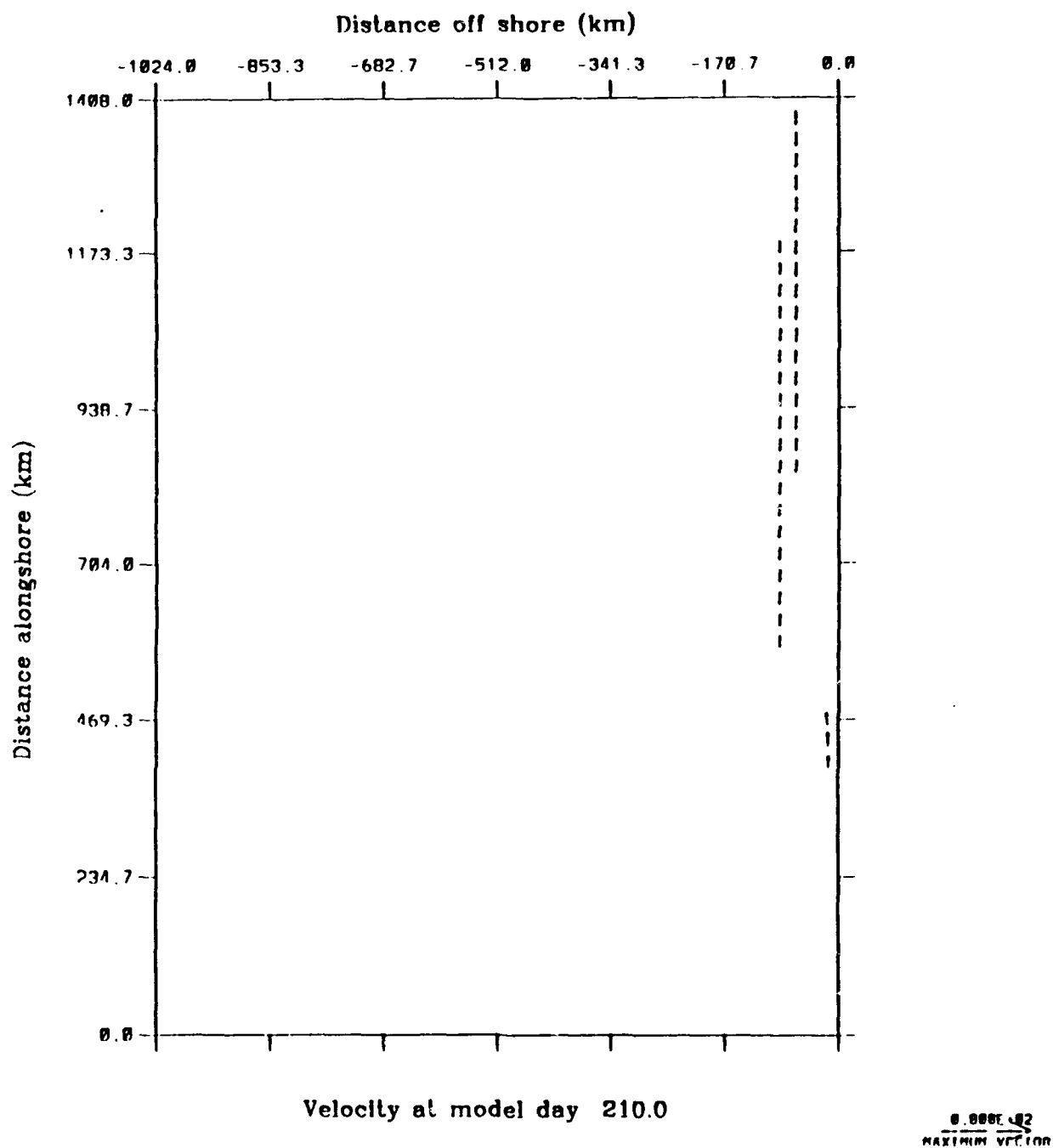


**Figure 4.19** Experiment 2: Layer 5 (316 m) velocity vectors at day 210. The maximum poleward velocity is  $5 \text{ cm s}^{-1}$  near  $y \sim 469 \text{ km}$ .

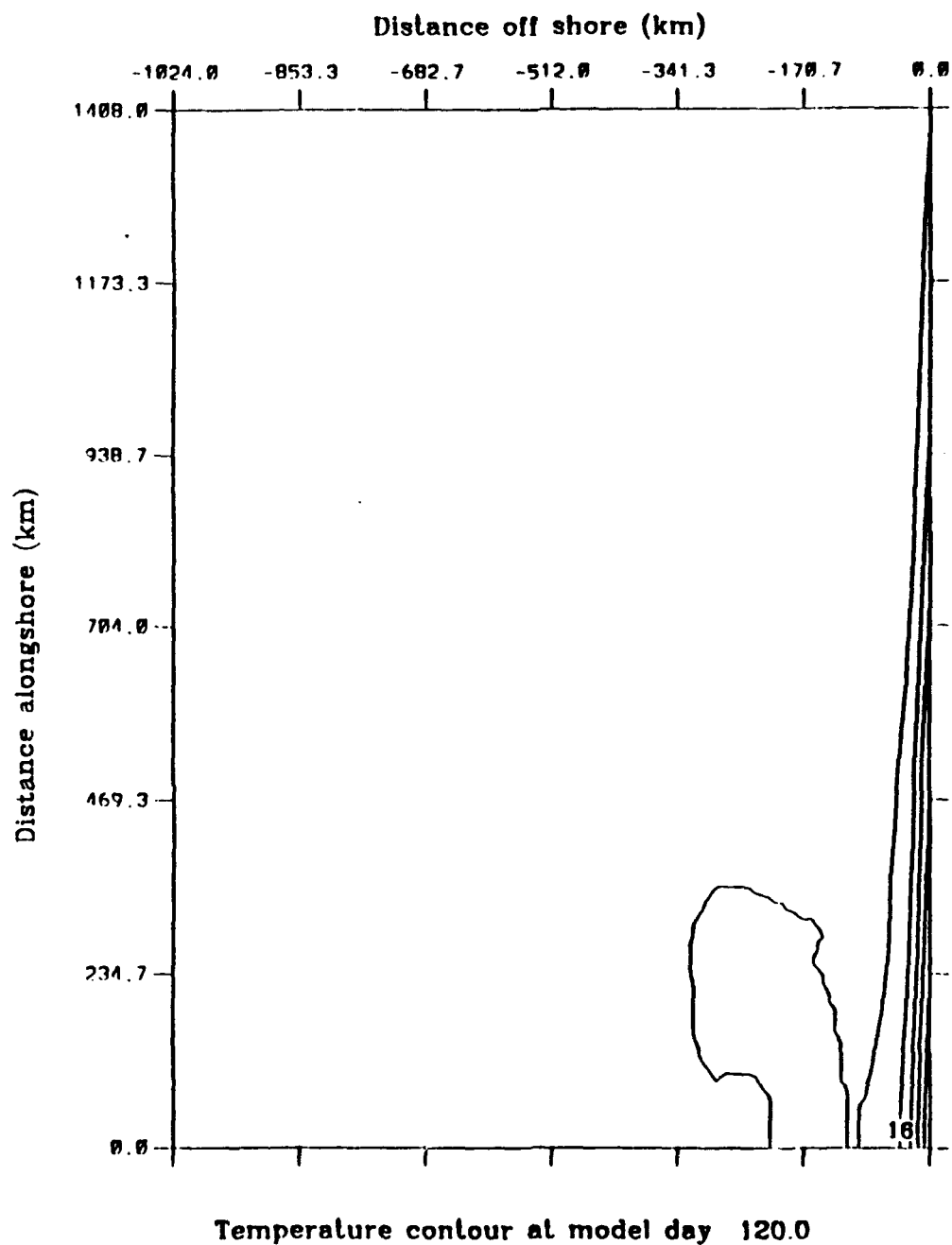


**Figure 4.20** Experiment 2: Surface temperature at day 120. The contour interval is  $1^{\circ}\text{C}$ . The temperature decreases towards the coast.

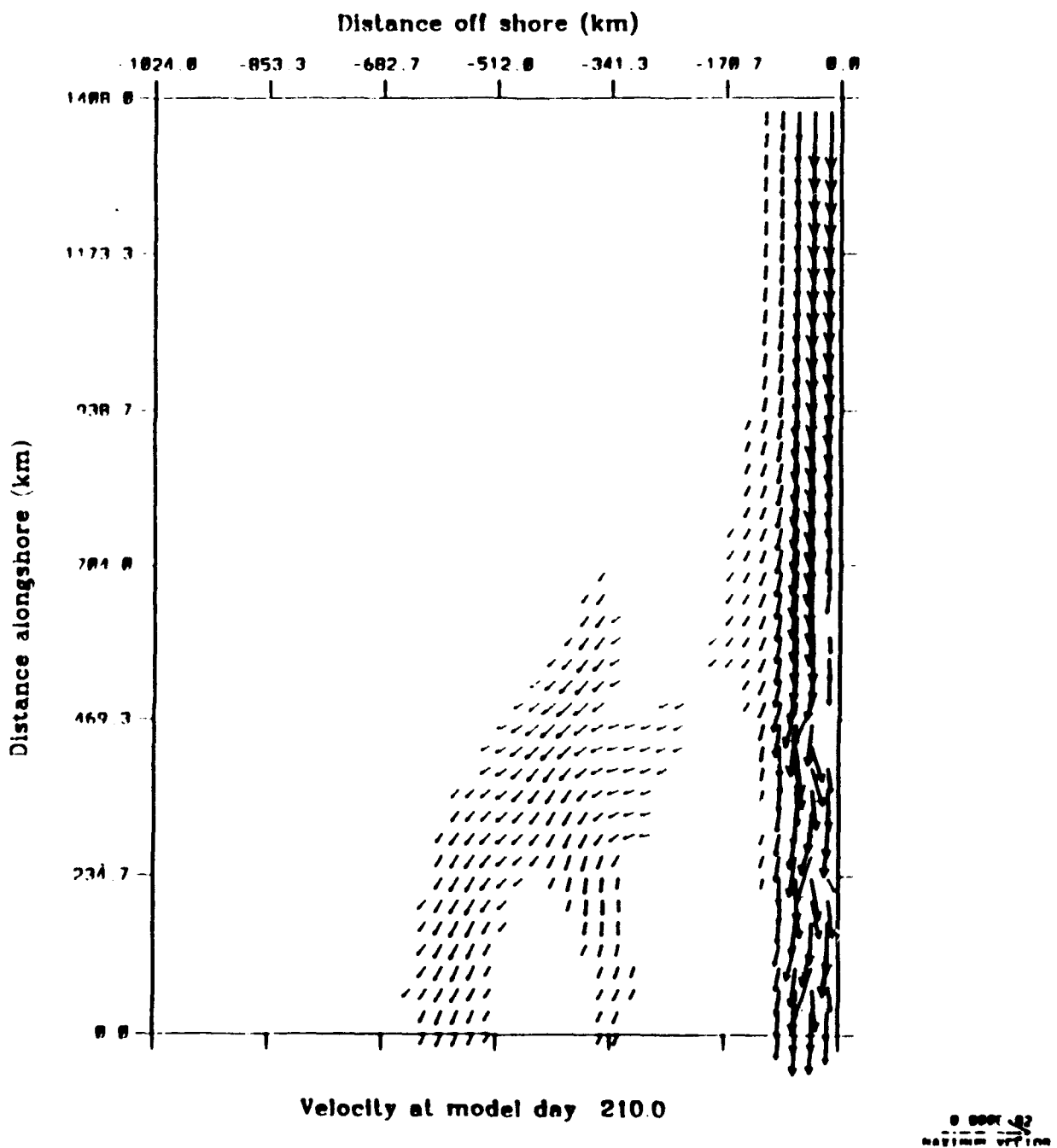


**Figure 4.21** Experiment 2: Surface velocity vectors at day 210. Note the meander near y=469 km.

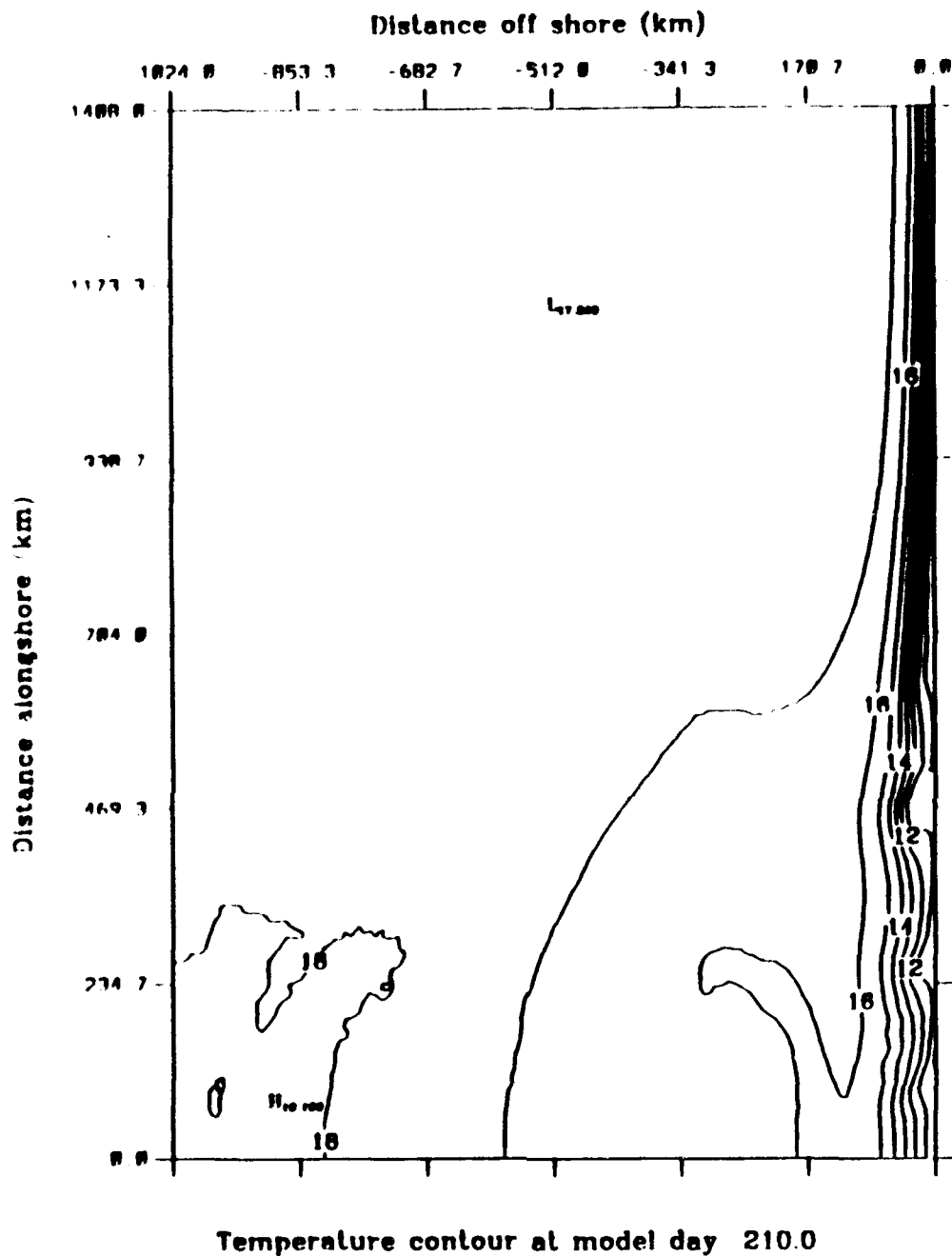


**Figure 4.22** Experiment 2: Surface temperature at day 210. The contour interval is  $1^{\circ}\text{C}$ . The temperature decreases towards the coast. Note the meander near  $y \sim 469$  km.

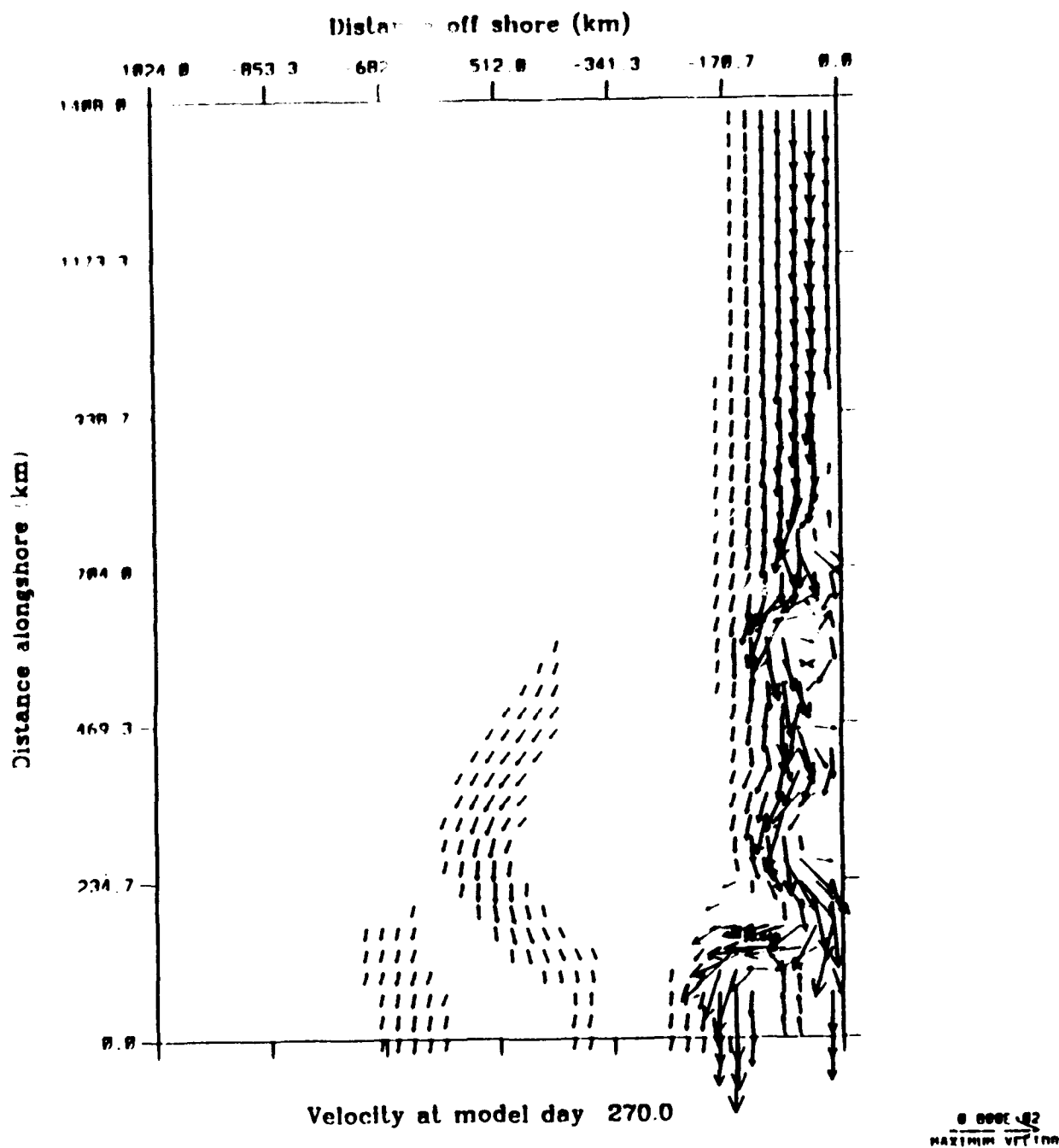


**Figure 4.23** Experiment 2: Surface velocity vectors at day 270. The number associated with the high at y~150 km corresponds to temperature, not velocity. Note the eddy near y~600 km.

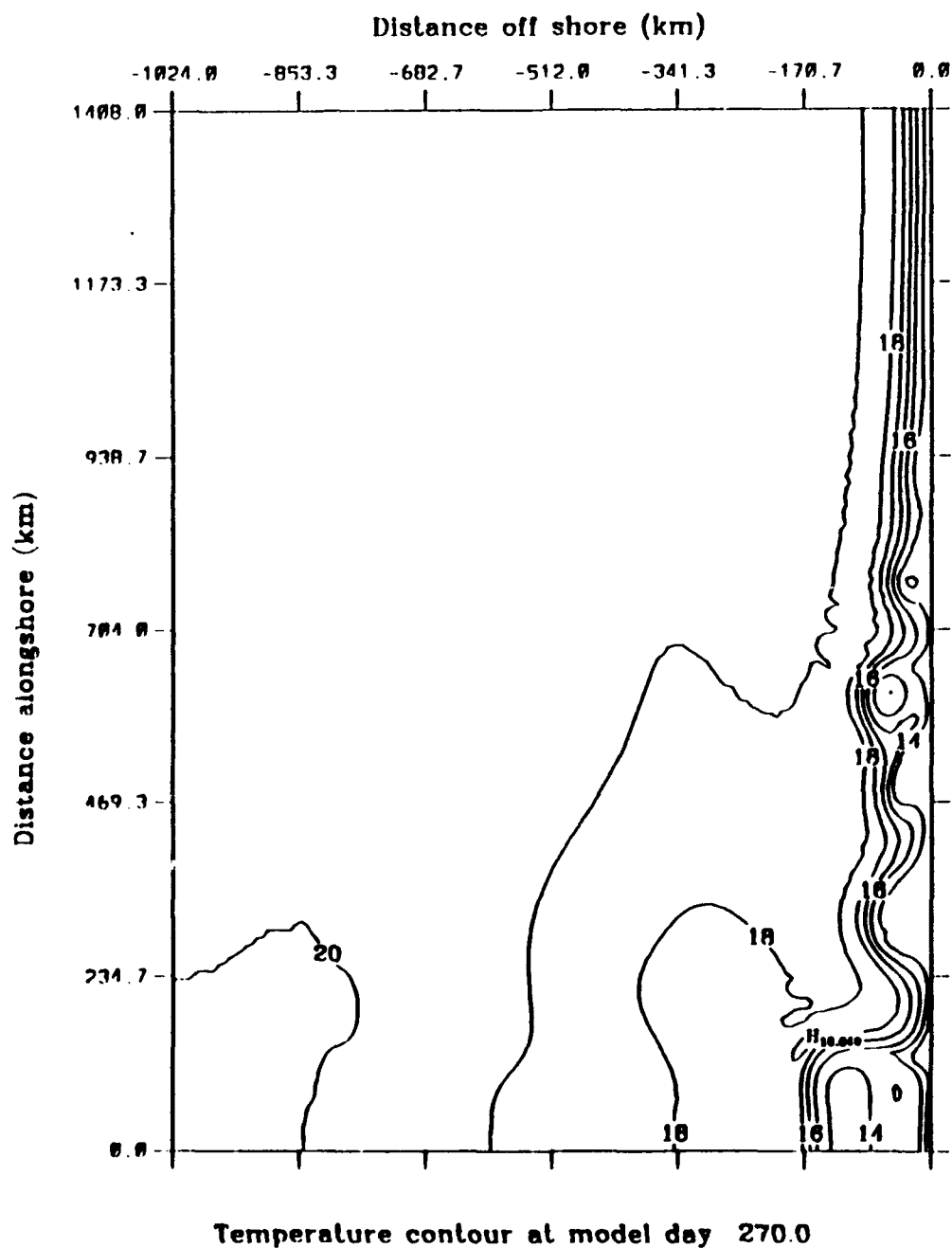
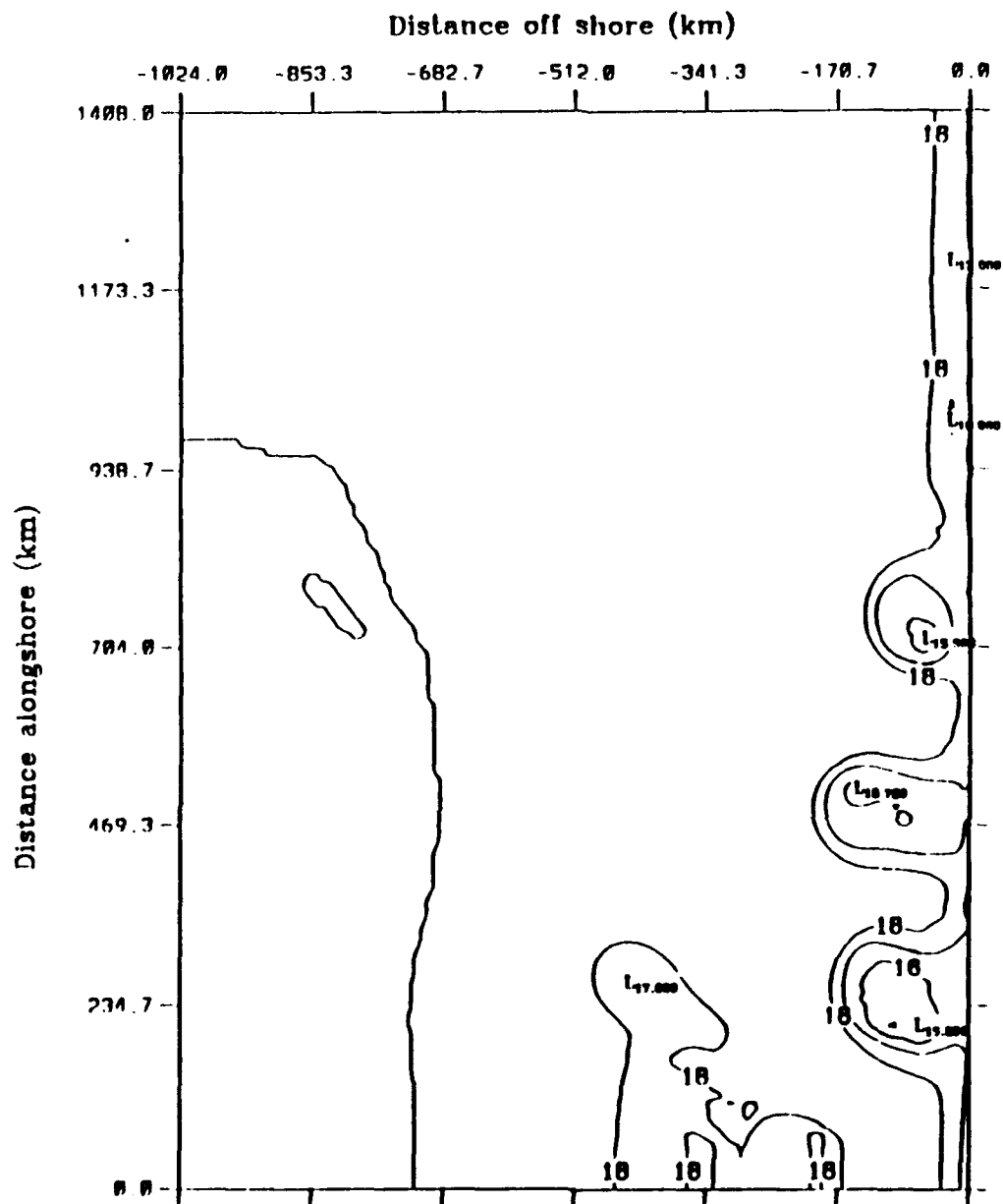


**Figure 4.24** Experiment 2: Surface temperature at day 270. The contour interval is  $1^{\circ}\text{C}$ . The temperature decreases towards the coast. Note the cold core eddy near  $y \sim 6000$  km.



Temperature contour at model day 360.0

**Figure 4.25** Experiment 2: Surface temperature at day 360. The contour interval is 1° C. The temperature decreases towards the coast. Note existence of meanders and embedded eddies.

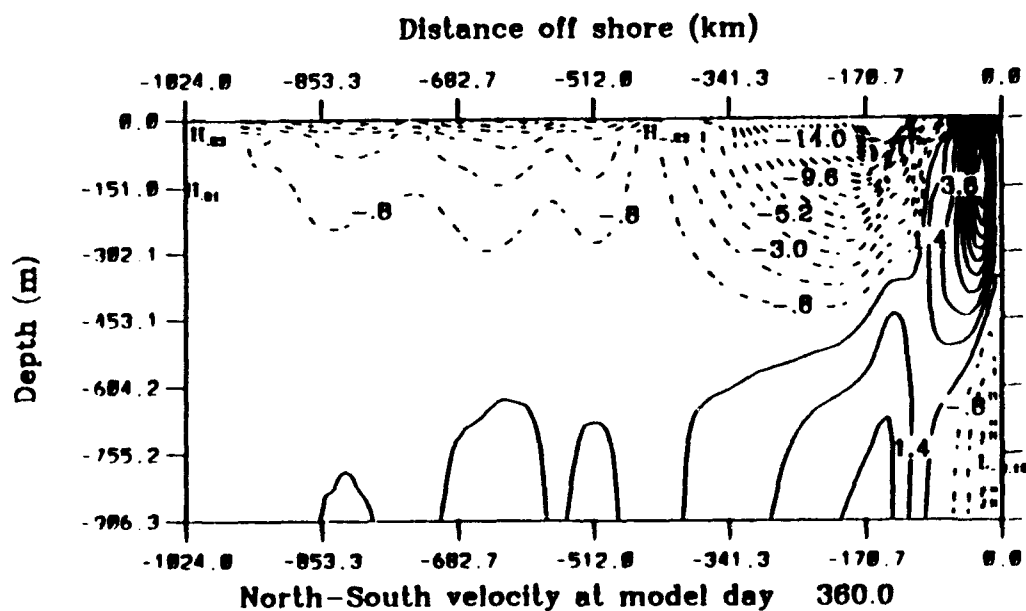


**Figure 4.26** Experiment 2: Cross-section at  $y=704$  km ( $41.25^\circ$  N) of the meridional component of velocity at day 360. Dashed lines indicate equatorward flow, while solid lines indicate poleward flow. Note existence of poleward undercurrent.



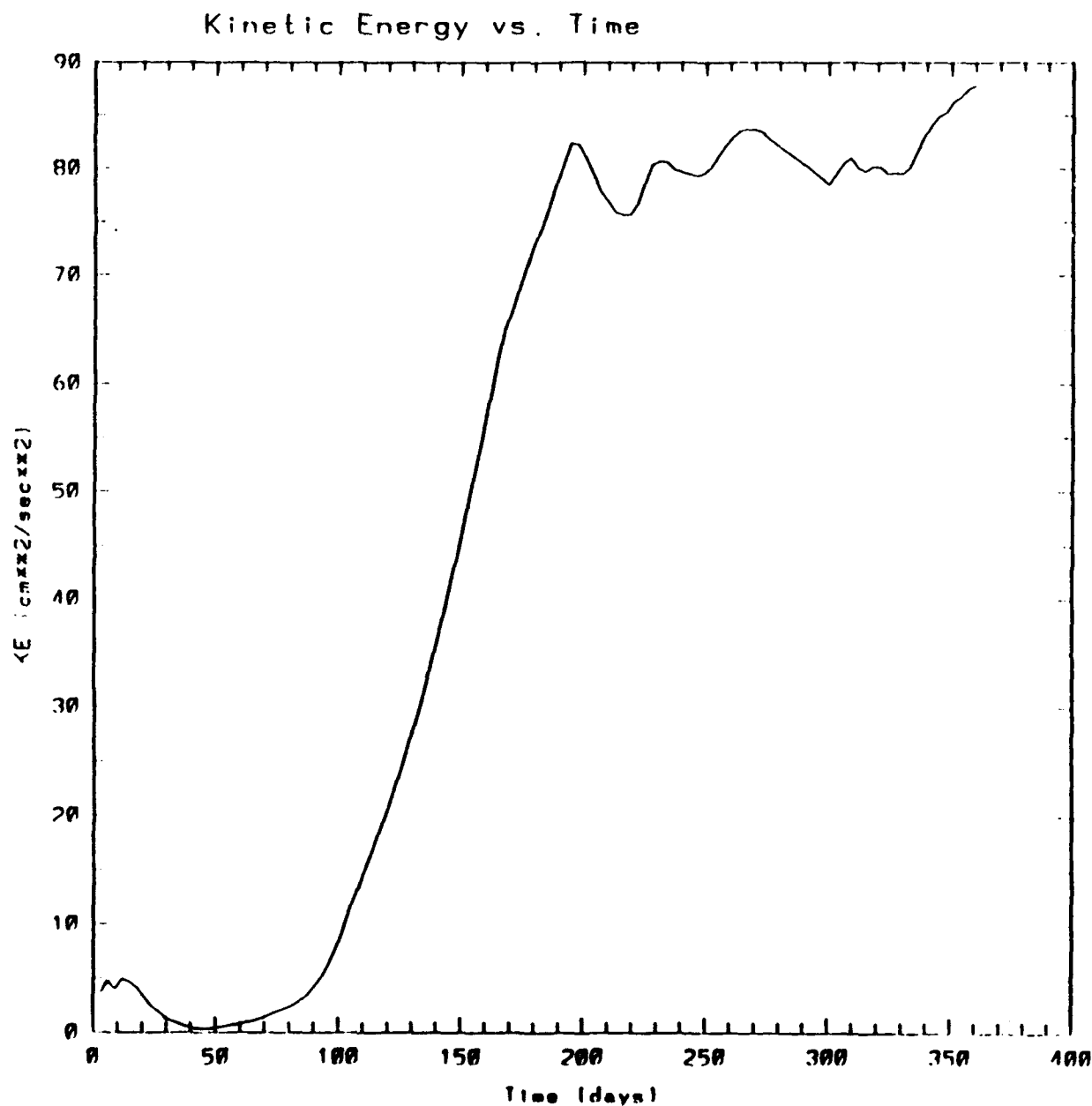


**Figure 4.27** Experiment 2: Total kinetic energy per unit mass time series for 1981 over the entire domain (Units of the kinetic energy are  $\text{cm}^2\text{s}^{-2}$ ). Quasi-steady periods: days 210-222, 240-252, 297-303, and 309-333.

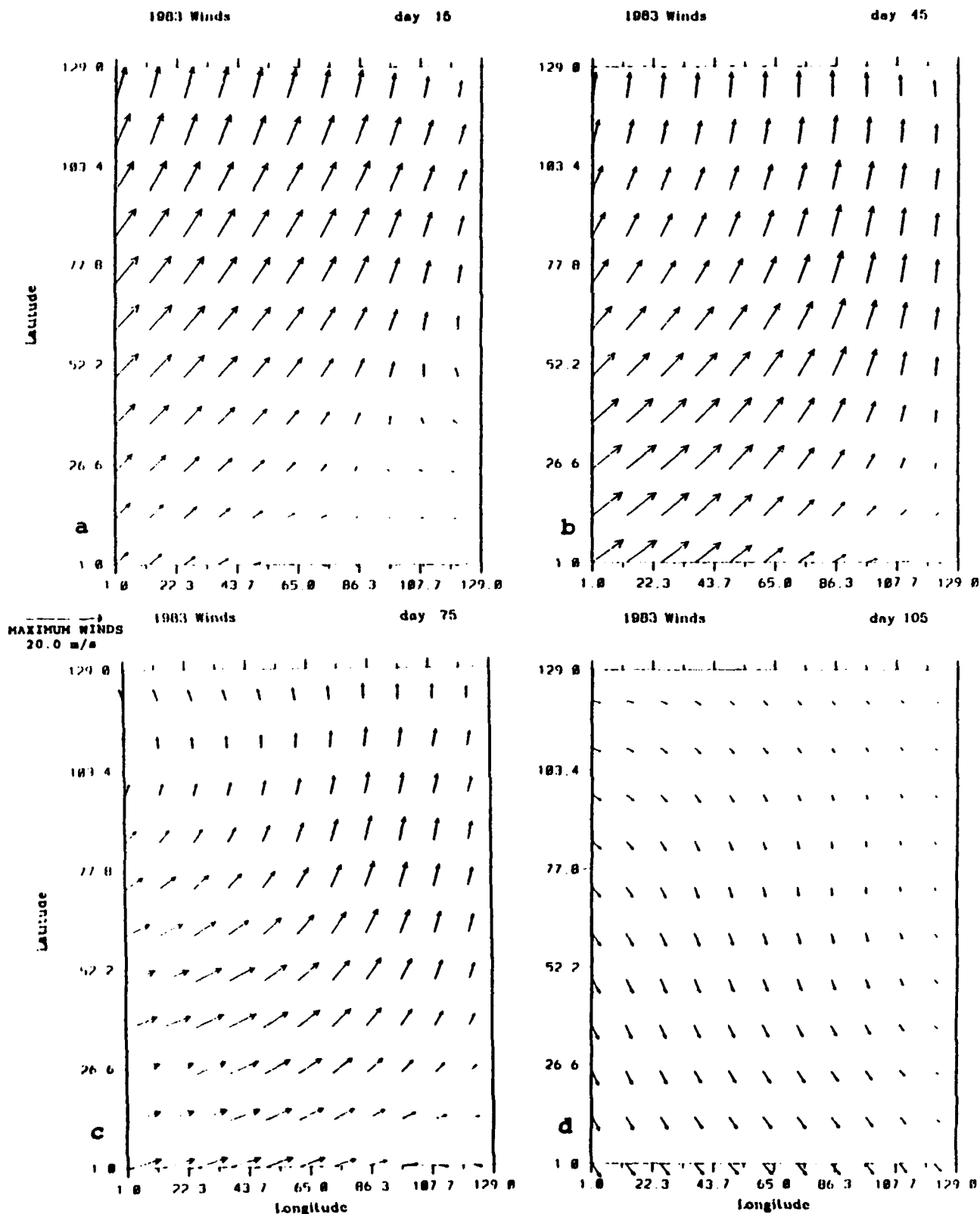


**Figure 4.28** Mid-monthly ECMWF winds for 1983 in  $\text{m s}^{-1}$ : (a) January, (b) February, (c) March, (d) April, (e) May, (f) June, (g) July, (h) August, (i) September, (j) October, (k) November, and (l) December. The latitudinal grid point 1 (129) corresponds to  $35^\circ \text{N}$  ( $47.5^\circ \text{N}$ ); so that the latitudinal grid point of 52 corresponds to  $40^\circ \text{N}$ . Maximum wind vector is  $20 \text{ m s}^{-1}$ .

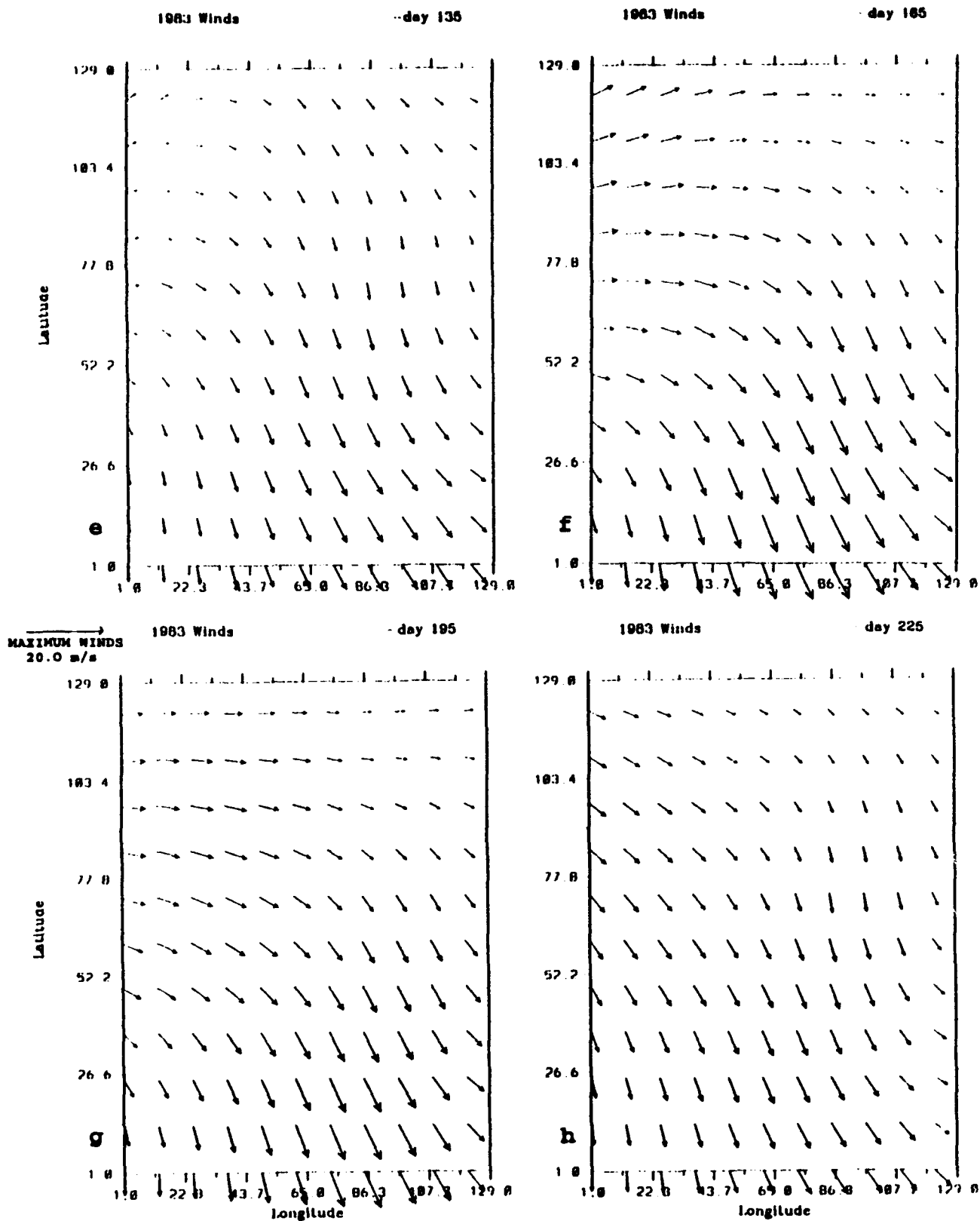


Figure 4.28 (continued).

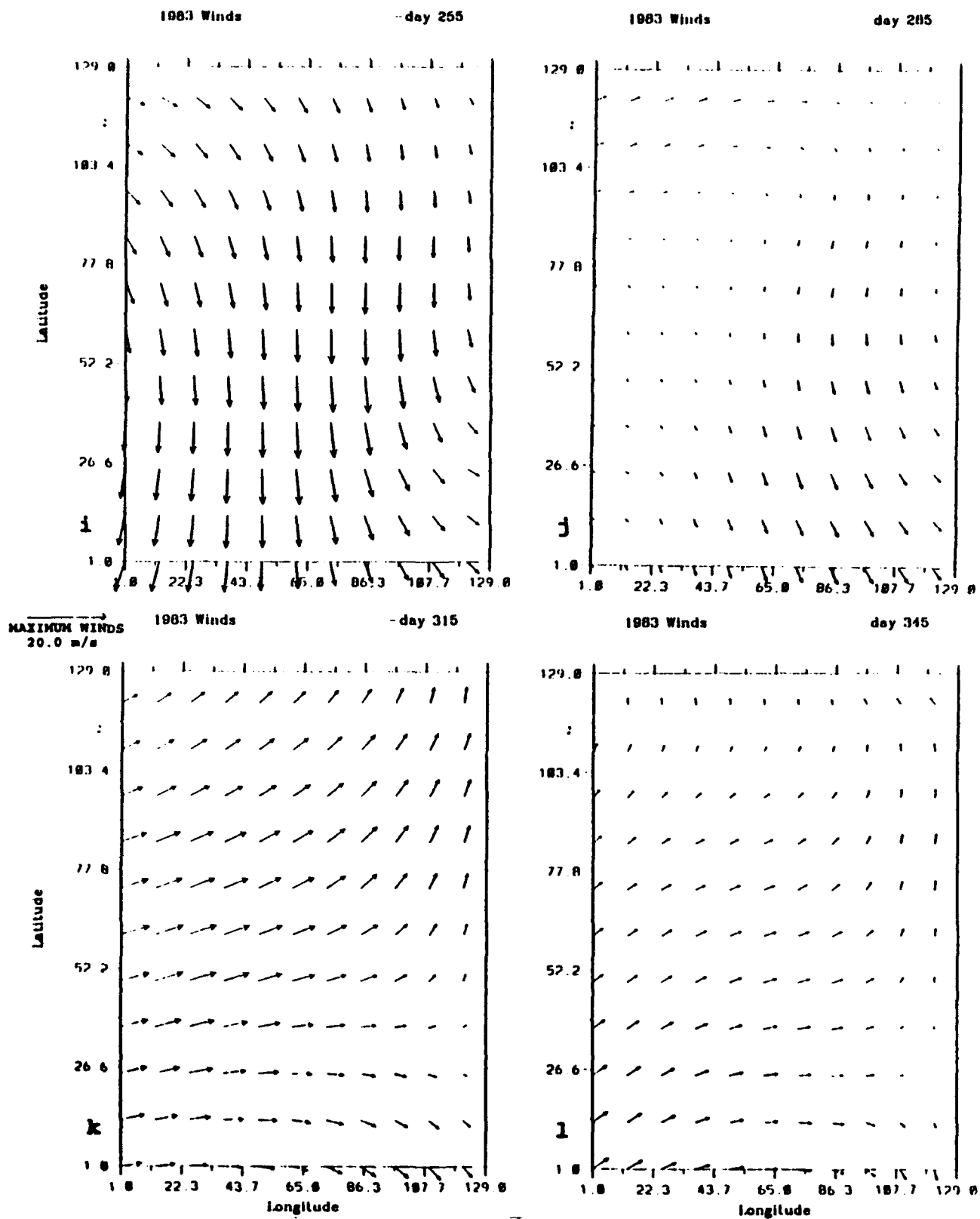
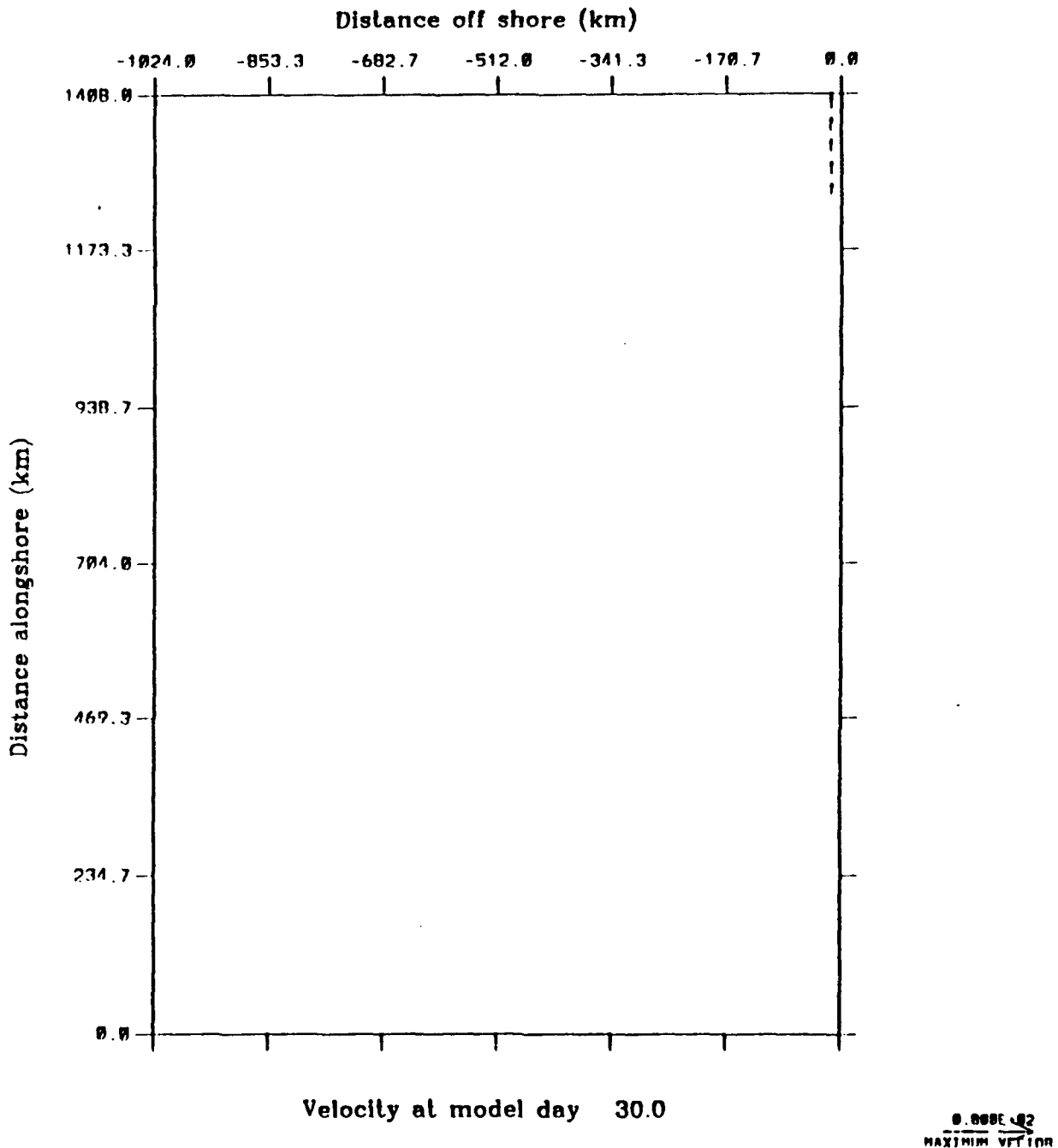
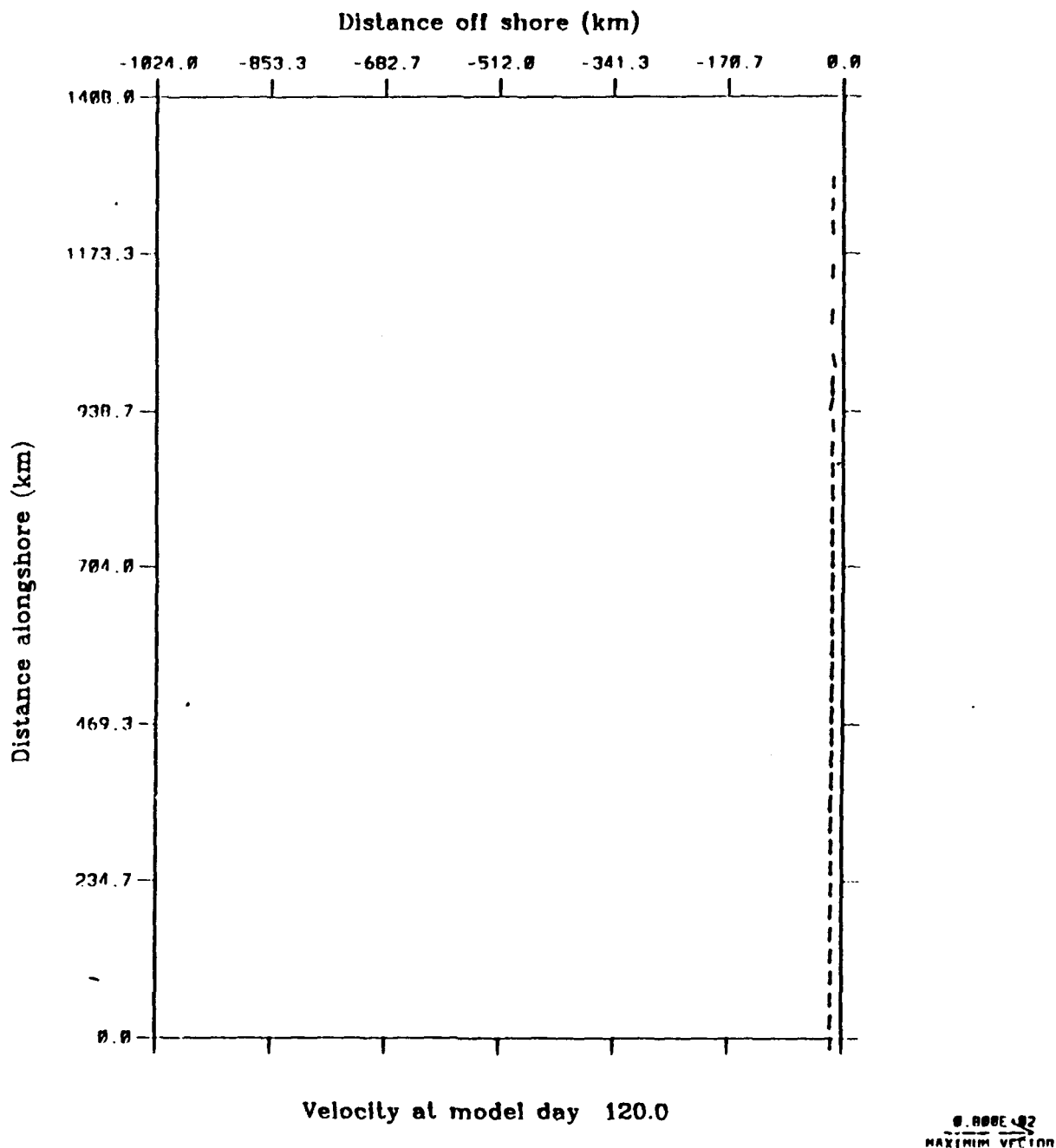


Figure 4.28 (continued).



**Figure 4.29** Experiment 3: Surface velocity vectors at day 30. To avoid clutter, velocity vectors are plotted at every third grid point in both the cross-shore and alongshore direction, and velocities less than  $5 \text{ cm s}^{-1}$  are not plotted. Note poleward flow to the north of  $y \sim 1200 \text{ km}$ .



**Figure 4.30** Experiment 3: Surface velocity vectors at day 120. To avoid clutter, velocity vectors are plotted at every third grid point in both the cross-shore and alongshore direction, and velocities less than  $5 \text{ cm s}^{-1}$  are not plotted. Note equatorward surface current dominates. The number associated with the high at  $y \sim 250 \text{ km}$  corresponds to temperature, not velocity.

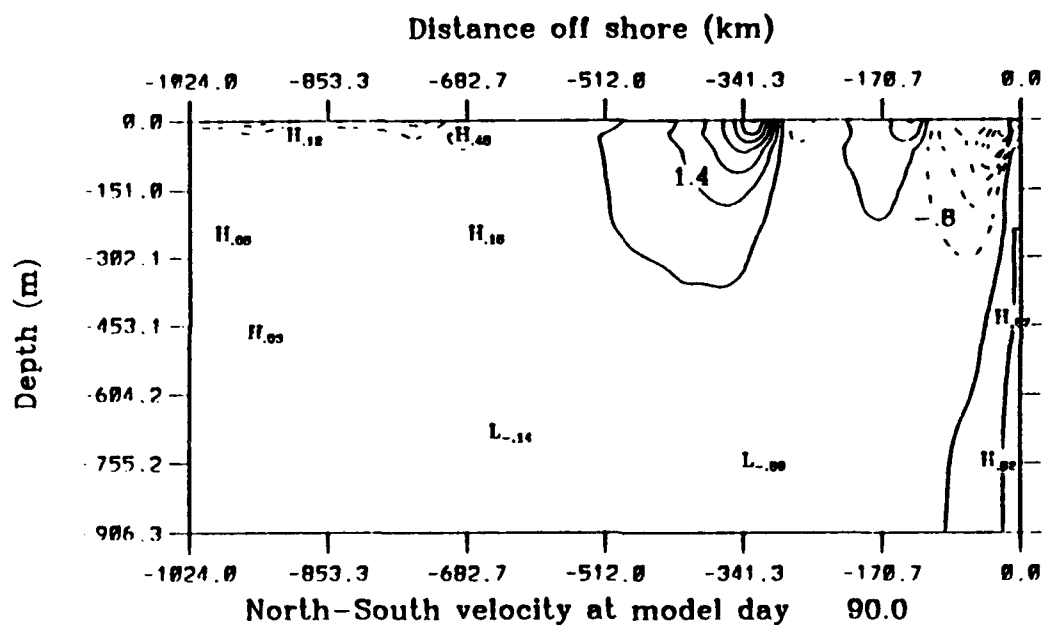


**Figure 4.31** Experiment 3: Cross-section at  $y \sim 704$  km ( $41.25^\circ$  N) of the meridional component of velocity at day 90. Dashed lines indicate equatorward flow, while solid lines indicate poleward flow.

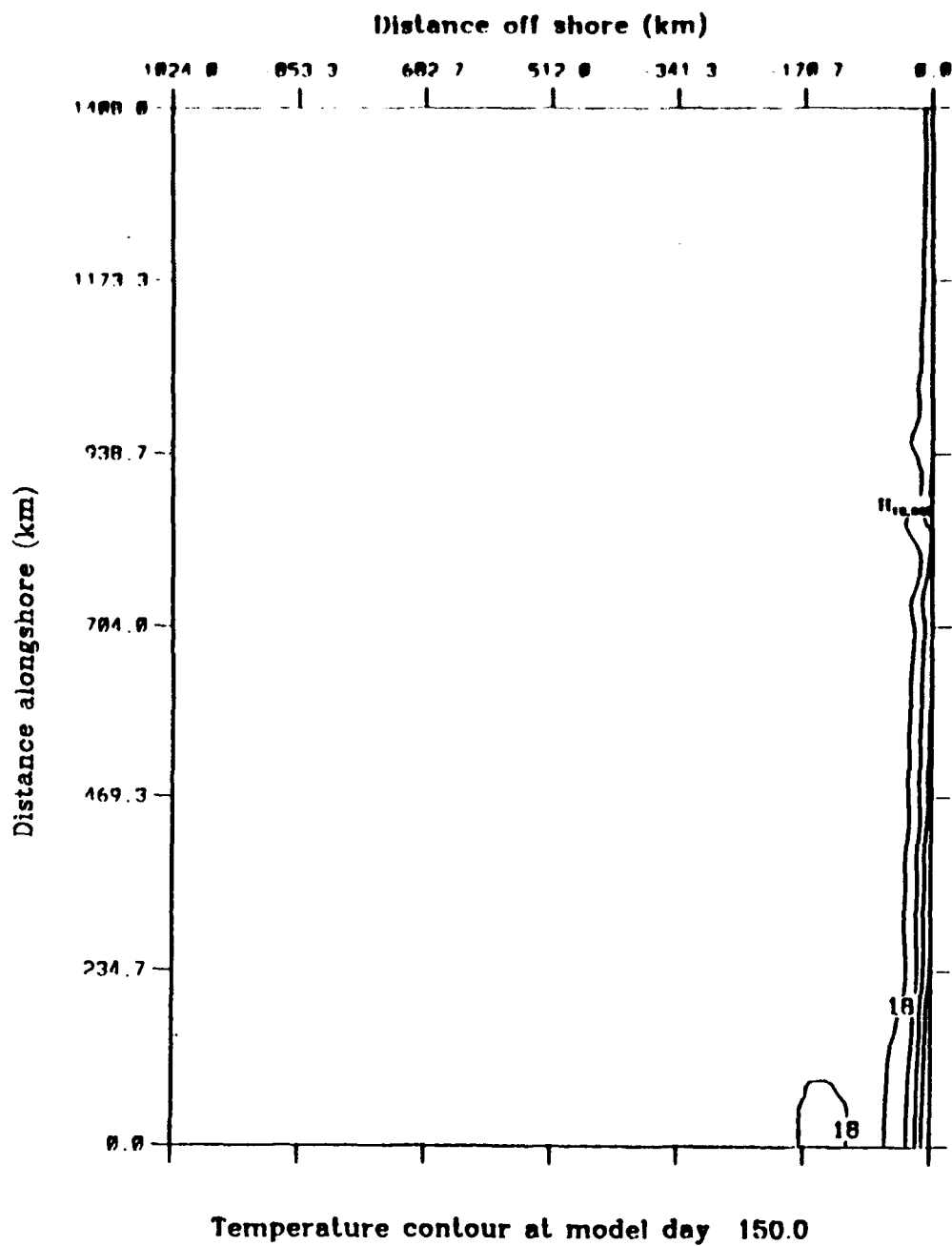


**Figure 4.32** Experiment 3: Surface temperature at day 150. The contour interval is  $1^{\circ}\text{C}$ . The temperature decreases towards the coast. Note the existence of upwelling and meanders.



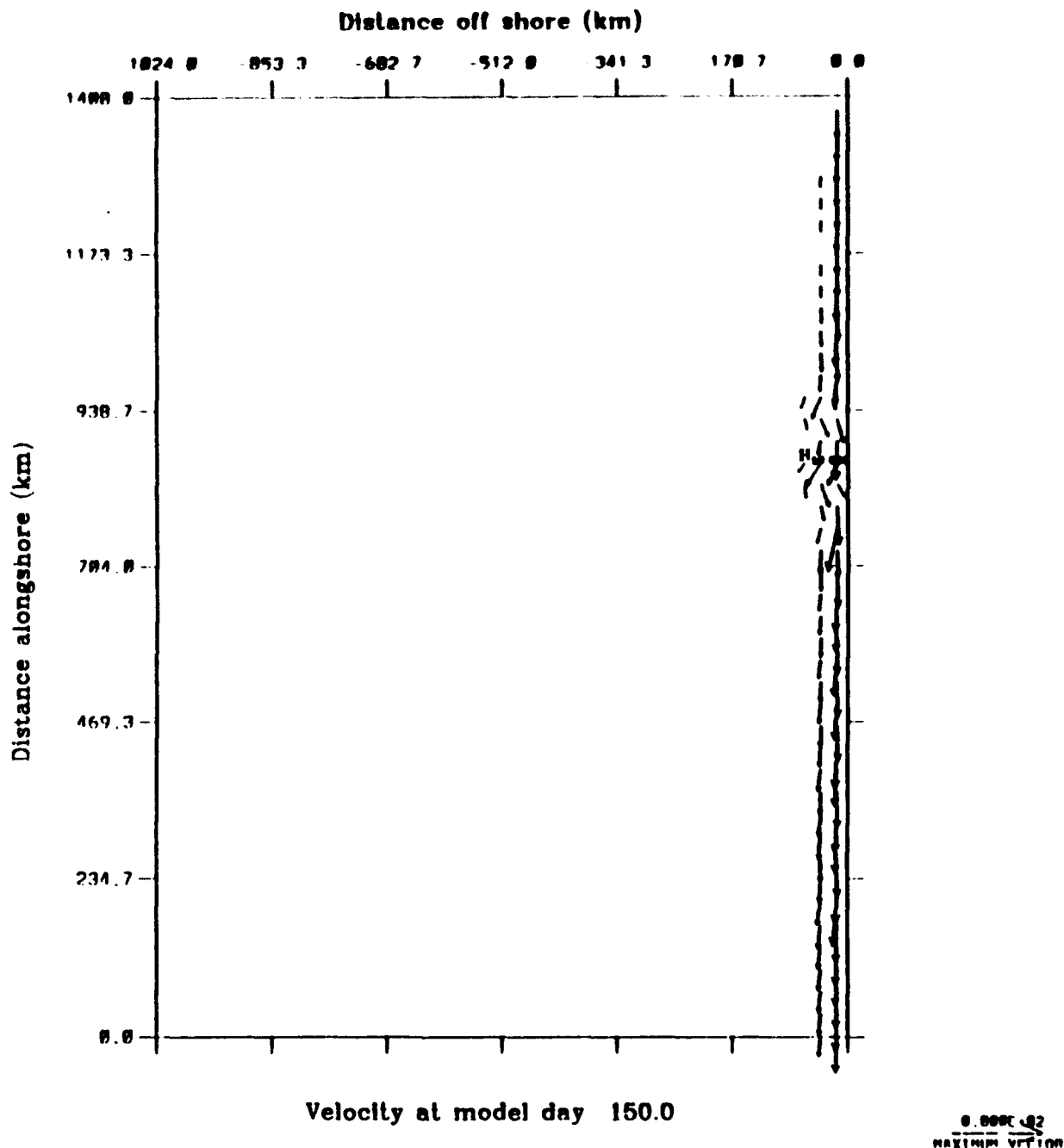


**Figure 4.33** Experiment 3: Surface velocity vectors at day 150. To avoid clutter, velocity vectors are plotted at every third grid point in both the cross-shore and alongshore direction, and velocities less than  $5 \text{ cm s}^{-1}$  are not plotted. The number associated with the high at y-850 km corresponds to temperature, not velocity. Note the meanders near y-938 km.

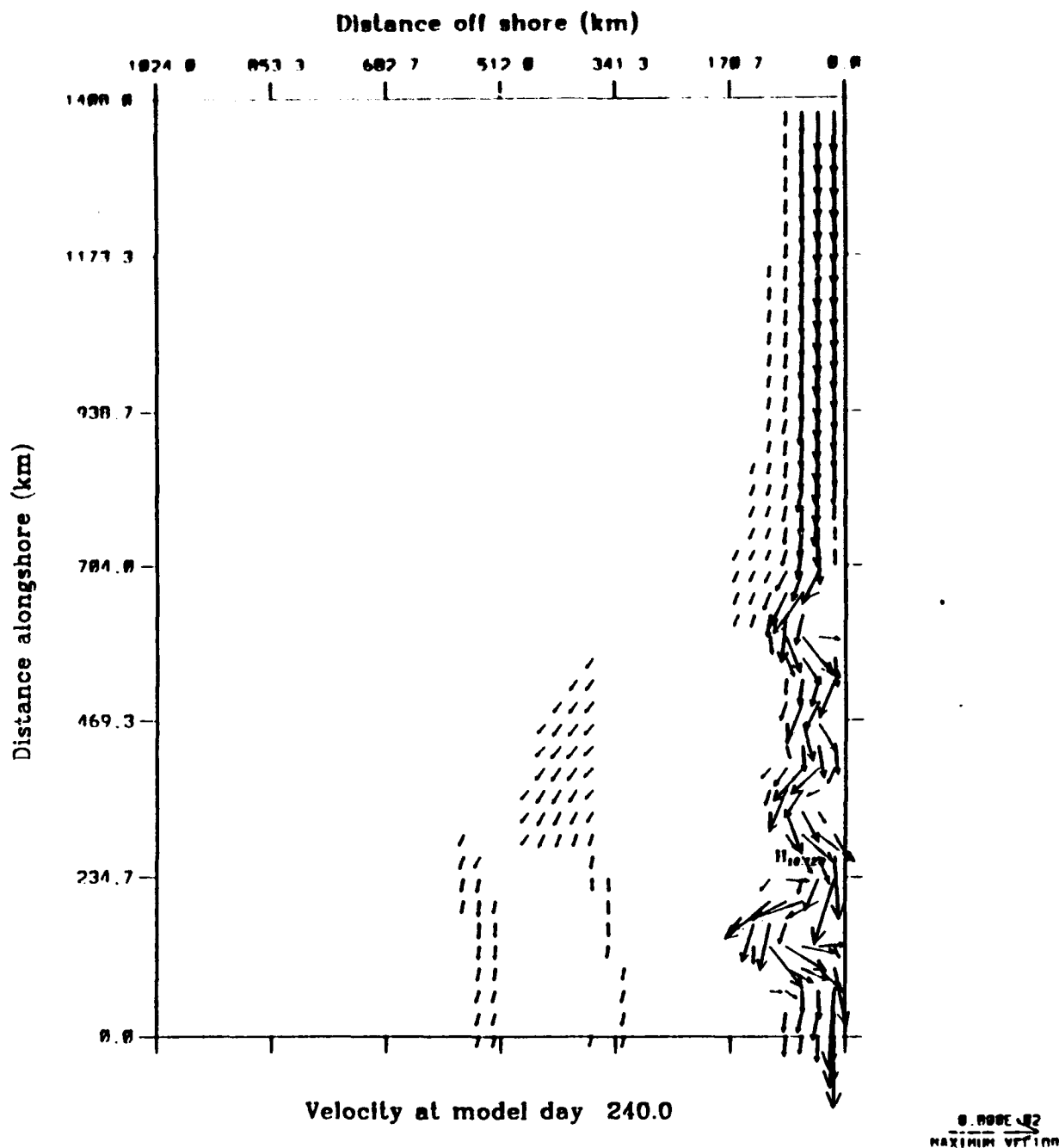


**Figure 4.34** Experiment 3: Surface velocity vectors at day 240. To avoid clutter, velocity vectors are plotted at every third grid point in both the cross-shore and alongshore direction, and velocities less than  $5 \text{ cm s}^{-1}$  are not plotted. The number associated with the high at  $y \sim 250$  km corresponds to temperature, not velocity. Note existence of eddies.

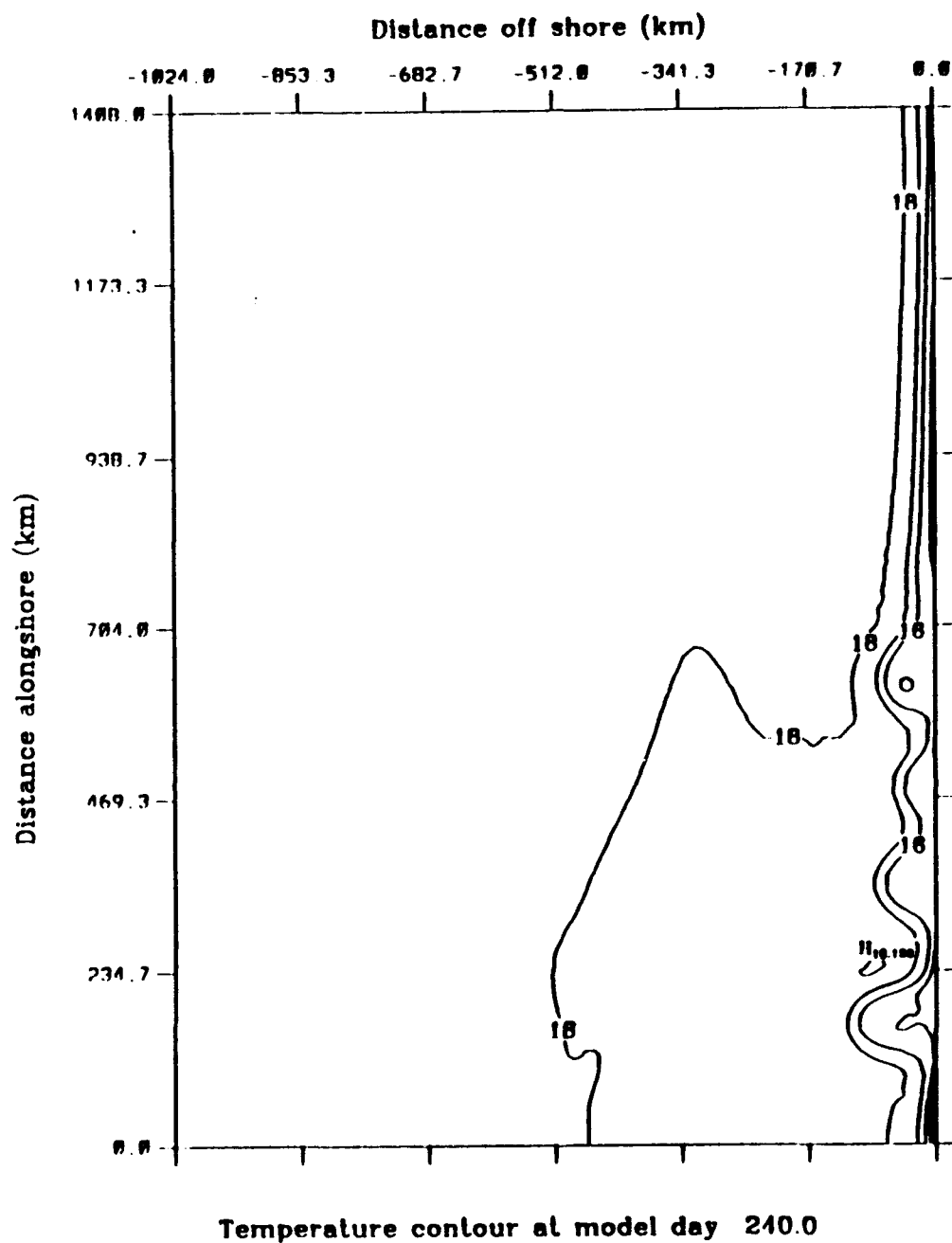
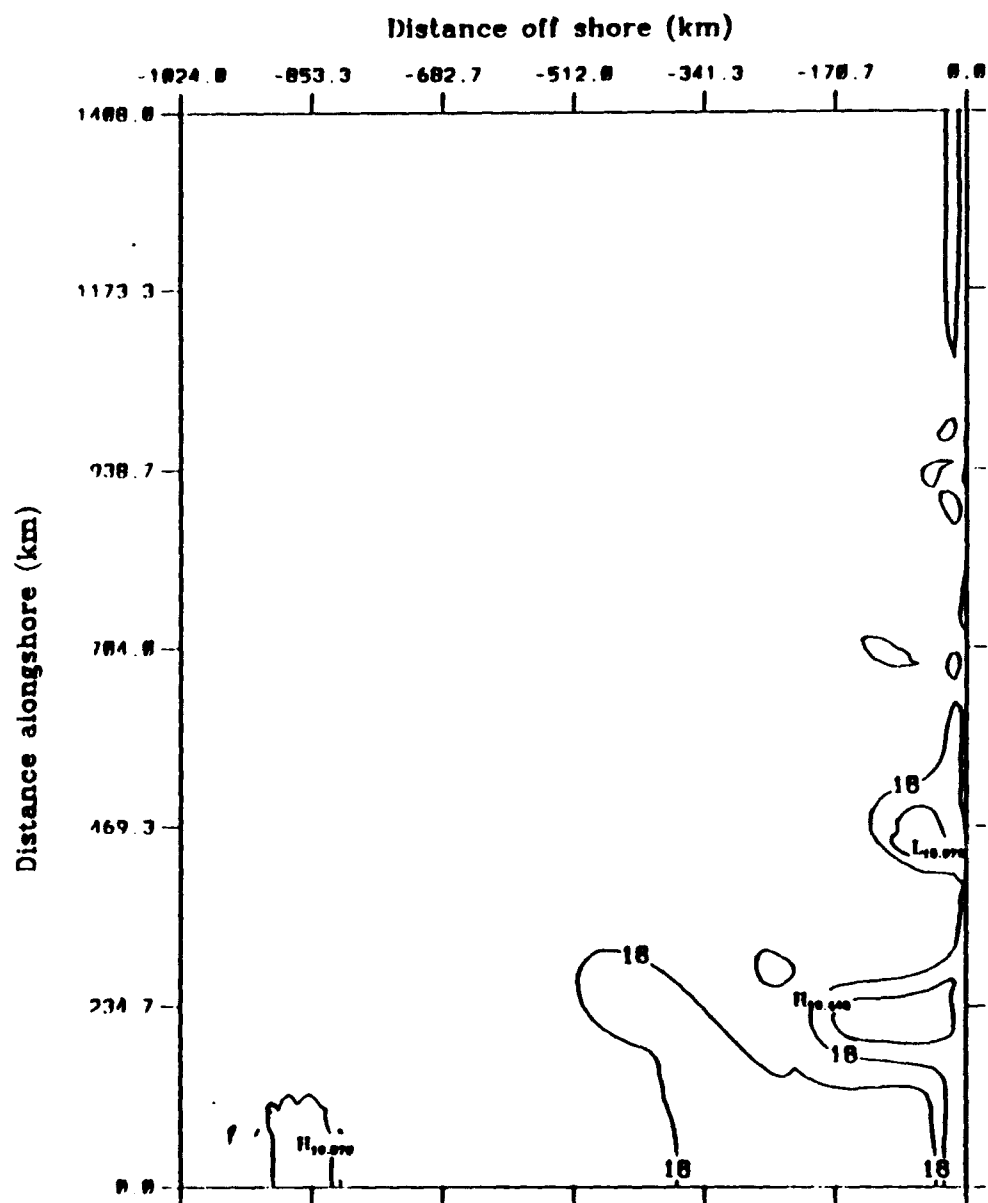


**Figure 4.35** Experiment 3: Surface temperature at day 240. The contour interval is  $1^{\circ}\text{C}$ . The temperature decreases towards the coast. Note existence of eddies.



Temperature contour at model day 360.0

**Figure 4.36** Experiment 3: Surface temperature at day 360. The contour interval is  $1^{\circ}\text{C}$ . The temperature decreases towards the coast. Note eddies remain at end of year.

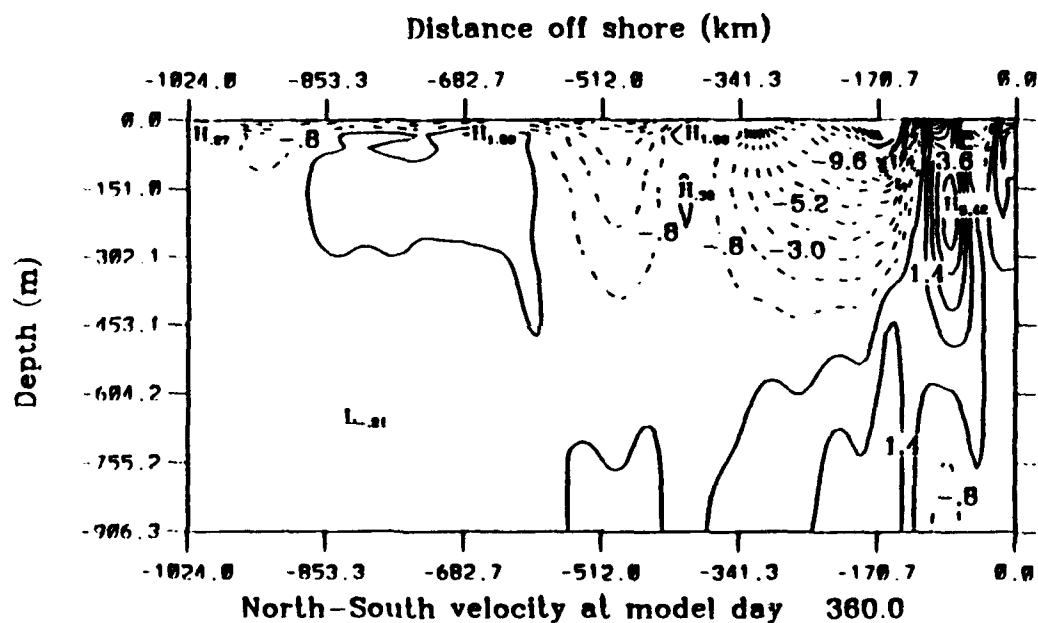


**Figure 4.37** Experiment 3: Cross-section at  $y \sim 704$  km ( $41.25^\circ$  N) of the meridional component of velocity at day 360. Dashed lines indicate equatorward flow, while solid lines indicate poleward flow. Note poleward undercurrent remains at end of year.

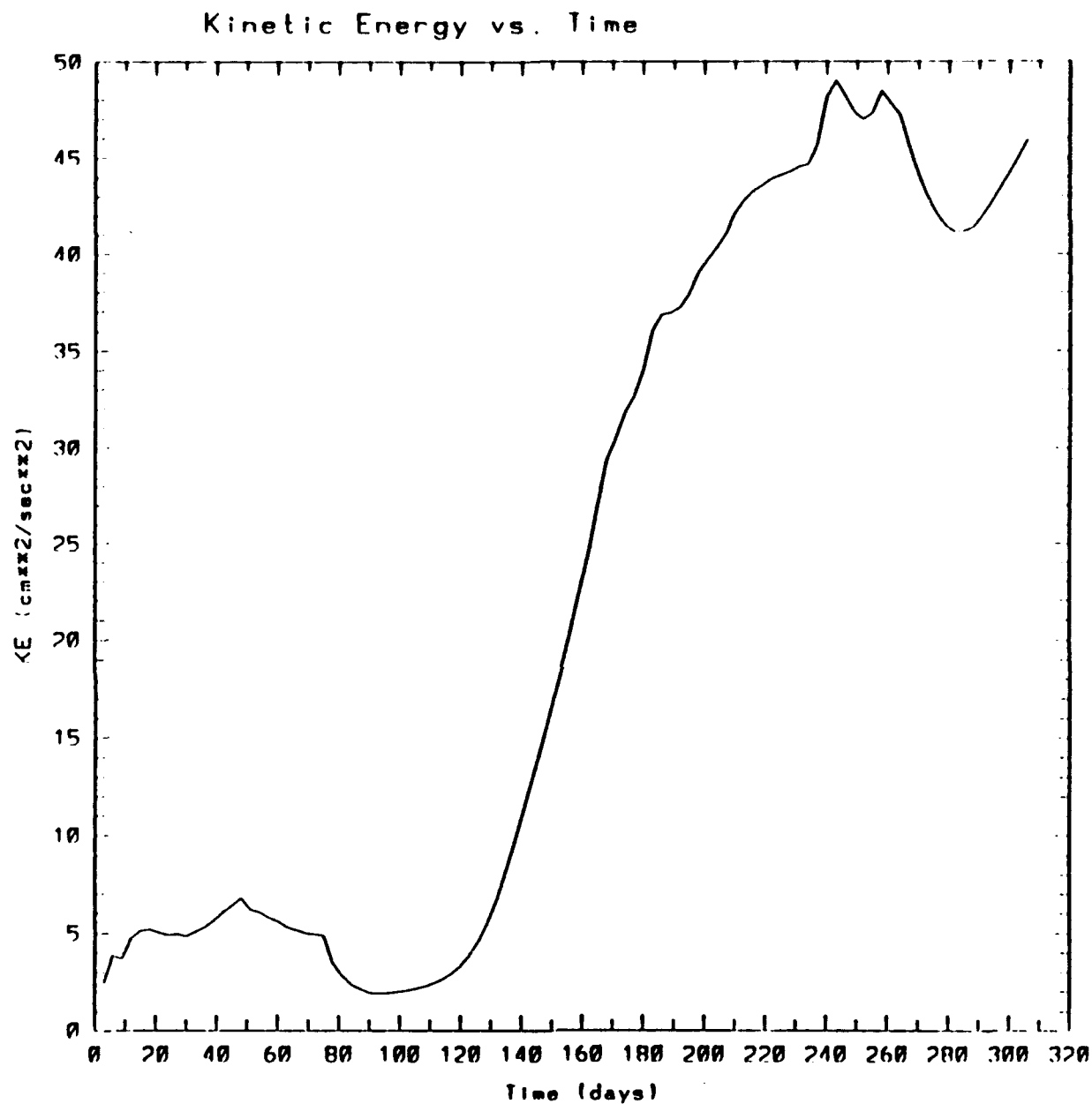


**Figure 4.38a** Experiment 3: Total kinetic energy per unit mass time series for 1983 (days 1-306) over the entire domain (Units of the kinetic energy are  $\text{cm}^2\text{s}^{-2}$ ). Quasi-steady periods: days 186-192, 222-234, 249-258, and 279-288.

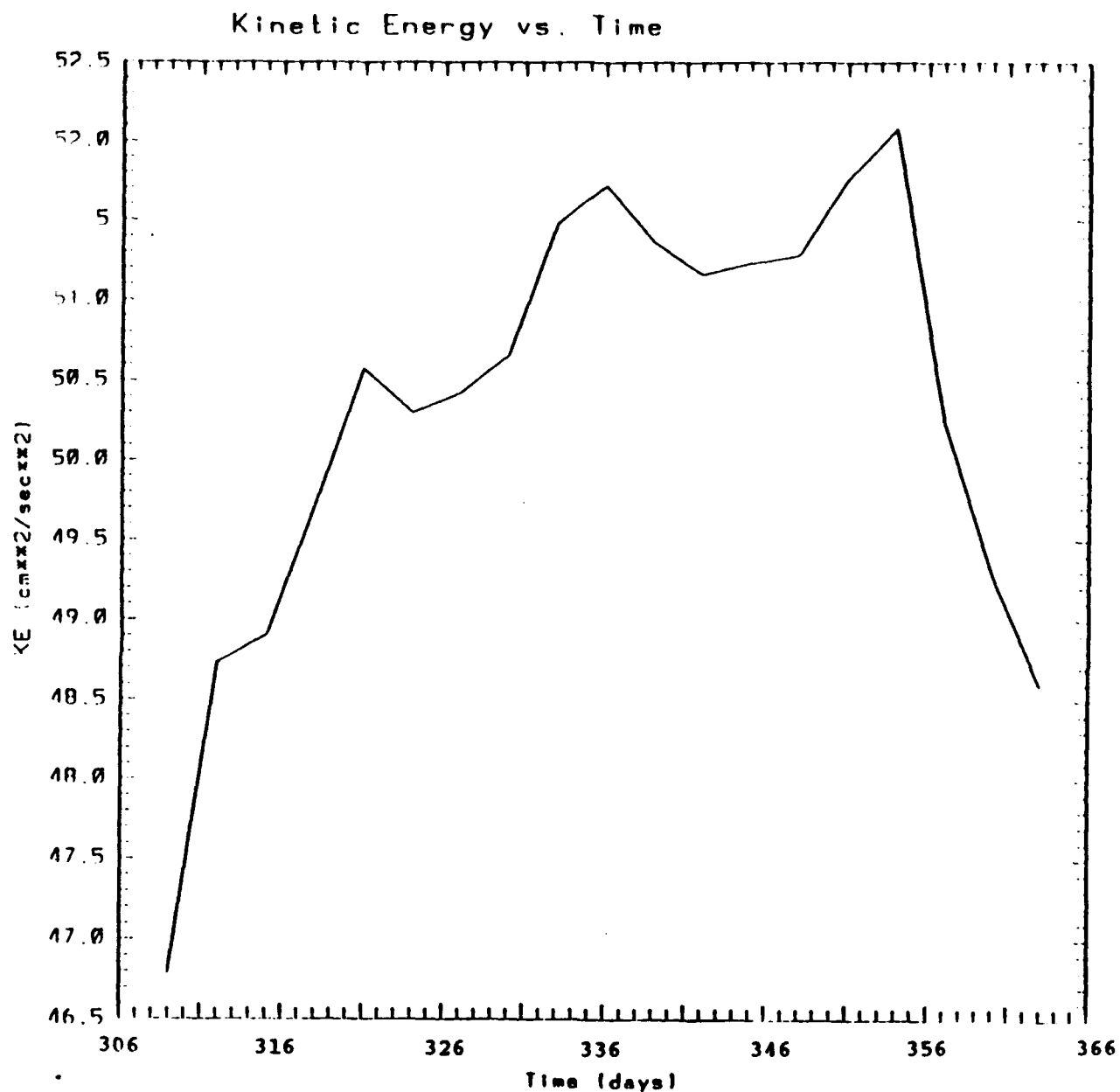


**Figure 4.38b** Experiment 3: Total kinetic energy per unit mass time series for 1983 (days 309-363) over the entire domain (Units of the kinetic energy are  $\text{cm}^2\text{s}^{-2}$ ). Quasi-steady periods: days 312-315, 324-327, and 342-348.

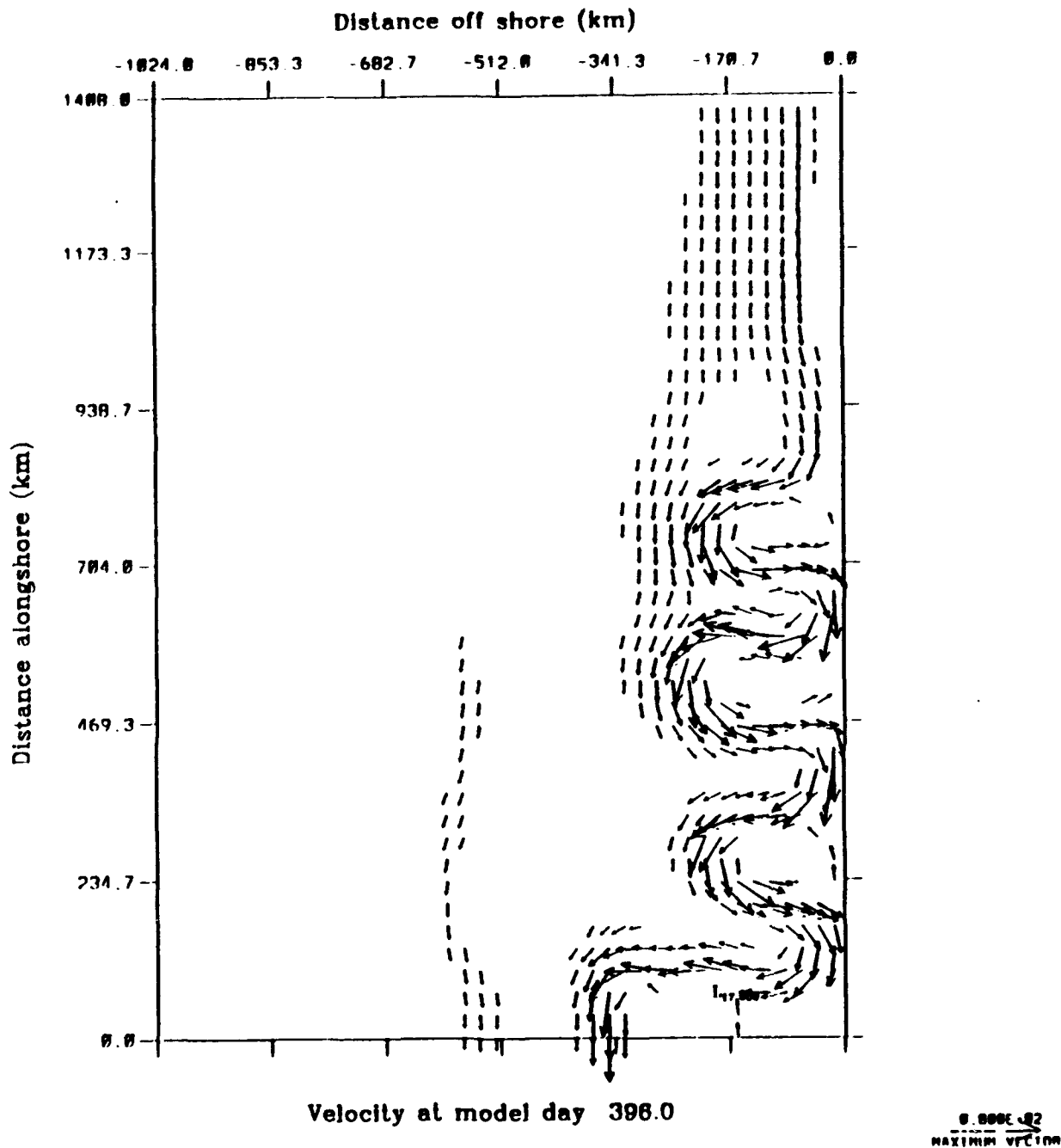


**Figure 4.39** Experiment 4: Surface velocity vectors at day 396 (yd 30). To avoid clutter, velocity vectors are plotted at every third grid point in both the cross-shore and alongshore direction, and velocities less than  $5 \text{ cm s}^{-1}$  are not plotted. The number associated with the low at  $y \sim 80 \text{ km}$  corresponds to temperature, not velocity. Note equatorward surface current with embedded meanders and cyclonic eddies.



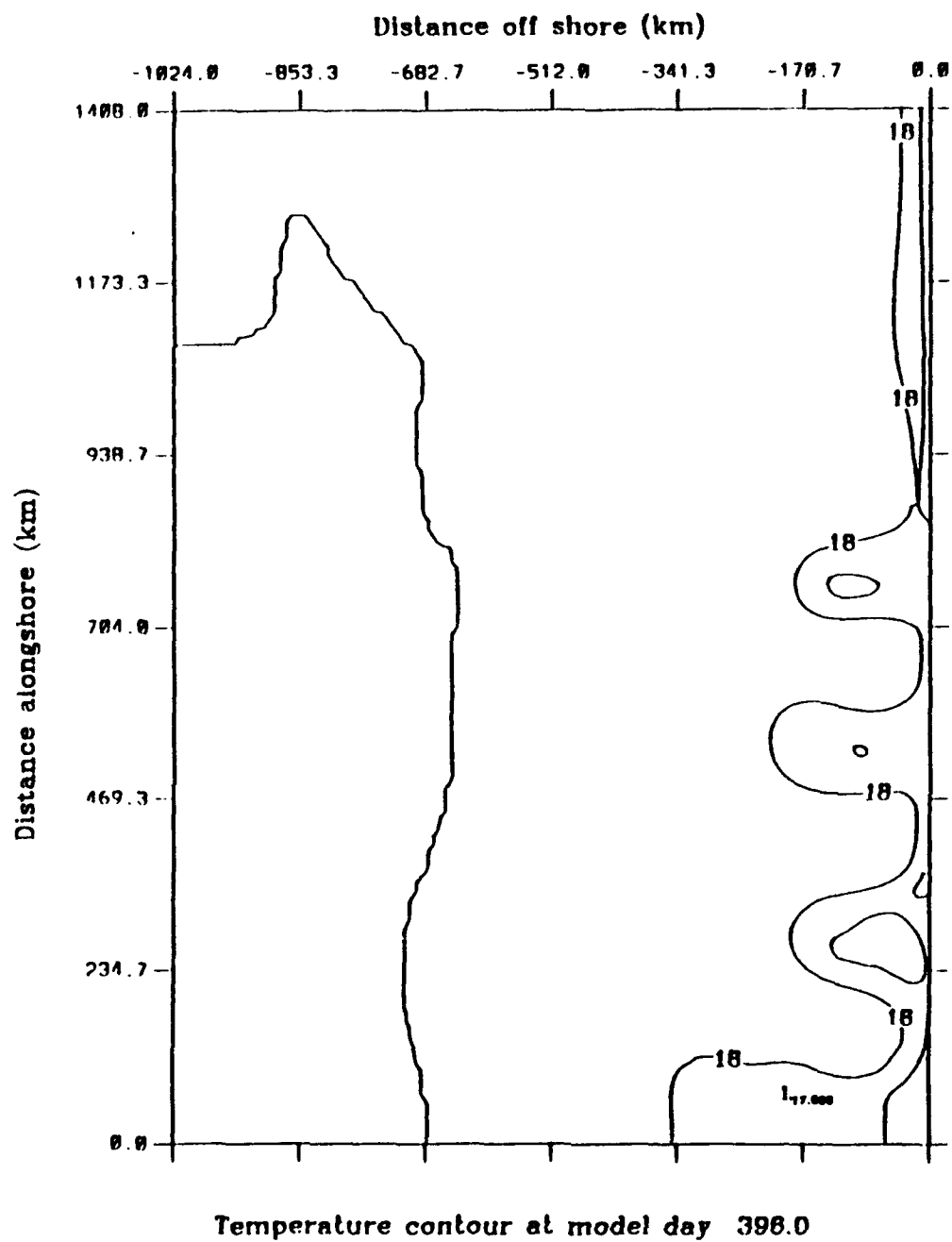


**Figure 4.40** Experiment 4: Surface temperature at day 396 (yd 30). The contour interval is 1° C. The temperature decreases towards the coast. Note cold core eddies.

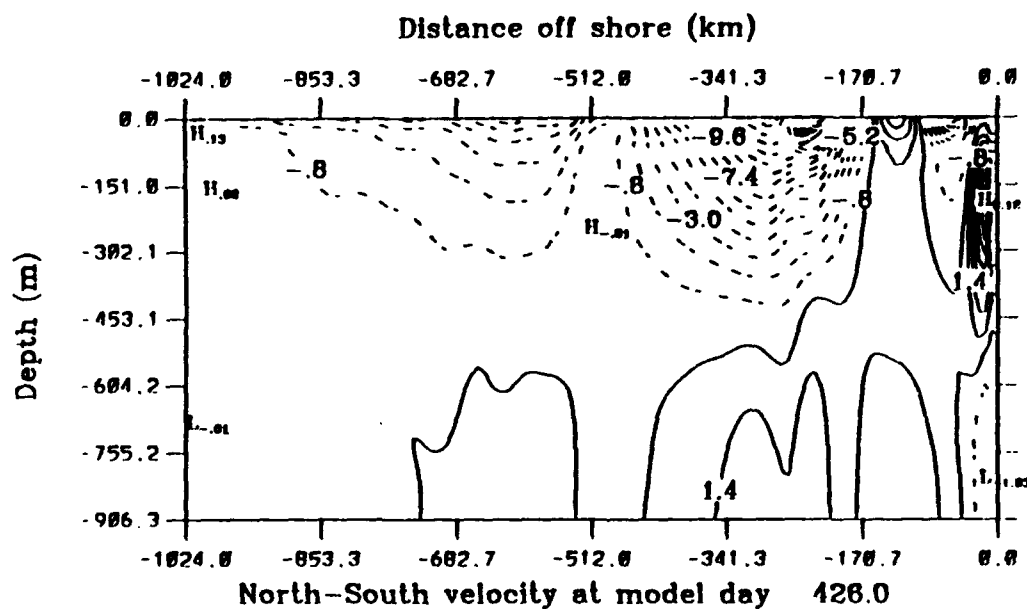
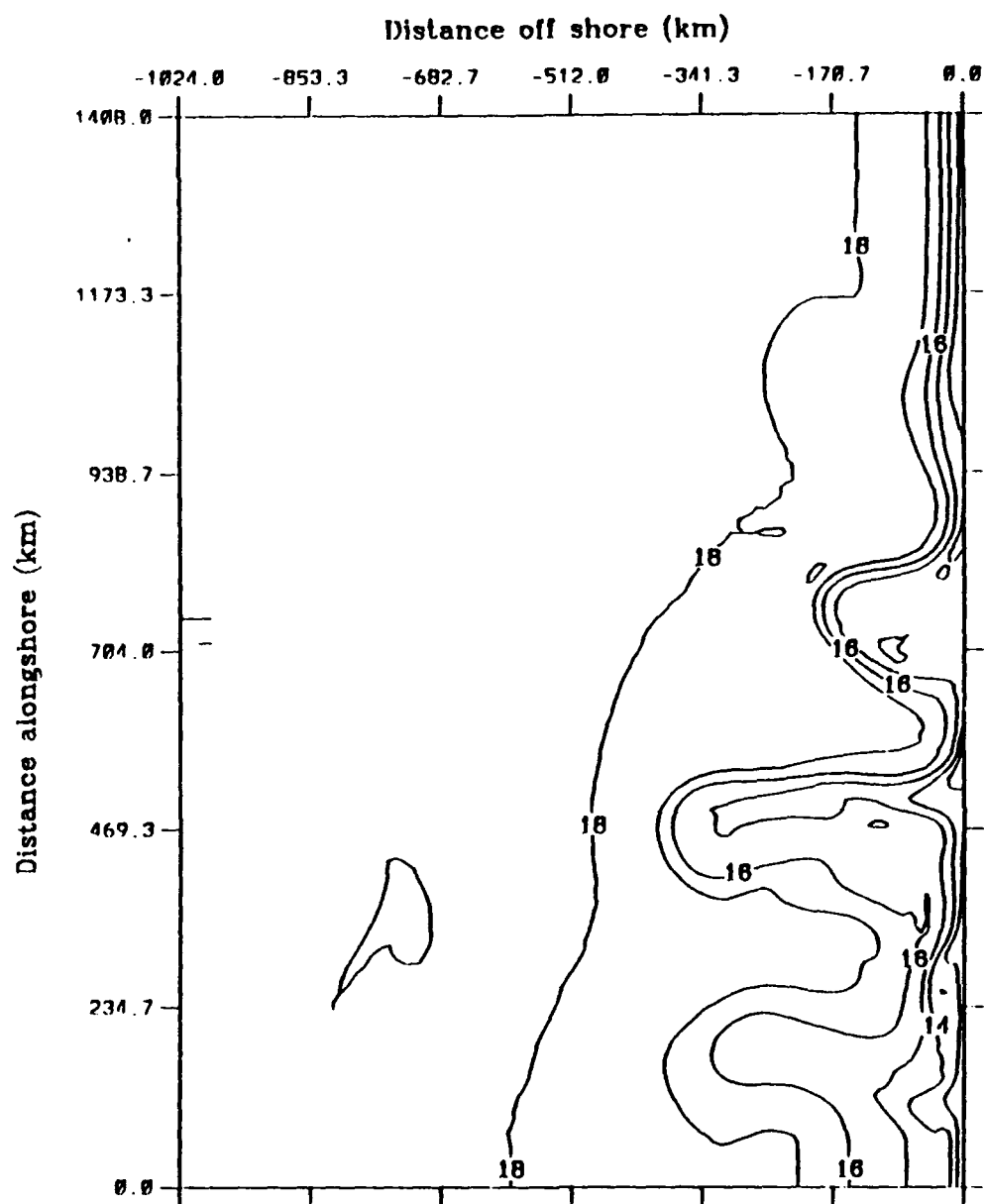


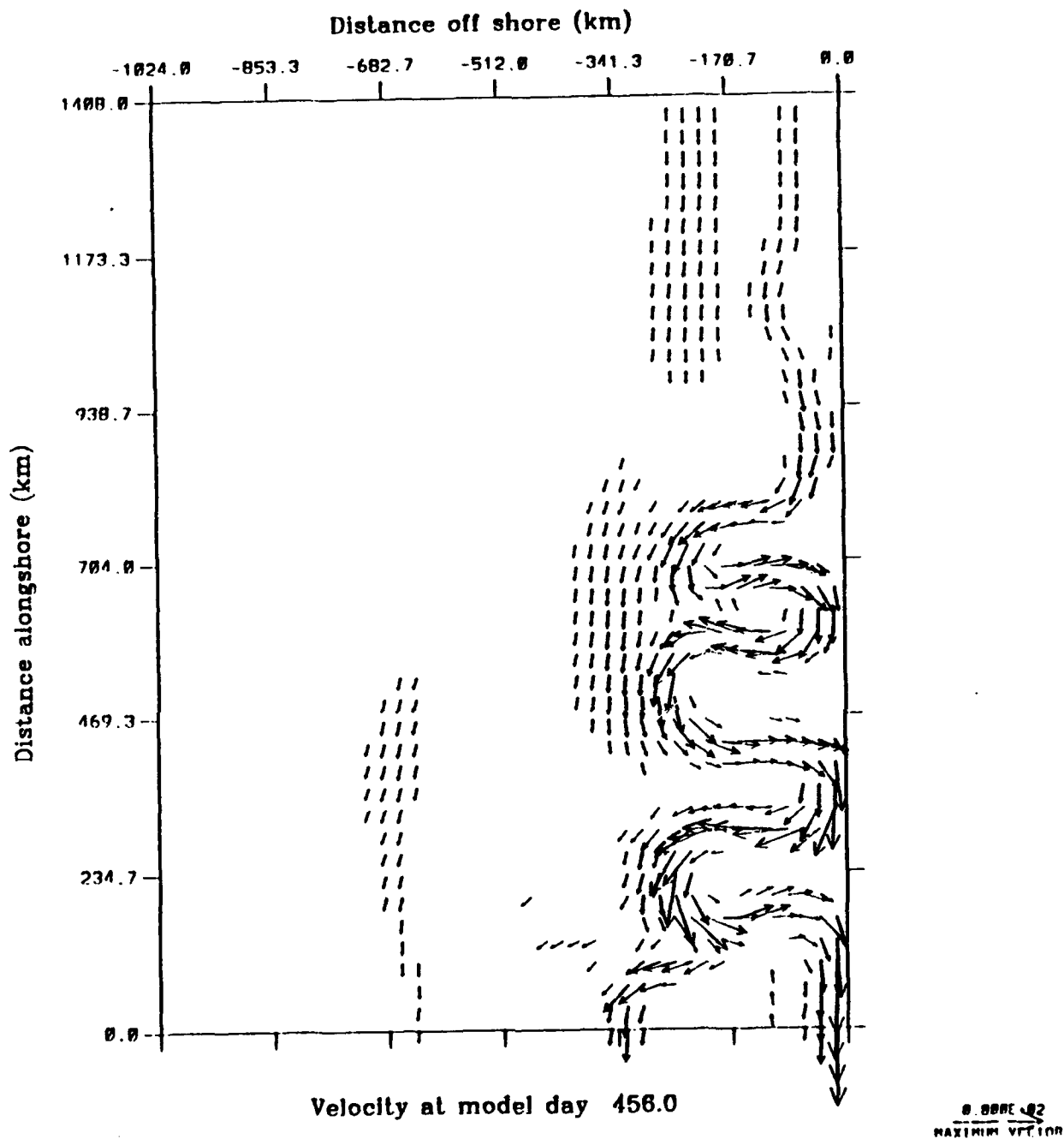
**Figure 4.41** Experiment 4: Cross-section at  $y \sim 704$  km ( $41.25^\circ$  N) of the meridional component of velocity at day 426 (yd 60). Dashed lines indicate equatorward flow, while solid lines indicate poleward flow. Note existence of poleward undercurrent.



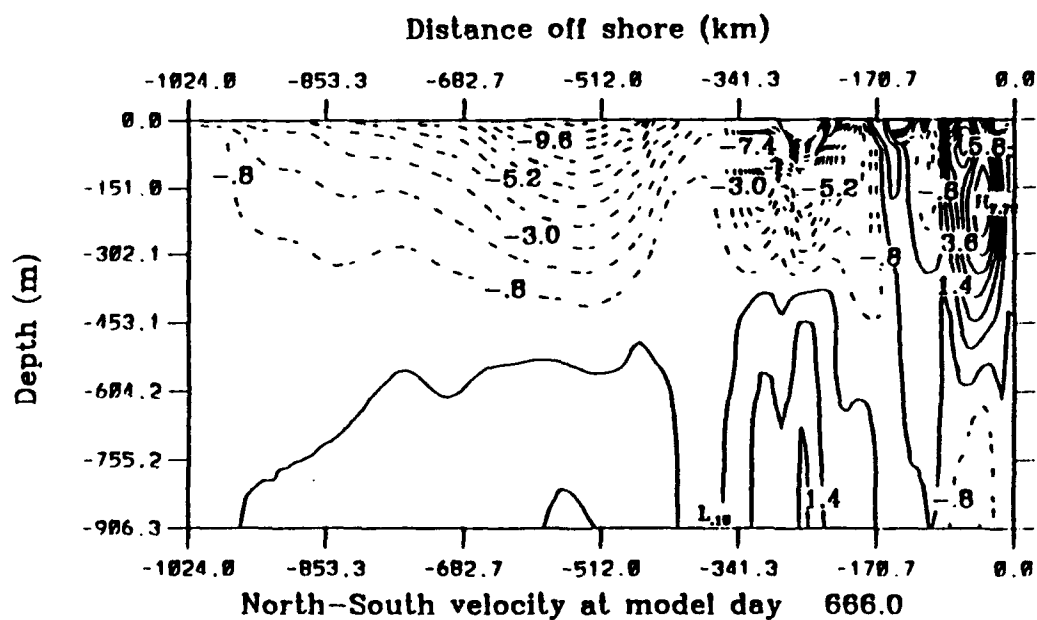


Temperature contour at model day 606.0

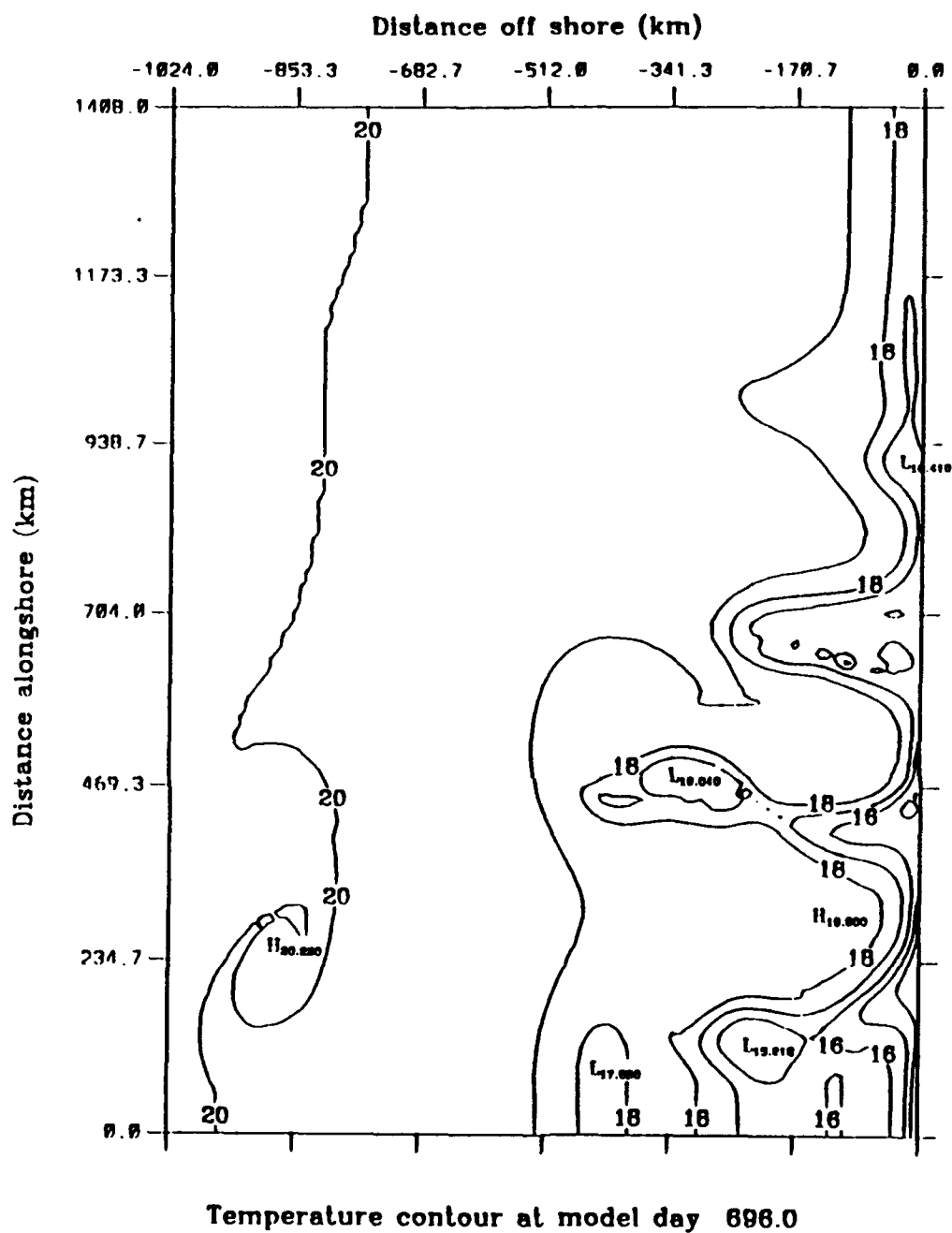
**Figure 4.43** Experiment 4: Surface temperature at day 606 (yd 240). The contour interval is  $1^{\circ}\text{C}$ . The temperature decreases towards the coast.



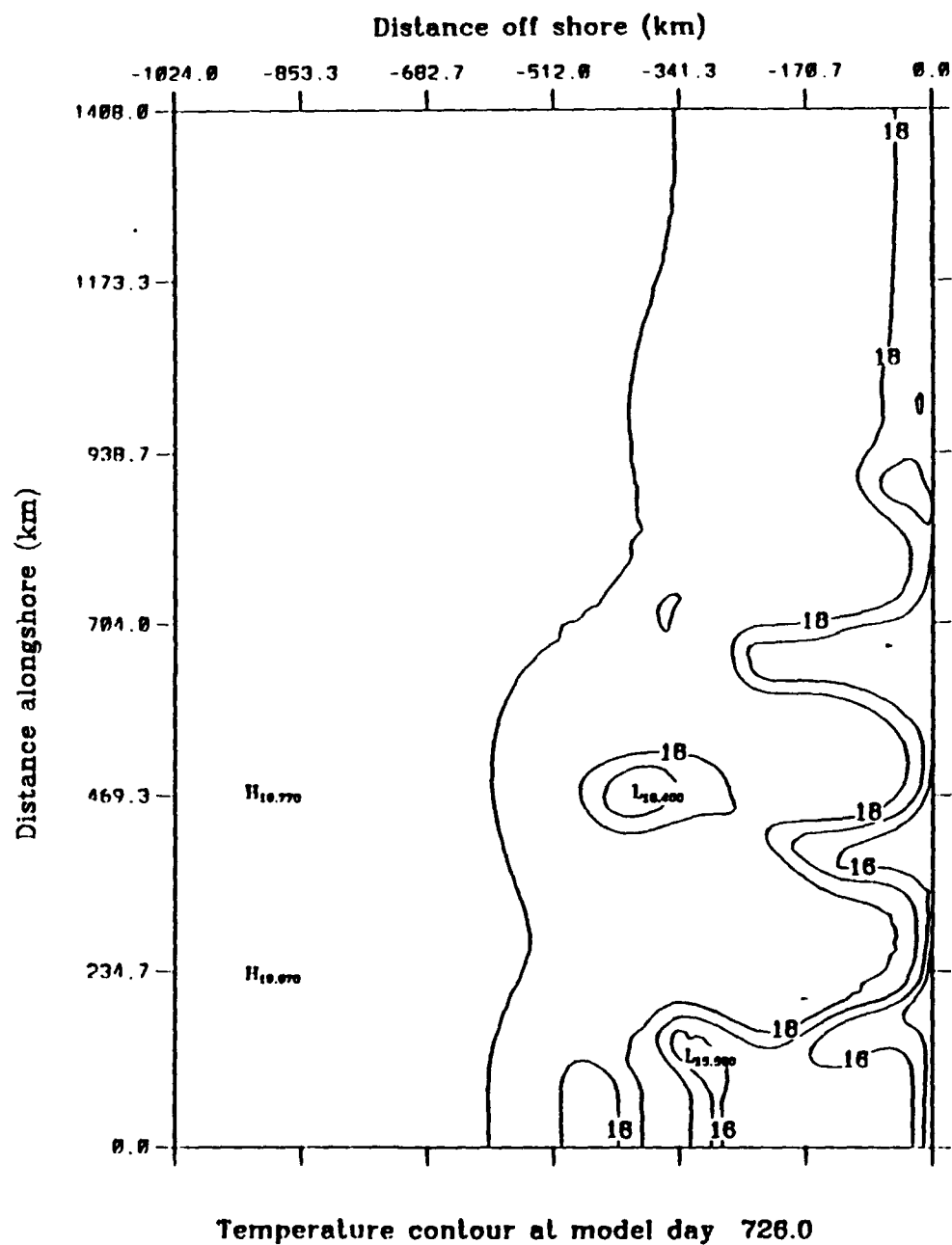
**Figure 4.44** Experiment 4: Surface velocity vectors at day 456 (yd 90). To avoid clutter, velocity vectors are plotted at every third grid point in both the cross-shore and alongshore direction, and velocities less than  $5 \text{ cm s}^{-1}$  are not plotted. Note anticyclonic eddy at  $y \sim 650 \text{ km}$ .



**Figure 4.45** Experiment 4: Cross-section at  $y \sim 704$  km ( $41.25^\circ$  N) of the meridional component of velocity at day 666 (yd 300). Dashed lines indicate equatorward flow, while solid lines indicate poleward flow.

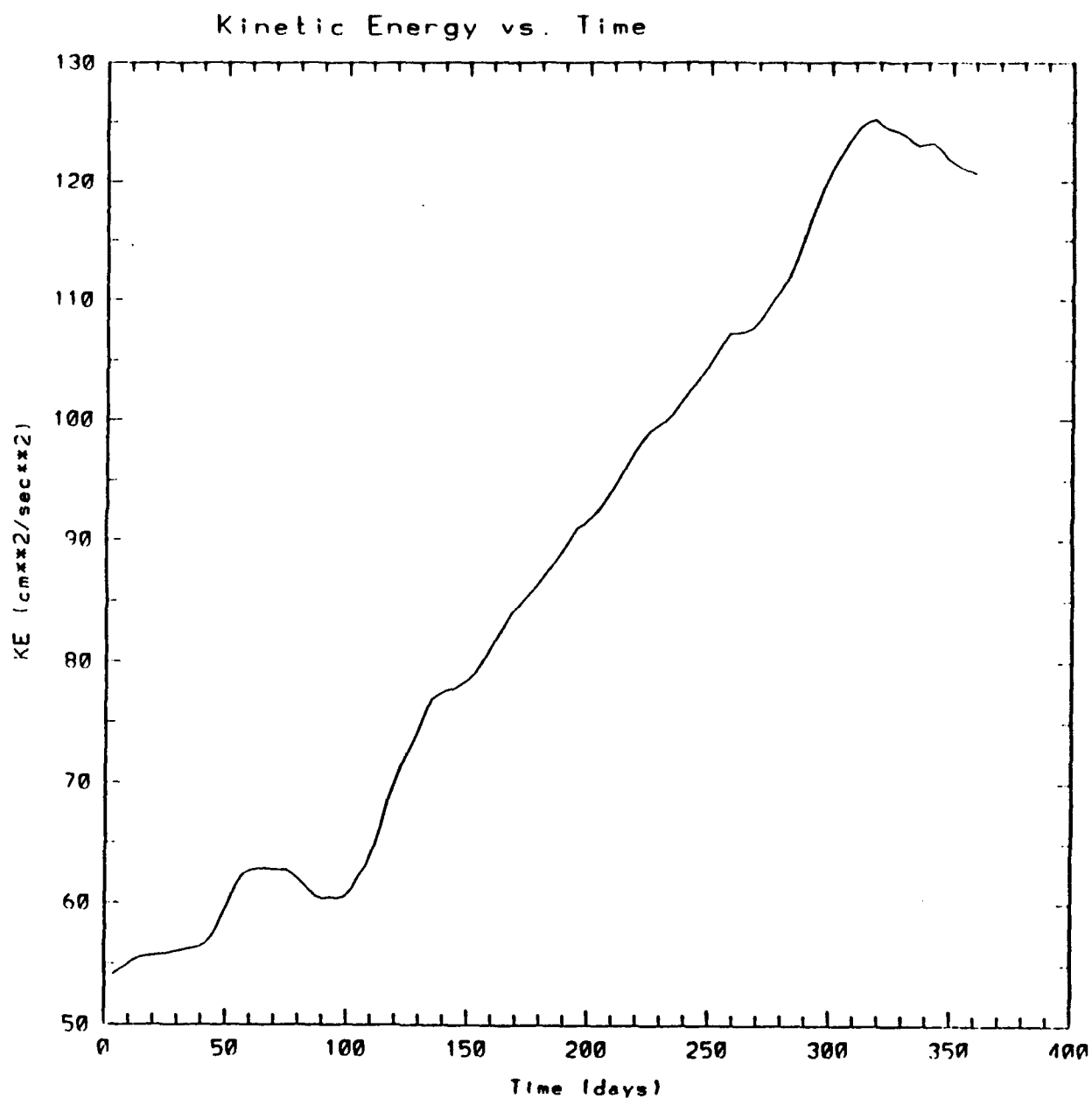


**Figure 4.46** Experiment 4: Surface temperature at day 696 (yd 330). The contour interval is 1° C. The temperature decreases towards the coast. Note formation of eddy from pinched off meander at y~469 km.

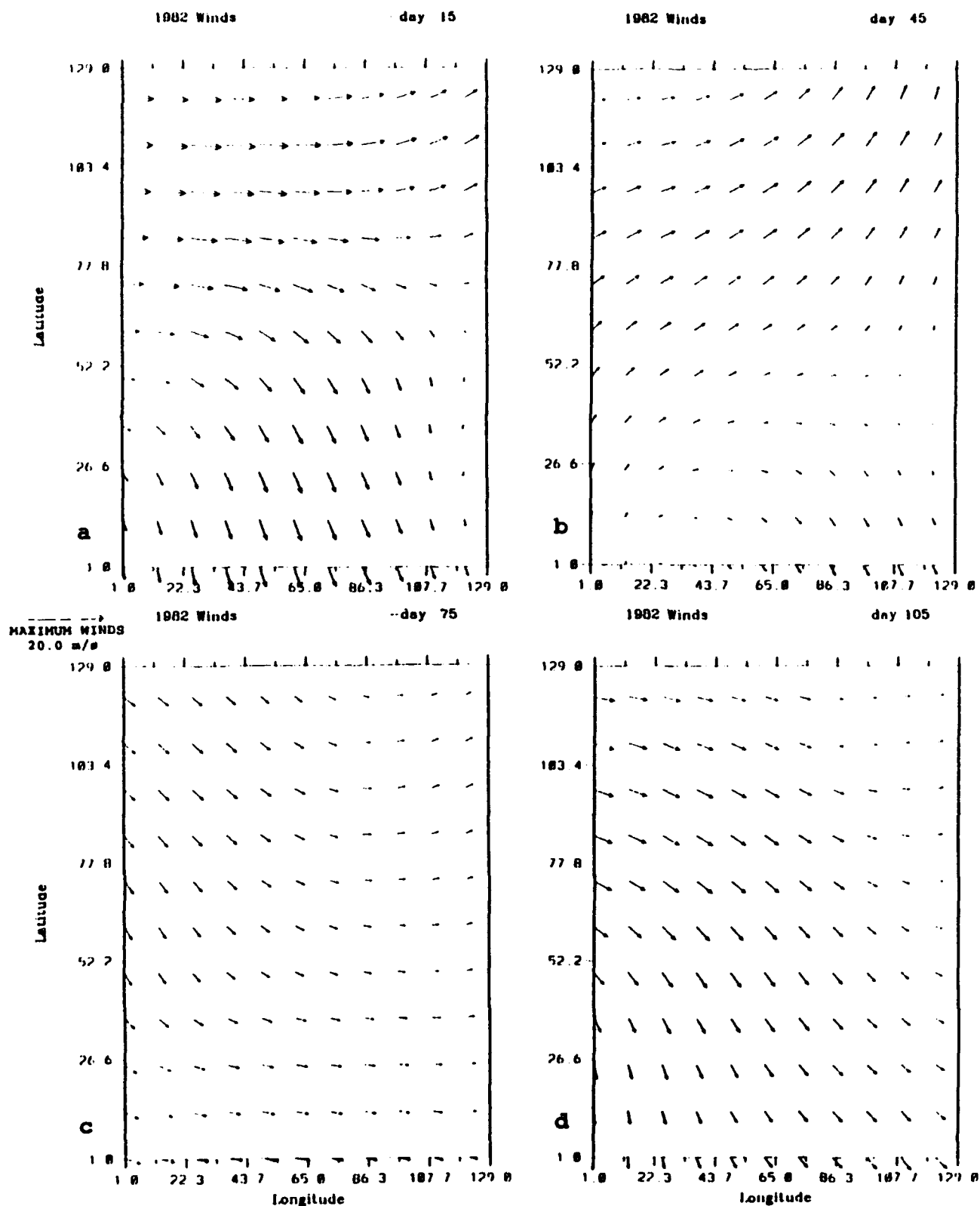


**Figure 4.47** Experiment 4: Surface temperature at day 726 (yd 360). The contour interval is 1° C. The temperature decreases towards the coast. Note formation of eddy from pinched off meander at y~469 km.



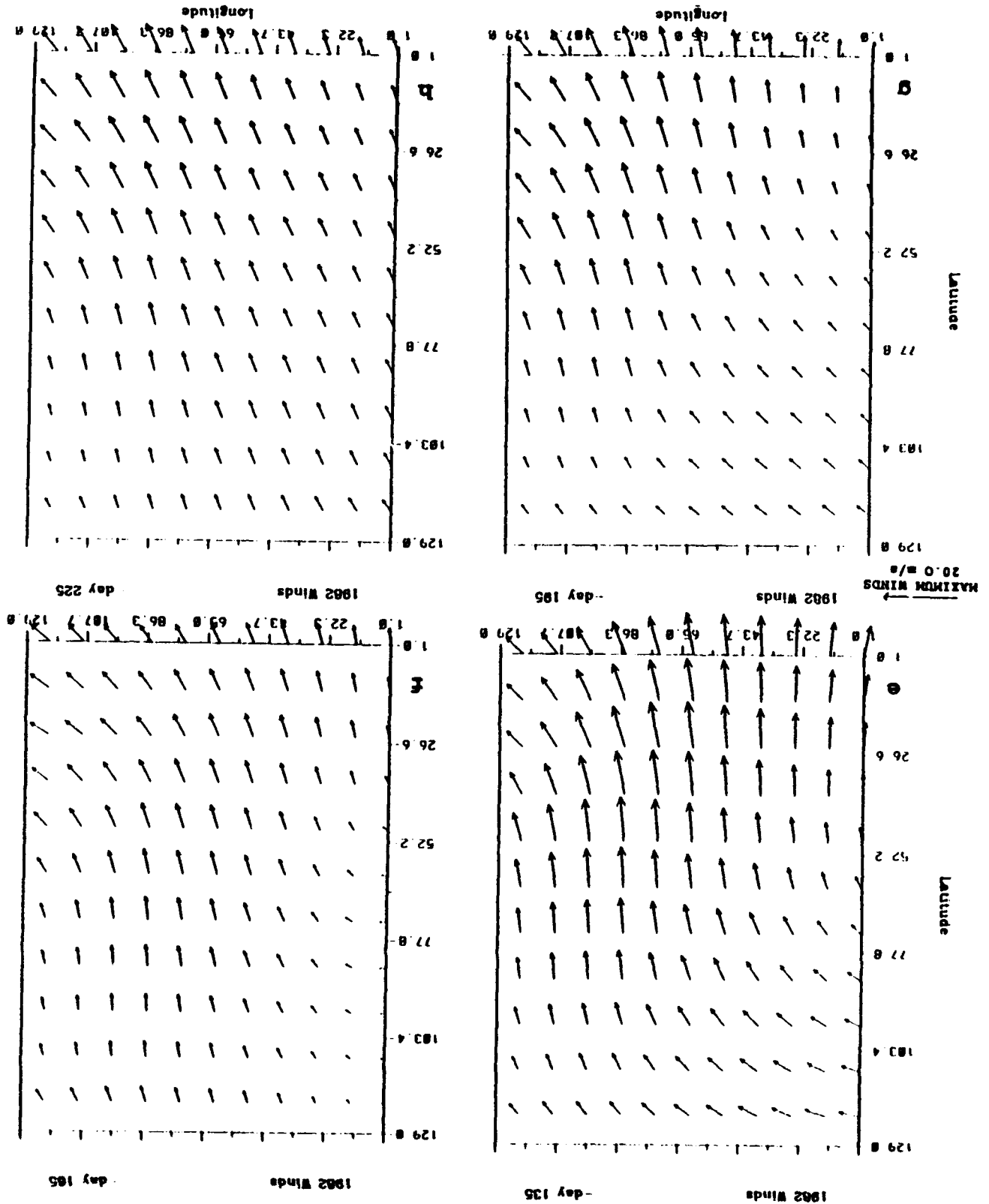


**Figure 4.48** Experiment 4: Total kinetic energy per unit mass time series for Climo II over the entire domain (Units of the kinetic energy are  $\text{cm}^2\text{s}^{-2}$ ). Quasi-steady periods: days 378-408 (yd 12-42), 453-465 (yd 87-89), 504-516 (yd 138-150), and 624-636 (yd 258-270).



**Figure 4.49** Mid-monthly ECMWF winds for 1982 in  $\text{m s}^{-1}$ :  
 (a) January, (b) February, (c) March, (d) April, (e) May,  
 (f) June, (g) July, (h) August, (i) September, (j) October,  
 (k) November, and (l) December. The latitudinal grid point  
 1 (129) corresponds to  $35^\circ \text{ N}$  ( $47.5^\circ \text{ N}$ ); so that the  
 latitudinal grid point of 52 corresponds to  $40^\circ \text{ N}$ . Maximum  
 wind vector is  $20 \text{ m s}^{-1}$ .

Figure 4.49 (continued).



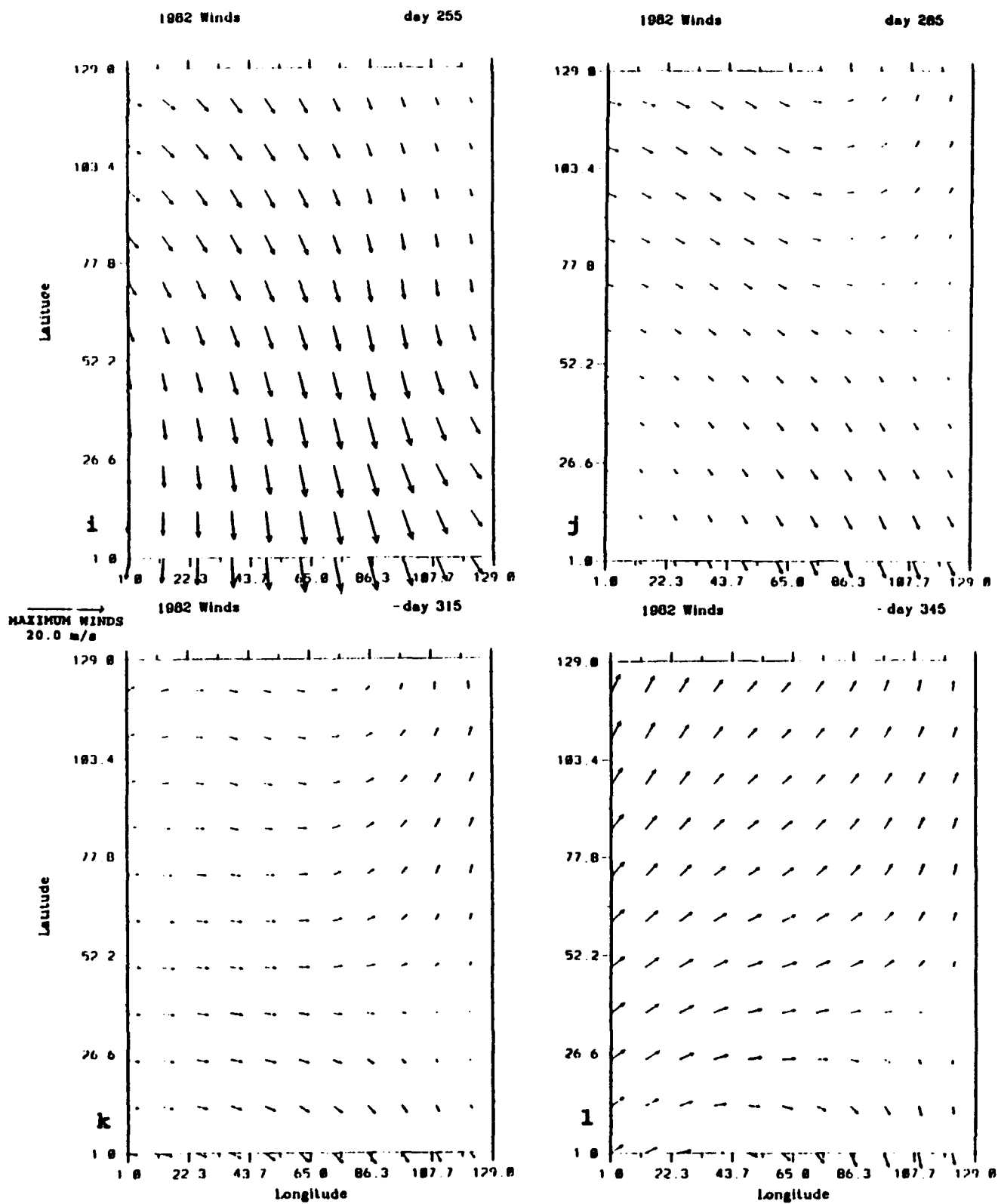
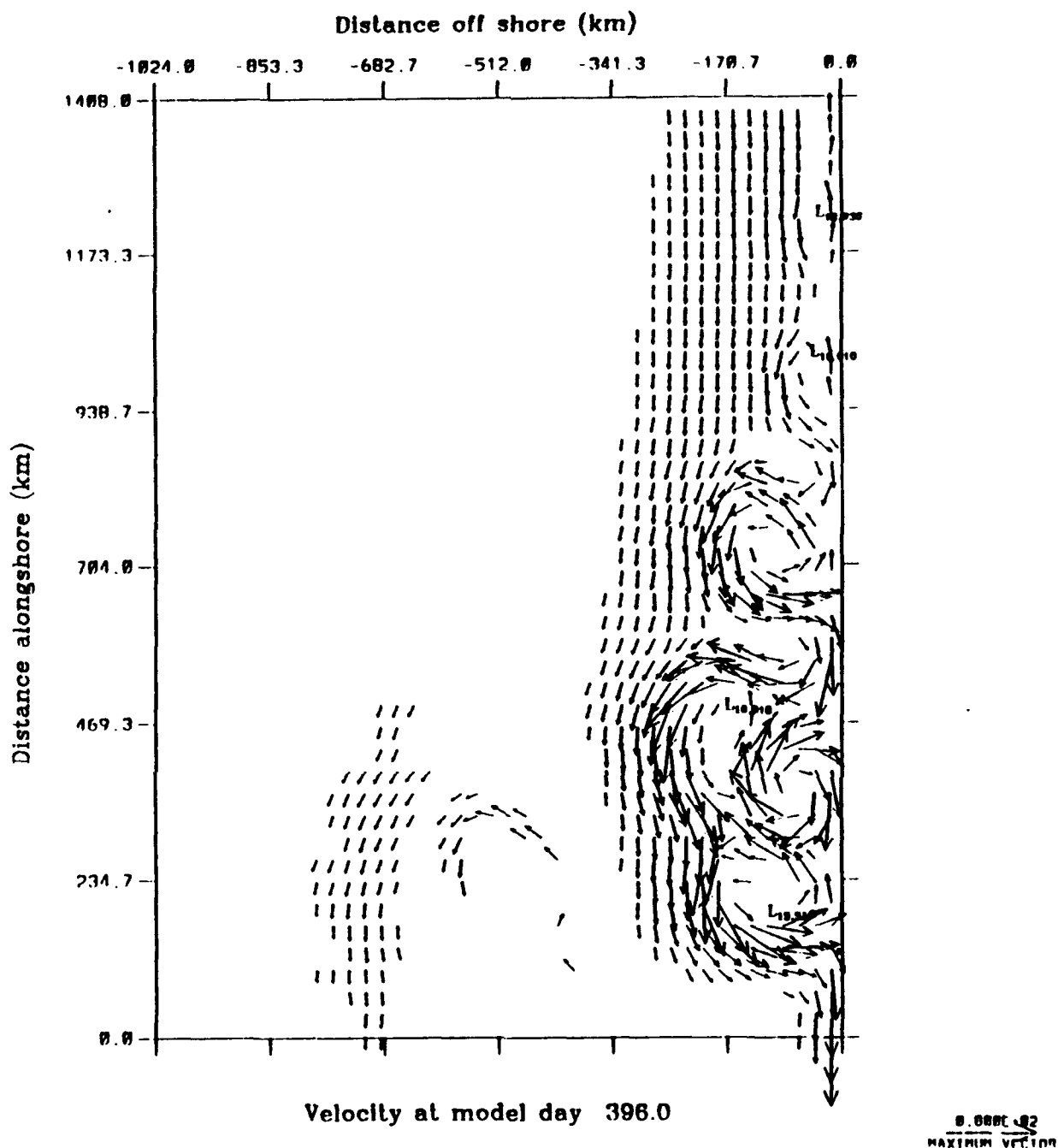
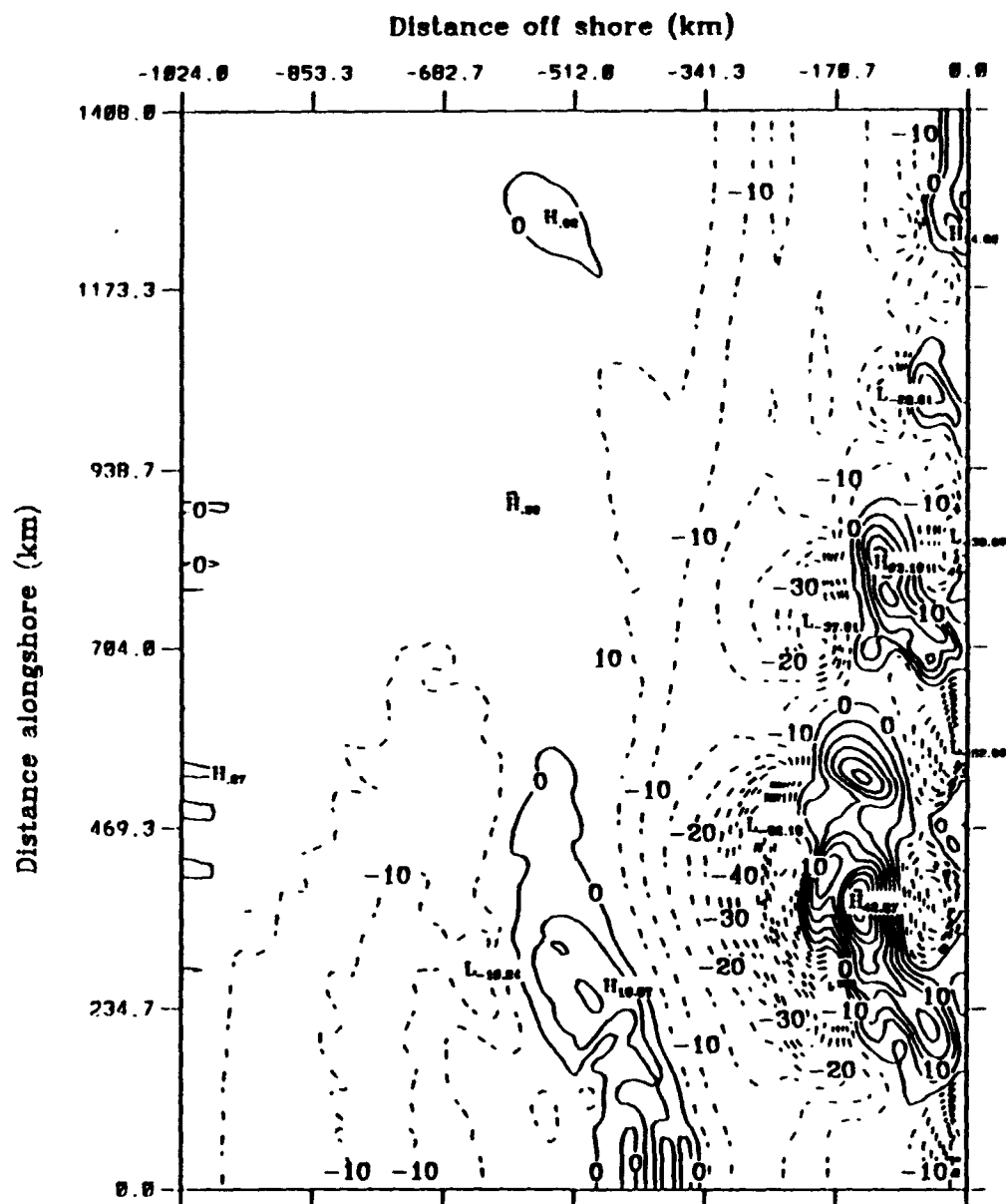


Figure 4.49 (continued).



**Figure 4.50** Experiment 5: Surface velocity vectors at day 396 (yd 30). To avoid clutter, velocity vectors are plotted at every third grid point in both the cross-shore and alongshore direction, and velocities less than  $5 \text{ cm s}^{-1}$  are not plotted. The numbers associated with the lows embedded in the meanders and eddies along the coast correspond to temperature, not velocity. Note fully developed equatorward surface current with embedded meanders and eddies, along with poleward surface current north of  $y \sim 1173 \text{ km}$ .



**Figure 4.51** Experiment 5: Surface meridional component of velocity at day 426 (yd 60). The contour interval is 5  $\text{cm s}^{-1}$ . The dashed lines indicate equatorward velocities. The maximum poleward velocity is  $\sim 15 \text{ cm s}^{-1}$ . Latitudinal alongshore distance 0 (1408) km corresponds to  $35^\circ \text{ N}$  ( $47.5^\circ \text{ N}$ ).

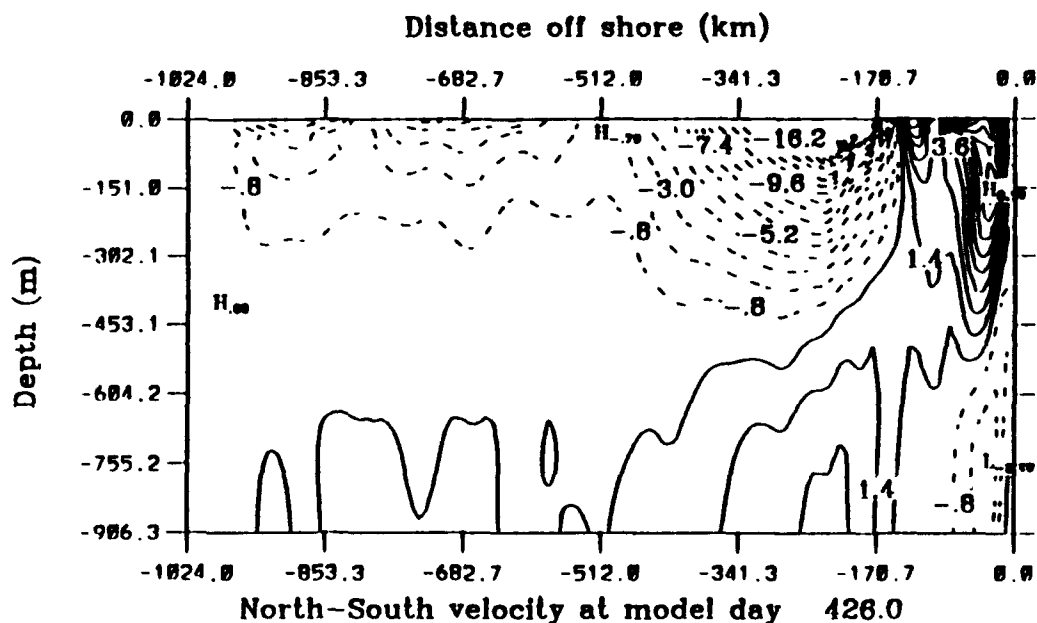


**Figure 4.52** Experiment 5: Cross-section at  $y \sim 704$  km ( $41.25^\circ$  N) of the meridional component of velocity at day 426 (yd 60). Dashed lines indicate equatorward flow, while solid lines indicate poleward flow. Note strong poleward undercurrent along with subsurface flow associated with an eddy.

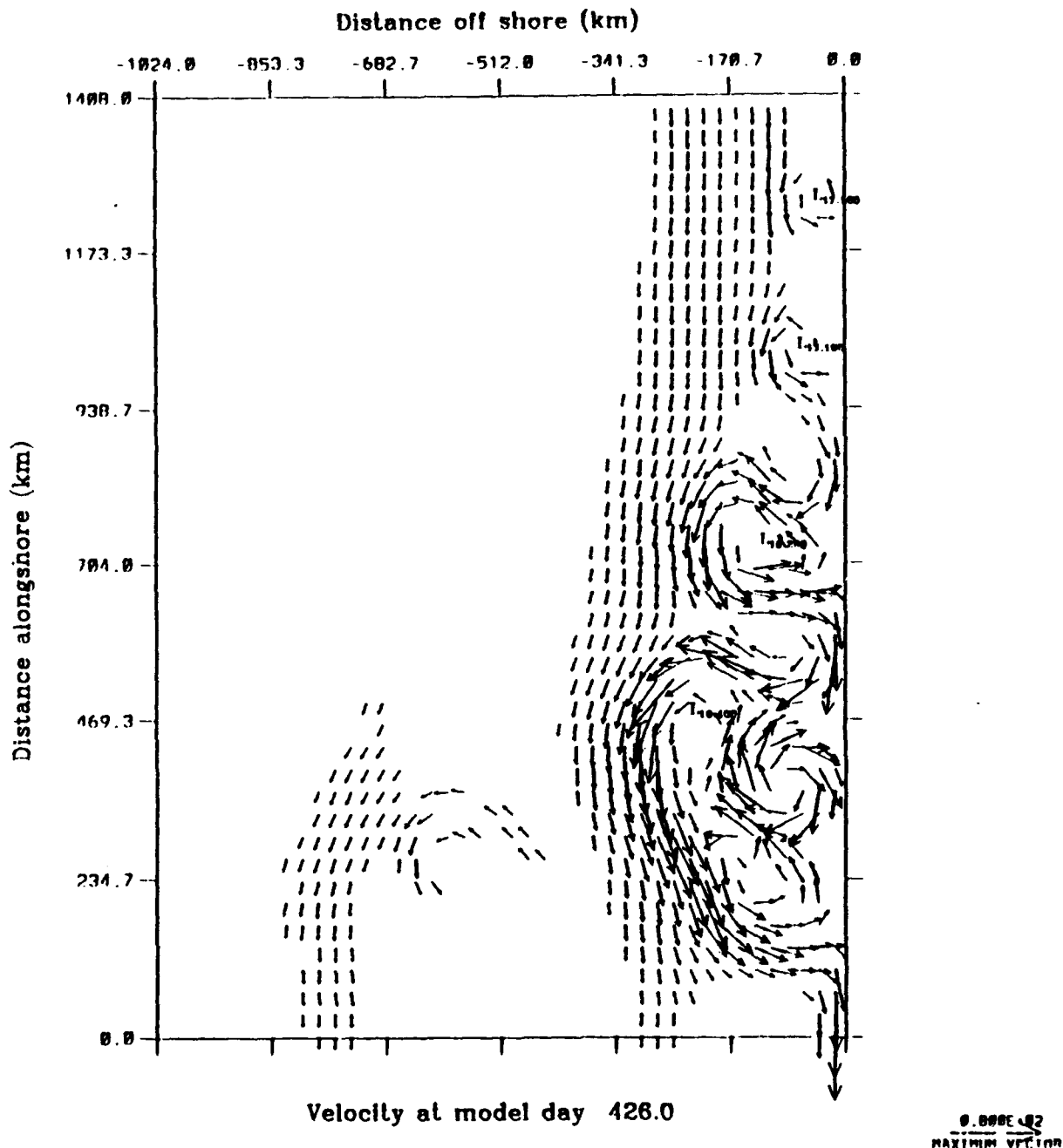
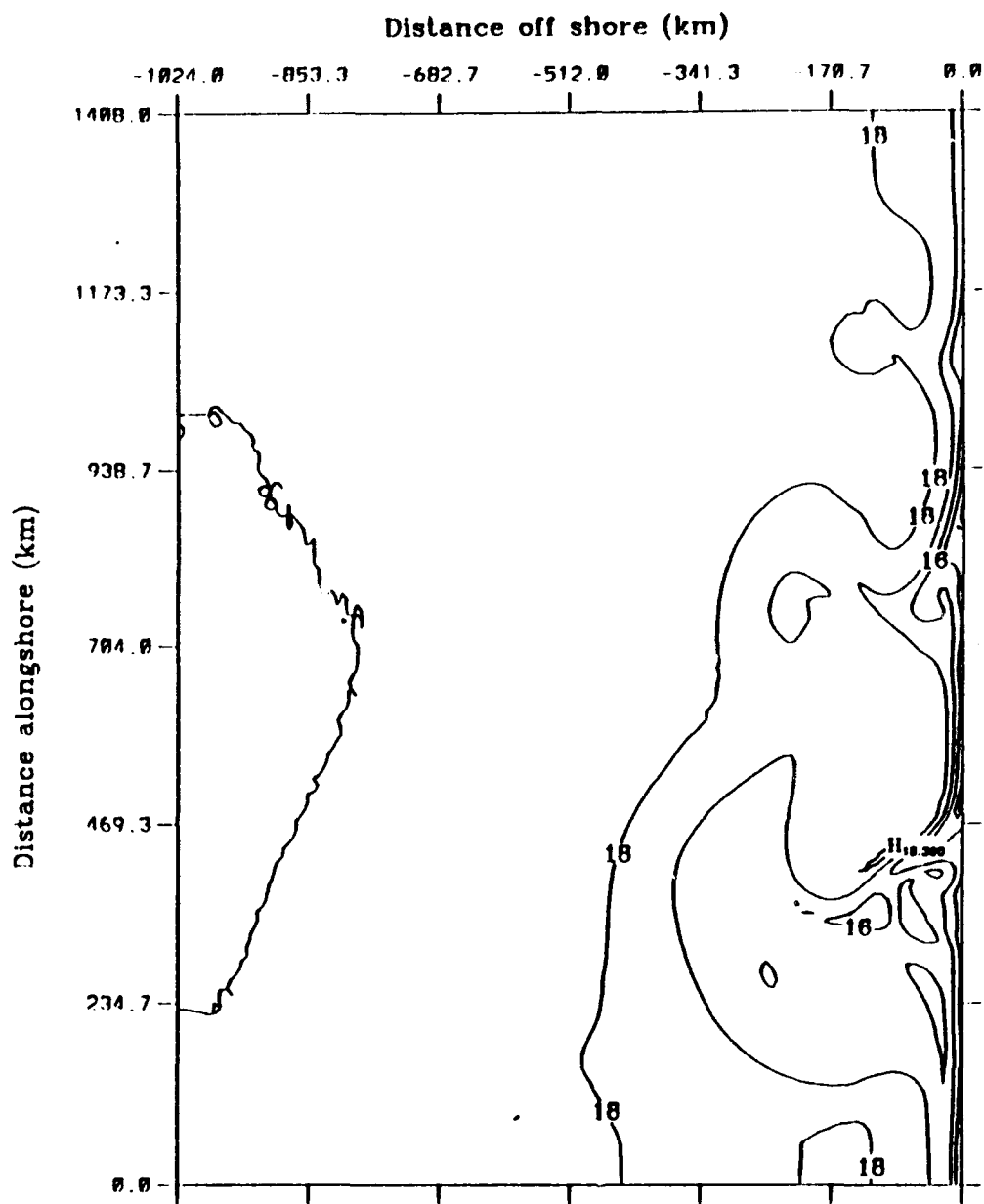


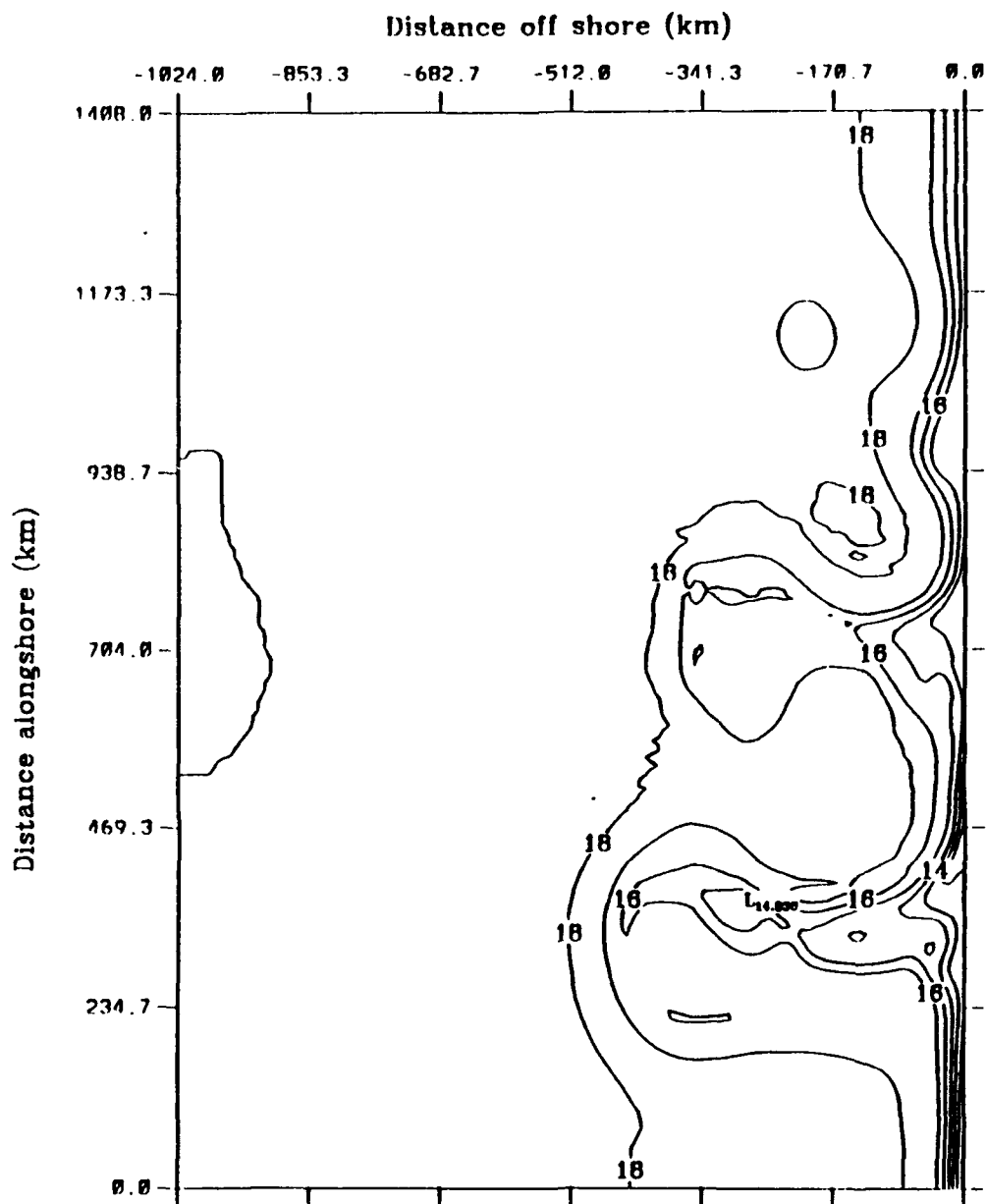
**Figure 4.53** Experiment 5: Surface velocity vectors at day 426 (yd 60). To avoid clutter, velocity vectors are plotted at every third grid point in both the cross-shore and alongshore direction, and velocities less than  $5 \text{ cm s}^{-1}$  are not plotted. The numbers associated with the lows embedded in the meanders and eddies along the coast correspond to temperature, not velocity.





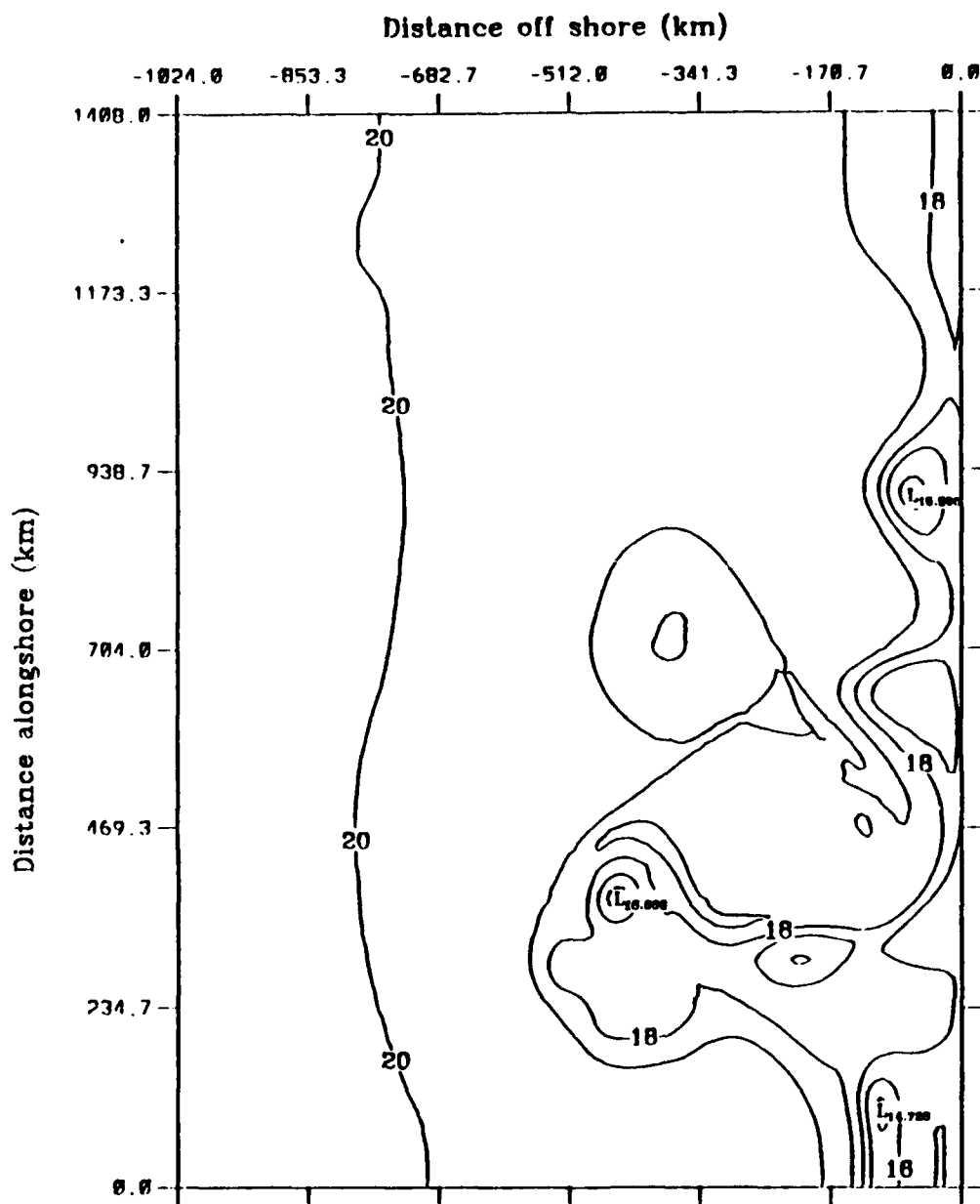
Temperature contour at model day 516.0

**Figure 4.54** Experiment 5: Surface temperature at day 516 (yd 150). The contour interval is  $1^{\circ}\text{C}$ . The temperature decreases towards the coast.



Temperature contour at model day 606.0

**Figure 4.55** Experiment 5: Surface temperature at day 606 (yd 240). The contour interval is  $1^{\circ}\text{C}$ . The temperature decreases towards the coast. Note maximum extent of upwelling.



Temperature contour at model day 696.0

**Figure 4.56** Experiment 5: Surface temperature at day 696 (yd 330). The contour interval is 1° C. The temperature decreases towards the coast. Note the disappearance of water cooler than 15° C.

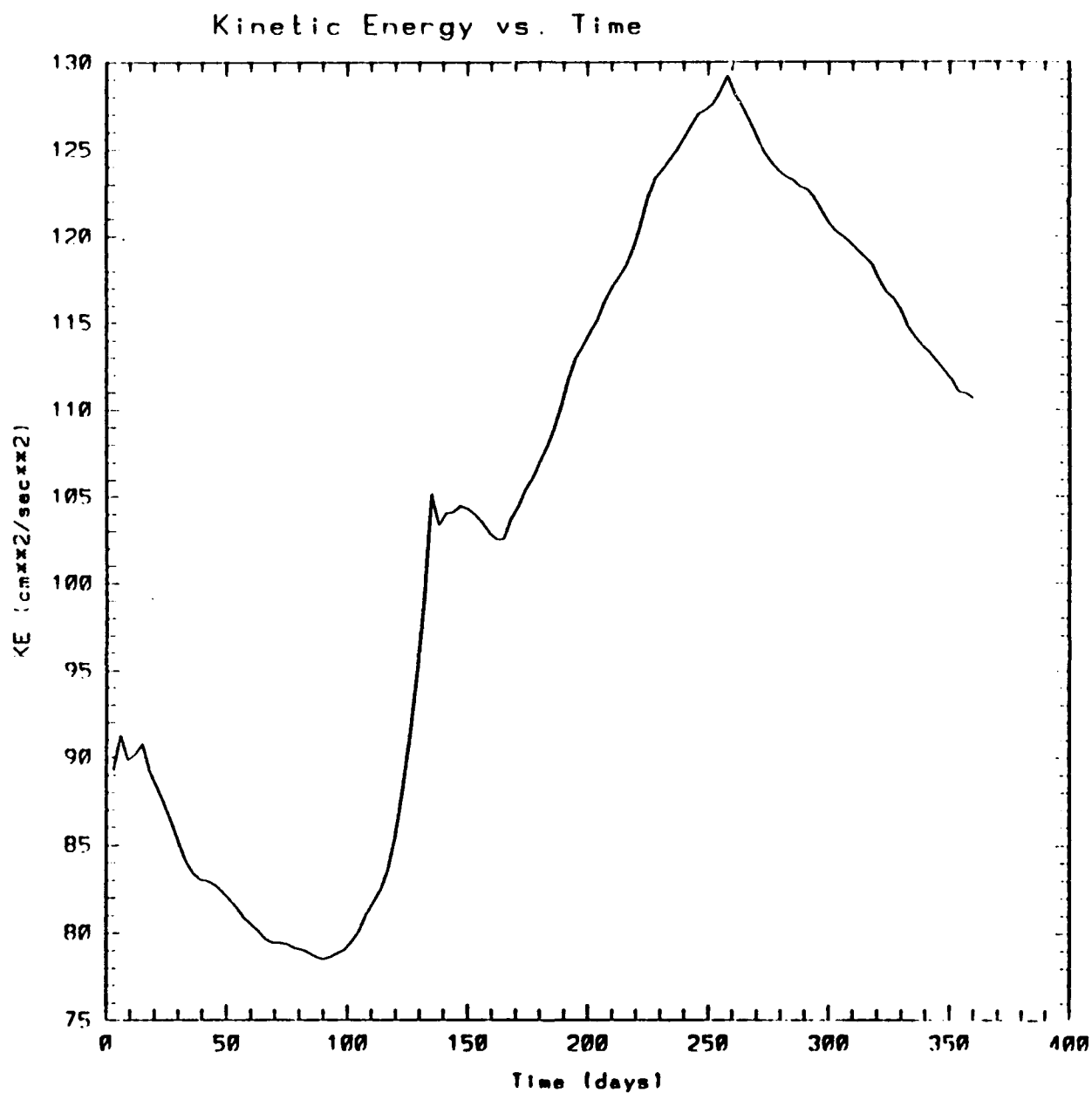


**Figure 4.57** Experiment 5: Total kinetic energy per unit mass time series for 1982 over the entire domain (Units of the kinetic energy are  $\text{cm}^2\text{s}^{-2}$ ). Quasi-steady periods: days 507-516 (yd 141-150), and 525-528 (yd 159-162).

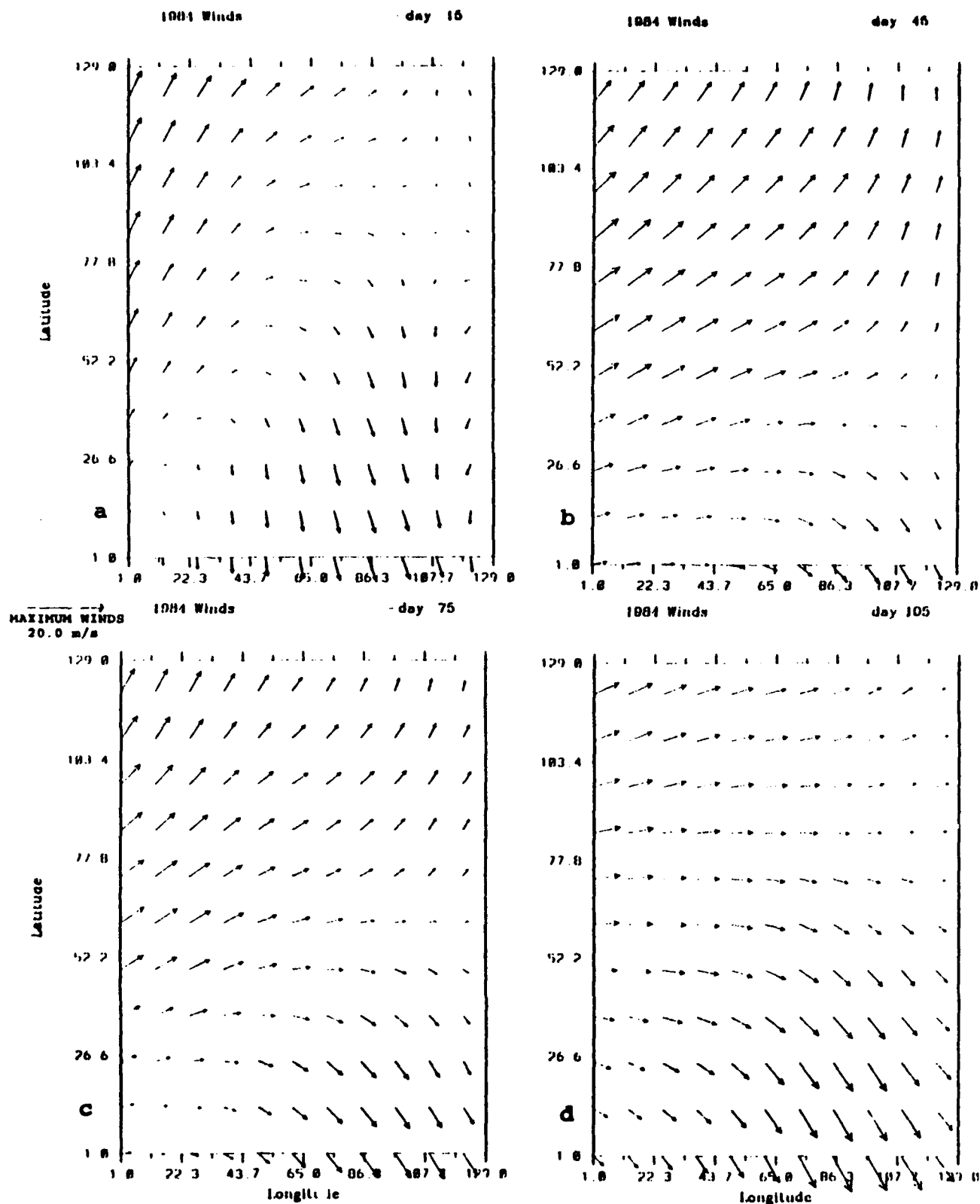


**Figure 4.58** Mid-monthly ECMWF winds for 1984 in  $\text{m s}^{-1}$ :  
 (a) January, (b) February, (c) March, (d) April, (e) May,  
 (f) June, (g) July, (h) August, (i) September, (j) October,  
 (k) November, and (l) December. The latitudinal grid point  
 1 (129) corresponds to  $35^\circ \text{N}$  ( $47.5^\circ \text{N}$ ); so that the  
 latitudinal grid point of 52 corresponds to  $40^\circ \text{N}$ . Maximum  
 wind vector is  $20 \text{ m s}^{-1}$ .

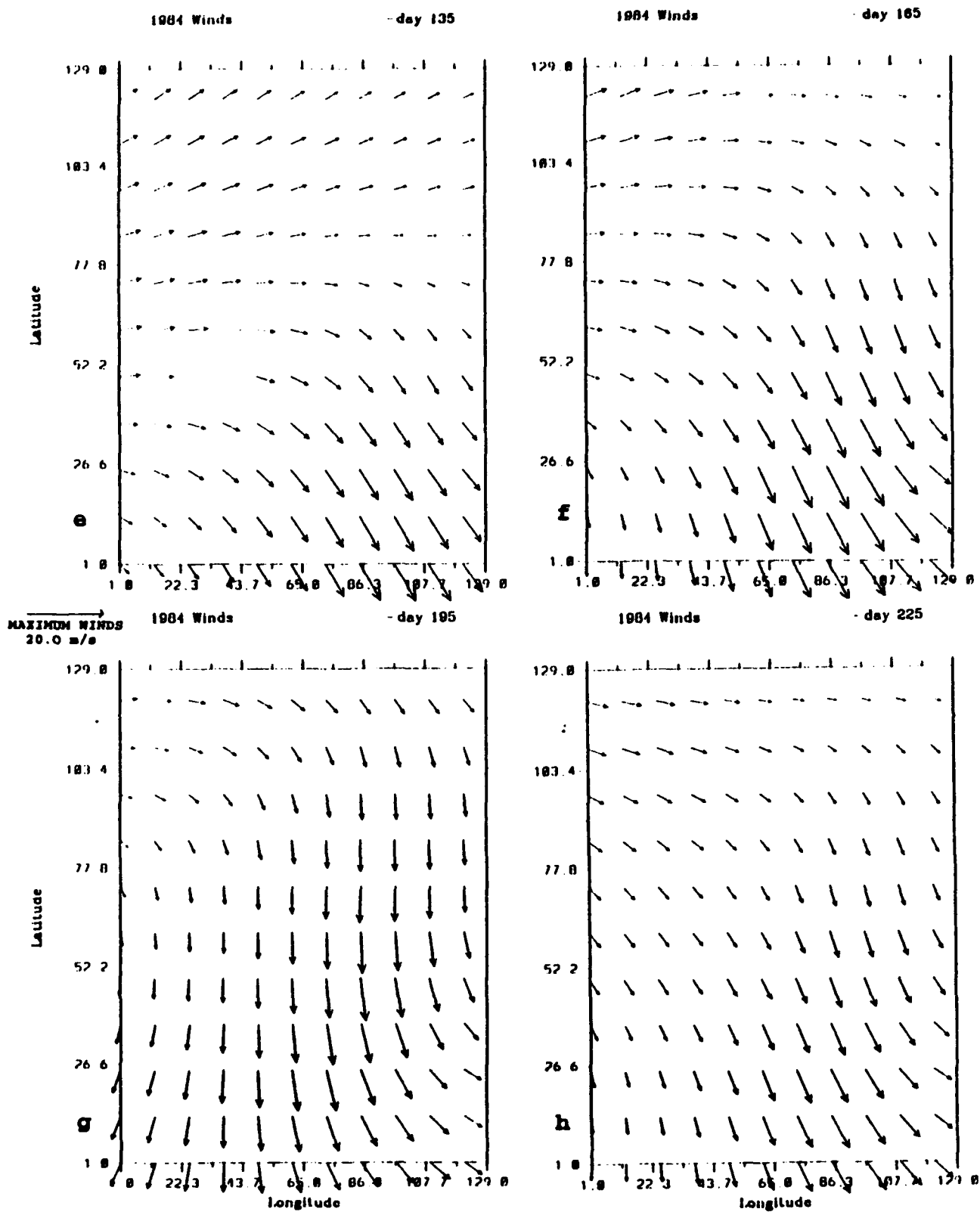


Figure 4.58 (continued).

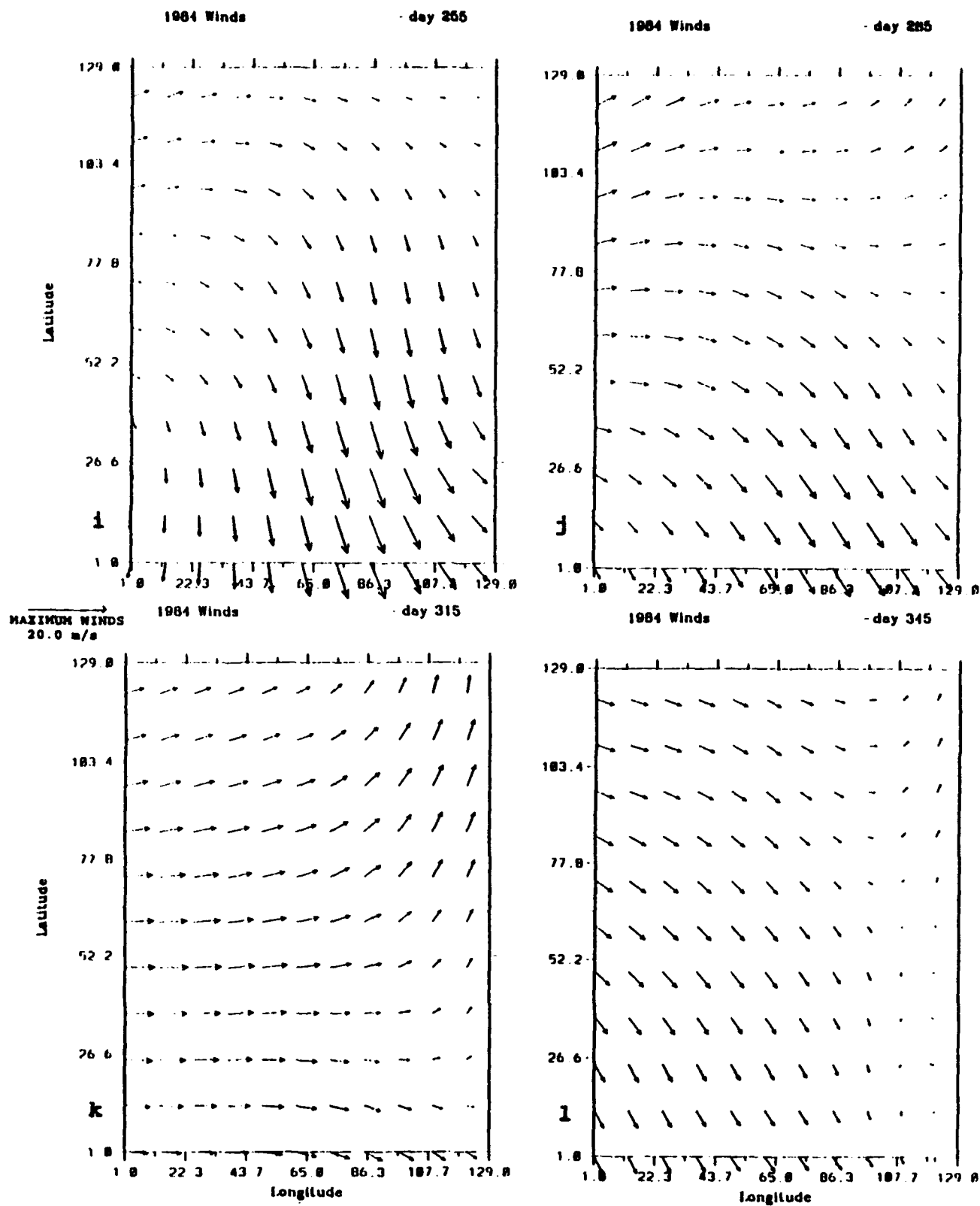
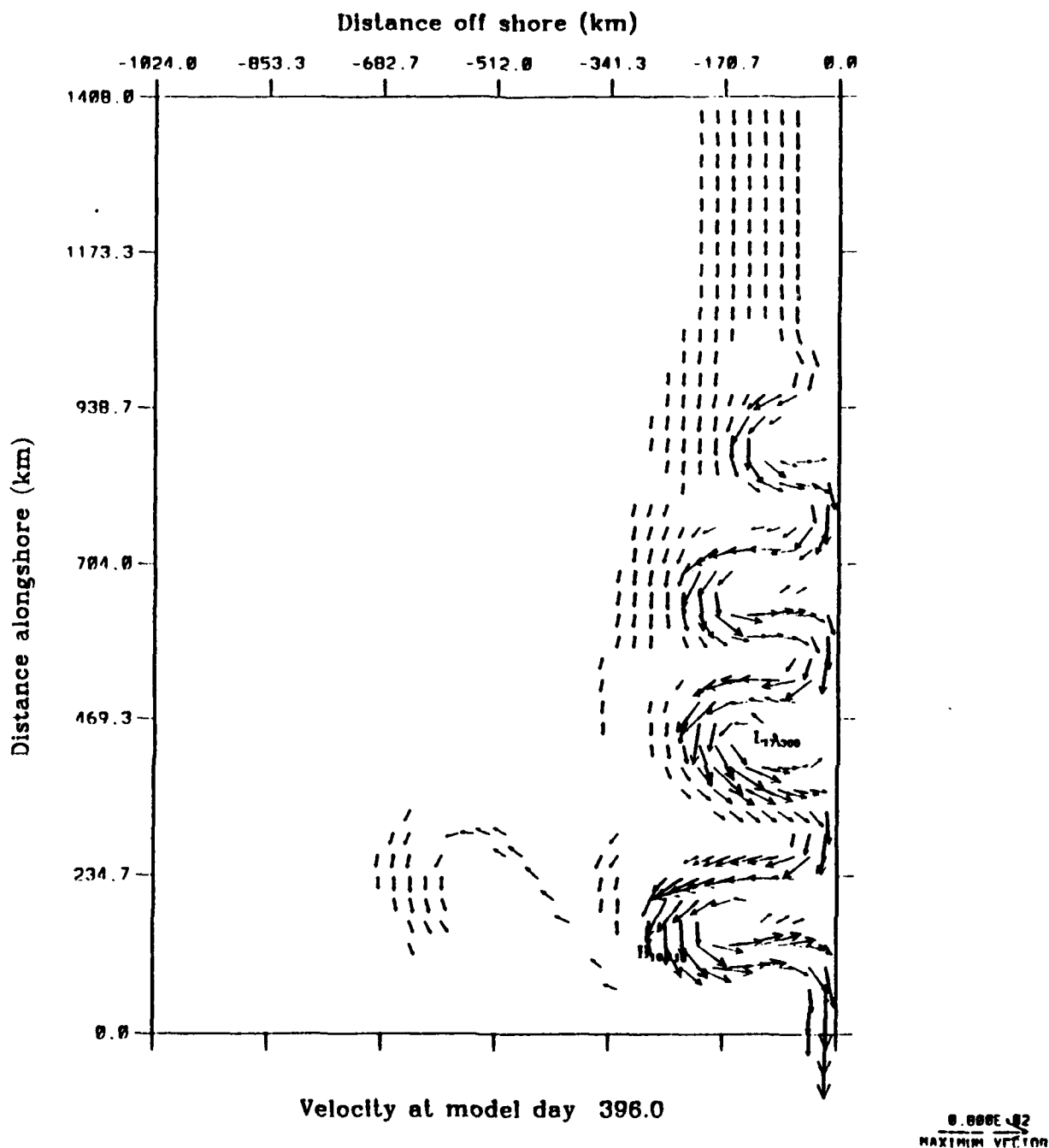


Figure 4.58 (continued).



**Figure 4.59** Experiment 6: Surface velocity vectors at day 396 (yd 30). To avoid clutter, velocity vectors are plotted at every third grid point in both the cross-shore and alongshore direction, and velocities less than  $5 \text{ cm s}^{-1}$  are not plotted. The numbers associated with the low and high embedded in the meanders and eddies along the coast correspond to temperature, not velocity. Note equatorward surface flow with embedded meanders and eddies.





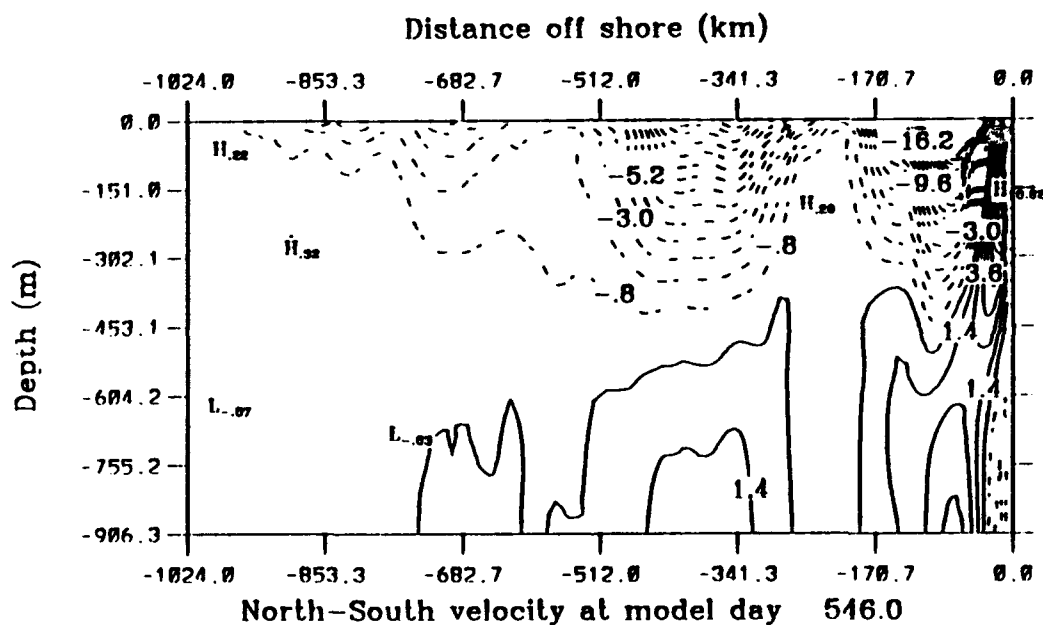


**Figure 4.61** Experiment 6: Cross-section at  $y \sim 704$  km ( $41.25^\circ$  N) of the meridional component of velocity at day 546 (yd 180). Dashed lines indicate equatorward flow, while solid lines indicate poleward flow. Note existence of poleward undercurrent.

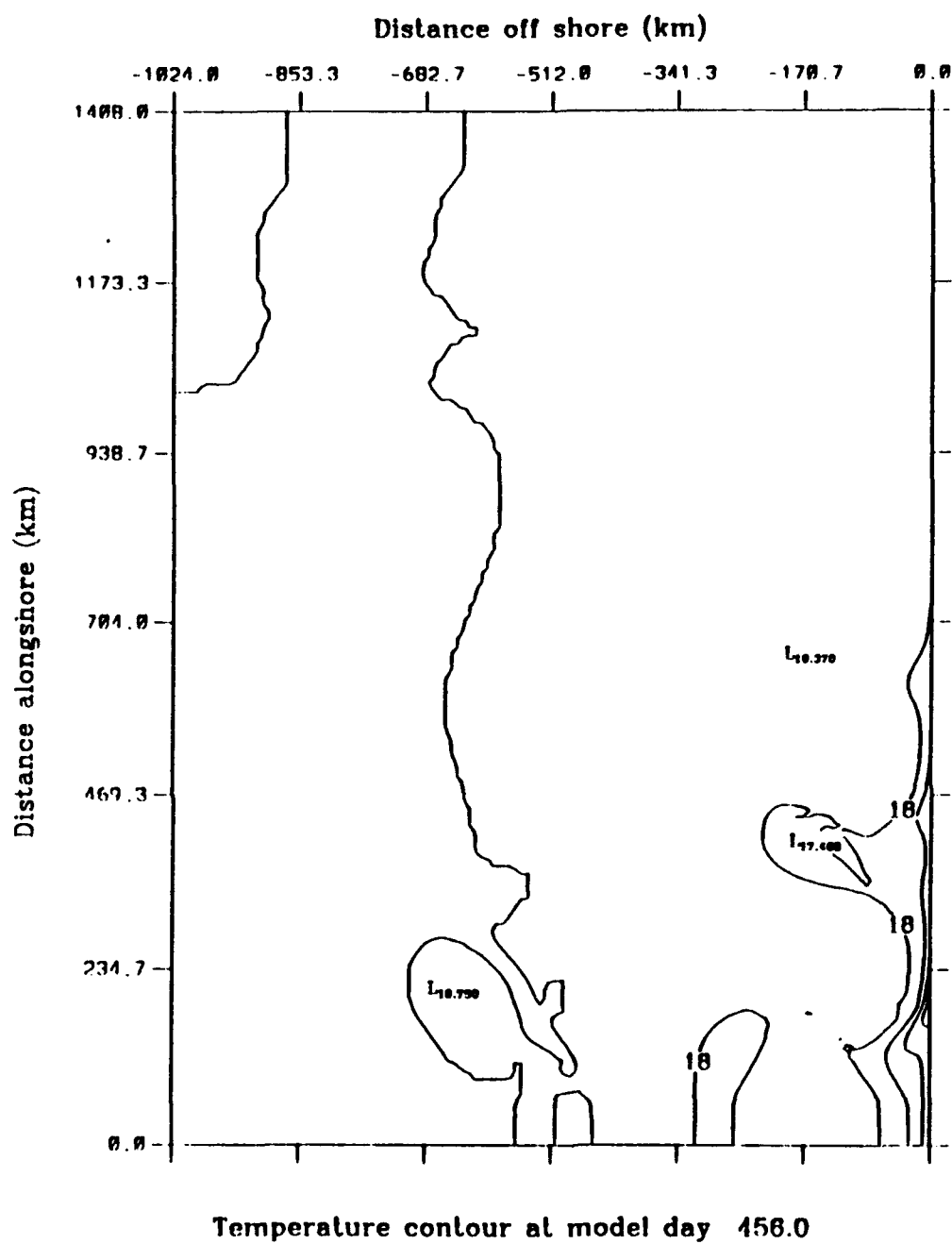


**Figure 4.62** Experiment 6: Surface temperature at day 456 (yd 90). The contour interval is 1° C. The temperature decreases towards the coast. Note start of upwelling.

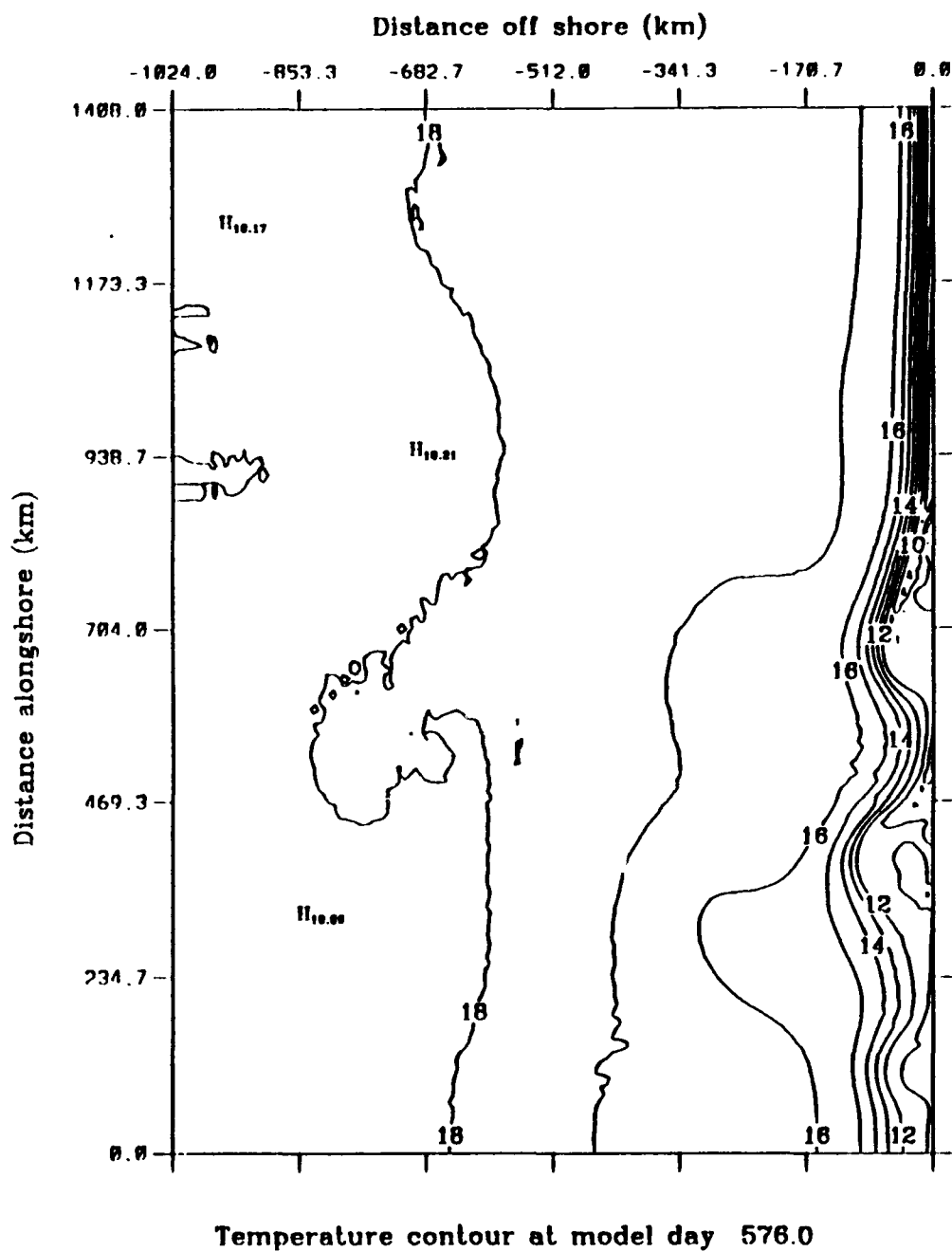


**Figure 4.63** Experiment 6: Surface temperature at day 576 (yd 210). The contour interval is  $1^{\circ}\text{C}$ . The temperature decreases towards the coast. Note maximum extent of upwelling.

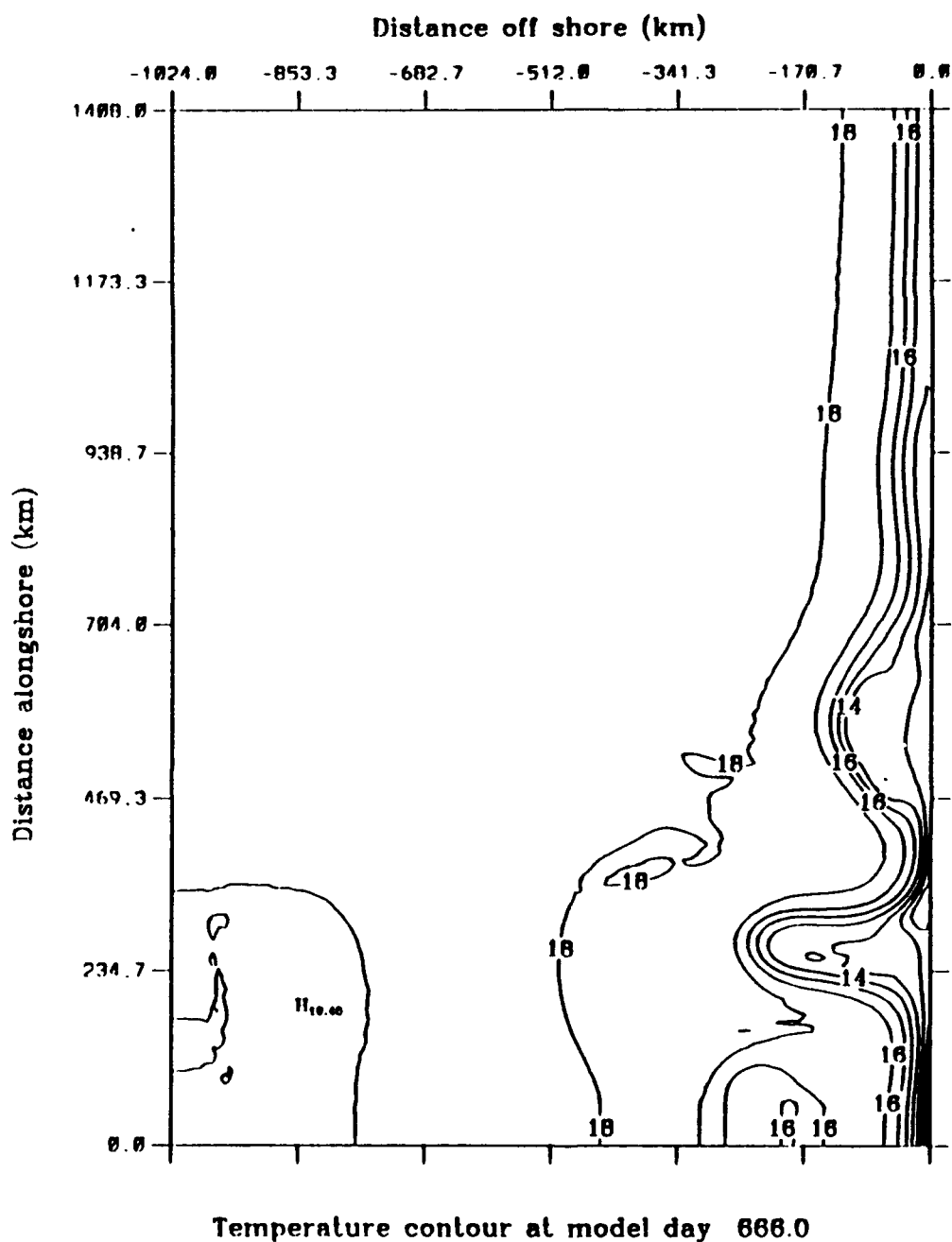


**Figure 4.64** Experiment 6: Surface temperature at day 666 (yd 300). The contour interval is  $1^{\circ}\text{C}$ . The temperature decreases towards the coast. Note occurrence of filament at  $y \sim 250\text{ km}$ .

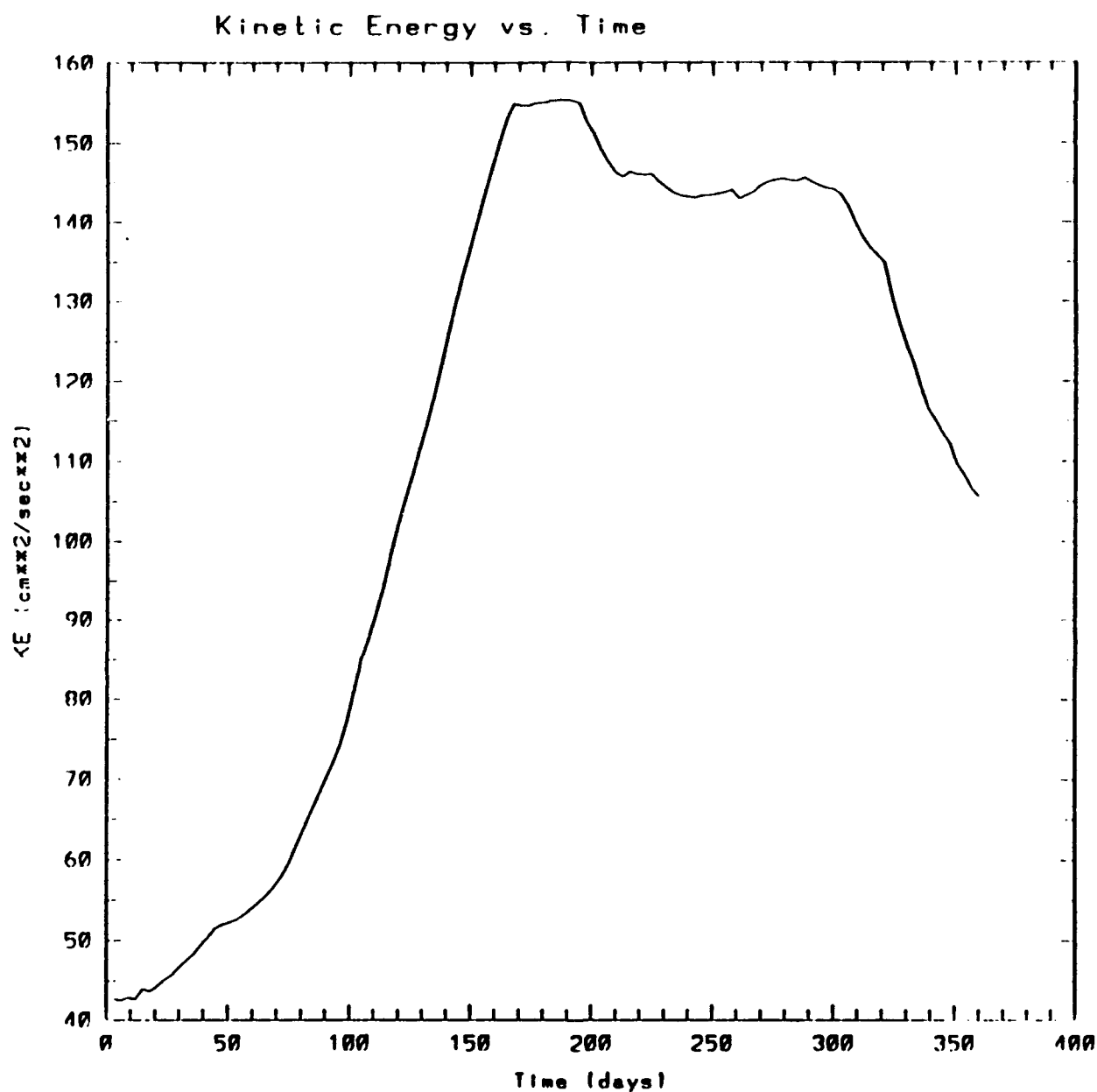


**Figure 4.65** Experiment 6: Total kinetic energy per unit mass time series for 1984 over the entire domain (Units of the kinetic energy are  $\text{cm}^2\text{s}^{-2}$ ). Quasi-steady periods: days 576-591 (yd 210-225), 606-624 (yd 240-258), and 645-657 (yd 279-291).

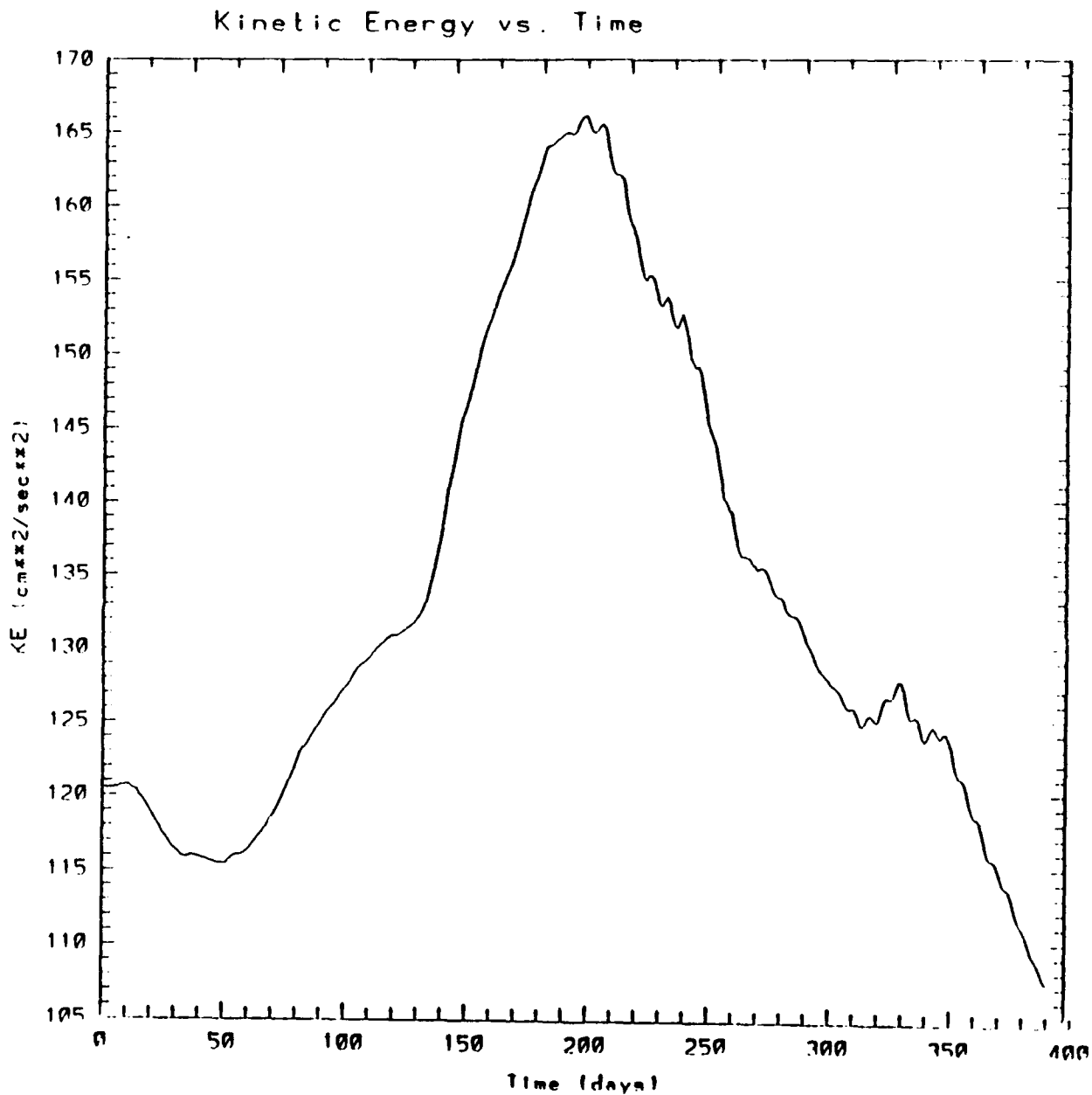


**Figure 4.66** Experiment 7: Total kinetic energy per unit mass time series for Climo III over the entire domain (Units of the kinetic energy are  $\text{cm}^2\text{s}^{-2}$ ). Peak value of  $166 \text{ cm}^2\text{s}^{-2}$  at day 915 (yd 185).

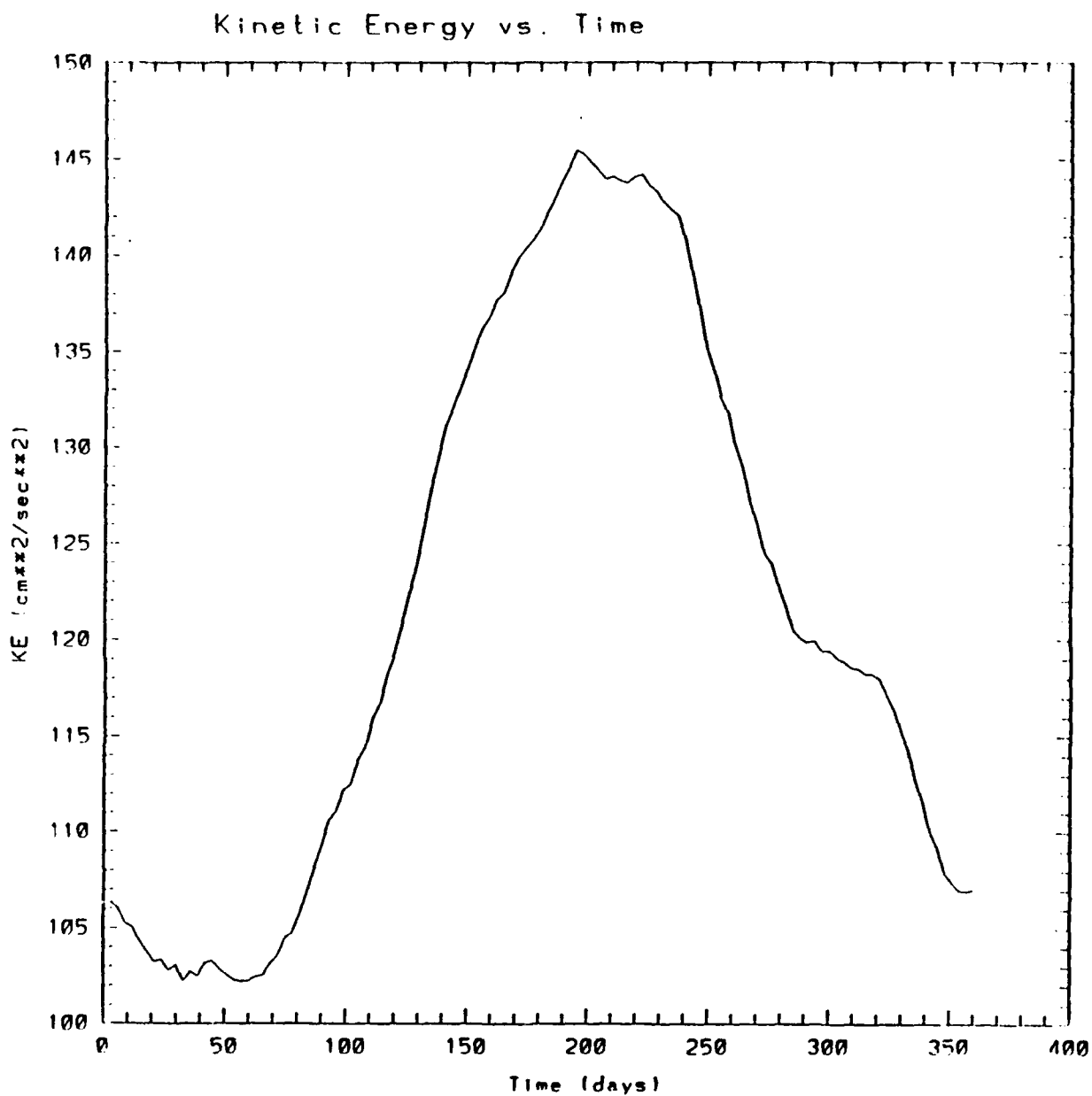


**Figure 4.67** Experiment 7: Total kinetic energy per unit mass time series for Climo IV over the entire domain (Units of the kinetic energy are  $\text{cm}^2\text{s}^{-2}$ ). Peak value of  $145 \text{ cm}^2\text{s}^{-2}$  at day 1293 (yd 198).



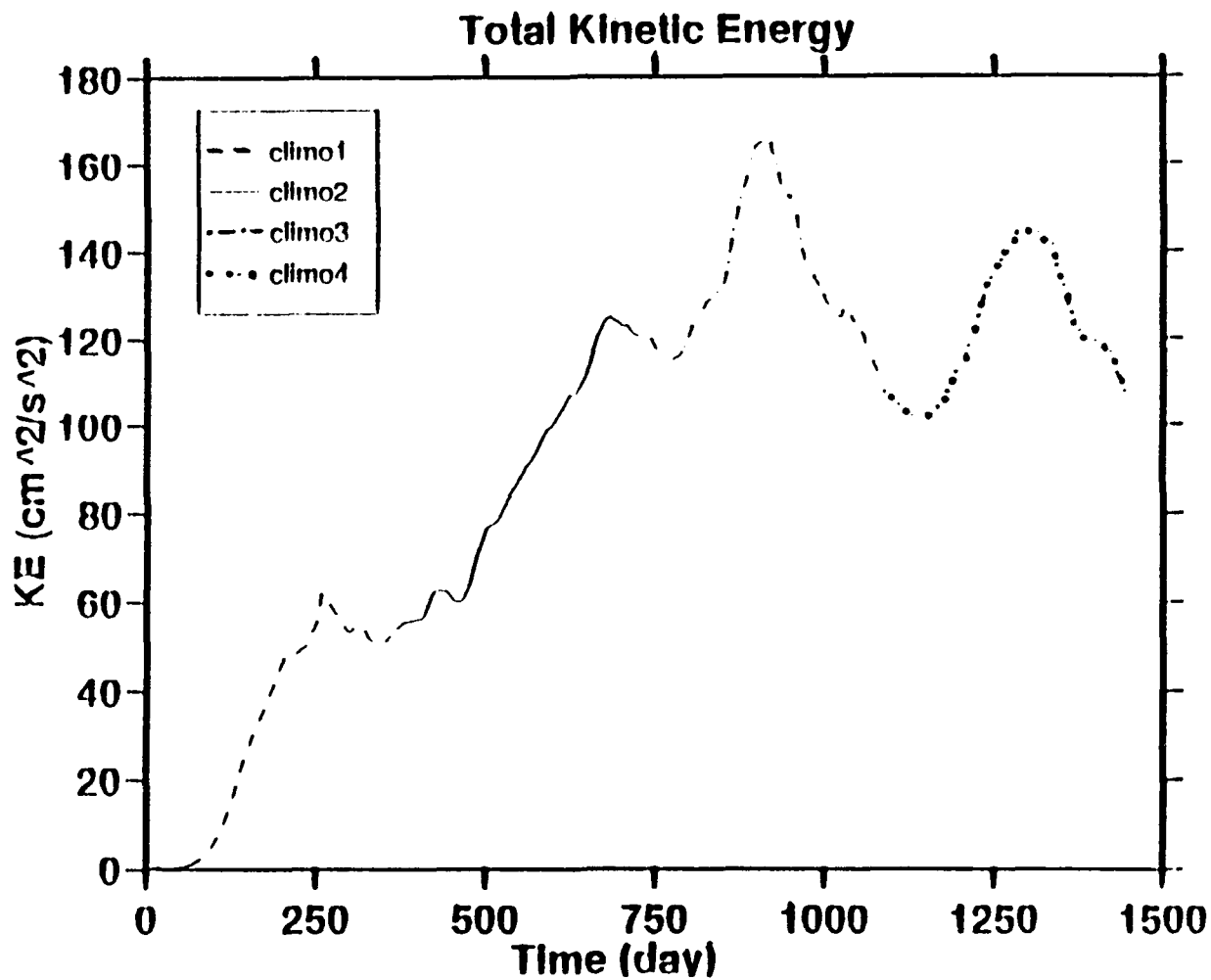


**Figure 4.68** Experiment 7: Total kinetic energy per unit mass time series for Climo, Climo II, Climo III, and Climo IV over the entire domain (Units of the kinetic energy are  $\text{cm}^2\text{s}^{-2}$ ).

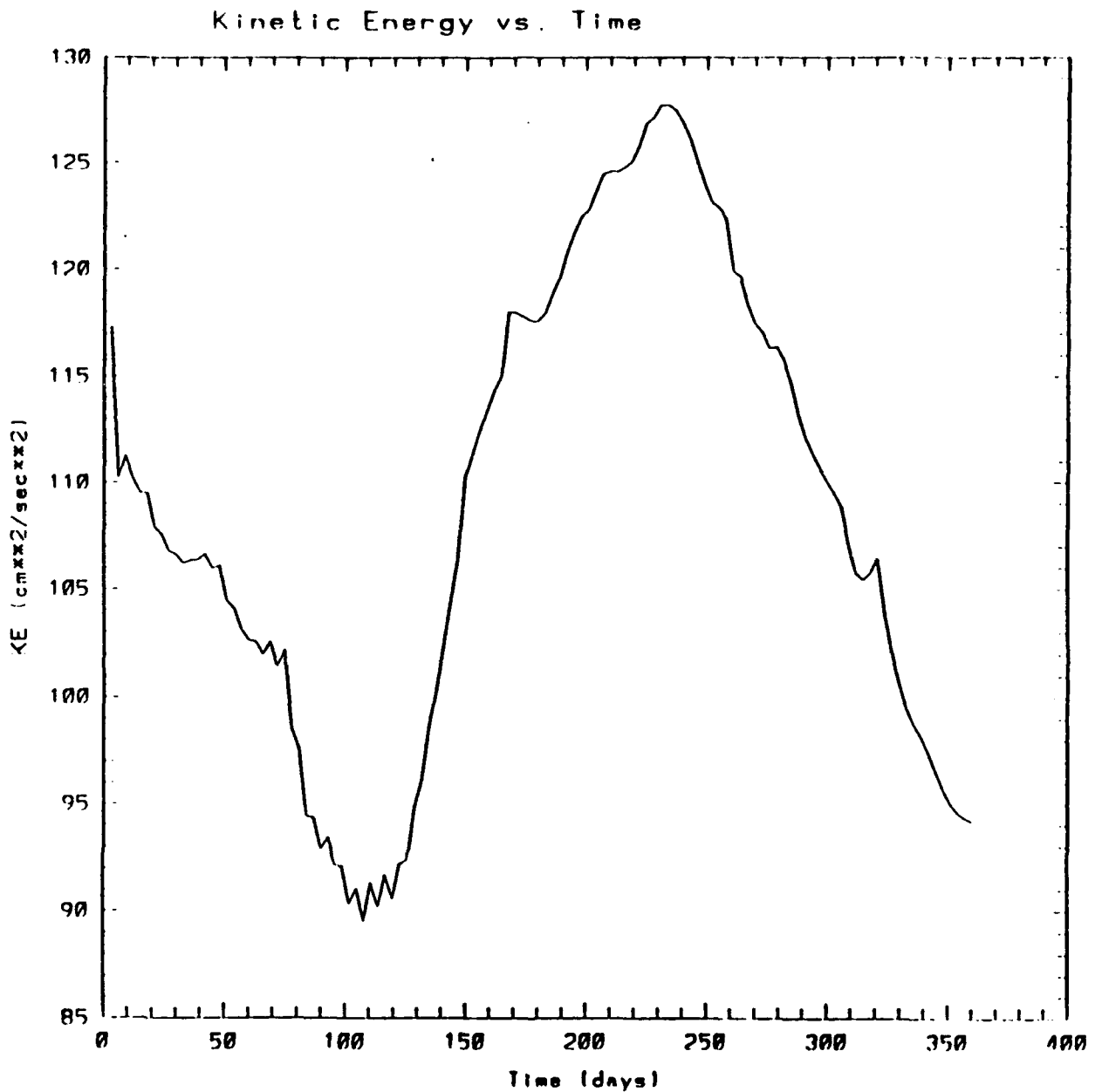


**Figure 4.69** Experiment 8: Total kinetic energy per unit mass time series for 1983 over the entire domain (Units of the kinetic energy are  $cm^2s^{-2}$ ). Peak value of  $128 cm^2s^{-2}$  at day 963 (yd 233).

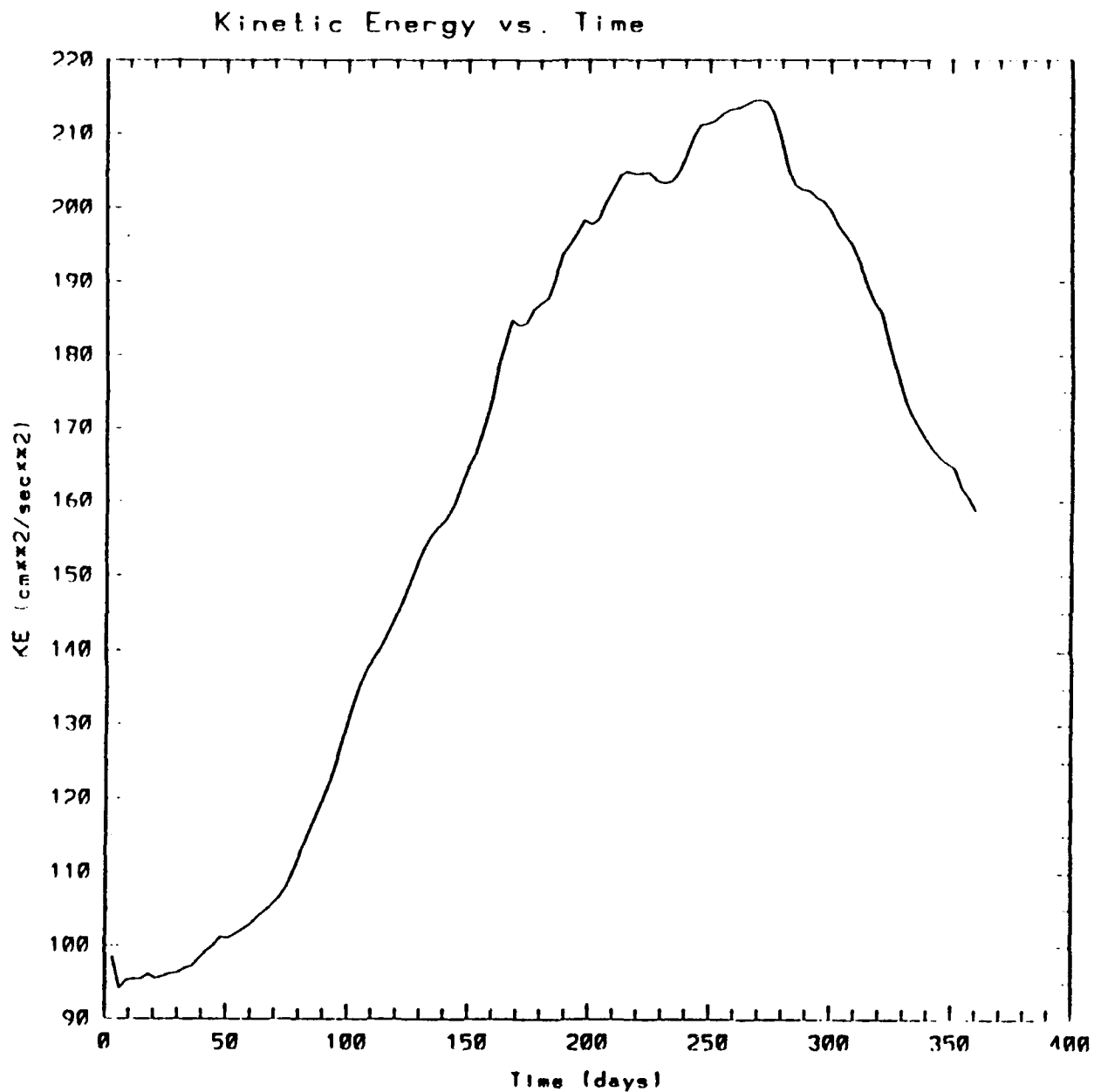


**Figure 4.70** Experiment 8: Total kinetic energy per unit mass time series for 1984 over the entire domain (Units of the kinetic energy are  $\text{cm}^2\text{s}^{-2}$ ). Peak value of  $215 \text{ cm}^2\text{s}^{-2}$  at day 1368 (yd 273).

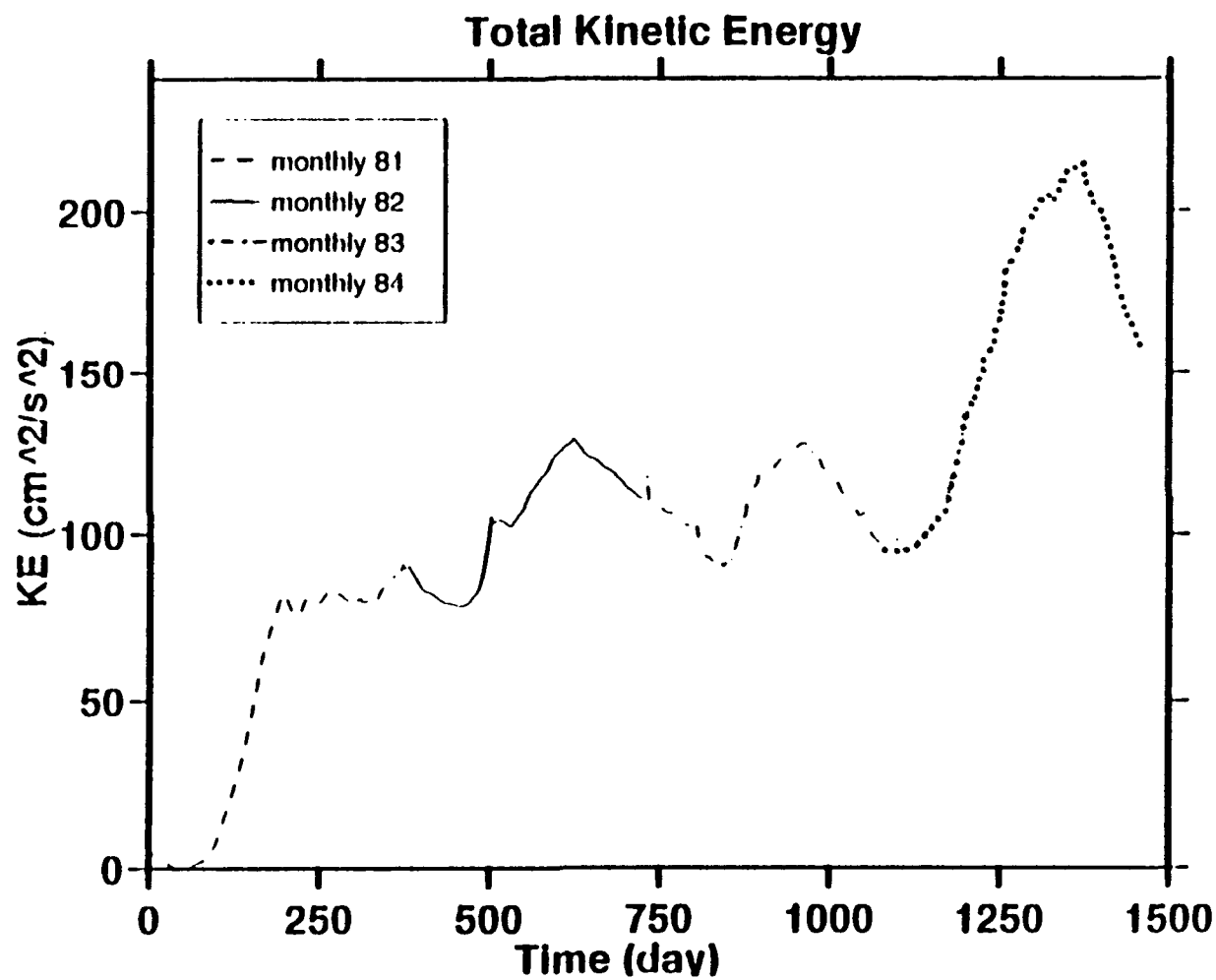


Figure 4.71 Experiment 8: Total kinetic energy per unit mass time series for 1981, 1982, 1983, and 1984 over the entire domain (Units of the kinetic energy are  $\text{cm}^2\text{s}^{-2}$ ).

## V. SUMMARY AND RECOMMENDATIONS

### A. SUMMARY

The different experiment runs are summarized in Tables 4.2, 4.4, and 4.5. In all first year runs (see Table 4.2), both a surface equatorward current and a poleward undercurrent developed. There was also a poleward coastal surface current present during the winter season. Upwelling was a seasonal feature which, as expected, had the coolest temperatures during a non-El Niño year (1981) and warmest temperatures during an El Niño year (1983). Both meanders and eddies were generated. The eddies were cold core, cyclonic, and had a size around the Rossby radius of deformation (30 km). Along with an equatorward surface current, both meanders and eddies remained at the end of each year. Instability analyses revealed that both barotropic and baroclinic processes were important eddy generation mechanisms. In all first year runs, no filaments were observed.

The follow-on (second year) model runs are summarized in Table 4.4. In general, a weak coastal poleward surface current was evident during the winter season in the northern region of the domain for all years (Climo II, 1982 and 1984). A meandering equatorward surface current, already

present, at the start of these experiments was maintained. A poleward undercurrent was generated in all experiments. The eddies, already present at the start of the experiments, were both cold core, cyclonic, and warm core, anticyclonic eddies in Climo II and 1982, while in 1984 there were only cold core, cyclonic eddies. The size and offshore extent of the eddies were consistent with the first experimental runs. Seasonal upwelling occurred with minimum temperatures of  $\sim 12^{\circ}\text{C}$  for Climo II and 1982, and of  $\sim 10^{\circ}\text{C}$  for 1984. The year 1984 had the largest extent of cool upwelled water as expected for a year with the strongest equatorward winds. Filaments developed in all three experiments, but was most pronounced (as expected) in 1984. The filaments had an offshore extent between 200 and 350 km. Instability analyses revealed that both barotropic and baroclinic processes were involved in eddy generation.

The last two years of the extended (four year) runs are summarized in Table 4.5. Listed here are Climo IV, 1983, and 1984. Similar results are obtained: A poleward coastal surface current, a surface equatorward current, a poleward undercurrent, along with embedded meanders and eddies. Of interest, upwelling occurs later in 1983 (at yd 150) than for the other years (yd 60 to yd 90). Although the minimum temperature is the same ( $11.0^{\circ}\text{C}$ ) for all years, 1984 experienced a larger area of cooler water (all along the coast) than that of the El Niño (1983) year. In all

experiments, there were both cold and warm core eddies. Finally, filaments were observed during Climo IV and 1984, but not during 1983.

Experiments 1 through 6 investigated the formation or generation of features such as currents, meanders, eddies, and filaments. In Experiments 7 and 8 a quasi-steady equilibrium state for the CCS was reached and the features observed to develop in previous years were maintained.

Figure 5.1 plots the mean, eddy, and total kinetic energy per unit mass for Climo, 1981, and 1983 (Experiments 1 - 3) together. During these first generation years, Figure 5.1a shows 1981 had the most total kinetic energy and 1983 (El Niño year) the least. This also holds true for both the mean and eddy kinetic energy per unit mass plots (Figures 5.1b and 5.1c). The decrease in kinetic energy (total and mean) during the last few days of 1983 is not an error, but rather an adjustment for continuation with the start of the 1984 kinetic energy plots.

Figure 5.2 plots the mean, eddy, and total kinetic energy per unit mass for Climo II, 1982, and 1984 (Experiments 4 - 6) together (the second years of generation). The largest values of total, mean, and eddy kinetic energy were observed during 1984 (Figure 5.2a through 5.2c). Climo II had the least total and eddy kinetic energy (Figures 5.2a and 5.2c), but both Climo II

and 1982 had nearly identical low mean kinetic energy (Figure 5.2b).

In all experiments, the atmospheric pressure cycle and subsequent movement of low and high pressure patterns affected the wind orientation and strength over the model domain. The surface current was observed to respond to the prevailing wind direction. As the wind turned equatorward and exerted stress on the water surface, Ekman transport offshore resulted in the upwelling of cooler water along the coast. Interannual variability was thus observed as expected.

In conclusion, the experiments showed that, due to the wind forcing, features such as currents, meanders, eddies and filaments could be generated and maintained. These results support the hypothesis that wind forcing is a very important mechanism for the generation of many of the observed features in the CCS.

#### **B. COMPARISON WITH OBSERVATIONS DURING AN EL NIÑO YEAR**

It has been shown that the model results qualitatively agree with available observations of the CCS during non-El Niño years. For example, the simulated surface and subsurface currents, along with eddies and filaments agree in size and magnitude with available observations of the CCS, as listed in Batteen et al. (1989).



Here the focus is shifted to comparisons of observed and model results during an El Niño year. Qualitative results from both of the El Niño experiments (3 and 8) along with some observations taken in the CCS during the 1983 El Niño are presented in Table 5.1. Because the model does not include remote forcing, the oceanic teleconnection will not be expressed in the model results. There is still good agreement between the model and observations taken during the 1983 El Niño within the model domain. In particular, warmer sea surface temperatures along with onshore advection are evident, especially during the first three months of the year. Poleward surface flow (for example Figure 5.3) is enhanced and the entire current system appears weaker than in the other model years. Based on these results, it is concluded that atmospheric forcing played a substantial role in the anomalous conditions observed in the CCS during the El Niño of 1983.

#### **C. NAVAL RELEVANCE**

As the Navy focus has recently shifted from blue water to the littoral, EBC models such as the one used here take on an increased importance. Although this EBC model would require a finer scale before it could be used to predict the location of features of interest, it is a start in the right direction.

Accurately predicting the location of meanders, eddies and regions of upwelling becomes critical for the successful use of mines, along with aviation, amphibious, and covert swimmer operations. The meanders and eddies could impact several aspects of mining (i.e., laying, known position, and mine removal). Smaller amphibious craft could get swept off course if caught up in a strong jet associated with a meander. The cold upwelled water may be nutrient rich and support a plankton bloom which could significantly reduce visibility in the water. In addition, the colder water adversely affects swimmer immersion times.

Fog often results in upwelling regions where warmer air is present over the cooler upwelled water. The effect of this fog is to reduce surface visibility, which could be a plus (such as to provide cover for an amphibious landing) or minus (such as when defending an area against covert operations). This decreased visibility may also affect aviation operations by requiring instrument flight rules (IFR) vice visual flight rules (VFR). Finally, other optical and infrared devices will be degraded by the presence of increased moisture in the atmosphere (i.e., fog).

#### **D. RECOMMENDATIONS**

Future studies should let the model run for multiple years, to allow for spin-up. As seen in multiple year

kinetic energy per unit mass time series plots, it appears that spin-up may take only three to four years, but this needs to be confirmed. Additional studies should use daily rather than monthly winds to examine the effects of events and relaxations. The incorporation of bottom topography and a more realistic coastline would allow preferred eddy generation areas to be identified. The incorporation of bottom topography could also lead to an even better depiction of the undercurrent, which plays an important role in eddy generation. Finally, finer horizontal and vertical resolution should be incorporated into the model to aid in more accurately predicting the location of meanders, eddies, and filaments.

TABLE 5.1 COMPARISON OF OBSERVED AND MODEL RESULTS DURING AN EL NIÑO YEAR (1983).

El Niño (1983) observations in CCS compared to mean	Experiment 3 (1983 cold restart)	Experiment 8 (1983 extended run)
Warmer SST (1, 2, 3)	Simulated	Simulated
Weaker overall current system (2)	Simulated	Simulated
Enhanced poleward flow (2, 3)	Simulated	Simulated
Enhanced onshore advection (1, 2, 3)	Simulated	Simulated
Maximum equatorward surface current farther offshore (2)	Simulated	Simulated

References: (1) Rienecker and Mooers (1986)  
(2) Simpson (1983)  
(3) Simpson (1984)

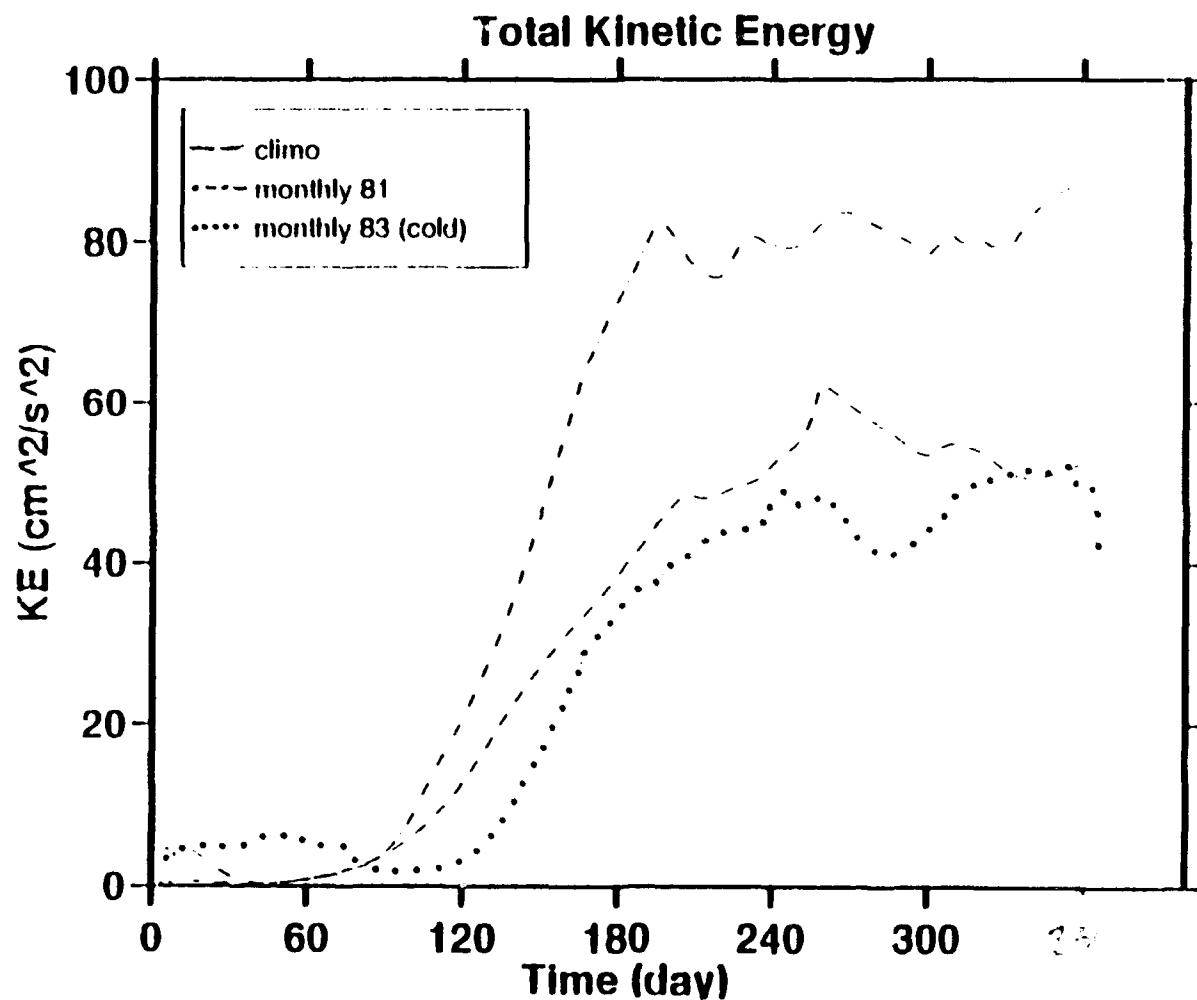


**Figure 5.1a** Experiments 1-3: Total kinetic energy per unit mass time series for climatology (1980-1989), 1981, and 1983 over the entire domain (Units of the kinetic energy are  $\text{cm}^2\text{s}^{-2}$ ).

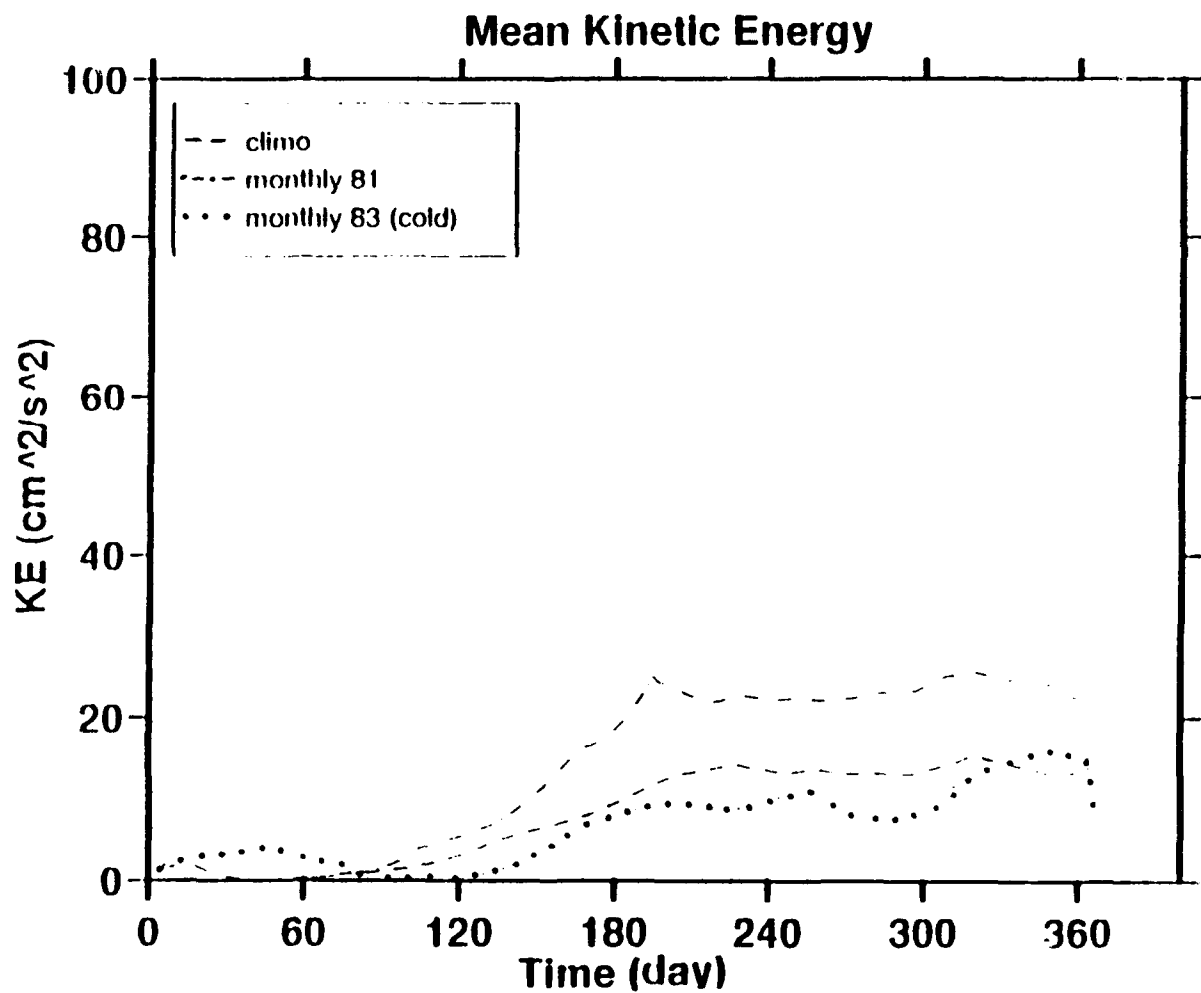
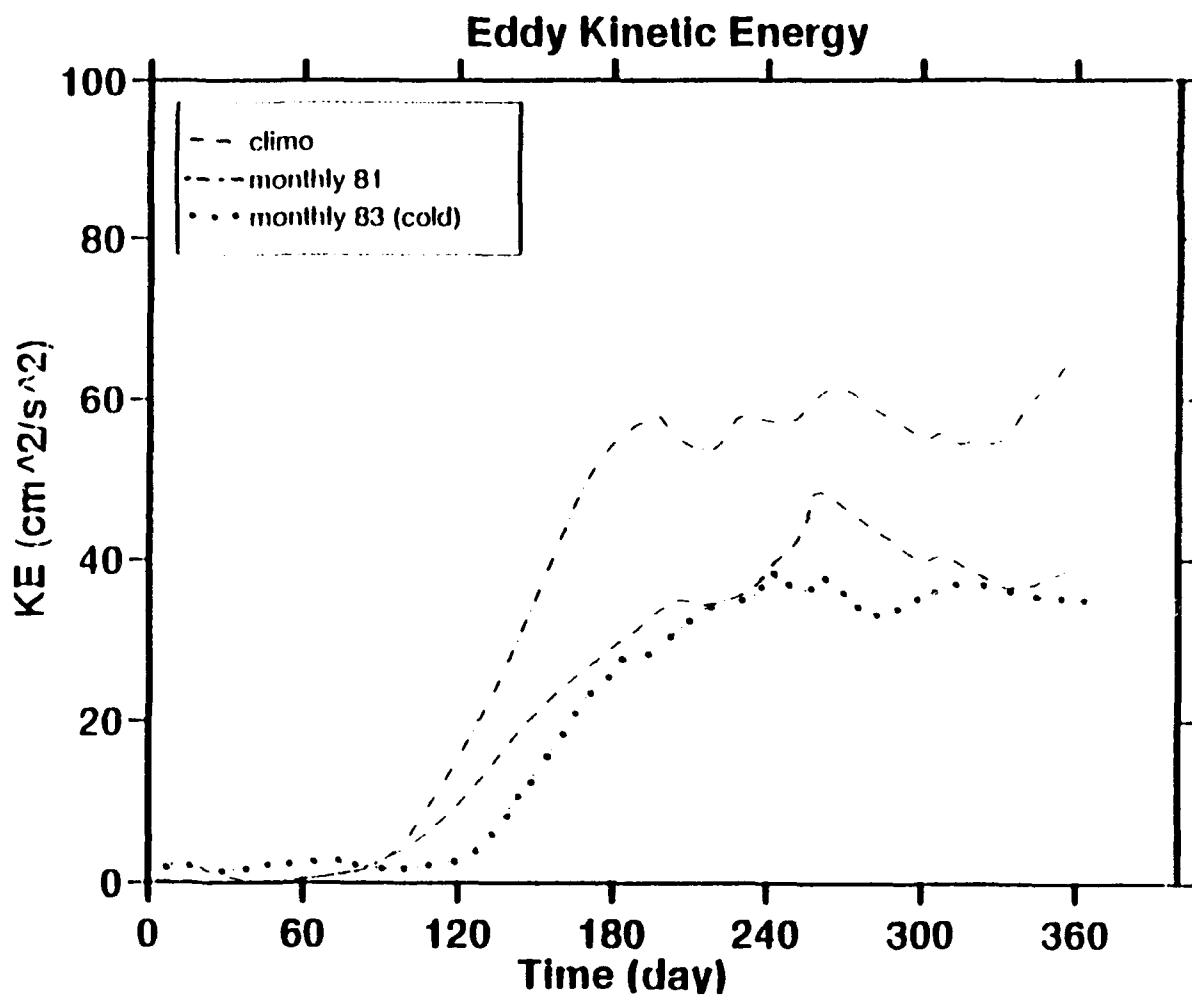
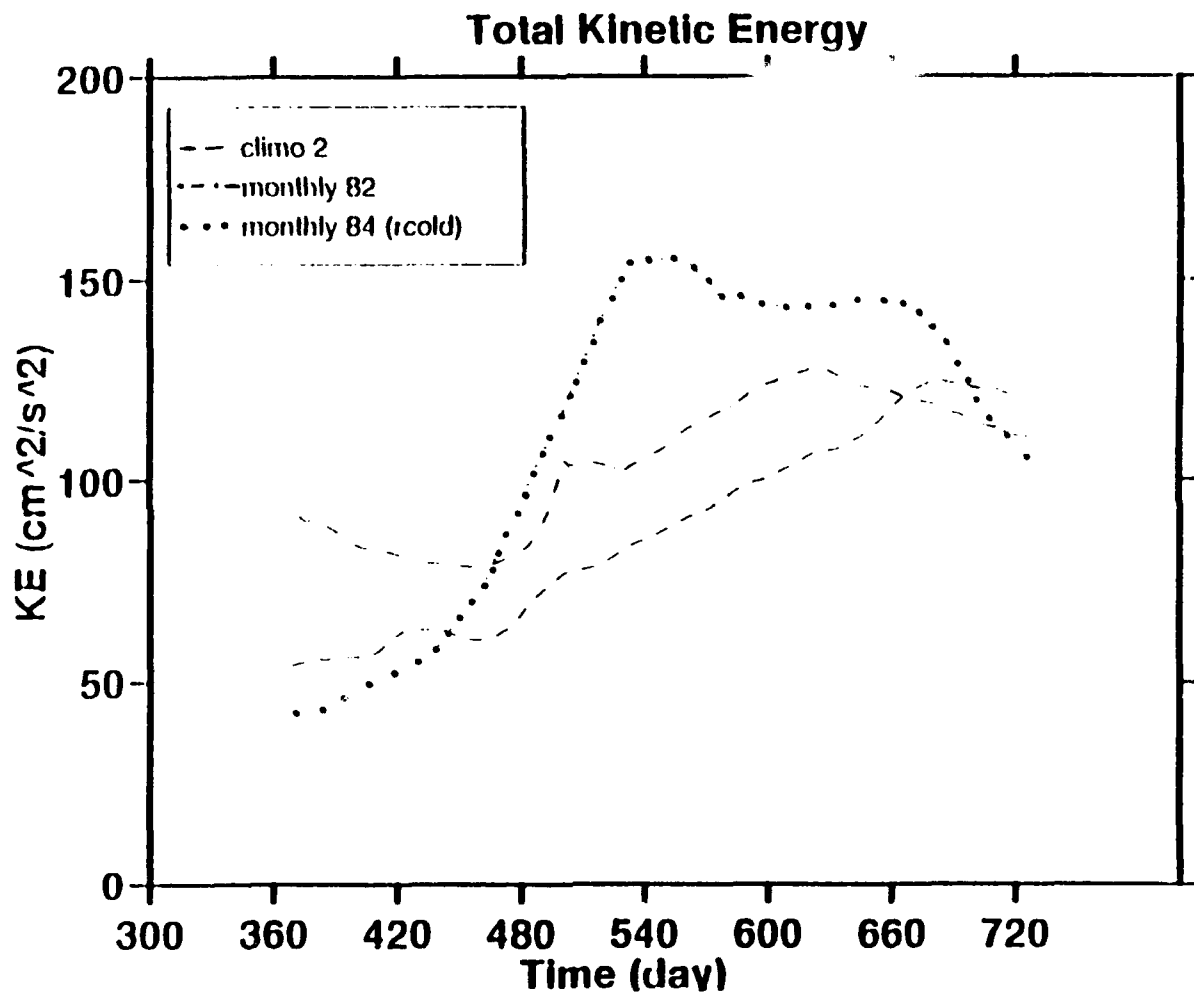


Figure 5.1b Experiments 1-3: Mean kinetic energy per unit mass time series for climatology (1980-1989), 1981, and 1983 over the entire domain (Units of the kinetic energy are  $\text{cm}^2\text{s}^{-2}$ ).



**Figure 5.1c Experiments 1-3: Eddy kinetic energy per unit mass time series for climatology (1980-1989), 1981, and 1983 over the entire domain (Units of the kinetic energy are  $\text{cm}^2\text{s}^{-2}$ ).**



**Figure 5.2a** Experiments 4-6: Total kinetic energy per unit mass time series for Climo II, 1981, and 1983 over the entire domain (Units of the kinetic energy are  $\text{cm}^2\text{s}^{-2}$ ).



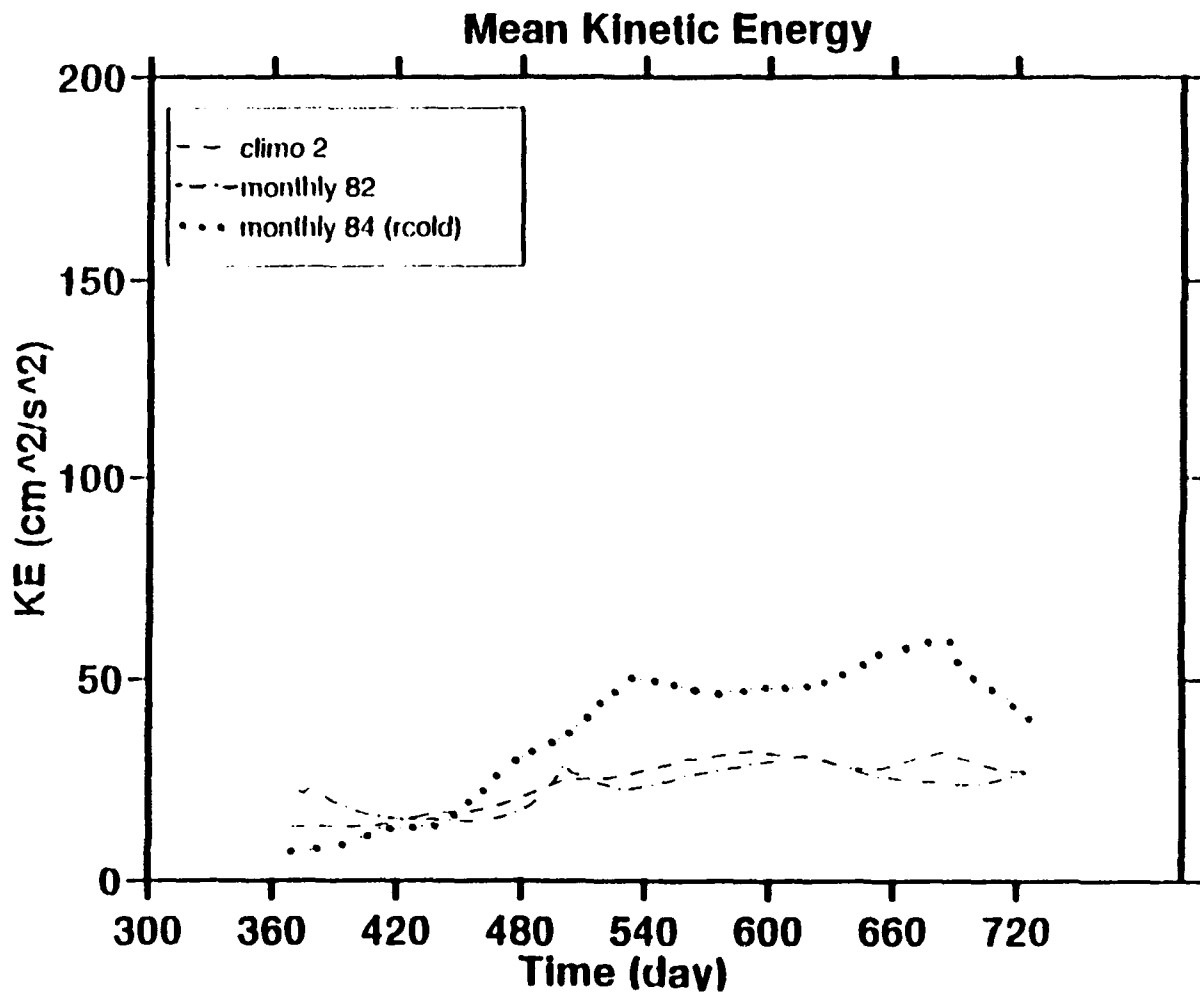


**Figure 5.2b Experiments 4-6: Mean kinetic energy per unit mass time series for Climo II, 1981, and 1983 over the entire domain (Units of the kinetic energy are  $\text{cm}^2\text{s}^{-2}$ ).**

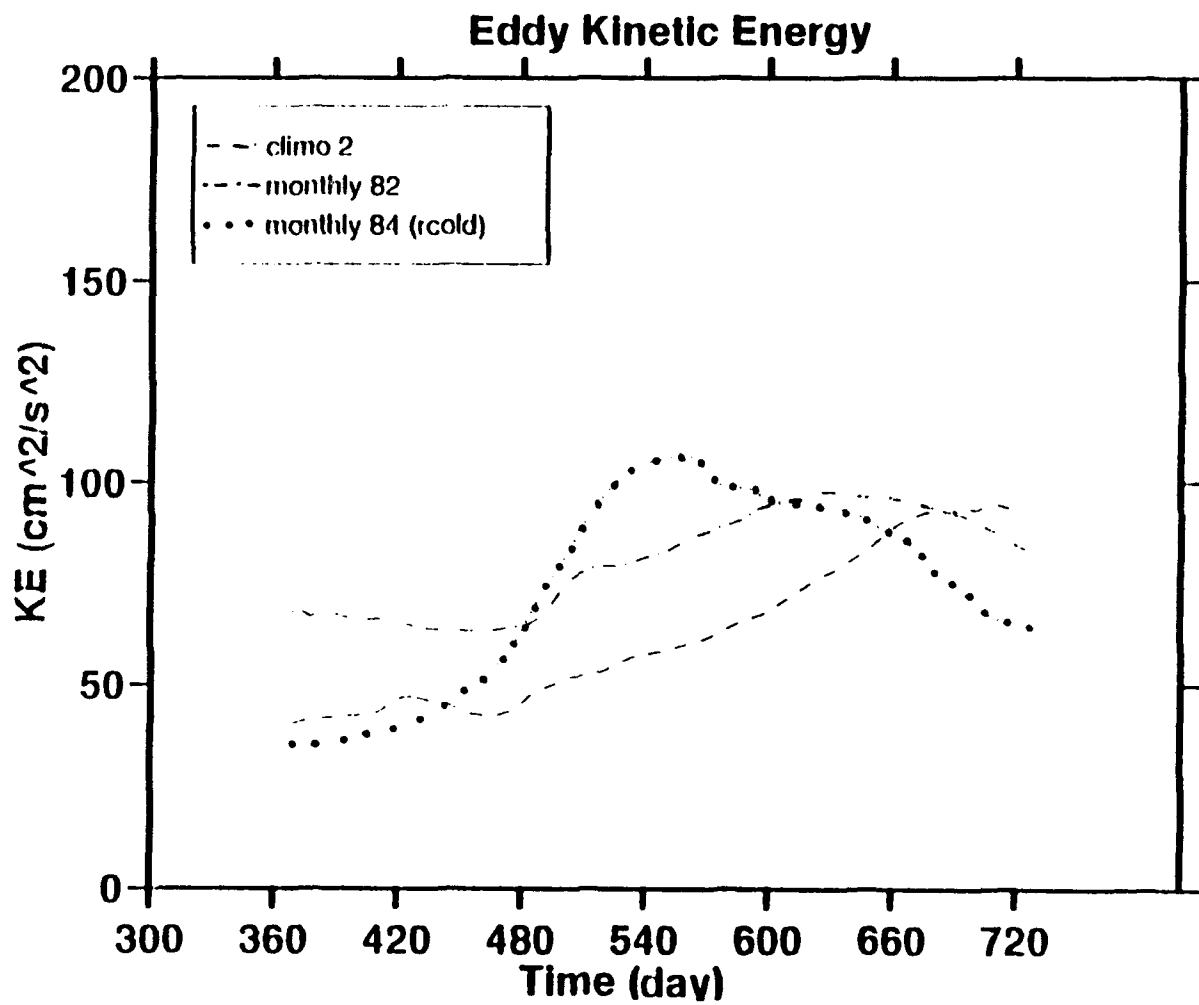


**Figure 5.2c Experiments 4-6: Eddy kinetic energy per unit mass time series for Climo II, 1981, and 1983 over the entire domain (Units of the kinetic energy are  $\text{cm}^2\text{s}^{-2}$ ).**

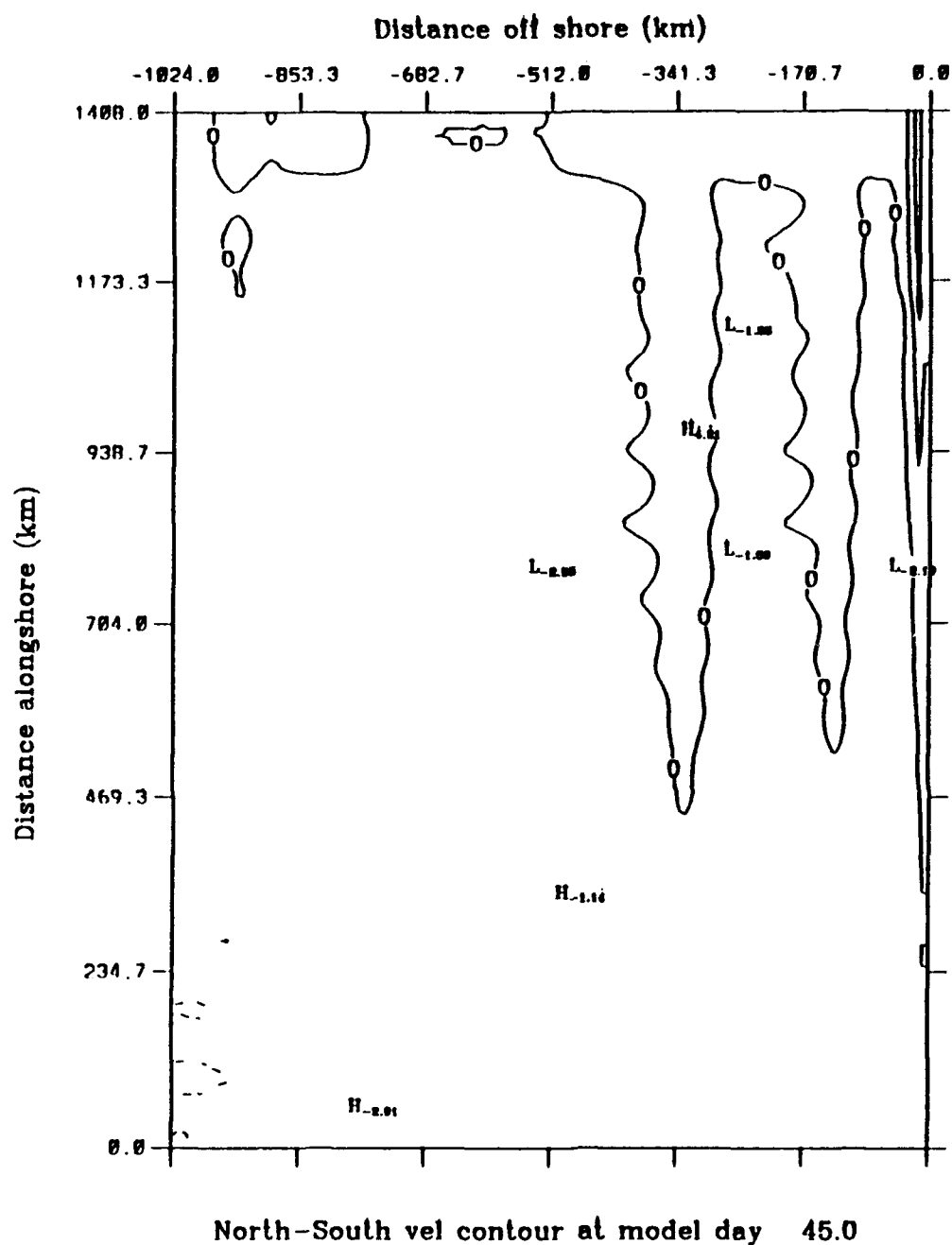


**Figure 5.3** Experiment 3: Surface meridional component of velocity at day 45. The contour interval is  $1 \text{ cm s}^{-1}$ . The dashed lines indicate equatorward velocities. Latitudinal alongshore distance 0 (1408) km corresponds to  $35^\circ \text{ N}$  ( $47.5^\circ \text{ N}$ ). Note enhanced poleward flow.



## **APPENDIX A. INSTABILITIES FOR EXPERIMENT 1 (CLIMO)**

This appendix contains additional analyses from Experiment 1 (climatological year) for the periods when the total kinetic energy per unit mass became quasi-steady. Energy transfer plots which consist of barotropic (mean kinetic energy to eddy kinetic energy) and baroclinic (eddy potential energy to eddy kinetic energy) were produced for the following model days: 207 - 216, 228 - 231, and 297 - 303. These plots appear as Figures A.1 through A.6.

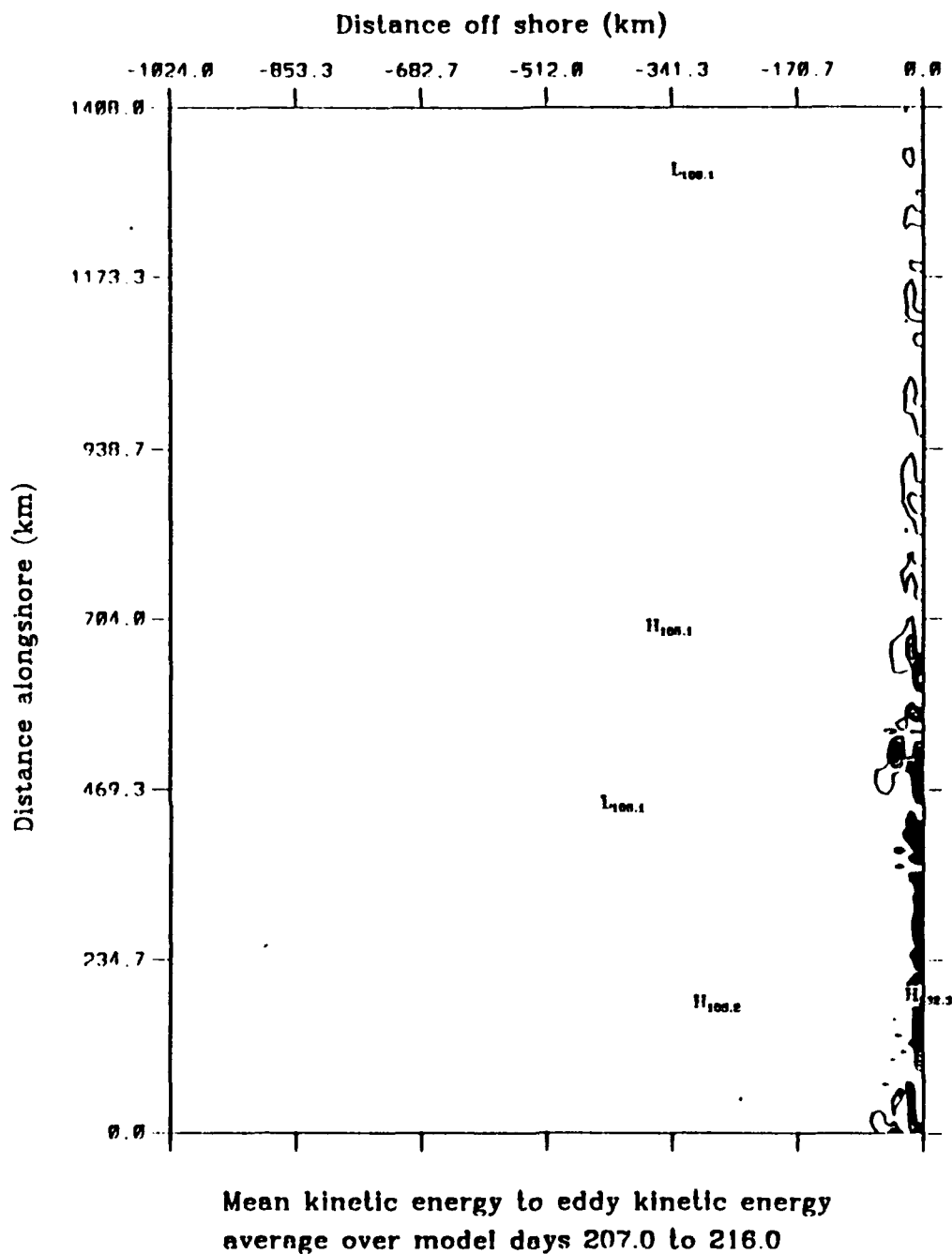


**Figure A.1** Experiment 1: Energy transfers of mean to eddy kinetic energy (i.e., barotropic energy transfer) for climatological (1980-1989) year, for model days 207 to 216. The contour interval is  $1 \text{ ergs cm}^{-3} \text{ s}^{-1}$ .



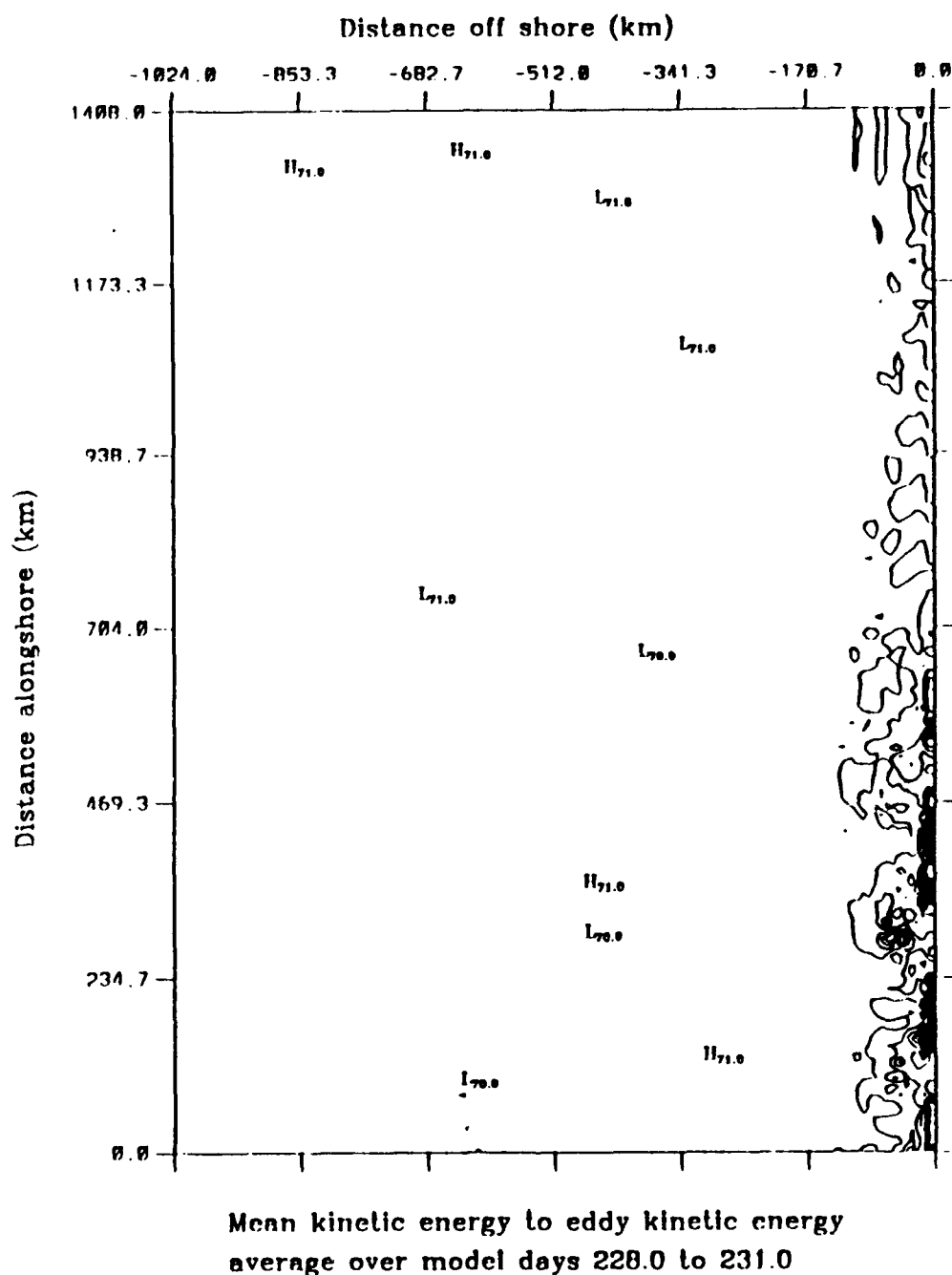


**Figure A.3** Experiment 1: Energy transfers of mean to eddy kinetic energy (i.e., barotropic energy transfer) for climatological (1980-1989) year, for model days 228 to 231. The contour interval is  $1 \text{ ergs cm}^{-3} \text{ s}^{-1}$ .



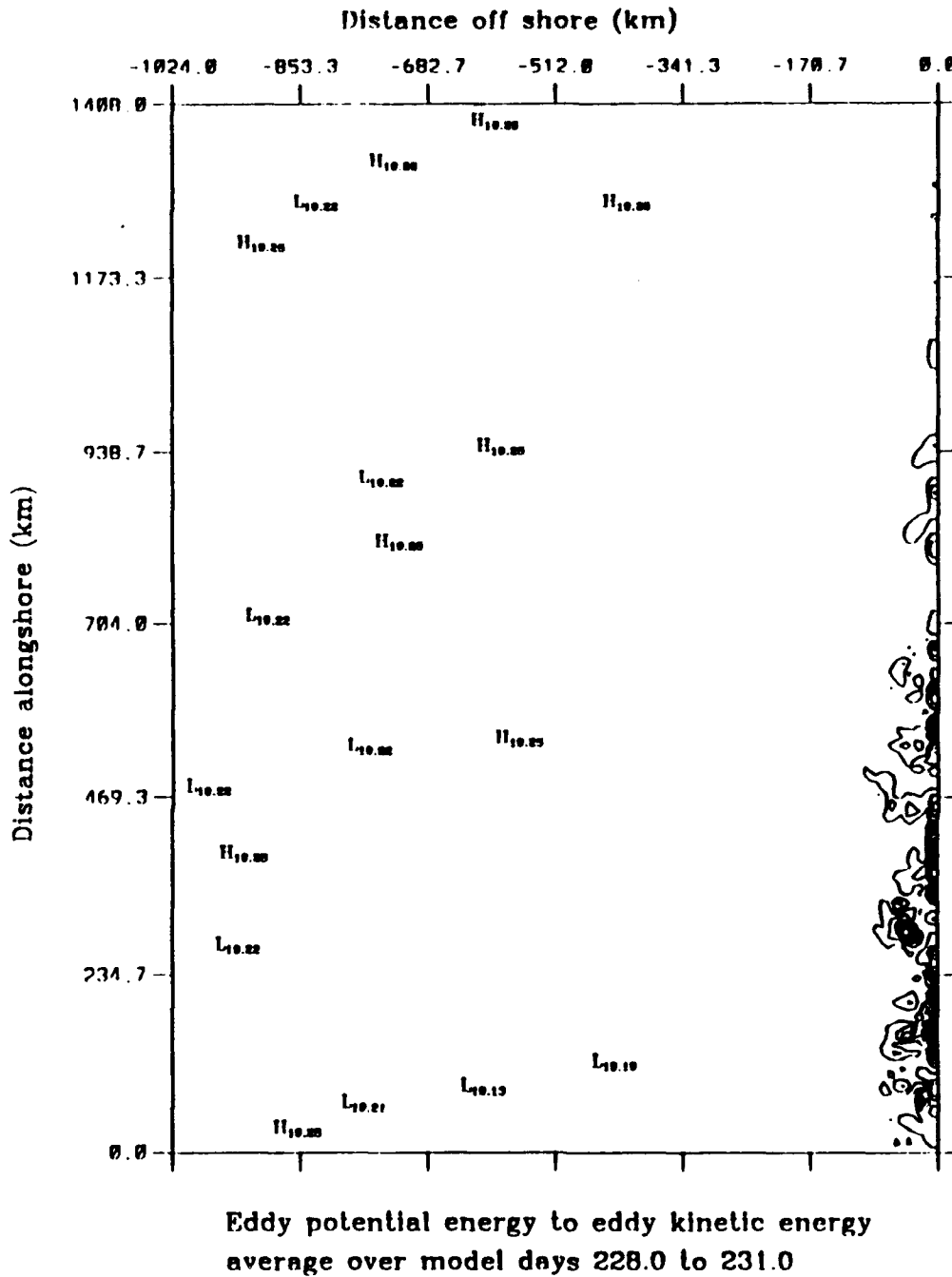


**Figure A.4** Experiment 1: Energy transfers of eddy potential to eddy kinetic energy (i.e., baroclinic energy transfer) for climatological (1980-1989) year, for model days 228 to 231. The contour interval is  $1 \text{ ergs cm}^{-3} \text{ s}^{-1}$ .

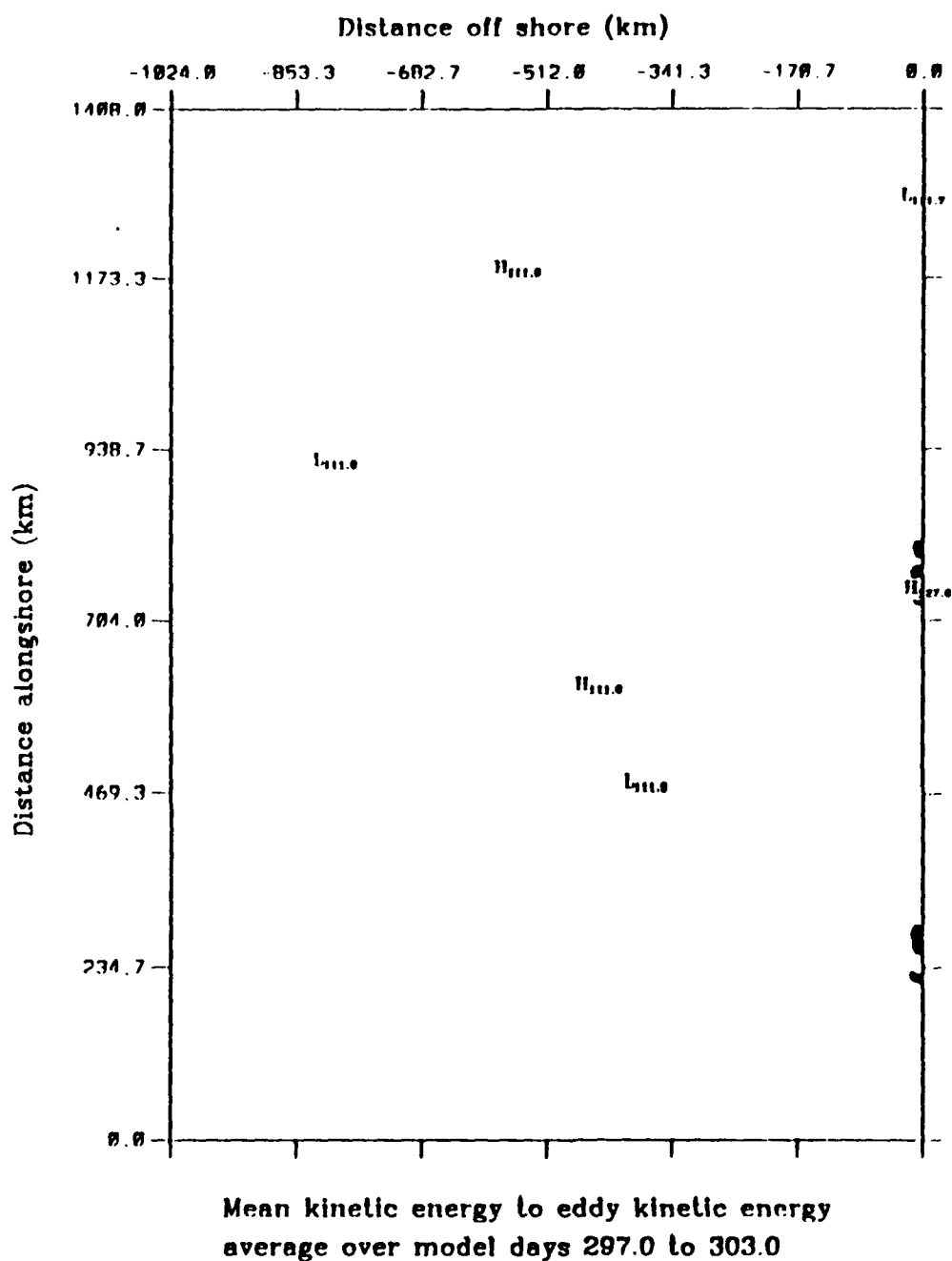
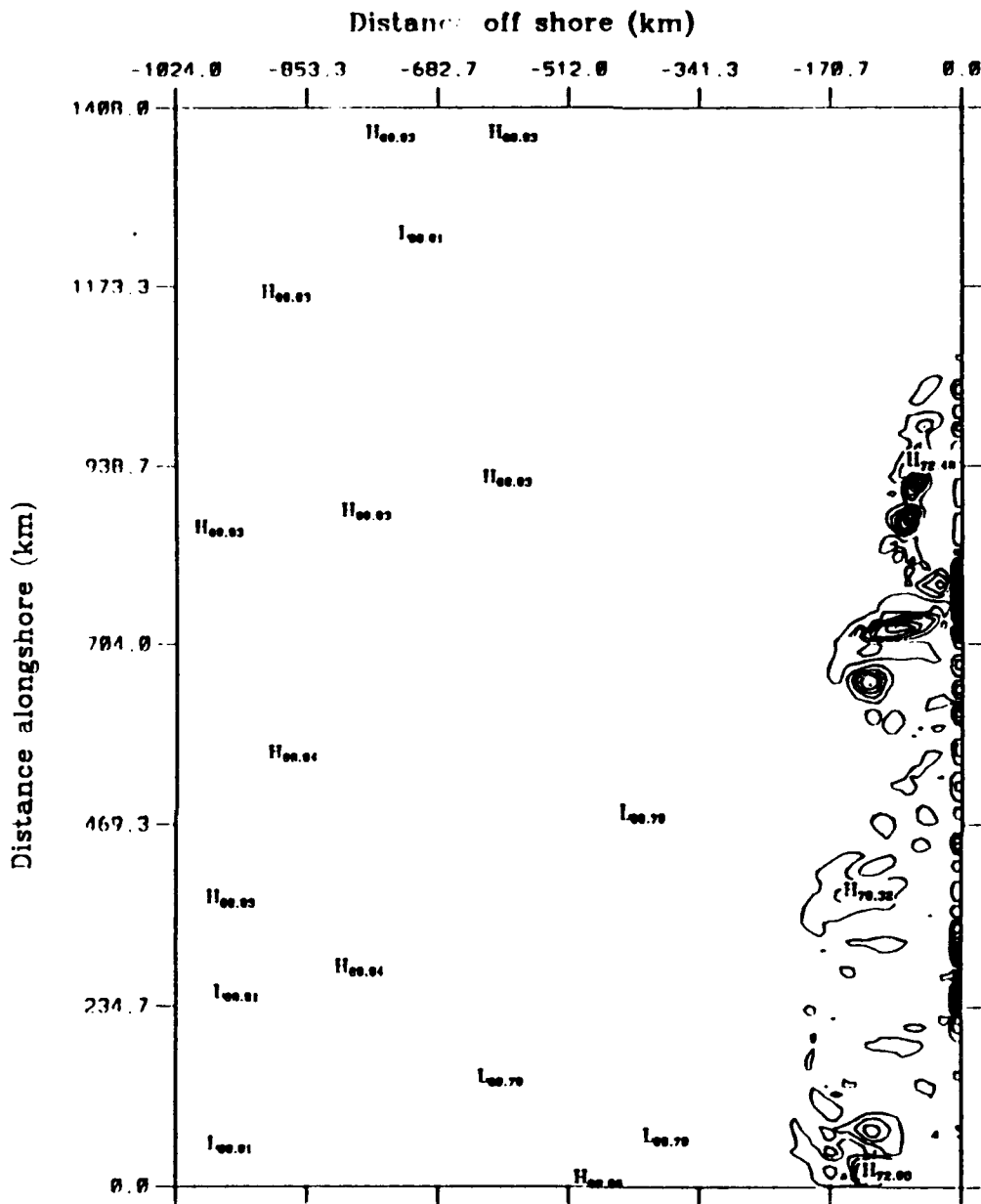


**Figure A.5** Experiment 1: Energy transfers of mean to eddy kinetic energy (i.e., barotropic energy transfer) for climatological (1980-1989) year, for model days 297 to 303. The contour interval is  $1 \text{ ergs cm}^{-3} \text{ s}^{-1}$ .



Eddy potential energy to eddy kinetic energy  
average over model days 297.0 to 303.0

**Figure A.6** Experiment 1: Energy transfers of eddy potential to eddy kinetic energy (i.e., baroclinic energy transfer) for climatological (1980-1989) year, for model days 297 to 303. The contour interval is  $1 \text{ ergs cm}^{-3} \text{ s}^{-1}$ .



## **APPENDIX B. INSTABILITIES FOR EXPERIMENT 2 (1981)**

This appendix contains additional analyses from Experiment 2 (1981) for the periods when the total kinetic energy per unit mass became quasi-steady. Energy transfer plots which consist of barotropic (mean kinetic energy to eddy kinetic energy) and baroclinic (eddy potential energy to eddy kinetic energy) were produced for the following model days: 210 - 222, 240 - 252, 297 - 303, and 309 - 333. These plots appear as Figures B.1 through B.8.

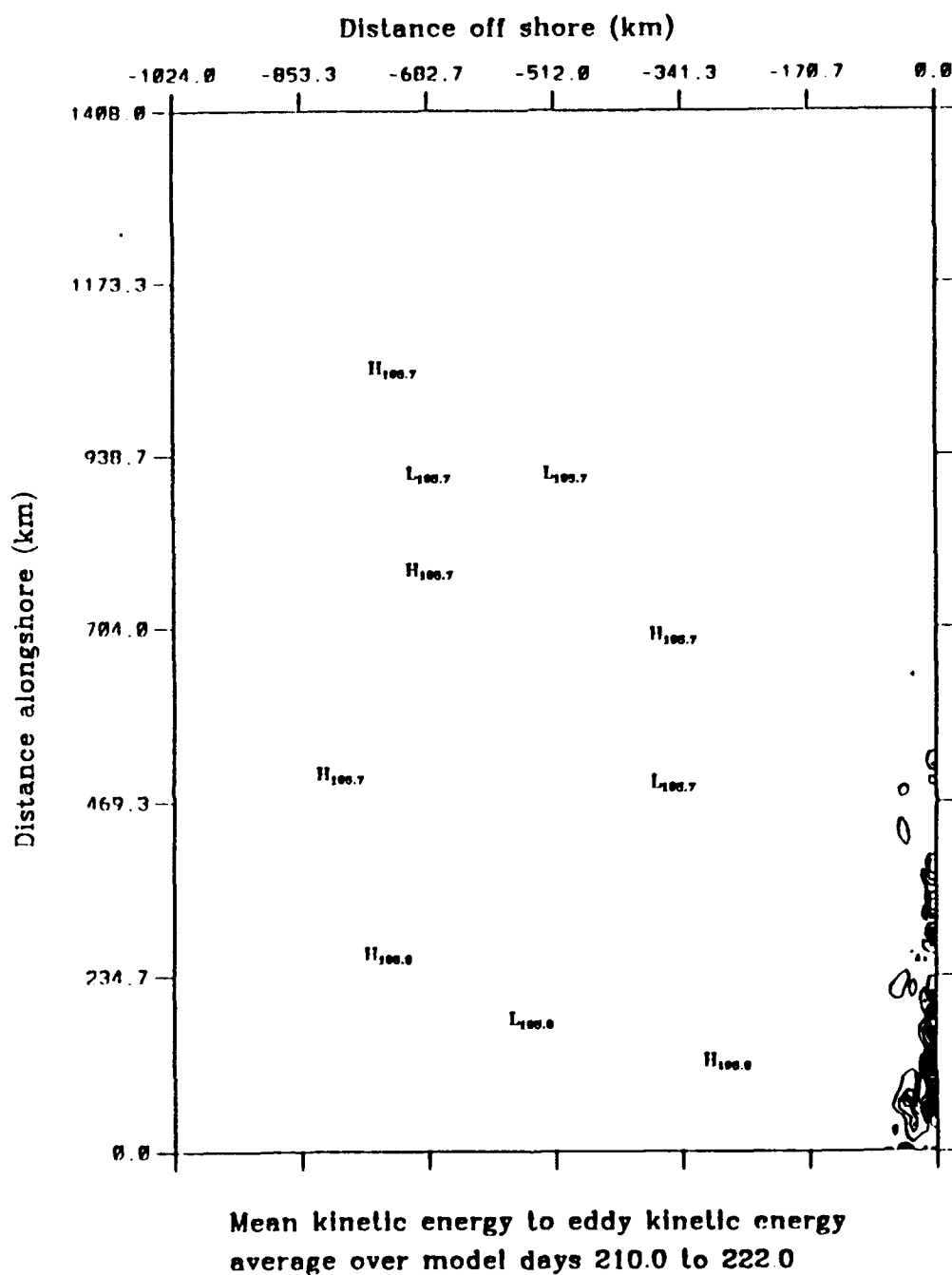


**Figure B.1** Experiment 2: Energy transfers of mean to eddy kinetic energy (i.e., barotropic energy transfer) for 1981, for model days 210 to 222. The contour interval is 10 ergs cm<sup>-3</sup> s<sup>-1</sup>.

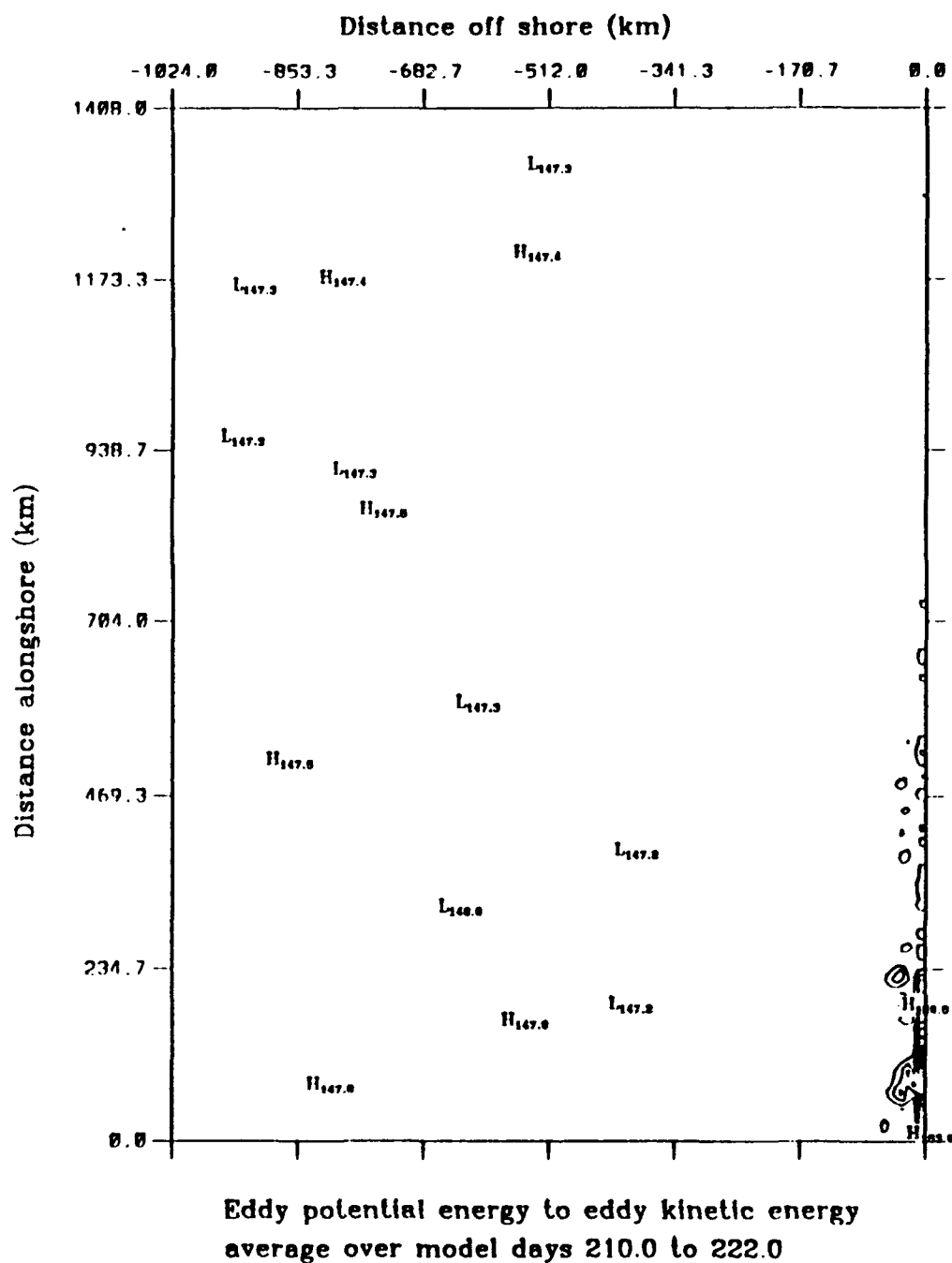


**Figure B.2** Experiment 2: Energy transfers of eddy potential to eddy kinetic energy (i.e., baroclinic energy transfer) for 1981, for model days 210 to 222. The contour interval is  $10 \text{ ergs cm}^{-3} \text{ s}^{-1}$ .

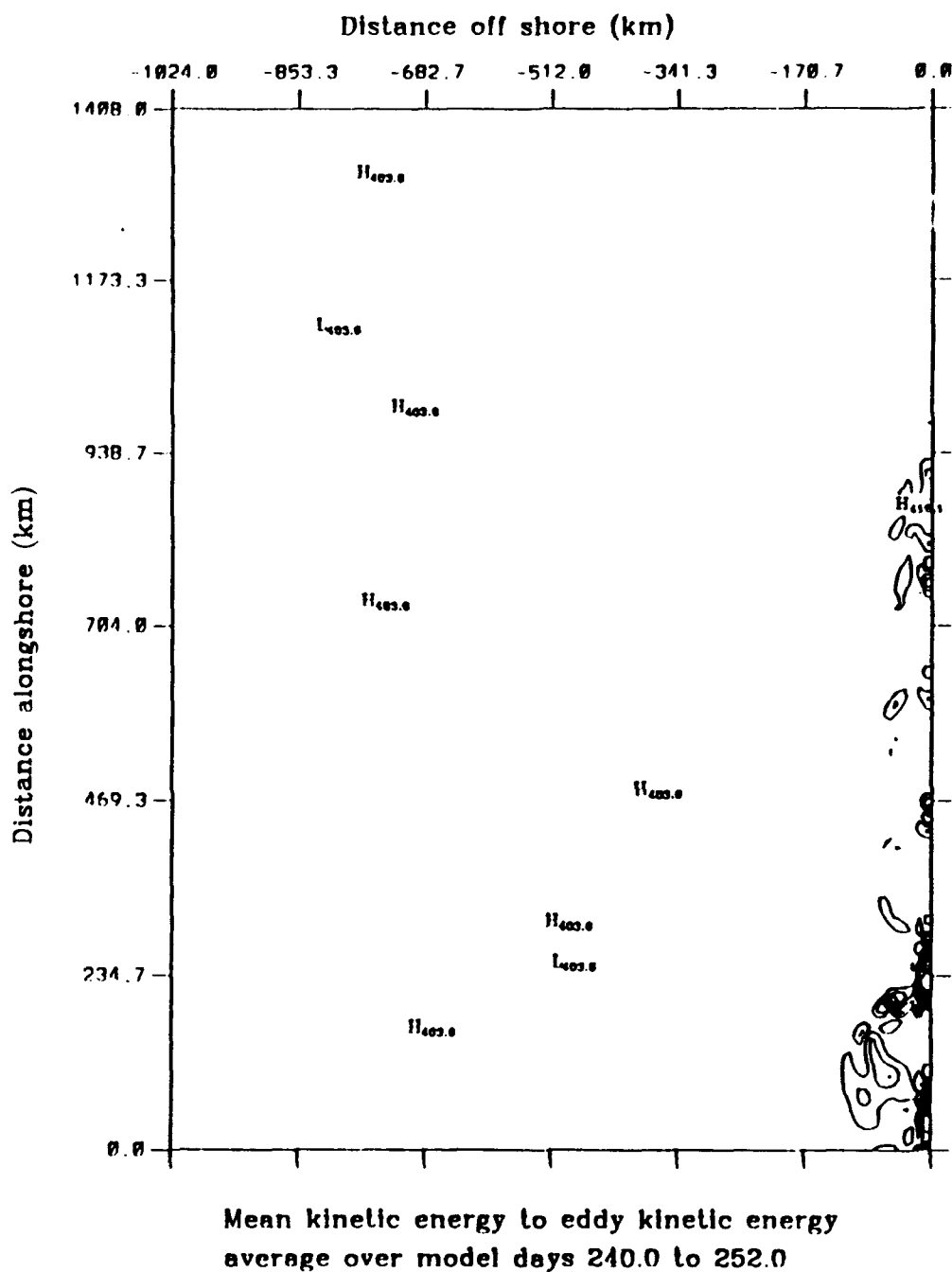


**Figure B.3** Experiment 2: Energy transfers of mean to eddy kinetic energy (i.e., barotropic energy transfer) for 1981, for model days 240 to 252. The contour interval is 10 ergs  $\text{cm}^{-3} \text{ s}^{-1}$ .





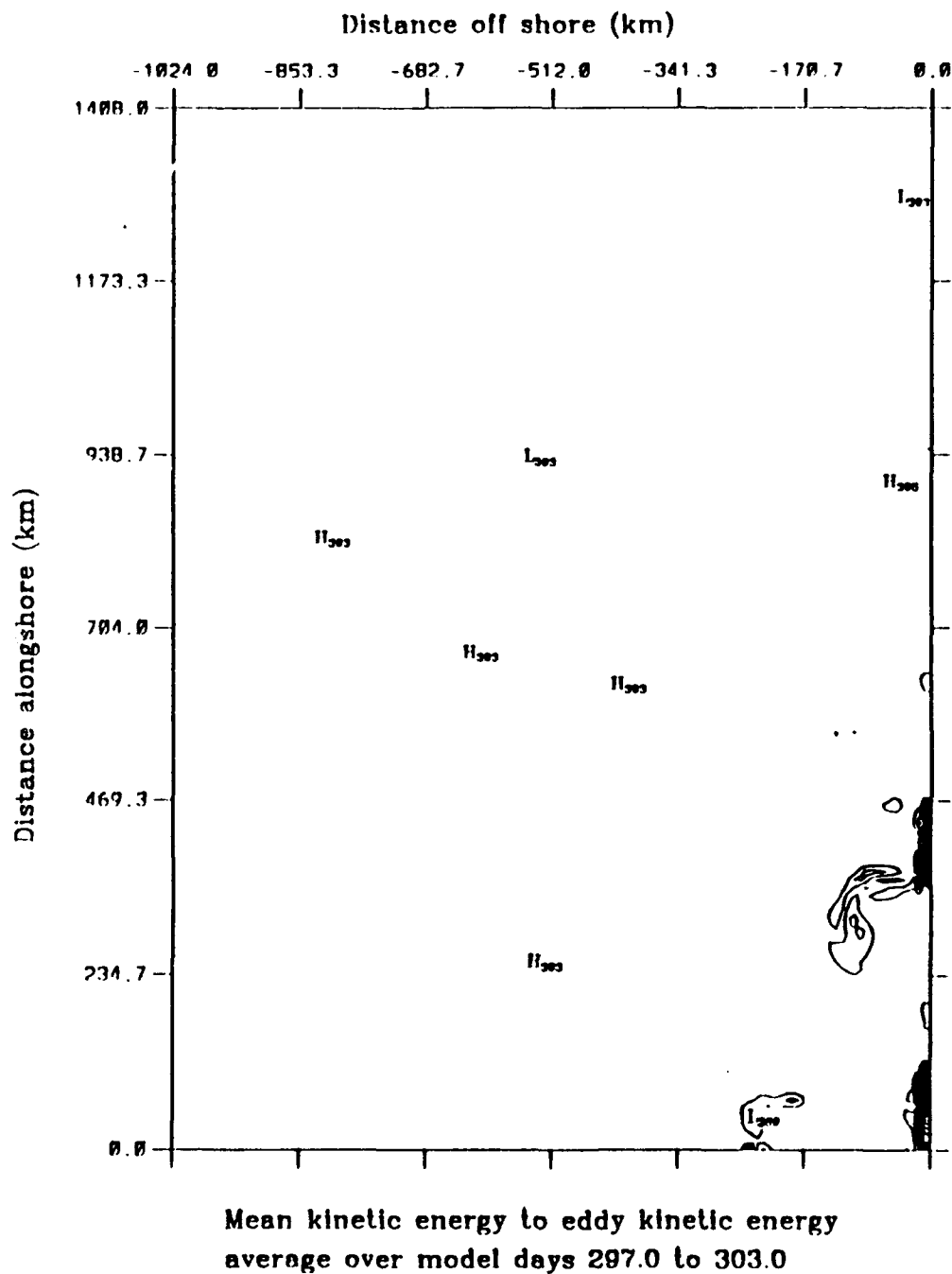


**Figure B.5** Experiment 2: Energy transfers of mean to eddy kinetic energy (i.e., barotropic energy transfer) for 1981, for model days 297 to 303. The contour interval is 10 ergs  $\text{cm}^{-3} \text{ s}^{-1}$ .

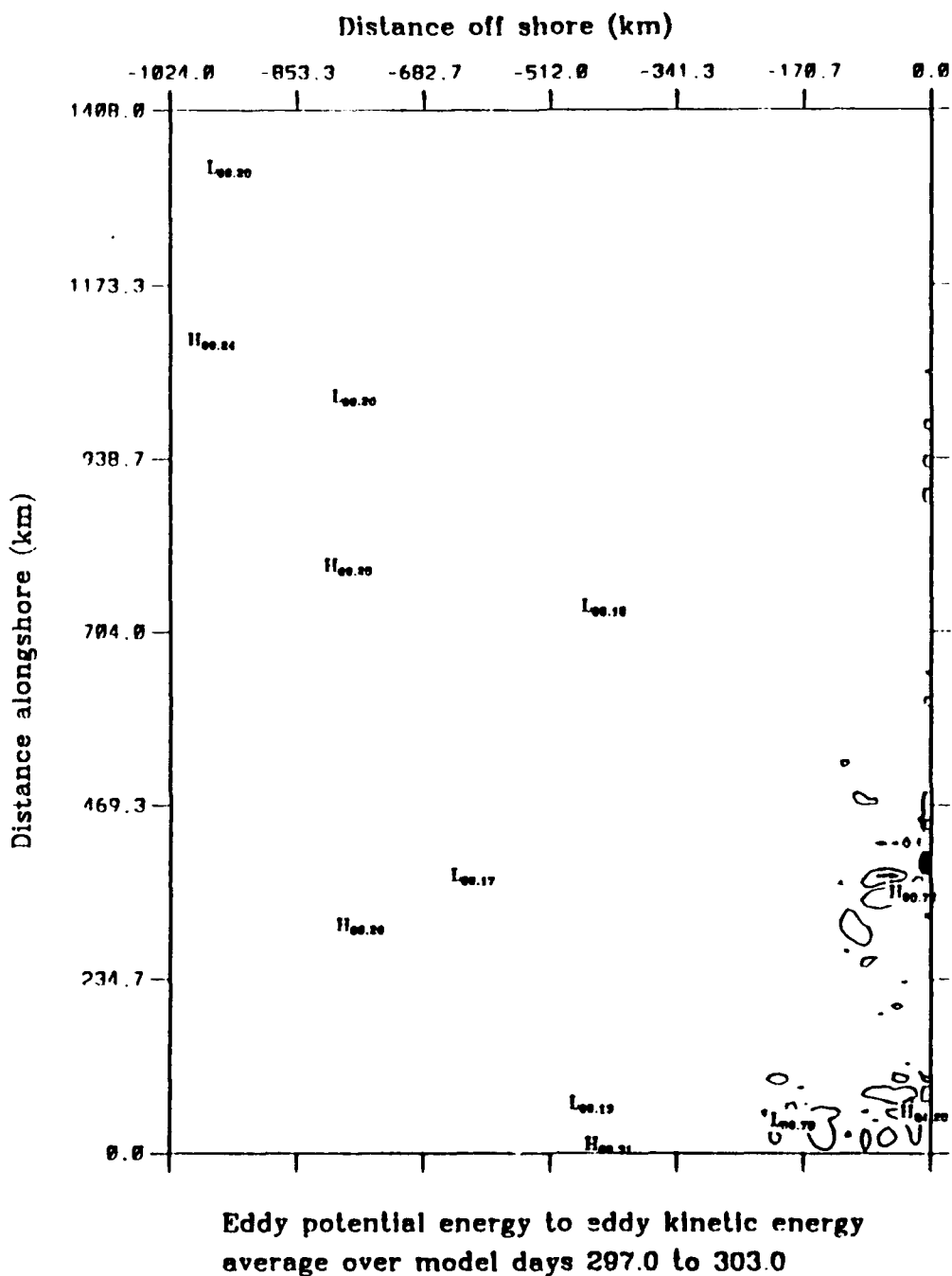


**Figure B.6** Experiment 2: Energy transfers of eddy potential to eddy kinetic energy (i.e., baroclinic energy transfer) for 1981, for model days 297 to 303. The contour interval is  $10 \text{ ergs cm}^{-3} \text{ s}^{-1}$ .

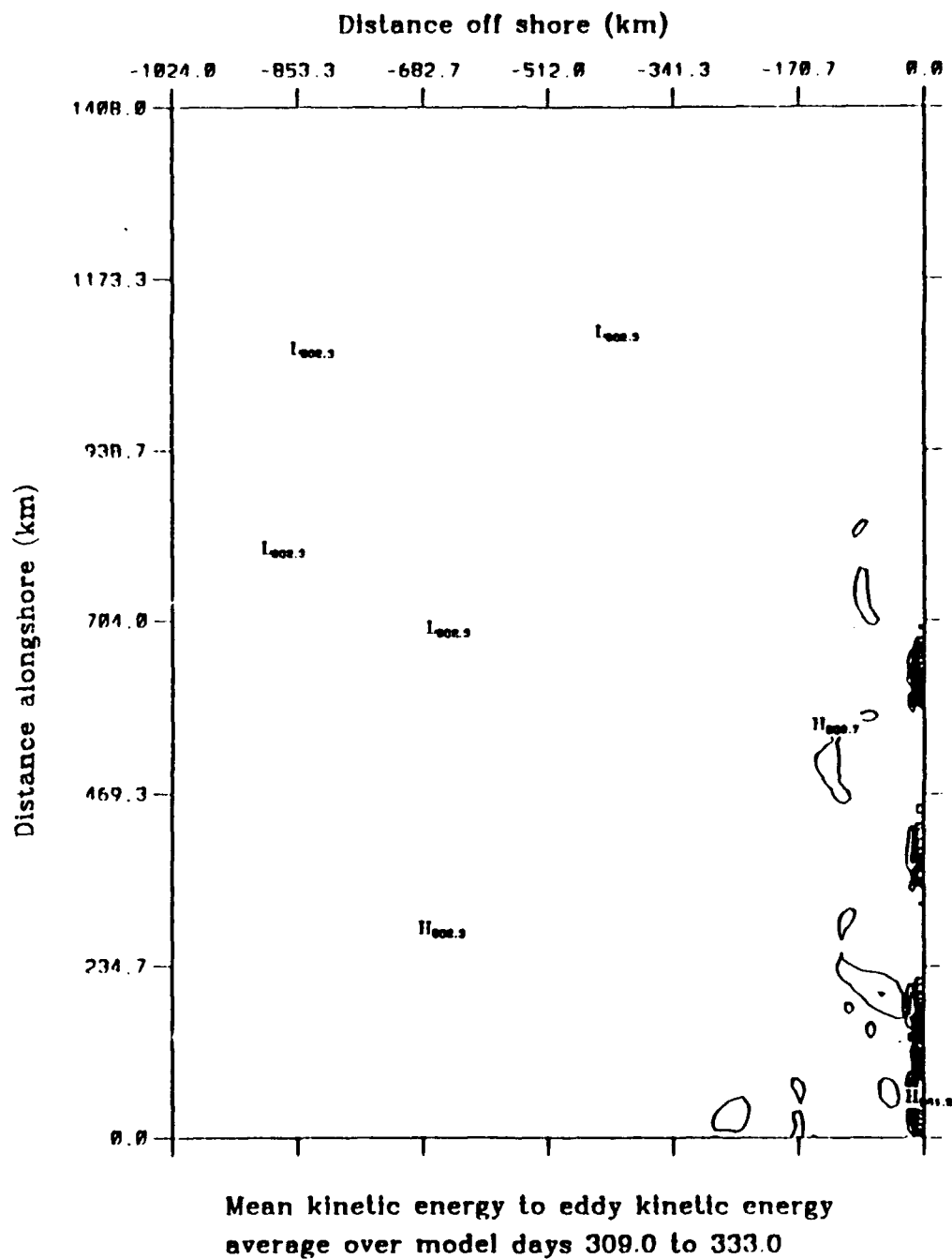


**Figure B.7** Experiment 2: Energy transfers of mean to eddy kinetic energy (i.e., barotropic energy transfer) for 1981, for model days 309 to 333. The contour interval is 10 ergs  $\text{cm}^{-3} \text{s}^{-1}$ .

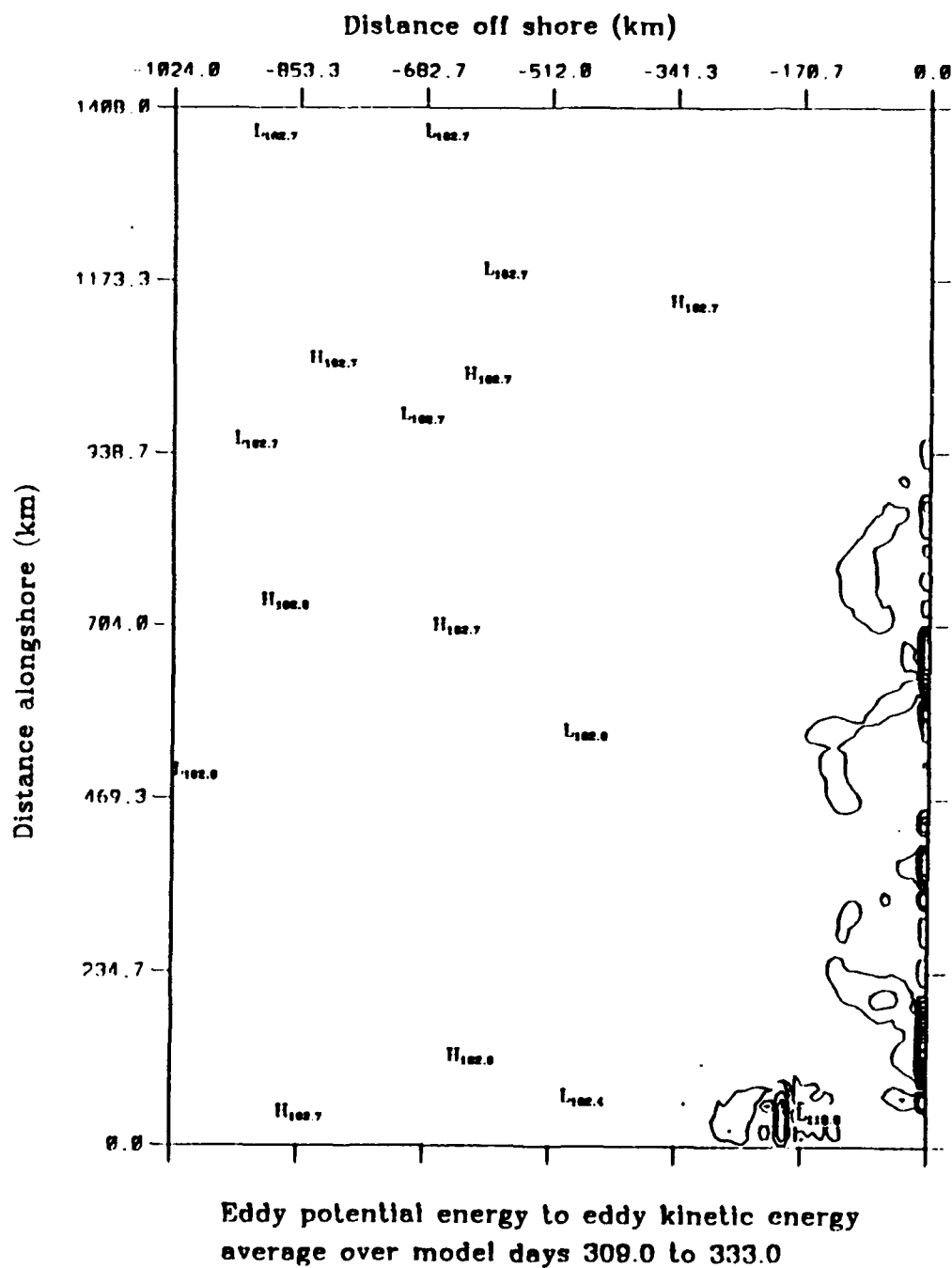


**Figure B.8** Experiment 2: Energy transfers of eddy potential to eddy kinetic energy (i.e., baroclinic energy transfer) for 1981, for model days 309 to 333. The contour interval is  $10 \text{ ergs cm}^{-3} \text{ s}^{-1}$ .



## **APPENDIX C. INSTABILITIES FOR EXPERIMENT 3 (1983)**

This appendix contains additional analyses from Experiment 3 (1983) for the periods when the total kinetic energy per unit mass became quasi-steady. Energy transfer plots which consist of barotropic (mean kinetic energy to eddy kinetic energy) and baroclinic (eddy potential energy to eddy kinetic energy) were produced for the following model days: 186 - 192, 222 - 234, 249 - 258, 279 - 288, 312 - 315, 324 - 327, and 342 - 348. These plots appear as Figures C.1 through C.14.

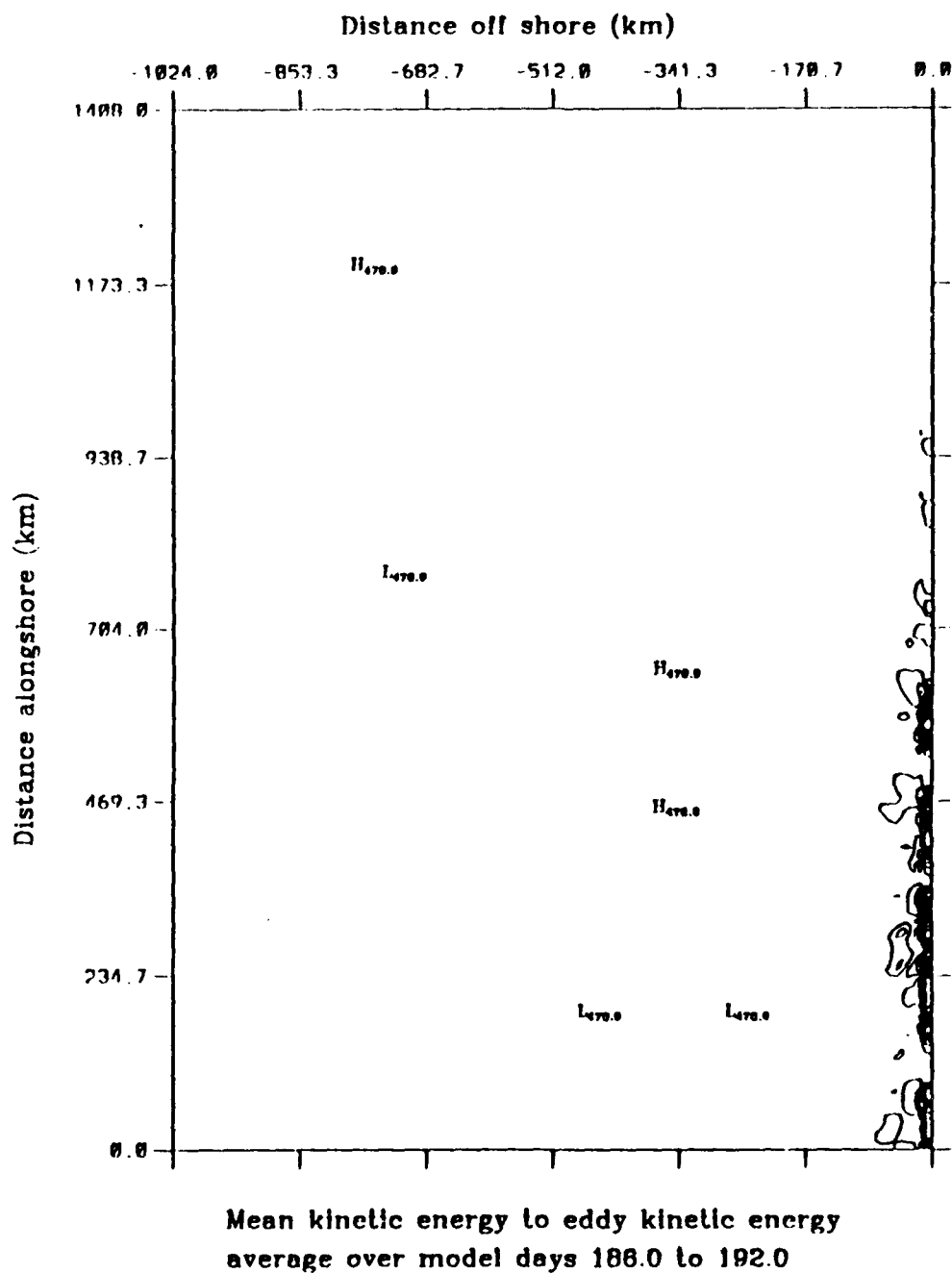


**Figure C.1** Experiment 3: Energy transfers of mean to eddy kinetic energy (i.e., barotropic energy transfer) for 1983, for model days 186 to 192. The contour interval is 10 ergs  $\text{cm}^{-3} \text{ s}^{-1}$ .



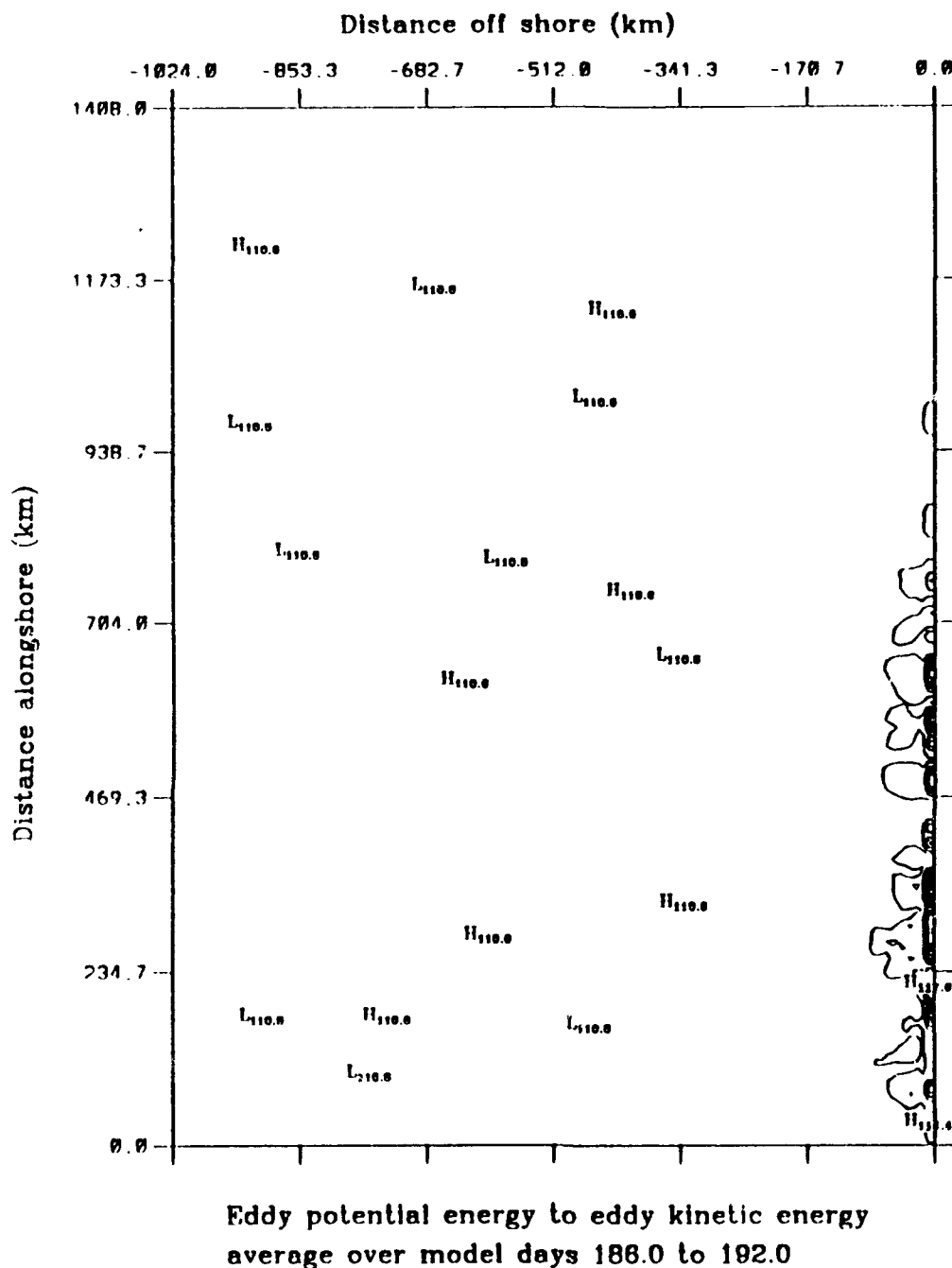


**Figure C.2** Experiment 3: Energy transfers of eddy potential to eddy kinetic energy (i.e., baroclinic energy transfer) for 1983, for model days 186 to 192. The contour interval is  $10 \text{ ergs cm}^{-3} \text{ s}^{-1}$ .

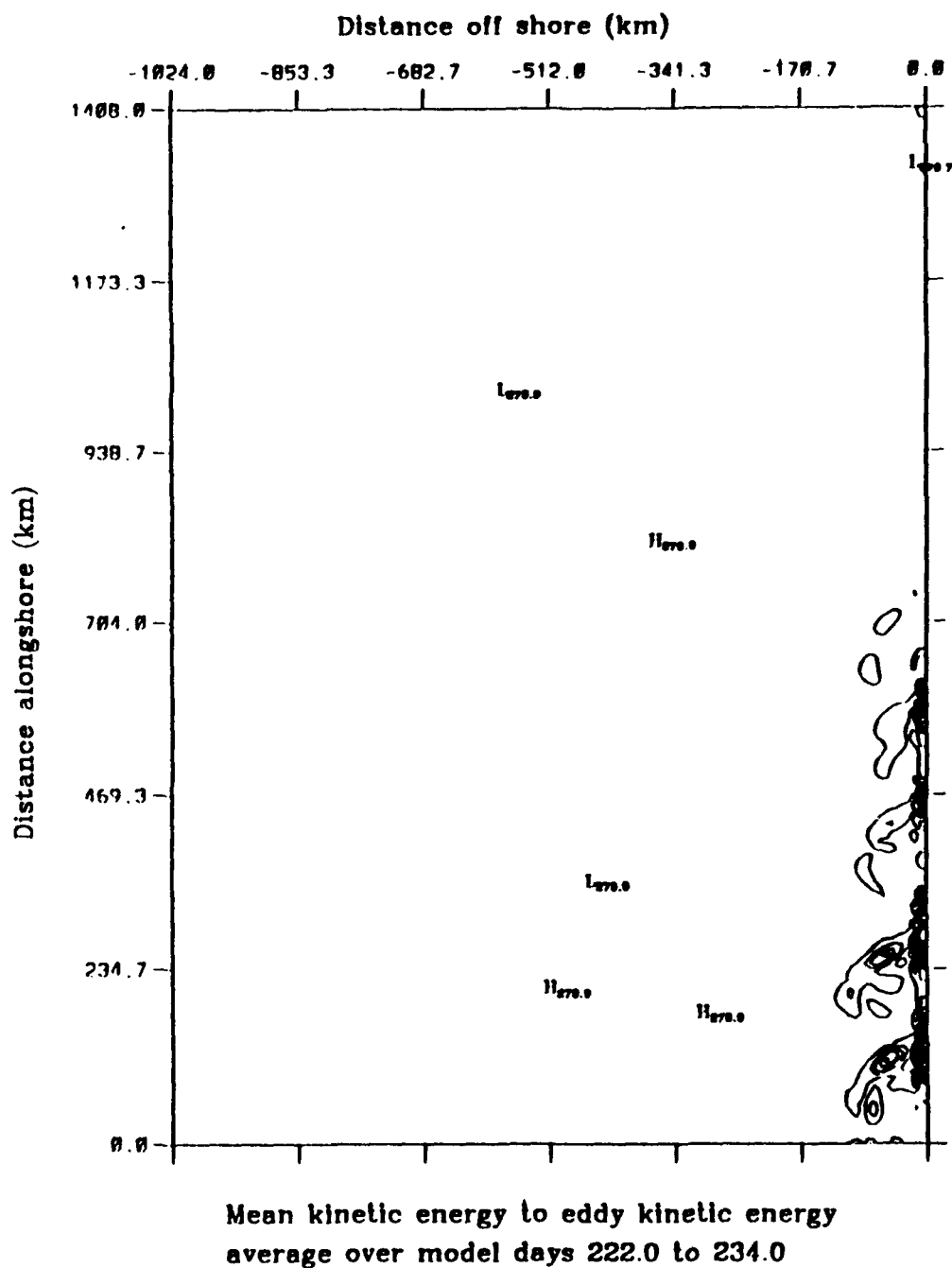
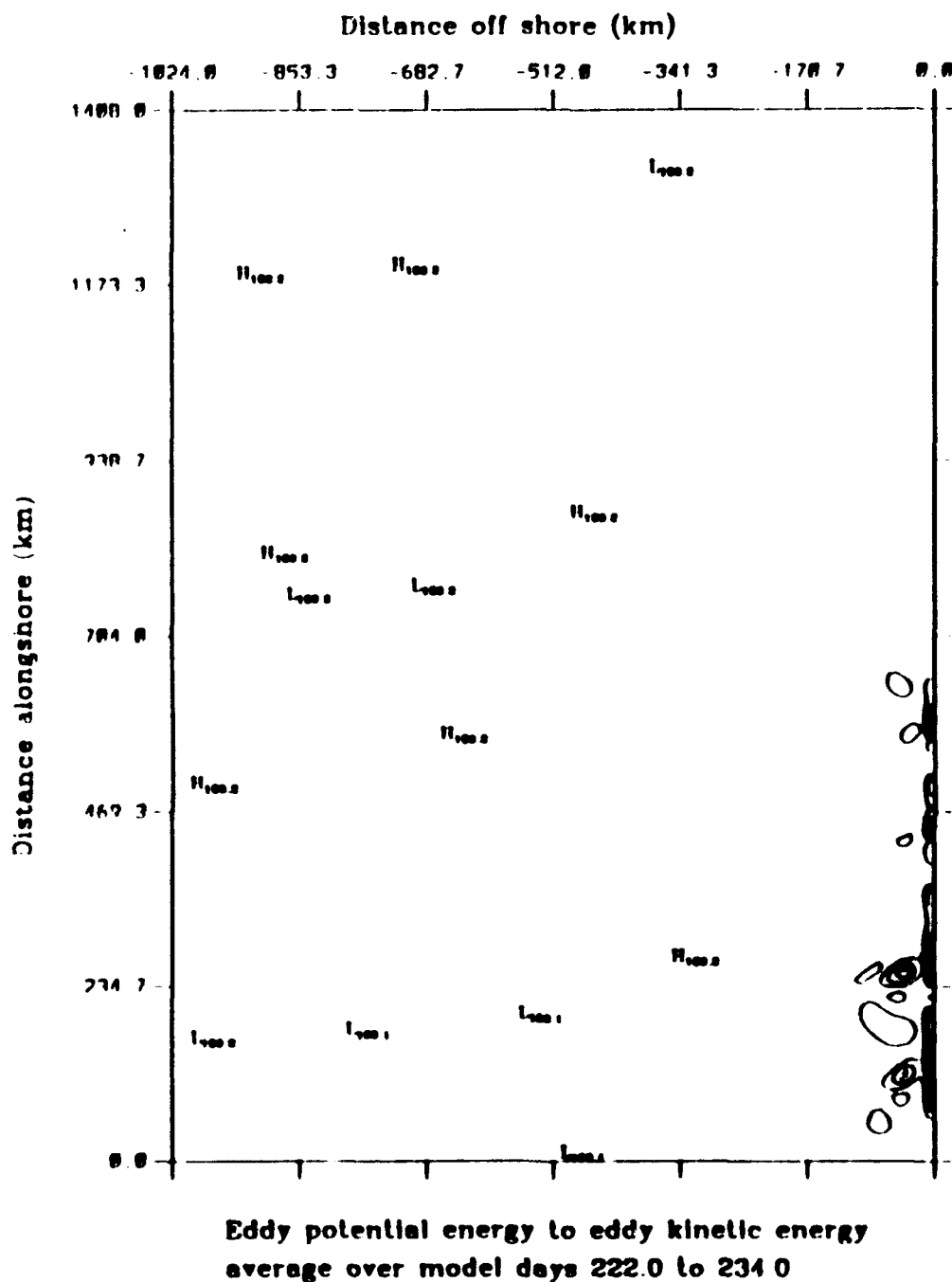


Figure C.3 Experiment 3: Energy transfers of mean to eddy kinetic energy (i.e., barotropic energy transfer) for 1983, for model days 222 to 234. The contour interval is 10 ergs  $\text{cm}^{-3} \text{ s}^{-1}$ .



**Figure C.4 Experiment 3: Energy transfers of eddy potential to eddy kinetic energy (i.e., baroclinic energy transfer) for 1983, for model days 222 to 234. The contour interval is  $10 \text{ ergs cm}^{-3} \text{ s}^{-1}$ .**





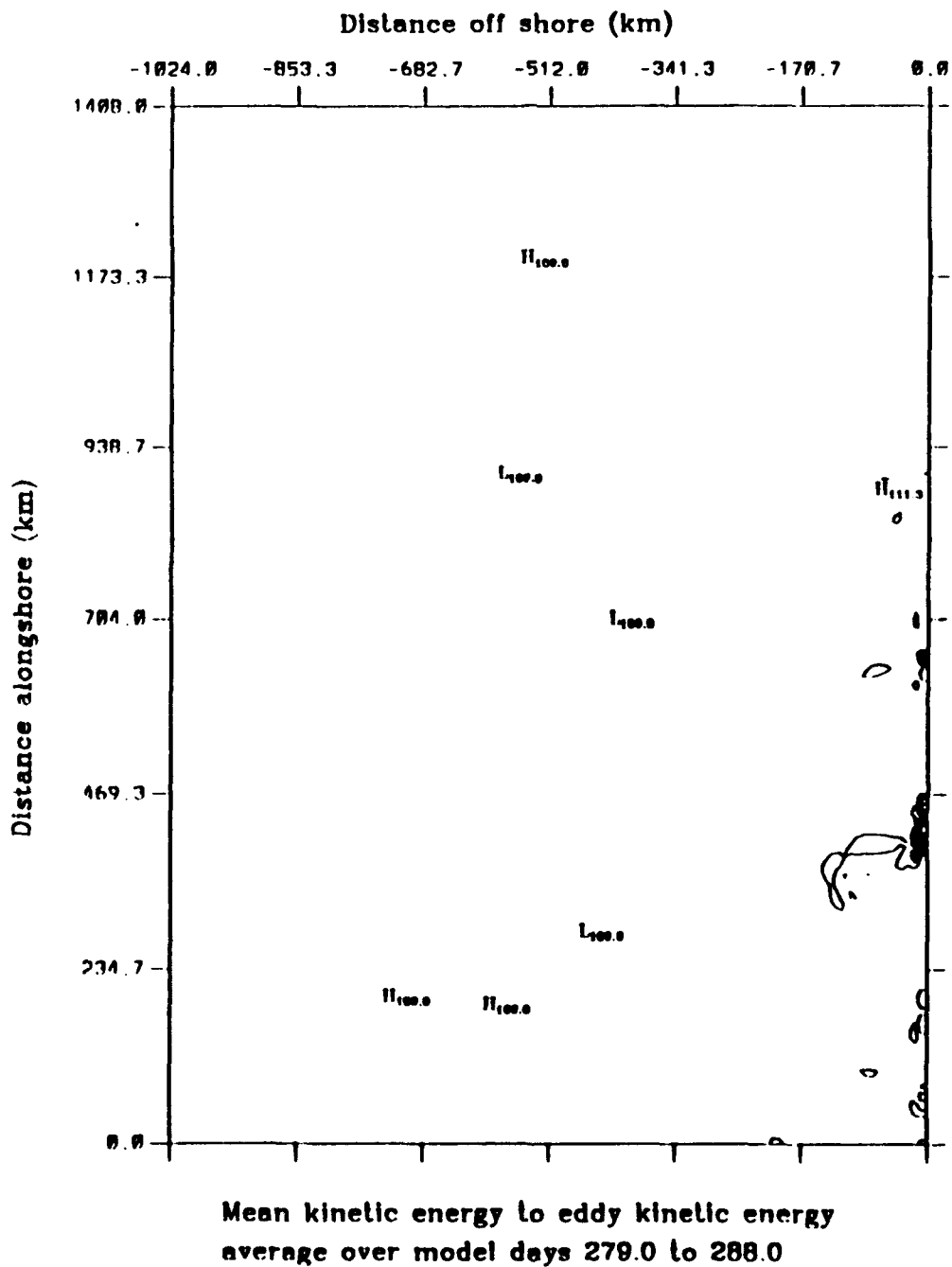
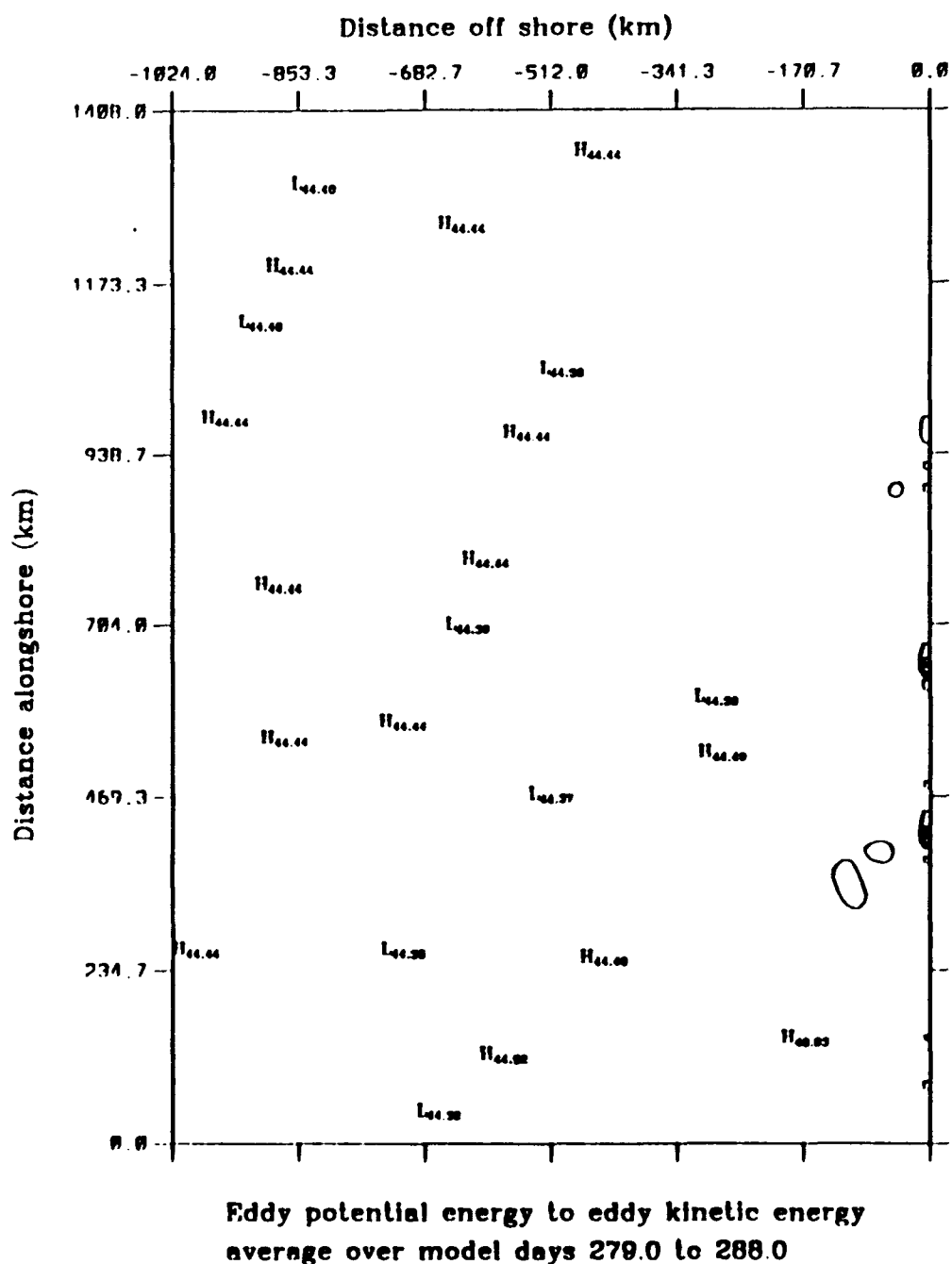


Figure C.7 Experiment 3: Energy transfers of mean to eddy kinetic energy (i.e., barotropic energy transfer) for 1983, for model days 279 to 288. The contour interval is 10 ergs  $\text{cm}^{-3} \text{ s}^{-1}$ .



**Figure C.8** Experiment 3: Energy transfers of eddy potential to eddy kinetic energy (i.e., baroclinic energy transfer) for 1983, for model days 279 to 288. The contour interval is  $10 \text{ ergs cm}^{-3} \text{ s}^{-1}$ .











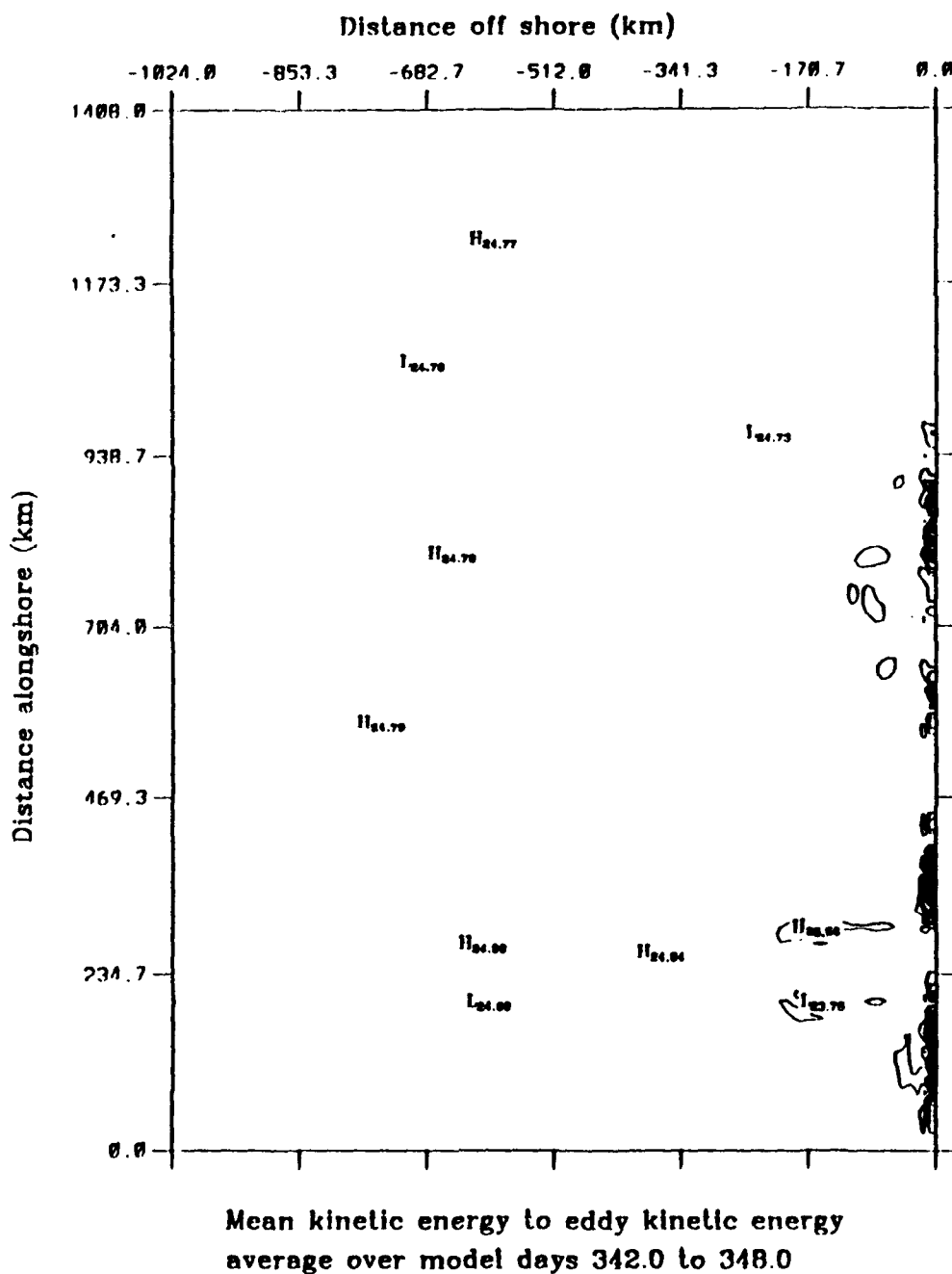


**Figure C.13** Experiment 3: Energy transfers of mean to eddy kinetic energy (i.e., barotropic energy transfer) for 1983, for model days 342 to 348. The contour interval is 1 ergs  $\text{cm}^{-3} \text{s}^{-1}$ .





#### APPENDIX D. INSTABILITIES FOR EXPERIMENT 4 (CLIMO II)

This appendix contains additional analyses from Experiment 4 (Climo II) for the periods when the total kinetic energy per unit mass became quasi-steady. Energy transfer plots which consist of barotropic (mean kinetic energy to eddy kinetic energy) and baroclinic (eddy potential energy to eddy kinetic energy) were produced for the following model days: 378 - 408 (yd 12 - 42), 453 - 465 (yd 87 - 99), 504 - 516 (yd 138 - 150), and 624 - 636 (yd 258 - 270). These plots appear as Figures D.1 through D.8.

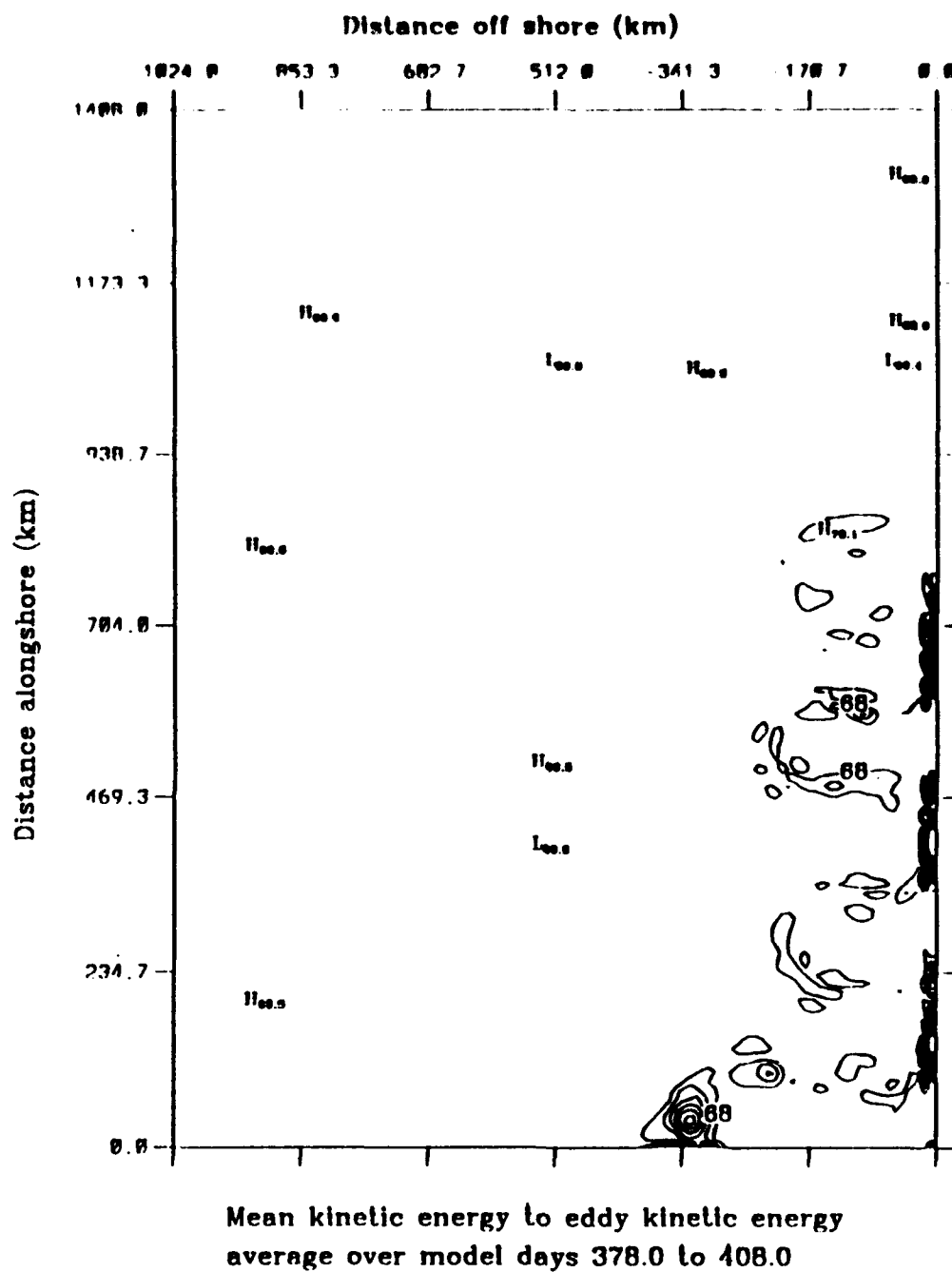


Figure D.1 Experiment 4: Energy transfers of mean to eddy kinetic energy (i.e., barotropic energy transfer) for Climo II, for model days 378 to 408 (yd 12 - 42). The contour interval is  $1 \text{ ergs cm}^{-3} \text{ s}^{-1}$ .









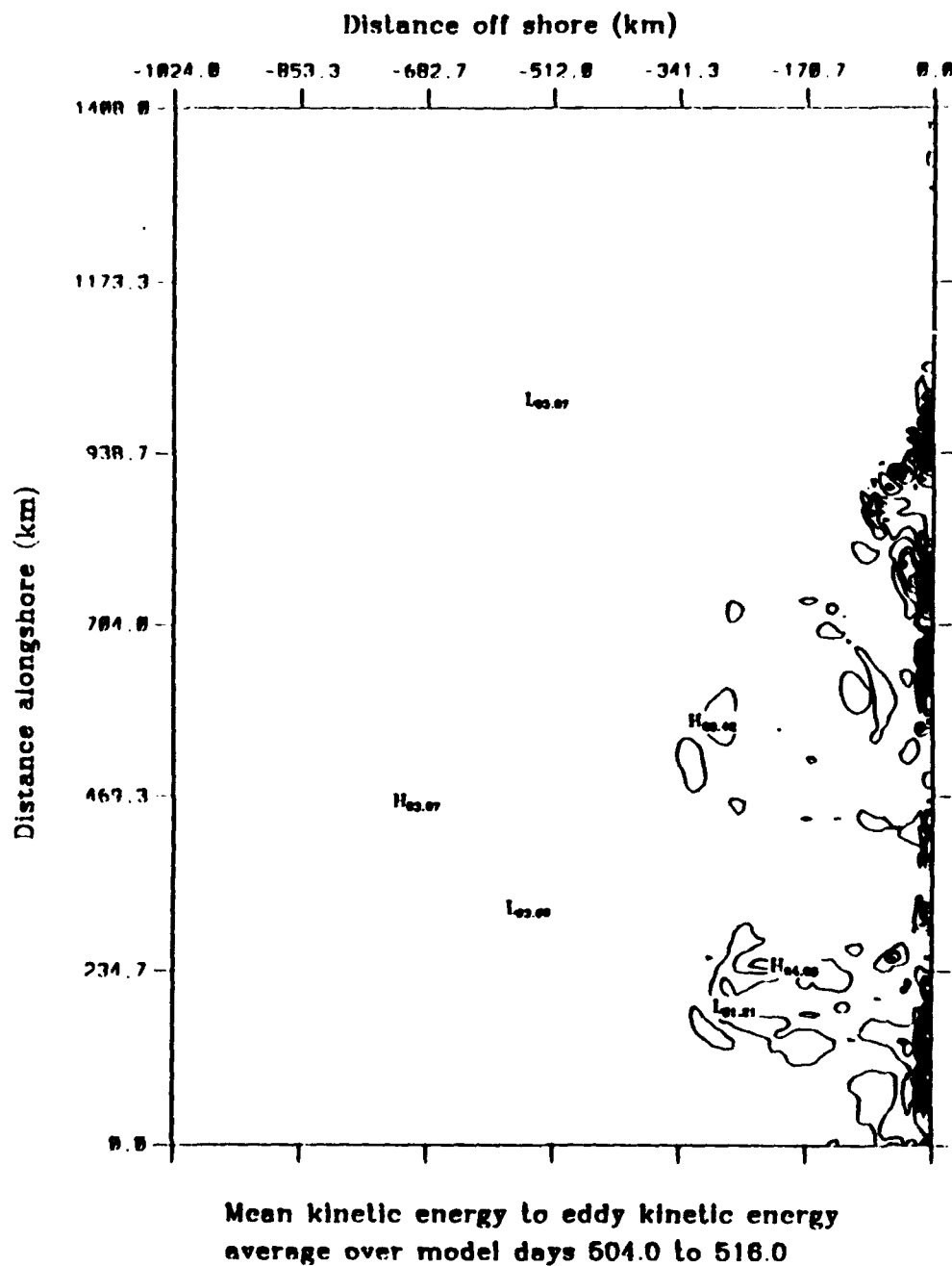


**Figure D.5** Experiment 4: Energy transfers of mean to eddy kinetic energy (i.e., barotropic energy transfer) for Climo II, for model days 504 to 516 (yd 138 - 150). The contour interval is  $1 \text{ ergs cm}^{-3} \text{ s}^{-1}$ .

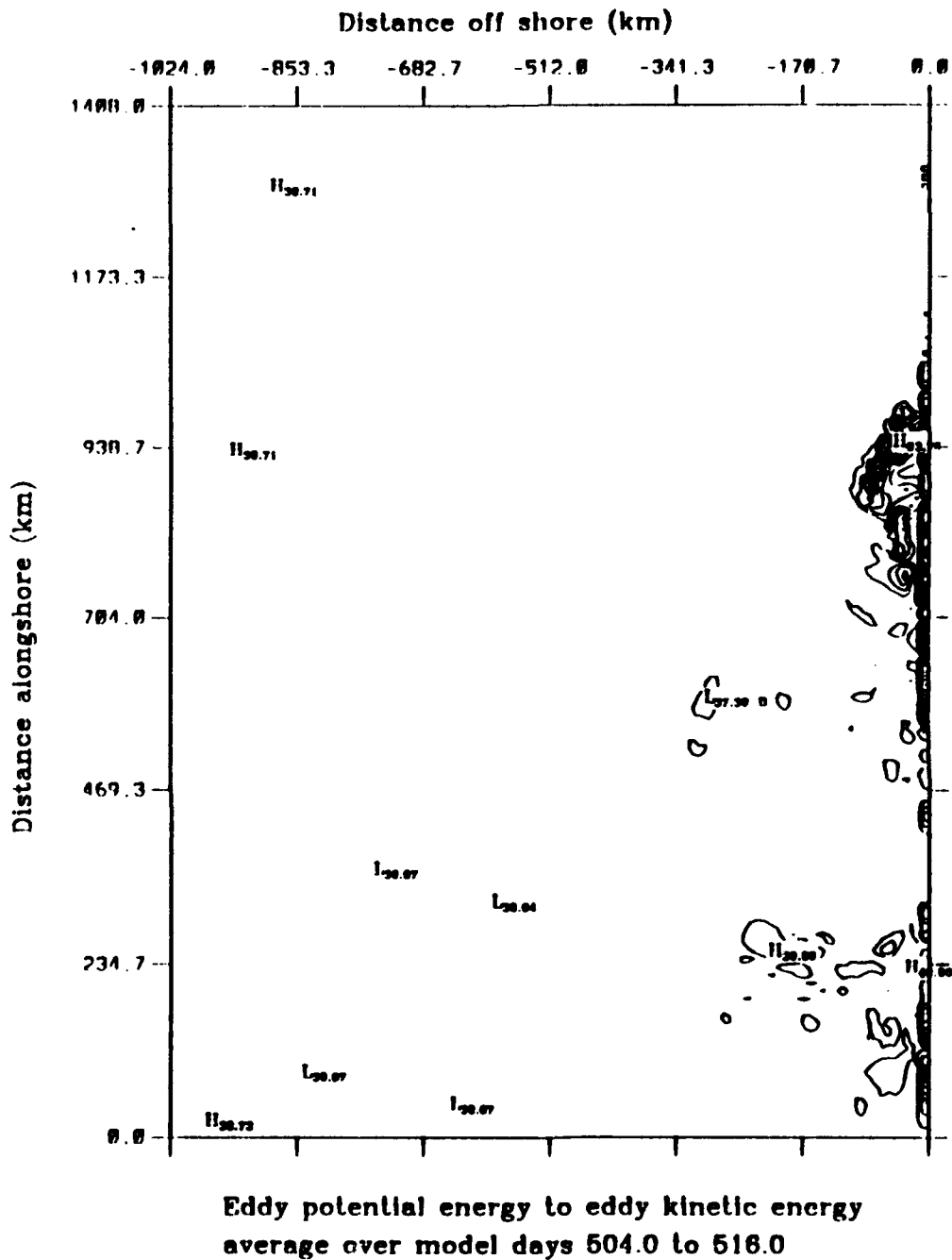


**Figure D.6** Experiment 4: Energy transfers of eddy potential to eddy kinetic energy (i.e., baroclinic energy transfer) for Climo II, for model days 504 to 516 (yd 138 - 150). The contour interval is  $1 \text{ ergs cm}^{-3} \text{ s}^{-1}$ .

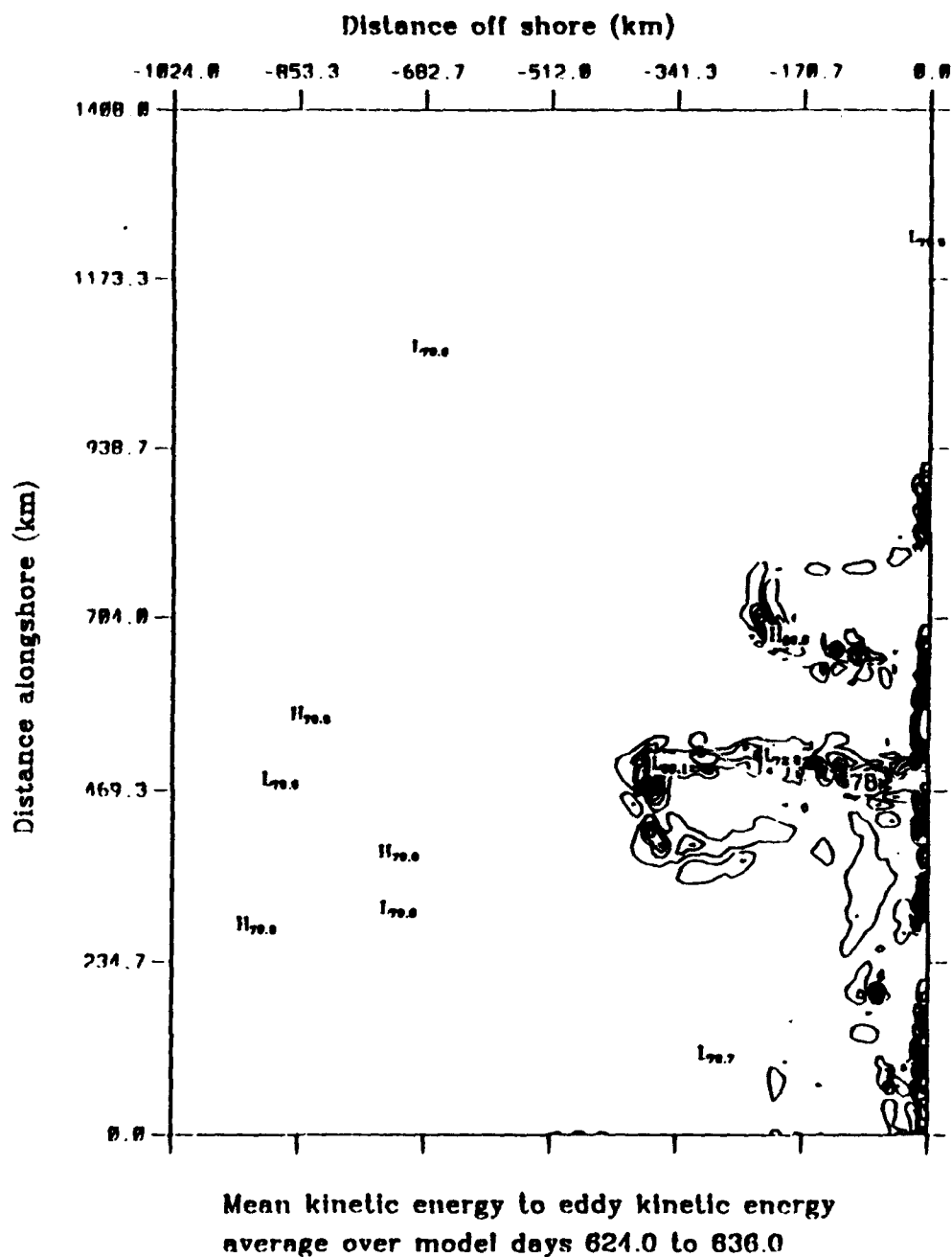


Figure D.7 Experiment 4: Energy transfers of mean to eddy kinetic energy (i.e., barotropic energy transfer) for Climo II, for model days 624 to 636 (yd 258 - 270). The contour interval is  $1 \text{ ergs cm}^{-3} \text{ s}^{-1}$ .







## **APPENDIX E. INSTABILITIES FOR EXPERIMENT 5 (1982)**

This appendix contains additional analyses from Experiment 5 (1982) for the periods when the total kinetic energy per unit mass became quasi-steady. Energy transfer plots which consist of barotropic (mean kinetic energy to eddy kinetic energy) and baroclinic (eddy potential energy to eddy kinetic energy) were produced for the following model days: 507 - 516 (yd 141 - 150), and 525 - 528 (yd 159 - 162). These plots appear as Figures E.1 through E.4.

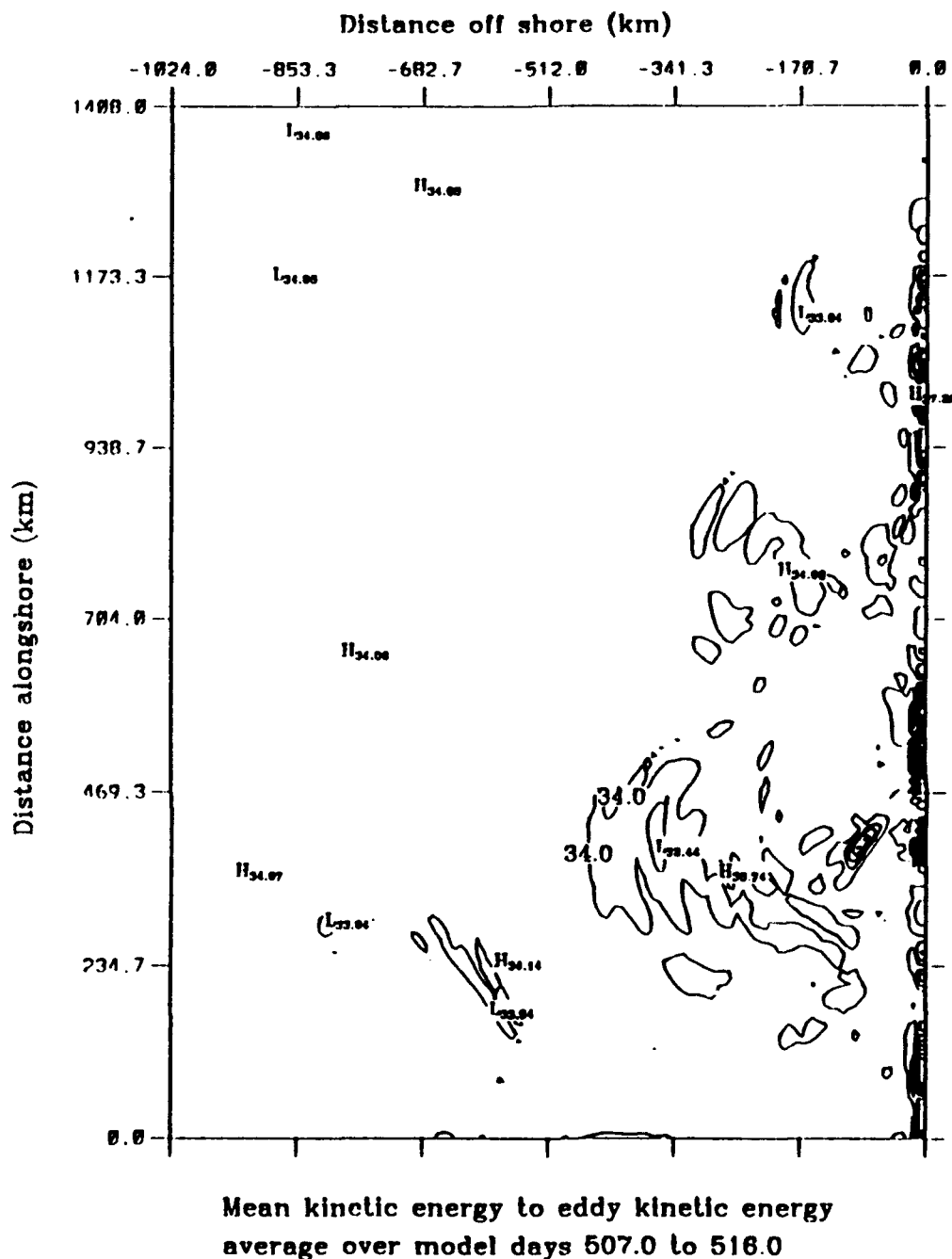


**Figure E.1** Experiment 5: Energy transfers of mean to eddy kinetic energy (i.e., barotropic energy transfer) for 1982, for model days 507 to 516 (yd 141 - 150). The contour interval is  $1 \text{ ergs cm}^{-3} \text{ s}^{-1}$ .

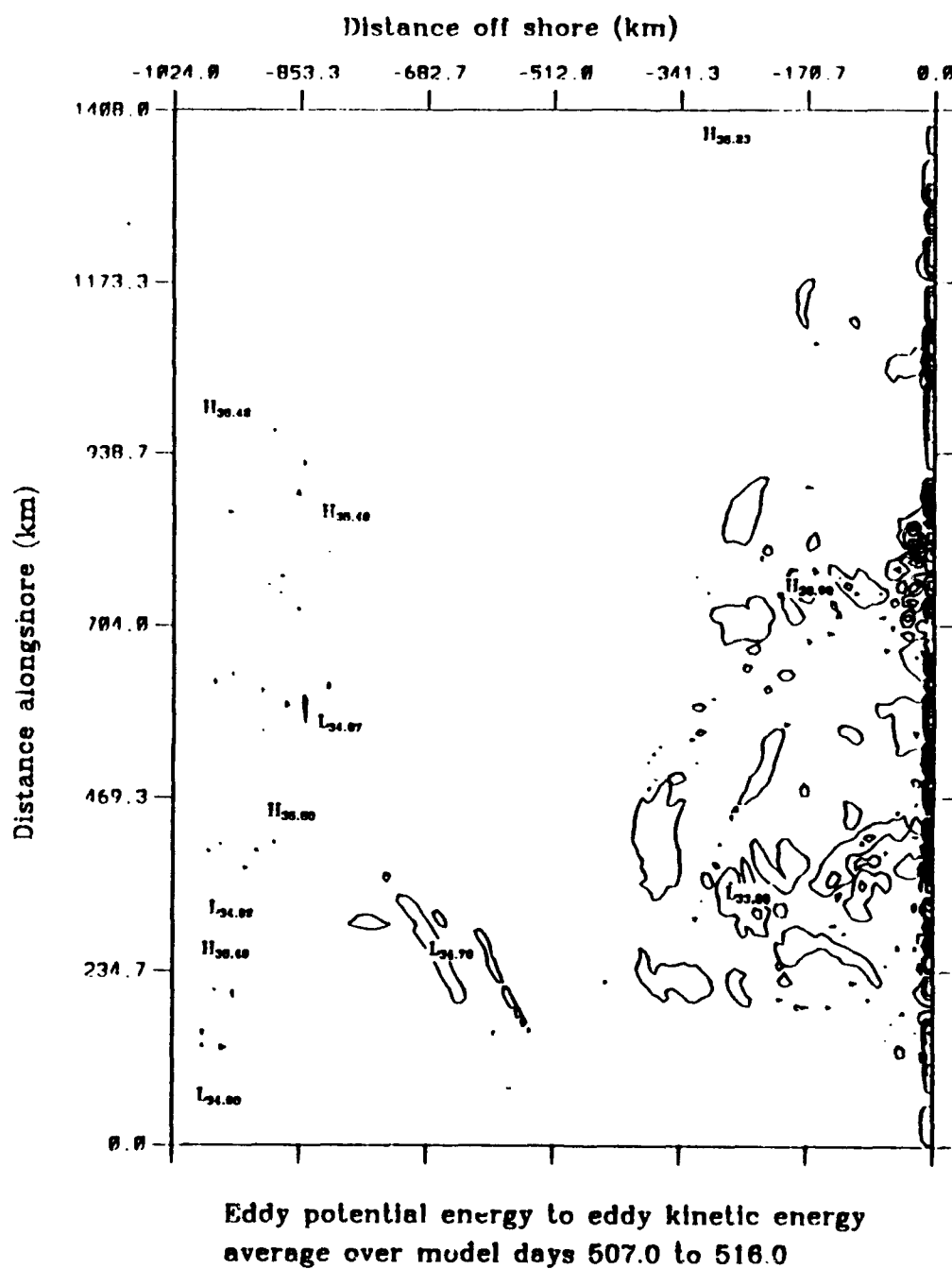
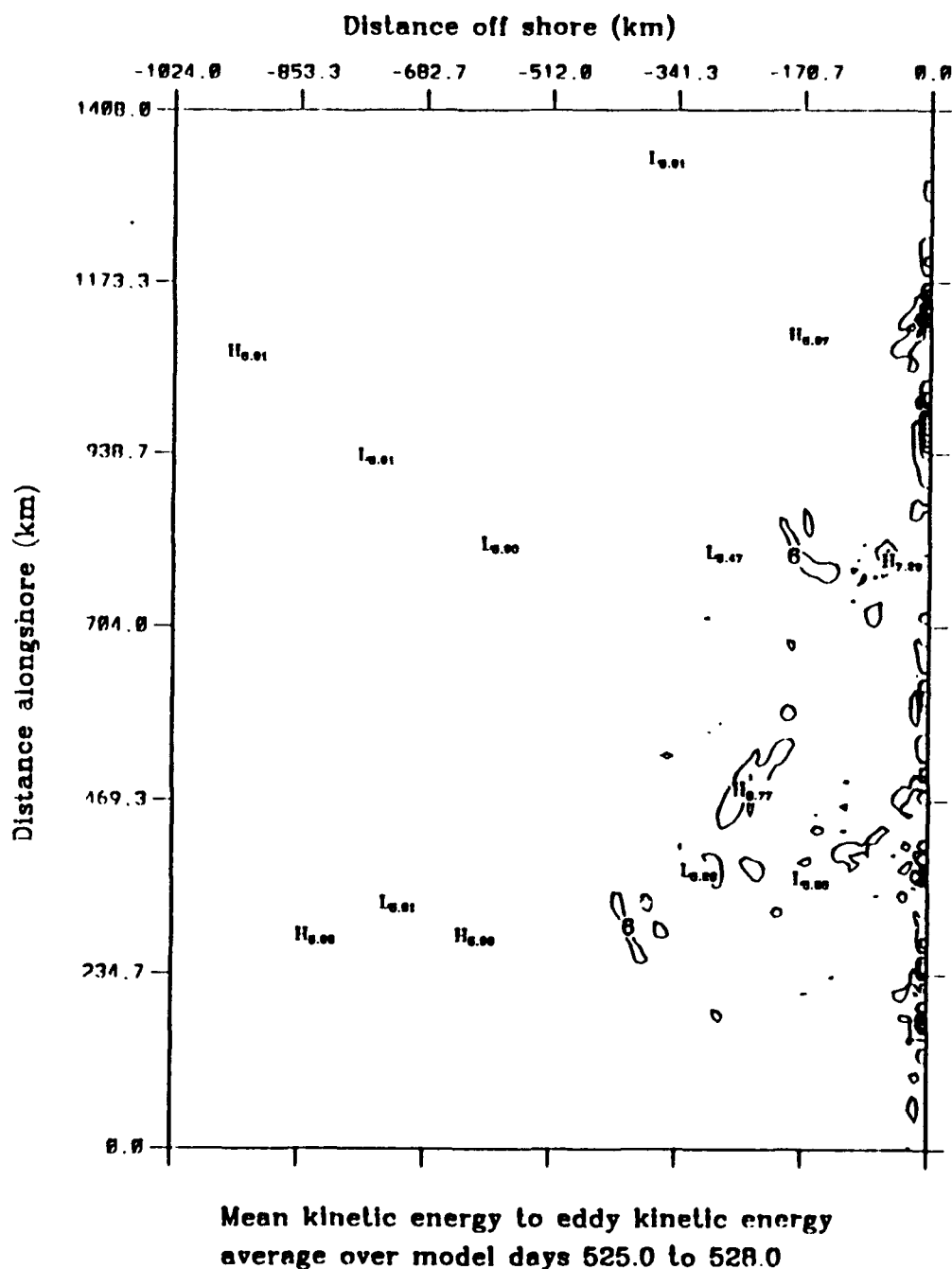


**Figure E.2** Experiment 5: Energy transfers of eddy potential to eddy kinetic energy (i.e., baroclinic energy transfer) for 1982, for model days 507 to 516 (yd 141 - 150). The contour interval is  $1 \text{ ergs cm}^{-3} \text{ s}^{-1}$ .



Mean kinetic energy to eddy kinetic energy  
average over model days 525.0 to 528.0

**Figure E.3** Experiment 5: Energy transfers of mean to eddy kinetic energy (i.e., barotropic energy transfer) for 1982, for model days 525 to 528 (yd 159 - 162). The contour interval is  $1 \text{ ergs cm}^{-3} \text{ s}^{-1}$ .





## **APPENDIX F. INSTABILITIES FOR EXPERIMENT 6 (1984)**

This appendix contains additional analyses from Experiment 6 (1984) for the periods when the total kinetic energy per unit mass became quasi-steady. Energy transfer plots which consist of barotropic (mean kinetic energy to eddy kinetic energy) and baroclinic (eddy potential energy to eddy kinetic energy) were produced for the following model days: 576 - 591 (yd 210 - 225), 606 - 624 (yd 240 - 258), and 645 - 657 (yd 279 - 291). These plots appear as Figures F.1 through F.6.

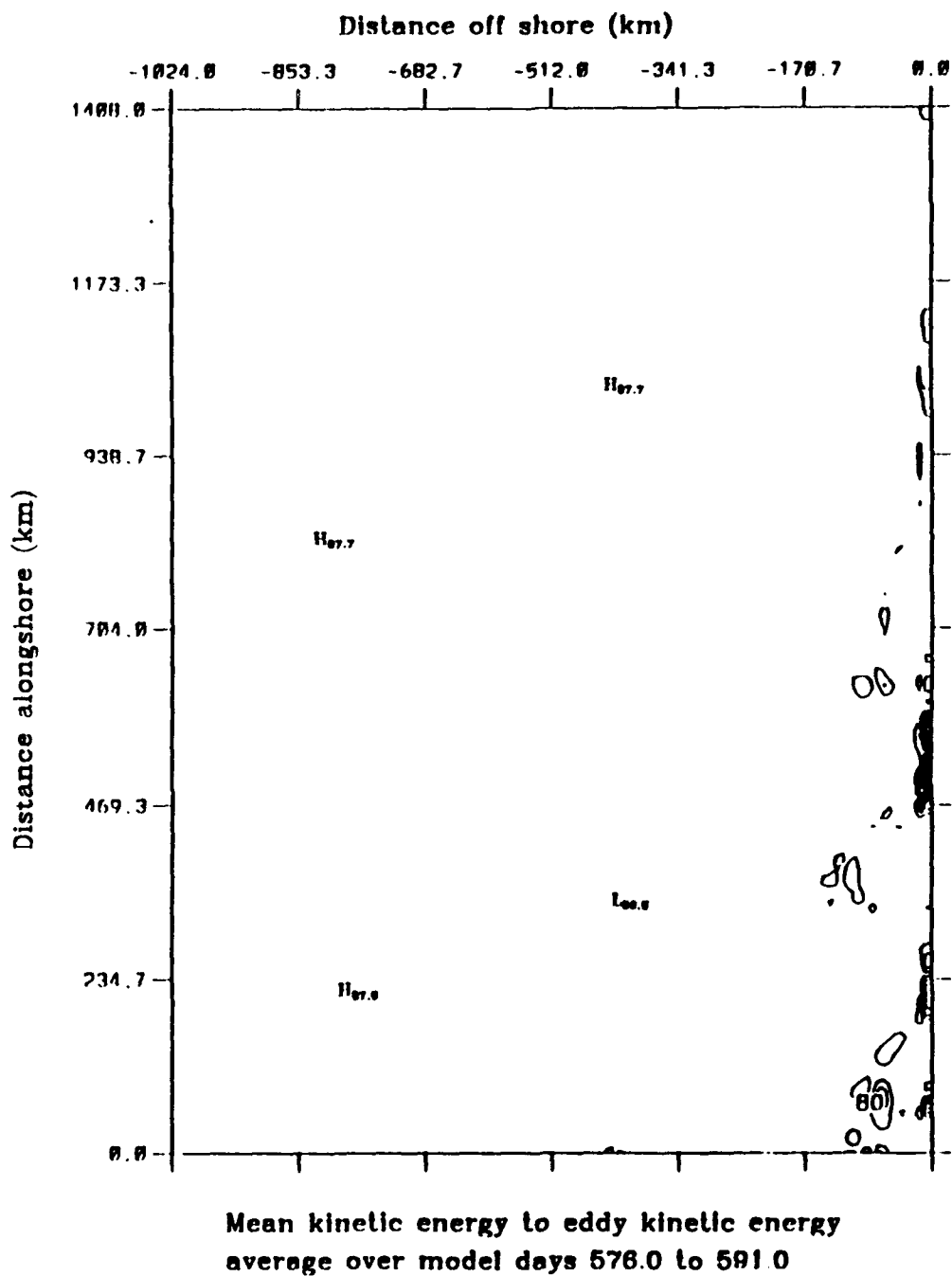


**Figure F.1** Experiment 6: Energy transfers of mean to eddy kinetic energy (i.e., barotropic energy transfer) for 1984, for model days 576 to 591 (yd 210 - 225). The contour interval is  $10 \text{ ergs cm}^{-3} \text{ s}^{-1}$ .







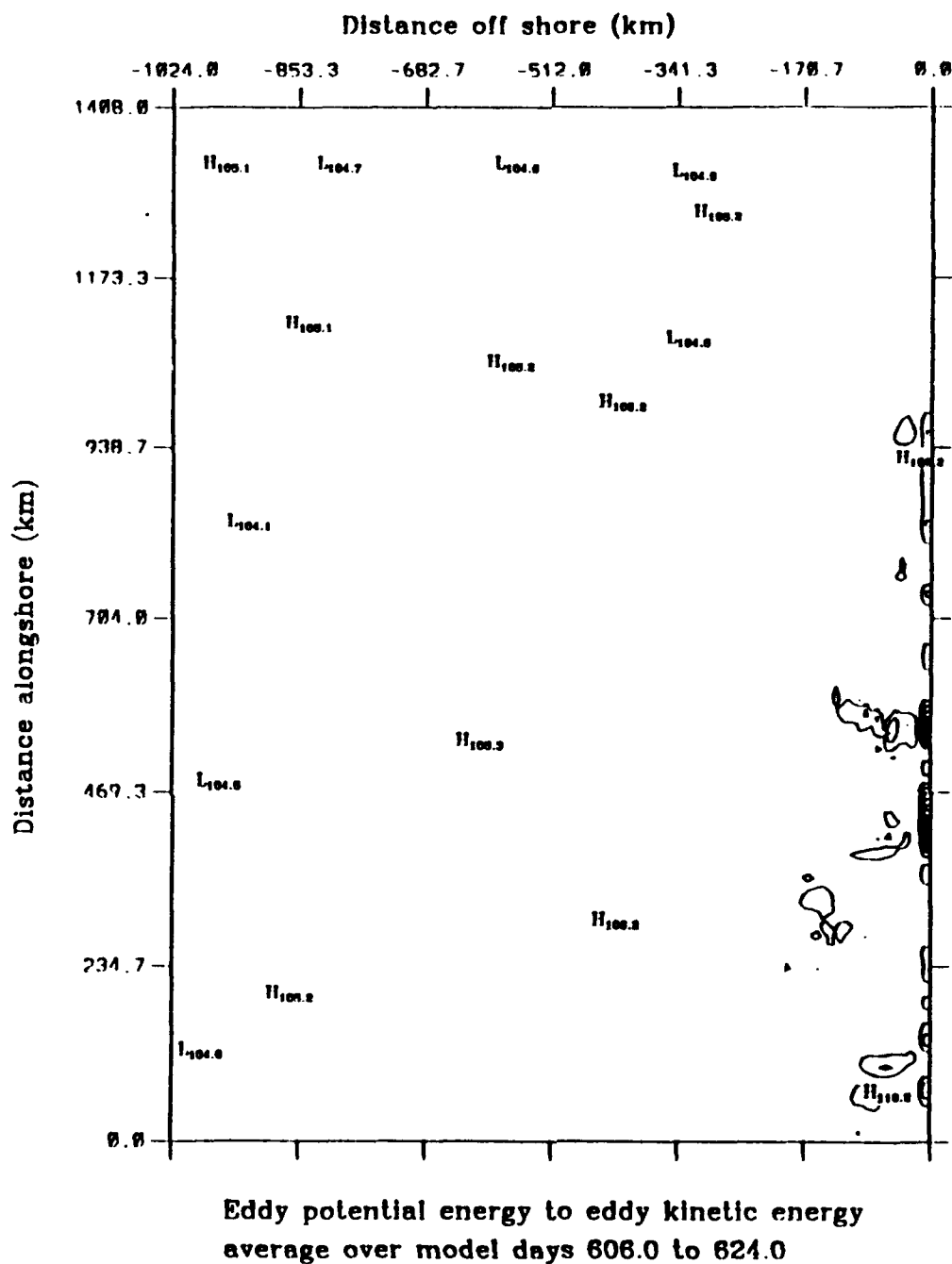


**Figure F.4** Experiment 6: Energy transfers of eddy potential to eddy kinetic energy (i.e., baroclinic energy transfer) for 1984, for model days 606 to 624 (yd 240 - 258). The contour interval is  $10 \text{ ergs cm}^{-3} \text{ s}^{-1}$ .

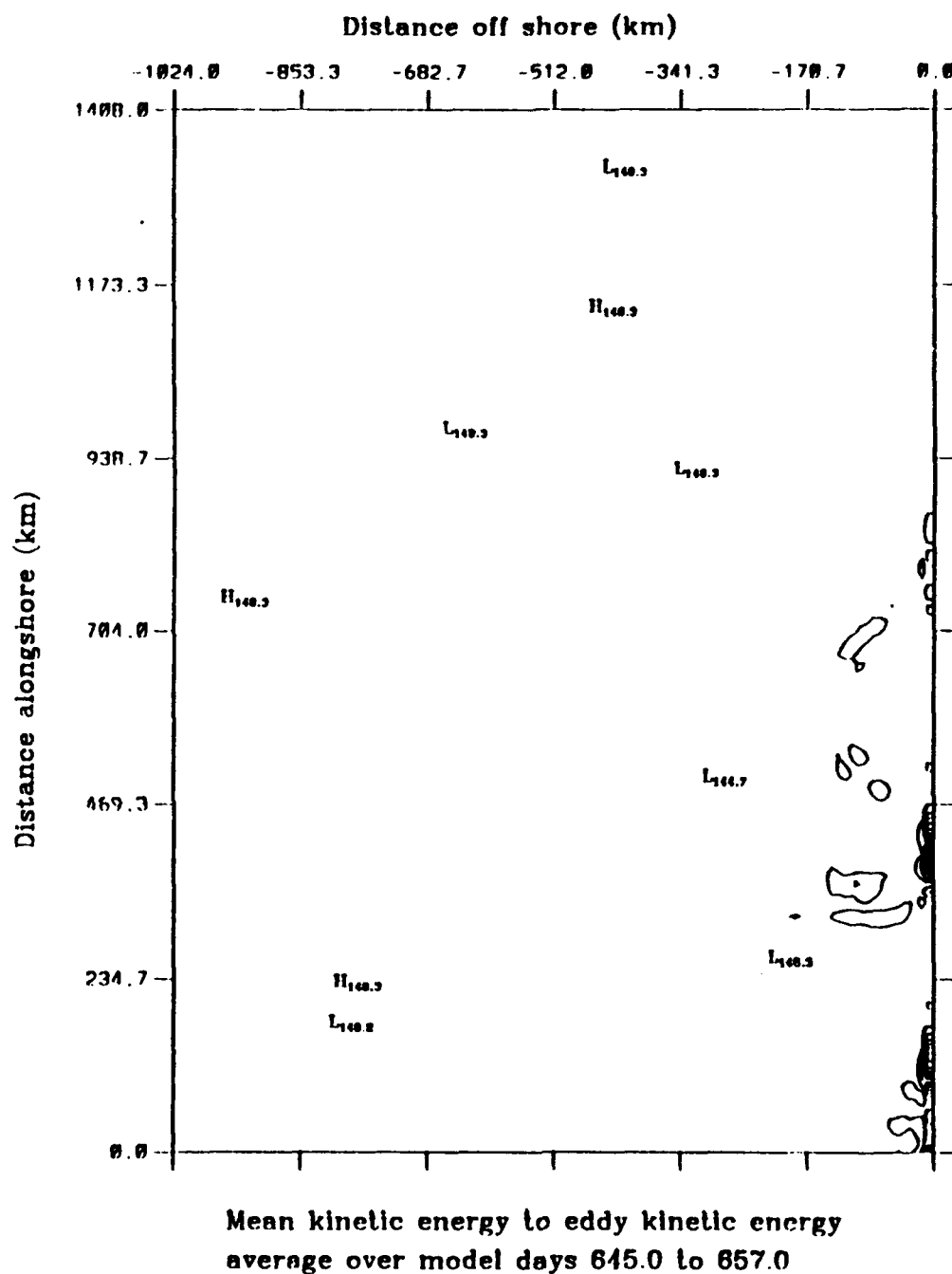


**Figure F.5** Experiment 6: Energy transfers of mean to eddy kinetic energy (i.e., barotropic energy transfer) for 1984, for model days 645 to 657 (yd 279 - 291). The contour interval is  $10 \text{ ergs cm}^{-3} \text{ s}^{-1}$ .

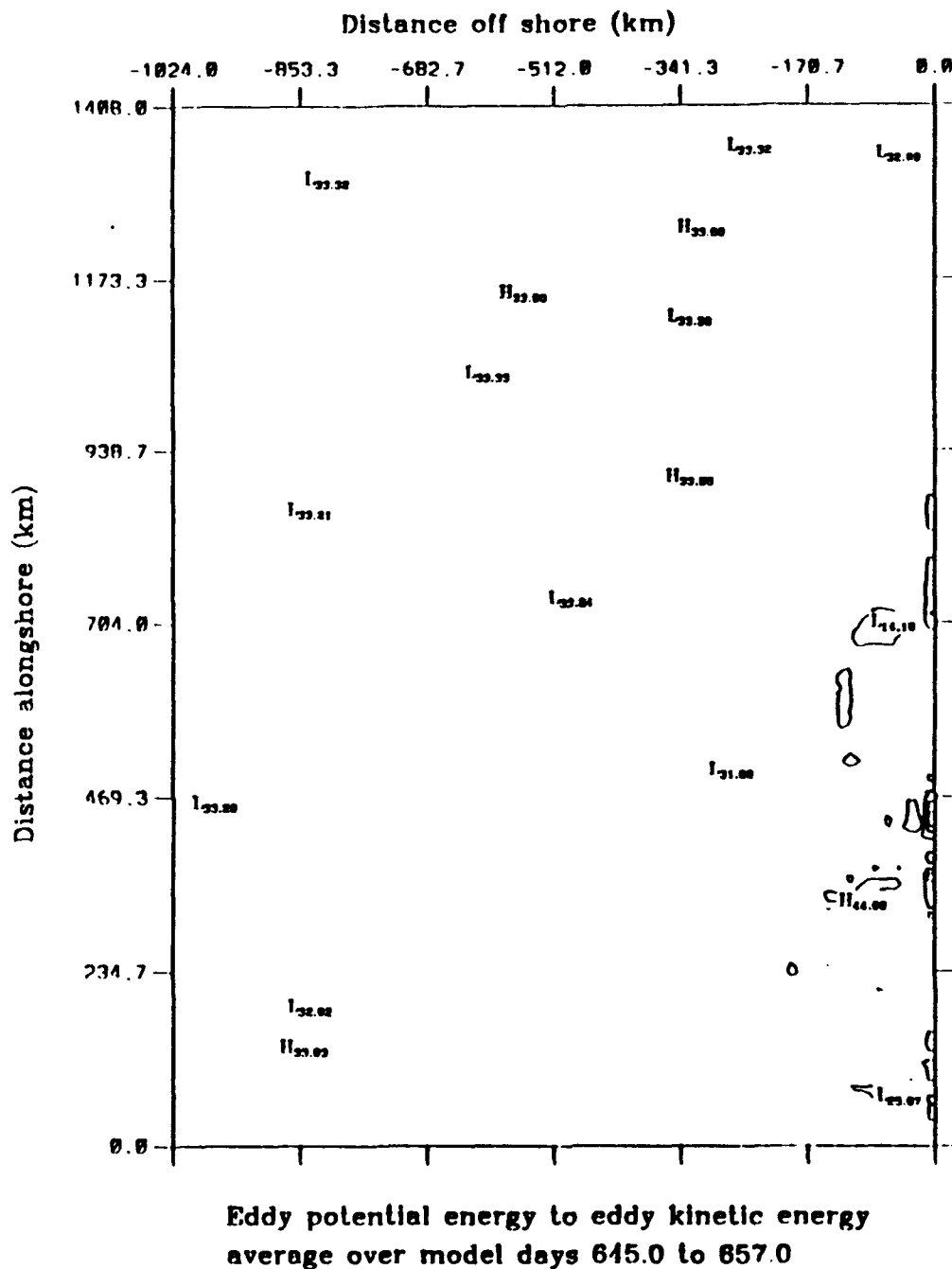


**Figure F.6** Experiment 6: Energy transfers of eddy potential to eddy kinetic energy (i.e., baroclinic energy transfer) for 1984, for model days 645 to 657 (yd 279 - 291). The contour interval is  $10 \text{ ergs cm}^{-3} \text{ s}^{-1}$ .



## LIST OF REFERENCES

- Allen, J.S., 1980: Models of wind-driven currents on the continental shelf. *Ann. Rev. Fluid Mech.*, 12, 389-433.
- Arakawa, A., and V.R. Lamb, 1977: Computational design of the basic dynamical processes of the UCLA general circulation model. In, *Methods in Computational Physics*, J. Chang, ed., Academic Press, 17, 173-265.
- Batteen, M.L., 1989: Model simulations of a coastal jet and undercurrent in the presence of eddies and jets in the California Current System. In, *Poleward Flows Along Eastern Ocean Boundaries*, S.J. Neshyba, C.N.K. Mooers, R.L. Smith and R.T. Barber, eds., Springer-Verlag, 263-279.
- Batteen, M.L., and Y.-J. Han, 1981: On the computational noise of finite-difference schemes used in ocean models. *Tellus*, 33, 387-396.
- Batteen, M.L., R.L. Haney, T.A. Tielking, and P.G. Renaud, 1989: A numerical study of wind forcing of eddies and jets in the California Current System. *J. Mar. Res.*, 47, 493-523.
- Batteen, M.L., M.J. Rutherford, and E.J. Bayler, 1992: A numerical study of wind- and thermal-forcing effects on the ocean circulation off Western Australia. *J. Phys. Oceanogr.*, 22, 1406-1433.
- Bjerknes, J., 1966: A possible response of the atmospheric Hadley circulation to equatorial anomalies of ocean temperature. *Tellus*, 18, 820-829.
- Blumberg, A.F., and G.L. Mellor, 1987: A description of a three-dimensional coastal ocean circulation model. In, *Three-dimensional Ocean Models*, N. Heaps, ed., American Geophysical Union, 4, 1-16.
- Breaker, L.C., and C.N.K. Mooers, 1986: Oceanic variability off the central California coast. *Prog. in Oceanogr.*, 17, 61-135.
- Camerlengo, A.L., and J.J. O'Brien, 1980: Open boundary conditions in rotating fluids. *J. Comput. Physics*, 35, 12-35.

- Carton, J.A., 1984: Coastal circulation caused by an isolated storm. *J. Phys. Oceanogr.*, 14, 114-124.
- Carton, J.A., and S.G.H. Philander, 1984. Coastal upwelling viewed as a stochastic phenomena. *J. Phys. Oceanogr.*, 14, 1499-1509.
- Chelton, D.B., 1984: Seasonal variability of alongshore geostrophic velocity off central California. *J. Geophys. Res.*, 89, 3473-3486.
- Enfield, D.B., 1989: El Niño, past and present. *Rev. Geophys.*, 27, 159-187.
- Haines, R.T., 1994: A numerical study of interannual wind forcing effects on the California Current System, 1980-1983. M.S. Thesis, Naval Postgraduate School, 138 pp.
- Halliwel, Jr., G.R., and J.S. Allen, 1987: The large-scale coastal wind field along the west coast of North America, 1981-1982. *J. Geophys. Res.*, 92, 1861-1884.
- Han, Y.-J., 1975: Numerical simulation of mesoscale eddies. PH.D. Thesis, University of California, Los Angeles, 154 pp.
- Haney, R.L., 1974: A numerical study of the response of an idealized ocean to large-scale surface heat and momentum flux. *J. Phys. Oceanogr.*, 4, 145-167.
- Haney, R.L., 1985: Midlatitude sea surface temperature anomalies: A numerical hindcast. *J. Phys. Oceanogr.*, 15, 787-799.
- Hickey, B.M., 1979: The California Current System - hypothesis and facts. *Prog. Oceanogr.*, 8, 191-279.
- Holland, W.R., 1978: the role of mesoscale eddies in the general circulation of the ocean - numerical experiments using a wind-driven quasigeostrophic model. *J. Phys. Oceanogr.*, 8, 363-392.
- Holland, W.R., and M.L. Batteen, 1986: The parameterization of subgrid scale heat diffusion in eddy-resolved ocean circulation models. *J. Phys. Oceanogr.*, 16, 200-206.
- Huyer, A., 1983: Coastal upwelling in the California Current System. *Prog. in Oceanogr.*, 12, 259-284.



- Huyer, A., P.M. Kosro, S.J. Lentz, and R.C. Beardsley, 1989: Poleward flow in the California Current System. In, *Poleward Flows Along Eastern Ocean Boundaries*, S.J. Neshyba, C.N.K. Mooers, R.L. Smith and R.T. Barber, eds., Lecture Notes on Coastal and Estuarine Studies, Springer-Verlag, 142-159.
- McCreary, J.P., P.K. Kundu, and S.-Y. Chao, 1987: On the dynamics of the California Current System. *J. Mar. Res.*, 45, 1-32.
- Mitchell, R.P., 1993: A numerical study of seasonal wind forcing effects on the California Current System. M.S. Thesis, Naval Postgraduate School, 125 pp.
- Mooers, C.N.K., and A.R. Robinson, 1984: Turbulent jets and eddies in the California Current and inferred cross-shore transports. *Science*, 223, 51-53.
- Nelson, C.S., 1977: Wind stress and wind stress curl over the California Current. *NOAA Tech. Rep. NMFS SSFR-714*, U.S. Dept. Commerce, 87 pp.
- O'Brien, J.J., R.M. Clancy, A.J. Clarke, M. Crepon, R. Elsbery, T. Gammelsrod, M. MacVean, L.P. Roed, and J.D. Thompson, 1977: Upwelling in the ocean: Two- and Three-dimensional model of upper ocean dynamics and variability. In, *Modelling and Prediction of the Upper Layers of the Ocean*, E.B. Kraus, ed., Pergamon Press, New York, 178-228.
- Pedlosky, J., 1974: Longshore currents, upwelling and bottom topography. *J. Phys. Oceanogr.*, 4, 214-226.
- Philander, S.G.H., 1990: *El Niño, La Niña, and the Southern Oscillation*. Academic Press, Inc., 289 pp.
- Philander, S.G.H., and J.-H. Yoon, 1982: Eastern boundary currents and coastal upwelling. *J. Phys. Oceanogr.*, 12, 862-879.
- Rienecker, M.M., and C.N.K. Mooers, 1986: The 1982-1983 El Niño signal off northern California. *J. Geophys. Res.*, 91, 6597-6608.
- Semtner, A.J., and Y. Mintz, 1977: Numerical simulation of the Gulf Stream and midocean eddies. *J. Phys. Oceanogr.*, 7, 208-230.

- Simpson, J.J., 1983: Large-scale thermal anomalies in the California Current during the 1982-1983 El Niño. *Geophys. Res. Lett.*, 10, 937-940.
- Simpson, J.J., 1984: El Niño-induced onshore transport in the California Current during 1982-1983. *Geophys. Res. Lett.*, 11, 233-236.
- Tielking, T.A., 1988: Wind forcing of eddies and jets in the California Current System. M.S. Thesis, Naval Postgraduate School, 107 pp.
- Tisch, T.D., S.R. Ramp, and C.A. Collins, 1992: Observations of the geostrophic current and water mass characteristics off Point Sur, California, from May 1988 through November 1989. *J. Geophys. Res.*, 97, 12535-12555.
- Trenberth, K.E., W.G. Large, and J.G. Olson, 1990: The mean annual cycle in global ocean wind stress. *J. Phys. Oceanogr.*, 20, 1742-1760.
- Weatherly, G.L., 1972: A study of the bottom boundary layer of the Florida Current. *J. Phys. Oceanogr.*, 2, 54-72.
- Wickham, J.B., A.A. Bird, and C.N.K. Mooers, 1987: Mean and variable flow over the central California continental Margin, 1978-1980. *Cont. Shelf Res.*, 7, 827-849.

# INITIAL DISTRIBUTION LIST

	No. Copies
1. Defense Technical Information Center Cameron Station Alexandria, VA 22304-6145	2
2. Librarian, Code 52 Naval Postgraduate School Monterey, CA 93943-5101	2
3. Chairman (Code OC/Bf) Department of Oceanography Naval Postgraduate School Monterey, CA 93943-5122	1
4. Chairman (Code MR/Hy) Department of Meteorology Naval Postgraduate School Monterey, CA 93943-5114	1
5. Dr. Mary L. Batteen, (Code OC/Bv) Department of Oceanography Naval Postgraduate School Monterey, CA 93943-5122	2
6. Dr. Curtis A. Collins, (Code OC/Co) Department of Oceanography Naval Postgraduate School Monterey, CA 93943-5122	1
7. Dr. Leslie K. Rosenfeld (Code OC/Ro) Department of Oceanography Naval Postgraduate School Monterey, CA 93943-5122	1
8. LT James Vann 12 Hedgerow Place Jackson, TN 38305	2
9. Director, Naval Oceanography Division Naval Observatory 34th and Massachusetts Ave, NW Washington, DC 20390	1

- |     |   |   |
|-----|---|---|
| 10. | Commander   | 1 |
|     | Naval Meteorology and Oceanography Command          |   |
|     | 1020 Balch Boulevard                                |   |
|     | Stennis Space Center, MS 39529-5005                 |   |
| 11. | Commanding Officer                                  | 1 |
|     | Naval Oceanographic Office                          |   |
|     | Stennis Space Center, MS 39529-5000                 |   |
| 12. | Commanding Officer                                  |   |
|     | Fleet Numerical Meteorology and Oceanography Center | 1 |
|     | 7 Grace Hopper Avenue, STOP 1                       |   |
|     | Monterey, CA 93943-5001                             |   |